Engineered Fiber-Reinforced Architected Cellular Composites: A Strategy to Develop Sustainable and Recyclable Advanced Materials

Ehsan Estakhrianhaghighi

Department of Bioresource Engineering
McGill University, Montreal

August 2023

A thesis submitted to McGill University in partial fulfillment of the requirements of the degree of Doctor of Philosophy

Abstract

Over the past few decades, the quest for lightweight and high-performance materials with multifunctional properties has driven the development of advanced fiber-reinforced composites and architected cellular solids. Exploiting the advantages of these two classes of engineered materials has led to the emergence of architected cellular fiber-reinforced composites (CFRC), a novel class of low-density materials with high stiffness-, strength- and energy absorption-to-mass ratios. Bio-based polymers and cellulose-based (herein wood) compounds are promising materials for developing sustainable CFRCs due to their renewability, biodegradability and low environmental impact. The development of CFRCs that use these sustainable materials can contribute to the creation of high-performance and environmentally friendly materials. Moreover, the use of additive manufacturing techniques facilitates the engineering of the underlying architecture of these materials leading to the realization of low-cost materials with controllable thermomechanical properties.

This thesis presents a comprehensive investigation on the thermomechanical properties of CFRCs composed of bio-based polymers and wood fibers. To better understand the effective thermomechanical properties of these materials, a multiscale standard mechanics homogenization method is introduced, named as multi-level method, to determine the effective properties of CFRCs. By generating Representative Volume Elements (RVEs) for a wide range of architectural and constituent materials' parameters, the efficacy of the multi-level approach is investigated compared to detailed multiscale analyses. Furthermore, strut-based quasi-isotropic bimaterial and trimaterial composite microarchitectures are engineered using the multi-level method and introduced analytical techniques to evaluate their thermomechanical properties. The quasi-isotropic mechanical properties of the designed two- and three-dimensional cellular composites

(named *Isomixed*, showing isotropic modulus of elasticity; and *Isoflex*, showing isotropic flexural rigidity) are experimentally assessed through a series of tests on 3D printed samples. The effect of cell topology and fiber volume fraction on enhancing the thermomechanical properties of a multi-material cellular composite is investigated numerically and experimentally. Moreover, a novel methodology is developed for integrating waste wood fibers, a versatile renewable resource of cellulose, into polylactic acid (PLA) polymers to produce sustainable WF-PLA filaments. High-performance architected cellular composites with enhanced thermomechanical properties-to-mass ratios are 3D printed using the produced WF-PLA filaments, and experimental dogbone tensile and three-point bending tests are conducted on the 3D printed samples.

The findings of this thesis show significant promise for developing sustainable and high-performance CFRCs for industrial sectors where utilizing lightweight and strong sustainable materials is essential. The use of bio-based polymers and wood fiber compounds in the development of CFRCs can contribute to reducing the environmental impact of structural materials, enhancing the thermomechanical properties, and storing carbon in construction materials, while providing a foundation for future research and development of advanced materials and manufacturing techniques for a more sustainable future.

Résumé

Au cours des dernières décennies, la recherche de matériaux légers et performants aux propriétés multifonctionnelles a conduit au développement de composites avancés renforcés de fibres et de solides cellulaires architecturés. L'exploitation des avantages de ces deux classes de matériaux d'ingénierie a conduit à l'émergence de composites architecturés renforcés de fibres cellulaires (CFRC), une nouvelle classe de matériaux à faible densité avec des rapports rigidité, résistance et absorption d'énergie sur masse élevés. Les polymères biosourcés et les composites à base de cellulose (bois) sont des matériaux prometteurs pour développer des CFRC durables en raison de leur renouvelabilité, de leur biodégradabilité et de leur faible impact environnemental. Le développement de CFRC utilisant ces matériaux durables peut contribuer à créer des matériaux performants et respectueux de l'environnement. De plus, l'utilisation de techniques de fabrication additive peut faciliter la conception de l'architecture sous-jacente de ces matériaux conduisant à la réalisation de matériaux à faible coût avec des propriétés thermomécaniques contrôlables.

Cette thèse présente une étude approfondie des propriétés thermomécaniques des CFRC composés de polymères biosourcés et de composés à base de cellulose (bois). Pour mieux comprendre les propriétés thermomécaniques effectives de ces matériaux, une méthode d'homogénéisation mécanique standard multi-échelles est introduite, appelée méthode multi-niveaux, pour déterminer les propriétés effectives des CFRC. En générant des éléments de volume représentatifs (RVE) pour une large gamme de paramètres architecturaux et de matériaux constitutifs, l'efficacité de l'approche multi-niveaux est étudiée par rapport à des analyses multi-échelles détaillées. En outre, de nouvelles microarchitectures composites bi-matériaux et tri-matériaux quasi-isotropes à base d'entretoises ont été conçues à l'aide de la méthode à plusieurs niveaux et ont introduit des techniques analytiques pour évaluer leurs propriétés

thermomécaniques. Les propriétés mécaniques quasi-isotropes des composites cellulaires 2D et 3D conçus (nommés « *Isomixed* », montrant un module d'élasticité isotrope, et « *Isoflex* », montrant une rigidité en flexion isotrope) ont été expérimentalement évaluées par une série de tests sur des échantillons imprimés en 3D. L'effet de la topologie cellulaire et de la fraction volumique des fibres sur l'amélioration des propriétés thermomécaniques d'un composite cellulaire multi-matériaux a été étudié expérimentalement et numériquement. De plus, une nouvelle méthodologie a été développée pour intégrer les déchets de fibres de bois, une ressource renouvelable polyvalente de cellulose, dans des polymères d'acide polylactique (PLA) pour produire des filaments WF-PLA durables. Des composites cellulaires architecturés hautes performances avec des rapports propriétés thermomécaniques/masse améliorés ont été imprimés en 3D à l'aide des filaments WF-PLA produits, et des tests expérimentaux de traction en os de chien et de flexion en trois points ont été effectués sur les échantillons imprimés en 3D.

Les résultats de cette thèse sont très prometteurs pour le développement de CFRC durables et performants pour les secteurs industriels où des matériaux durables légers et solides sont essentiels. L'utilisation de polymères biosourcés et de composés à base de cellulose (bois) dans le développement des CFRC peut contribuer à réduire l'impact environnemental des matériaux et à améliorer les propriétés thermomécaniques et fournit une base pour la recherche et le développement futurs de matériaux et de techniques avancés pour un avenir plus durable.

Contents

List of Figures

List of Tables

Acknowledgments

I would like to take this opportunity to express my deep appreciation and gratitude to Prof. Abdolhamid Akbarzadeh and Prof. Larry Lessard, my esteemed supervisor and co-supervisor, for their invaluable guidance and unwavering supports during my PhD journey. Their active involvement in my research endeavors and insightful feedbacks on my studies have been instrumental in shaping my academic growth.

Furthermore, I am incredibly grateful for the financial supports provided to our research activities in Advanced Multifunctional and Multiphysics Metamaterials Lab (AM^3L) through Natural Sciences and Engineering Research Council of Canada (NSERC), Canada Foundation for Innovation (CFI), McGill Sustainability Systems Initiative (MSSI) Ideas Fund, CREPEC, Canada Research Chairs program in Multifunctional Metamaterials, Centre SÈVE – Centre de Recherche en Sciences du Végétal, McGill Graduate Excellence Award, and McGill Bioresource Engineering Award.

I am deeply thankful to my colleagues and friends in AM^3L lab, including Armin Mirabolghasemi, Alireza Seyedkanani, Jiahao Shi, Shahin Eskandari, Hossein Mofatteh, Jun Cai, Youjian Li and Hamed Niknamjahromi, to name a few, for their unwavering supports and friendship throughout the years of my Ph.D. study.

Lastly, I want to express my heartfelt gratitude to my family for their unwavering support, encouragement and love throughout my life. Their constant efforts and the joy, hope and passion they bring to my life have been the cornerstone of my success and happiness.

Contribution to Original Knowledge

Chapters 2 to **4** present the main contributions of the current thesis. These contributions are summarized as follows:

Chapter 2:

- It provides a methodology for using waste-wood fibers to produce sustainable wood fiber-reinforced polylactic-acid (PLA) filaments for 3D printing high-performance architected cellular composites.
- It discusses how introducing cellulose-based (wood) compounds into bio-based polymers can improve their thermomechanical properties. The experimental results show that the 3D printed composites made of optimal wood fiber contents have increased stiffness, ultimate strength, fracture strain, toughness and thermal conductivity and reduced overall density compared to PLA.
- It introduces a novel mixed square (named *Isomixed*, showing isotropic modulus of elasticity) microarchitecture 3D printed out of WF-PLA filaments, which shows higher ultimate strength and isotropic stiffness compared to commonly used hexagonal cells.
- The WF-PLA architected composites offer a low-cost strategy to additively manufacture sustainable advanced materials with enhanced thermomechanical properties from waste materials.

Chapter 3:

- A multiscale standard mechanics homogenization with periodic boundary conditions is introduced to evaluate the properties of the created representative cells. The method's efficacy

is evaluated by creating various periodic fiber-reinforced representative cells and assessing the effects of different parameters on their thermomechanical properties. The approach is corroborated by comparing numerical and experimental data for Young's moduli of cellular metamaterials 3D printed out of pure and carbon-fiber-reinforced PETG polymer.

- The thesis introduces a hierarchical material design methodology to manipulate and manufacture cellular metamaterials with tunable isotropic/anisotropic thermomechanical properties.

Chapter 4:

- This thesis discusses the potential usage of renewable resources (bio-based polymers reinforced with waste wood fibers) in sustainable advanced materials to enhance their flexural properties and reduce their mass.
- It examines the flexural mechanical properties of FDM 3D printed polylactic-acid (PLA) composites reinforced with waste wood fiber at different percentages.
- This thesis also designs different bimaterial and trimaterial 2D architected composite cells (named *Isoflex*, showing isotropic flexural rigidity) made out of composites with varying fiber content to demonstrate the improvement in flexural rigidity and quasi-isotropic flexural rigidity property.
- The findings showed that wood fiber-reinforced engineered cellular composites offer a sustainable approach to designing and manufacturing advanced materials with tunable flexural mechanical properties.

Contribution of authors

According to the McGill University guidelines, this dissertation is organized as a Manuscript-based thesis. Three peer-reviewed scientific articles comprise this thesis in **Chapters 2** to **4** as follows:

Published journal papers:

- **Estakhrianhaghighi, E**., Mirabolghasemi, A., Zhang, Y., Lessard, L. & Akbarzadeh, A. 3D-Printed Wood fiber-reinforced Architected Cellular Composites. *Advanced Engineering Materials* **22**, 2000565, (2020). This paper is presented in *chapter two*.

  Contributions: E.E. programmed FE analysis for homogenization-based analysis, 3D printed the samples, implemented the tests and obtained the results, and wrote the paper. A.H.A. and L.L. planned the framework, provided supervision, and edited the paper. A.M. provided advisory comments, performed analytical design and edited the paper. Y.Z. worked on SEM and in the experimental section of the paper.

- **Estakhrianhaghighi, E**., Mirabolghasemi, A., Shi, J., Lessard, L. & Akbarzadeh, A. H. Architected cellular fiber-reinforced composite. Composites Part B: Engineering 238, 109894, (2022). This paper is presented in *chapter three*.

  Contributions: E.E. conducted detailed finite element analysis, analytical design, 3D printing and experimentation on cellular samples and wrote and edited the paper. A.M. provided advisory comments, performed analytical design, and edited the paper. J.S. provided comments and revised the paper. A.H.A. and L.L. planned the framework, provided supervision and wrote and edited the paper.

Submitted journal paper:

- **Ehsan Estakhrianhaghighi**, Armin Mirabolghasemi, Larry Lessard, Abdolhamid Akbarzadeh, Engineered Flexural Properties of 3D Printed Wood fiber-reinforced Architected Cellular Composite, Submitted to Additive Manufacturing (Revision requested in August 2023), May 2023. This paper is presented in *chapter four*.

Contributions: E.E. conducted detailed finite element analysis, analytical design, manufacturing process, 3D printing and experimentation on cellular samples and wrote and edited the paper. A.M. provided advisory comments, performed analytical design, and edited the paper. A.H.A. and L.L. planned the framework, provided supervision and wrote and edited the paper.

Peer-reviewed conference papers:

- **Estakhrianhaghighi, E**., Mirabolghasemi, A., Zhang, Y., Lessard, L. & Akbarzadeh, FDM 3D Printed Wood fiber-reinforced Architected Composites, Canadian Society for Mechanical Engineering International Congress, June 2021.

Contributions: E.E. programmed the FE analysis for homogenization-based analysis, 3D printed the samples, implemented tests, obtained and discussed the results, and wrote and edited the paper. A.M. provided advisory comments, performed analytical design, and edited the paper. Y.Z. was responsible for working on SEM and contributed to the experimental section of the paper. A.H.A. and L.L. planned the framework, supervised the project and edited the paper.

- **Estakhrianhaghighi, E.**, Mirabolghasemi, A., Zhang, Y., Lessard, L. & Akbarzadeh, 3D Printed Sustainable Architected Cellular Composites, Holistic Innovation in Additive Manufacturing, HI-AM Conference, June 2020.

Contributions: E.E. programmed the FE analysis for homogenization-based analysis, 3D

printed the samples, implemented tests, obtained and discussed the results, as well as writing and editing the paper. A.M. provided advisory comments, performed analytical design, and edited the paper, while Y.Z. contributed to the experimental section of the paper by working on SEM. A.H.A. and L.L. planned the framework, supervised the project and also edited the paper.

- **Estakhrianhaghighi, E.**, Mirabolghasemi, Y., Lessard, L. & Akbarzadeh, Architected Wood Fiber-reinforced Cellular Composite with Enhanced Flexural Properties, Holistic Innovation in Additive Manufacturing, HI-AM Conference, June 2023 to be presented.

Contributions: E.E. was responsible for conducting a detailed finite element analysis, analytical design, manufacturing process, 3D printing and experimentation on cellular samples. E.E. also wrote and edited the paper. A.M. provided advisory comments, performed analytical design, and edited the paper. A.H.A. and L.L. planned the framework, provided supervision and also wrote and edited the paper.

1 Chapter one: Introduction and literature review

Following the significance of material development in human history, the various stages of growth throughout history are known as the Stone age, Copper age, Bronze age and Iron age. Material scientists designed and realized alternative materials with novel characteristics over the past century. Composites, polymers, ceramics, carbon nanotubes and superalloys are just a few examples [1-3]. Each of these materials has contributed to extending charts for material selection in various areas, such as stiffness, toughness, strength, strain at failure and thermal conductivity. This development has made it possible to build and produce structures for new applications in extreme environments, such as within the human body, combustion chambers, or space travel [4]. The manipulation of molecular structures at the nano/microscale (e.g., semiconductors and biomaterials) or the special preparation of the basic materials at the macroscale (e.g., thermal treatment of metals and polymers) are the two main approaches used to accomplish distinctive characteristics in engineering materials. However, both methods require specialized tools and are frequently costly [5, 6].

1.1 Cellular materials

Since the middle of the 1970s, "Cellular Materials" have drawn increasing interest as an alternative for creating novel lightweight materials to cover the gaps in material selection patterns [7]. “An interconnected network of solid struts or plates that form the edges and faces of cells” is referred to as a cellular material or a cellular solid [8]. Cellular materials are characterized by their porous microstructure that is comprised of solid and void networks. Consequently, new properties can be augmented in the base/parent materials following a cellular solid material design approach. The expansion of the material selection chart using cellular material is shown in **Figure 1-1** for

density, thermal conductivity, Young's modulus and compression strength.

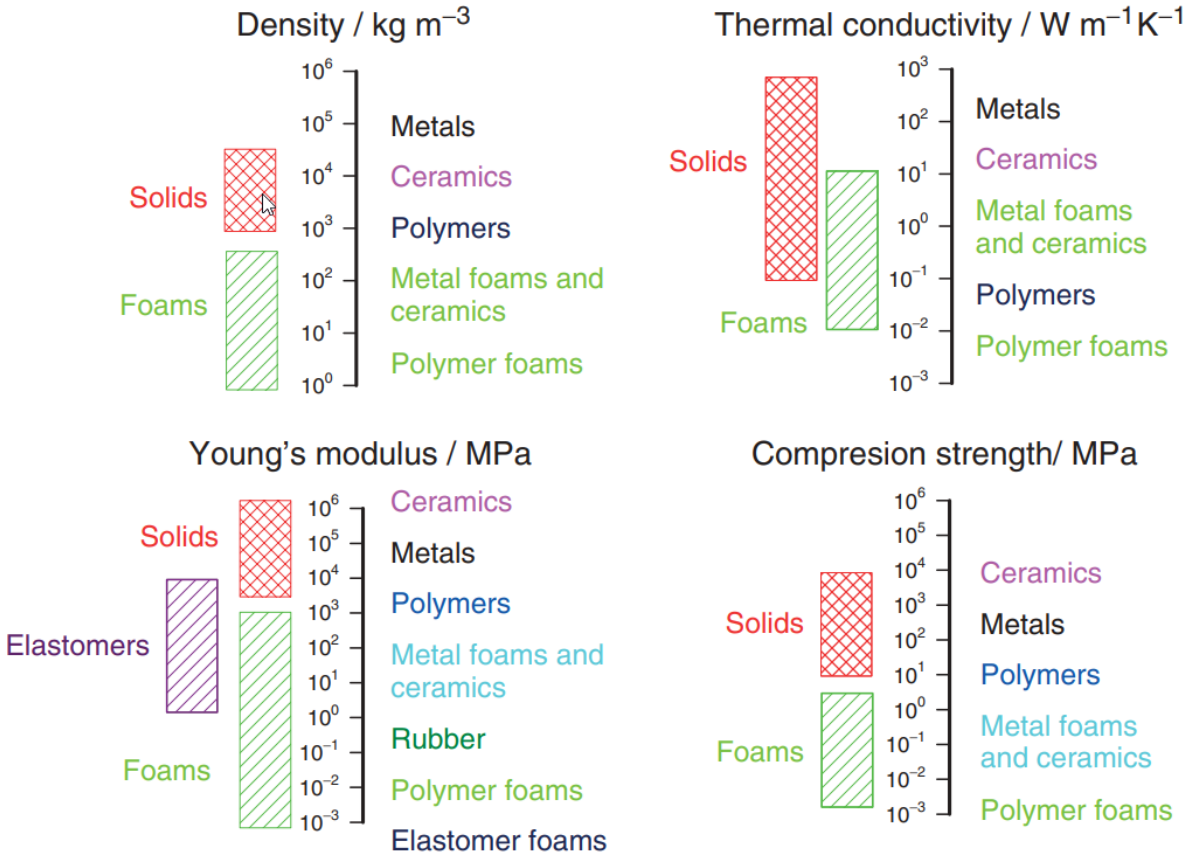

Figure 1 - 1: Comparison of density, thermal conductivity, Young's modulus and strength of dense and foam materials found in engineering applications, adopted from Ref. [9].

Metallic cellular solids can be produced with thermal conductivity and density comparable to polymers; cellular polymers can be designed and fabricated to deliver rigidity at the same level as elastomers. Based on the spread of porous unit cells, cellular materials can be split into two major categories: Stochastic structures (*foams*) and Non-Stochastic structures (*lattices*) (**Figure 1-2**). Both stochastic foams and lattices can be referred to as "cellular"; hence, in the literature, the two terms are sometimes used interchangeably [10]. In foams, such as sponge and wood foam, pores or voids are spread stochastically without having a particular pattern. Gas is frequently injected into a heated substance to create manmade foams. Foam is referred to as a closed-cell if the gas

creates distinct pockets encircled by objects and an open-cell if the gas pockets are connected [11]. On the other hand, in lattices such as hexagonal honeycombs and re-entrant architectures, cells are tessellated in a periodic or predefined pattern. Architected cellular materials are often referred to as lattice structures (or lattices), especially when they are comprised of struts and nodes. Lattices can be two or three dimensions, whereas foams are usually dispersed in space. Two-dimensional (2D) lattices possess a planar structure with cells arranged in a periodic manner, while 3D cellular materials extend the concept into the third dimension, incorporating a volumetric arrangement of cells.

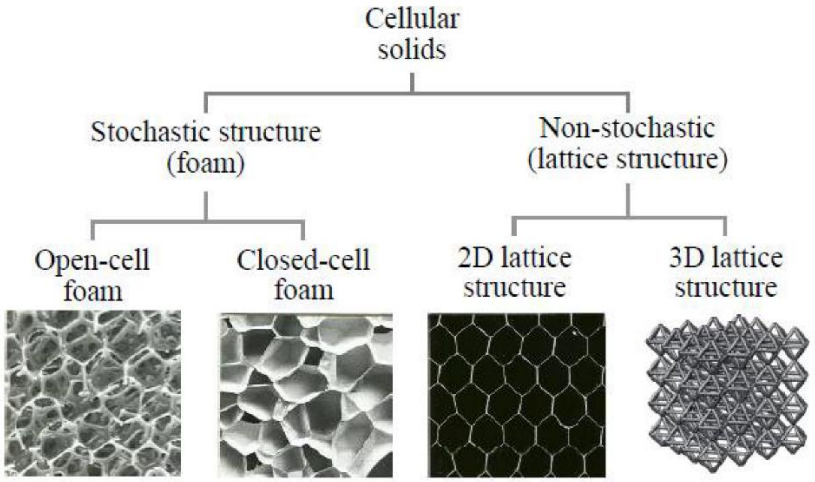

Figure 1 - 2: Different cellular solid types: Closed-cell foam, Open-cell foam, 2D extruded lattice and 3D lattice, adopted from Ref. [12].

The base material, relative density and topology are the three significant variables that determine the properties of cellular materials [8]. *Base material*: The substance that makes up the cellular material's solid portions serves as the compound's base material. Even though the idea of cellular materials allows for creating distinctive material properties, researchers are constrained by the predetermined boundaries of the base materials. *Relative Density*: The relative density of the cells in cellular materials refers to the ratio of the density of the cell material to the density of the bulk material. It is a measure of how much the cellular structure contributes to the overall density

of the material. Lower relative densities indicate a higher porosity and less mass, whereas higher relative densities indicate a denser material with less porosity. The most crucial structural factor that determines the characteristics of cellular materials is relative density. Similar to the base material, relative density sets upper and lower limits on various cellular structure characteristics. *Topology*: Topological differences allow for the acquiring of controllable properties while keeping the base material and overall mass constant. Topology can refer to the variations in geometry within the structure/architecture or the geometrical characteristics of a representative volume in lattices.

1.2 Cellular material applications

As previously mentioned, cellular materials have made it possible to achieve extraordinary properties that may not be present in any other class of materials. As a result, many industries have benefited from them, including the aerospace, automotive, energy production and construction sectors [13, 14]. Next, examples are given to show how cellular materials can increase the functionality of conventional materials and be superior in performance in multiple physical fields such as mechanical, thermal, electrical, etc.

1.2.1 Mechanical applications

While some mechanical functions might be slightly impacted, adding voids to a solid can significantly decrease its mass. Nature has used this approach to reduce mass while retaining the biological materials' strength and structural durability. Bone and wood are two examples of naturally occurring cellular materials with a high load-carrying capacity. Sandwich structures, as another example, are the most well-known mechanical components that make use of cellular architectures. Sandwich structures are three-layer structures with a low-density core in the midsection and two thin skin layers on the top and bottom sides [15]. The core typically has

significant compressive and shear strength, whereas the outside layers have high rigidity. When these two are combined, this configuration provides the sandwich structure with a high flexural modulus. The high energy absorption capacities of cellular structures are another excellent mechanical characteristic. For prevention against overloading, which lowers the stress to a level below the damage criterion, an intermediary medium is necessary. Examples of such a medium include cellular materials where the existence of the voids allows for a substantial volume reduction at constant pressure [16]. Since energy must be dissipated or absorbed to prevent harm to people or more sensitive goods, cellular solids are used in applications like vehicle bumpers, elevator shock absorbers and in the packaging industry.

1.2.2 Thermal applications

A broad range of applications utilize polymeric, ceramic and glass-based cellular materials [17] as thermal insulators. Polymer and glass have poor thermal conductivity, which can be further decreased by adding air, another low-conductivity phase. Furthermore, lattice and foam can be combined to create insulators with a much lower thermal mass than solid component materials [8]. These insulators are now used in both low-tech and high-tech products, including disposable cups, postmodern structures, turbine insulation blankets and refrigerated containers [18, 19].

1.2.3 Filtration applications

At various levels, foams and lattices can be used as filters. The most apparent use for foams in filtering is noise reduction, such as in headphone cushions. They have, however, also been employed in more complex constructions. For instance, cellular membranes are developed and used in industrial facilities to filter liquid [20]. Porous ceramic solids accomplish high-quality metal casting; impurities are removed by flowing molten metal through a cellular ceramic [21].

1.2.4 Electrical applications

The electrical characteristics of cellular materials are frequently underutilized, but their ability to dampen electromagnetic radiation serves a supplementary purpose. For instance, polymeric foams significantly lower their dielectric loss factor, which is advantageous for generator enclosures [22].

In **Figure 1-3**, kind of cellular solids applications based on porosity type are illustrated.

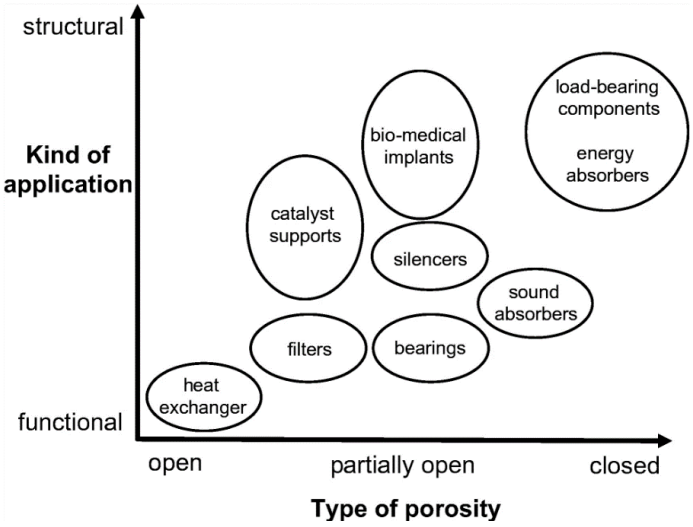

Figure 1 - 3: Kinds of cellular solids applications based on porosity type are Illustrated, adopted from Ref. [23].

1.3 Manufacturing methods of cellular solids

Although cellular materials have extended the design possibilities and applicability of lightweight structures, challenges in manufacturing their complex microarchitectures have slowed the development of this field of study and the application of these materials. Due to these constraints, the ability to create complicated geometries with various forms is hampered, which has slowed the progress of experimental studies of different cellular solids. The base material, geometry, and whether the cellular solid is foam or lattice all affect their best production

techniques. This part briefly summarizes the most popular methods for fabricating cellular solids.

The primary techniques for creating foam are powder metallurgy, hollow spheres and lotus-type. A comparatively new technology, powder metallurgy, was developed initially for manufacturing aluminum foams [24]. In this procedure, a foaming ingredient is first added to metal powder before being compressed at the proper pressure. The combination is then heated to the point at which the metal melts to boost the crystal structure. The foams will develop pores after consolidation [25]. In the hollow sphere technique, pre-fabricated hollow spheres are cast in a metal matrix after being consolidated with an adhesive matrix. Hollow spherical methods, as opposed to powder metallurgy, can be used to create both open- and closed-cell foams [26]. In the lotus-type technique, a gas, usually hydrogen or a hydrogen-helium mixture, is diffused into molten metal. The gas escapes from the steel as it solidifies, leaving porosities within the solid [27].

One of the known lattice structures, honeycomb, has traditionally been made using three techniques: expansion, corrugation and molding. The expansion method involves cutting a sheet into the required dimensions and printing adhesive strips on it. The adhesive is employed in a way that adhesive prints on adjacent sheets are offset by half the distance between adjacent points on the same sheet. After the adhesive has solidified and cured, the cut block is split into slices with the required thickness for the core and finally expanded to create honeycombs [28]. In the corrugated method, the substrate is in sheet form and is passed through corrugated rollers to pre-form the core walls. The surfaces are coated with adhesive before the sheets are stacked. In order to cure the adhesive, the stacks are then put in an oven [29]. Lastly, in the moulding technique, a rigid matrix or mould is constructed, and liquid material is poured into it. Exposure to the required environmental conditions creates cellular solids. These techniques were all initially used to create

periodic metallic honeycombs. The development of cellular materials using different base materials and arbitrary complicated topologies has been accomplished in recent decades by novel manufacturing methods [23]. Press forming technology, in which a sheet is punctured to form a pattern and then bent at the nodes, can be used to create a three-dimensional spatial periodic cellular structure. Through using metal wire techniques, tougher and harder metals, including Inconel, were also used to form lattice structures [30].

However, the invention of additive manufacturing (AM) technology marked a significant advancement in the fabrication of three-dimensional complex topology cellular materials. The production of engineered topologies that cannot be produced using other techniques has been achieved by additive manufacturing, also known as 3D printing [31-33]. The most traditional additive manufacturing techniques, such as stereolithography (SLA) and fused deposition molding (FDM), have been used to form 2D and 3D cellular shapes [34]. Selective laser melting (SLM) has been used to create metallic smooth-shell structures with elaborate gyroid and shell-like lattice designs [35]. **Table 1-1** shows the comparison of the different 3D printing processes.

Table 1 - 1: Comparison of benefits and limitations of different processes in 3D printing [36].

Process	Advantages	Disadvantages
Stereolithography	High surface finish; Good for manufacturing complicated parts; High accuracy. High thermal durability; and serving the printed parts as patterns for casting.	Less surface area exposed to Laser (about 0.15mm); Slow process; High initial investment cost; Difficult to manufacture overhanging parts; and difficult to handle the photosensitive resin.
Fused Deposition Modeling	High surface finish; Less initial investment cost; Easy to make complex shapes; No scrap generation; and high flexibility.	Slow process; and has less quality than SLS.
Powder Bed Fusion	Low cost; No need for external support; Wide material choice; and powder recycling.	Require post-processing; Weak structural properties of 3D printed parts; and time-consuming process.

Selective Laser Sintering	Easy to manufacture complex parts; No need for external supports; Suitable for mass production; and Good accuracy.	High cost of manufacturing; Post-processing surface requirement; and difficult to print tiny holes accurately.
Binder Jetting	High resolution; High surface finish; No need for post-processing; and multiple printings at one time	Limited materials; Low part strength; and the substrate requirement for printing.
Direct Energy Deposition	Denser parts creation; Directional solidification; and effective for repairing and refurbishing components.	Time-consuming process; Poor resolution and surface finish; and Limited available material.
Laminated Object Manufacturing	No need for external support; Inexpensive; Quick process; Suitable for large parts.	Post-processing requirement; Poor dimensional accuracy; Poor surface finish; and difficult in manufacturing complex parts.

1.4 Modeling response of cellular solids

Cellular solids are modeled to predict their behavior under different loading or environmental factors without the need for experimental testing. Three categories of modeling techniques can be made for the reactions of cellular solids: analytical, numerical and homogenization models. The benefits and drawbacks of these modeling strategies will be briefly explained.

Analytical modeling: As previously mentioned, cellular structure behavior is strongly influenced by cell shape. This aspect has made it difficult to give an analytical model to forecast how cellular solids with complicated structures will respond. The analytical modeling method can only be easily used for a few straightforward shapes or generating mechanical responses. One-dimensional beam theories, for instance, were used by Gibson and Ashby [11] to predict the bending load, yield stress, modulus and flexural rigidity of honeycomb structures. Other 2D shapes like triangular, rectangle and Kagome cells have also been given similar formulas [37]. These models, however, have a narrow range of applications and cannot be extended for intricate three-dimensional structures.

Numerical modeling: Finite element (FE) analysis has made it possible to investigate the

behavior of cellular solids with any shape and under various loading conditions. Two-dimensional [38], three-dimensional [39] and foam lattices [40] have all been examined using FE modeling. Both commercial and open-source software has been used to run various studies, including compression [41], tension [42], bending [43] and thermal conductivity [44]. For the most part, experiments have confirmed the accuracy of the findings. While detailed software modeling is frequently a good substitute for experiments, it can occasionally be computationally costly. The number of elements needed for discretization in finite element modeling significantly rises when the number of cells forming the cellular structure rises or the topology is complicated. This method will therefore be laborious to compute.

Homogenization modeling: Modeling by homogenization means substituting an equivalent homogenous material with a representative volume element (RVE) of a cellular structure. In this approach, the effective properties of the cellular solid are first evaluated using finite element (FE) or other numerical techniques, and the corresponding simplified model is then solved using either analytical or numerical methods [45, 46]. This technique significantly reduces the processing time for detailed numerical simulations of cellular materials and structures. The flexural modulus, flexural rigidity, impact and other studies have all made use of it [47, 48]. The homogenization modeling's primary flaw is its inability to capture local phenomena. As a result, this technique frequently cannot be used for studies involving large deformation or failure. However, novel homogenization methods have been suggested in recent works that can capture plasticity or nonlinear behaviors [49].

1.5 Cellular fiber-reinforced composites (CFRC)

Material and structural properties are crucial for achieving optimal and multifunctional structural products in engineering design. With the increasing emphasis on limited material and

energy resources, economic constraints and environmental concerns, the development of advanced lightweight and durable materials has become a major engineering challenge. As a result, various advanced materials are being developed, including engineered cellular materials. Engineered cellular materials are fabricated out of composite materials to simultaneously satisfy multiple functionalities, ranging from structural stiffness to thermal insulation and energy harvesting. The most commonly used composite material is the fiber-reinforced polymer composite, composed of short or long fibers and a polymer matrix. This type of composite material offers high specific stiffness. Cellular fiber-reinforced composites (CFRC) is an emerging class of high-performance structural materials that combine the properties of both fiber-reinforced composites and cellular materials, making it ideal for applications where high-performance materials are required, such as sandwich panels, energy absorbers and vibration-dampers. Developing advanced materials such as CFRC is critical for addressing the economic and environmental challenges in engineering design. By leveraging the properties of fiber-reinforced composites and cellular materials, CFRC offers a promising solution for achieving optimized and multifunctional structural products. CFRCs can have real-life applications in a variety of industrial sectors, from aerospace (e.g., structural and interior components), marine (e.g., boat hulls and decks) and automotive (e.g., door panels, bumper beams and dashboard) in addition to energy production (e.g., wind turbine blades, hydroelectric turbines and supports for solar panels) [50-56]. CFRCs are also increasingly finding applications in the field of medicine due to designs that have biocompatibility, mechanical strength and the ability to be customized for specific applications, including orthopedic implants (e.g., bone plates, screws and pins), dental restorations (e.g., crowns and bridges), prosthetic limbs (e.g., artificial legs and arms), wound dressings (e.g., bandages and dressings for burns and chronic wounds) and tissue engineering (e.g., scaffolds to support the growth of new tissue) [57-59].

1.6 Numerical analysis of cellular fiber-reinforced composites (CFRC)

Cellular fiber-reinforced composites (CFRC) may become a popular material for various applications in the automotive and aerospace domains due to their outstanding thermomechanical properties [60, 61]. Measuring and optimizing these properties can be achieved by fabricating various samples and obtaining their properties, but this method is time-consuming and costly. To overcome this challenge, different analytical and numerical techniques, such as Random Sequential Adsorption (RSA) and Monte Carlo Algorithm, have been developed to model the CFRCs with random fiber distribution. Among these methods, Finite Element Method (FEM) is the most prevalent numerical tool used to compute material behavior. Various factors contribute to the effective properties of CFRC, including volume fractions, cellular material relative densities, fiber specifications and cell topology. Although detailed modeling of these factors is possible, it poses a challenge in predicting the effective properties of CFRC due to the vast number of possible configurations and limitations of detailed analysis methods. Therefore, a feasible strategy is required to reduce the complexity of the analysis while keeping the predictions accurate. This thesis implements an in-depth study of the relation between the fiber parameters and the effective thermomechanical properties of CFRC [62, 63].

1.7 Engineered fiber-reinforced cellular composites

The properties of cellular materials, such as their elastic modulus, strength and flexural rigidity, can be tailored by varying their cellular topology and relative density. Traditional cellular topologies, such as hexagonal cells, have been widely used for this purpose. However, exploiting topology engineering can create new cellular architectures with specific and customized features that are impossible with conventional topologies. The systematic design approach for tailoring the

material architecture to minimize the anisotropic properties of cellular material for specific applications has yet to be developed. In this thesis, novel mechanically quasi-isotropic composite cells, called *Isomixed* and *Isoflex*, are developed by implementing energy methods combined with mechanical analysis and Euler–Bernoulli beam theory, respectively. The *Isomixed* and *Isoflex* cells are inspired by the deep-sea sponge's skeletal system and have better mechanical performance compared to conventional cells (**Figure 1-4**). This thesis contributes to the field of cellular-based mechanical metamaterials with anomalous properties, such as negative Poisson's ratio, negative incremental stiffness and ultrahigh multifunctional figures of merit. The *Isomixed* and *Isoflex* cells have potential applications in various fields, including aerospace, biomedical and energy [64, 65].

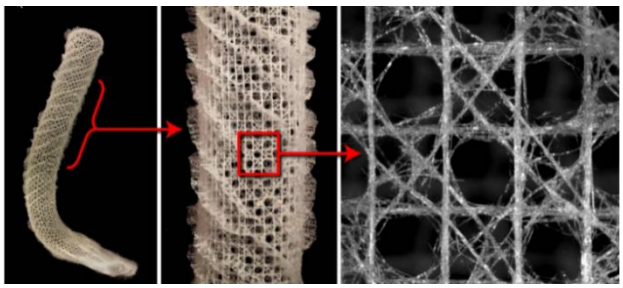

Figure 1 - 4: Progressively magnified views of the deep-sea sponge's skeletal system, adopted from Ref. [66].

1.8 FDM 3D printing of fiber-reinforced cellular composites and sustainable biocomposites

Recent advances in 3D printing, also known as additive manufacturing (AM), have opened up new possibilities for the design and fabrication of advanced materials with controlled material composition and architectural complexity. The ability to rapidly prototype, minimize material waste, achieve design flexibility and produce complex geometries are among the main advantages of 3D printing. The process of 3D printing involves the layer-by-layer fabrication of materials, which allows for the creation of complex free-form geometries that would not be possible with traditional manufacturing techniques. Several methods are available for 3D printing, each with

unique advantages and limitations. Fused Deposition Modeling (FDM) is one of the most commonly used 3D printing technologies because of its simplicity, reliability, affordability, multi-material printing capability, and adaptability to new materials and composites. However, the properties of FDM 3D printed parts can be affected by factors such as filament material, manufacturing process parameters, nozzle diameter and temperature, printing speed, filament feeding rate and bed temperature. The most commonly used feedstock materials for the FDM process are thermoplastic polylactic acid (PLA) and acrylonitrile butadiene styrene (ABS). 3D printing also provides new opportunities for creating sustainable bio-based and biodegradable composites with enhanced mechanical properties by using new or recycled materials as reinforcements [67-73].

1.9 Natural fiber-reinforced cellular polymer biocomposites

Fiber-reinforced polymer composites have been widely used in various industries, but the disposal of these materials has posed a significant challenge. Industries have typically relied on landfill and incineration as the primary disposal techniques, but these methods have a negative impact on the environment. In recent years, there has been growing interest in developing sustainable disposal strategies for composite materials. Sustainable composites made from bio-based components such as wood, vegetable waste, corn, nutshells and algae have been introduced as a viable alternative to traditional composite materials [74-76]. The use of natural fibers as reinforcement in composites has gained significant attention due to their abundance, sustainability and low cost. Cellulose-based (wood) natural composites have found applications in various fields, including automotive interior components, thermal management, electronics, construction and packaging [77-79]. The development of green biocomposites made from plant-derived fiber and crop-derived plastics with higher bio-based and biodegradable content is becoming increasingly

popular as a recyclable and renewable feedstock. Processing techniques such as compression molding, injection molding, resin transfer, and extrusion have been used to process natural fiber-reinforced composites. By introducing new recycling methods and recyclable materials, sustainable composites can reduce the carbon footprint and minimize the environmental impact [80-89].

1.9.1 Wood fiber as a bio-based filler

Wood waste is a significant problem worldwide, with large quantities of waste wood being generated every year from construction, demolition, renovation and packaging activities. Landfilling this waste is not only costly but also has negative environmental impacts, such as greenhouse gas emissions and depletion of landfill space. Hence, finding ways to convert waste wood into useful products has become a critical research focus in recent years. Wood fibers have unique properties that make them attractive for use in composites with bio-based polymer matrices. The combination of wood fibers and polymers results in wood fiber-reinforced polymer composites, which have several advantages over pristine polymers, including lower material costs and improved mechanical properties. These composites can find applications in various fields, such as automotive [90], aerospace [91-93] and construction industries [94].

However, the processing of wood-reinforced composites presents several challenges. The quality of the raw material is variable, with variations in the physical and mechanical properties of the wood fibers. The hydrophilic nature of wood fibers makes them incompatible with hydrophobic polymer matrices, leading to poor interfacial adhesion between the two components. Furthermore, the thermal instability of wood fibers and the shape variation of wood components can affect the processing and properties of the resulting composites. Overcoming these challenges is essential for the successful development of wood-polymer composites. Research into wood-

polymer composites has investigated the microstructure and mechanical properties of different wood types, including hardwood and softwood. Wood is a natural three-dimensional composite consisting primarily of cellulose, hemicelluloses and lignin (**Figure 1-5**). The mechanical properties of wood fiber-reinforced composites depend on the type, size, shape and aspect ratio of the wood fibers used. For instance, increasing fiber size reduces elongation and energy to break but improves the strength and stiffness of the composites. The use of waste wood and thermoplastics in producing wood-polymer composites is gaining attention as a way to address environmental and recycling issues. The characteristics of these materials vary depending on their waste type, origin and age. Researchers have investigated the properties of waste wood and thermoplastics and their potential for use in composite materials.

In summary, research into wood-polymer composites has the potential to address significant environmental and recycling issues by converting waste wood into valuable products. While processing these composites presents challenges, advances in understanding the microstructure and mechanical properties of wood-polymer composites and the use of waste wood have opened up new opportunities for sustainable composite development [95-102].

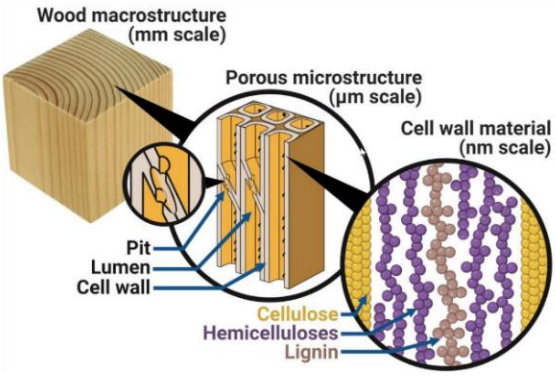

Figure 1 - 5: Wood structure on different size scales: Wood macrostructure (used in this thesis) with annular rings; porous microstructure with pits that are pathways through cell walls and connect adjacent cells lumina (singular: lumen); and cell wall material made from cellulose, hemicelluloses and lignin, adopted from Ref. [98].

1.9.2 PLA as a bio-based and bio-degradable polymer

Polylactic Acid (PLA) has emerged as a promising candidate for reducing environmental concerns, but its low-impact strength and brittle nature have limited its use in various sectors. As a solution to this problem, researchers have explored the potential of using natural fibers, such as wood or wood waste fibers, to reinforce PLA and improve its mechanical properties. The use of wood fibers as a reinforcing agent for PLA has gained attention due to its biodegradability, renewability and sustainability. The combination of PLA with wood fibers has resulted in composite materials that offer improved mechanical and physical properties, including high strength, stiffness and toughness. Moreover, using wood fibers as a reinforcement in PLA composites reduces the cost of the material and provides a solution for the disposal of wood waste. The incorporation of wood fibers in the PLA matrix requires consideration of several factors, such as fiber aspect ratio, fiber size and fiber content, to achieve optimum properties. The compatibility of wood fibers with the PLA matrix can be improved by using coupling agents and surface treatments, which enhance the interfacial adhesion between the wood fibers and the PLA matrix. The combination of PLA with wood fibers is a promising strategy for producing sustainable composites, and the application of 3D printing technology in this field has the potential to create advanced materials for various sectors, including packaging, biomedical, automotive and structural sectors [103-110].

1.9.3 Wood fiber-reinforced PLA composite as a low cost alternative

The wood fiber-reinforced PLA composite, produced via 3D printing, presents an economically viable alternative compared to its counterparts. Wood fibers, sourced from sustainable forestry practices, offer a cost-effective raw material. Wood fiber prices typically range from 2 to 4 CA$/Kg [111, 112]. PLA, as a bio-based polymer, is also advantageous in terms of

cost, with prices ranging from 4.4 to 11 CA$/Kg [113]. In the realm of processing costs, 3D printing demonstrates substantial savings. The additive manufacturing process eliminates the need for conventional molds and tooling, resulting in significant cost reductions [114]. Additionally, the highly automated nature of 3D printing minimizes labor costs, as the process requires minimal human intervention. Furthermore, waste generation is markedly reduced due to the precision of 3D printing, contributing to savings in material costs and waste disposal5. Energy consumption during 3D printing remains relatively low, with estimated costs ranging from 0.8 to 1.6 CA$/g [115].

Conversely, the utilization of synthetic fibers and traditional matrix materials entails higher costs. Carbon fibers, renowned for their exceptional mechanical properties, command a price range of 30 to 50 CA$/Kg [116]. High-performance variants can escalate costs to more than $100 CA$/Kg [117]. Glass fibers, often selected for their affordability, range from $3 to $8 CA$/Kg [118]. Epoxy resins, favored for their excellent bonding characteristics, exhibit a price range of $25 to $140 CA$/Kg, influenced by factors such as cure time and mechanical properties [119]. The processing costs linked to traditional manufacturing methods, such as hand layup, contribute to elevated labor and operational expenses. For example, energy-intensive techniques such as autoclave curing can lead to energy costs up to CA$340 per process [120].

In summary, the comprehensive cost analysis underscores the financial advantages of the wood fiber-reinforced PLA composite produced through 3D printing. The utilization of cost-effective wood fibers and PLA, in combination with the efficient 3D printing process, results in a compelling low-cost alternative. This sharply contrasts with the higher costs associated with synthetic fibers, epoxy resins, and labor-intensive manufacturing methods. Moreover, the reduced reliance on specialized tooling, minimized waste generation, and efficient energy consumption

during 3D printing validate its economic feasibility. The wood fiber-reinforced PLA composite, harnessed through 3D printing, emerges as a promising low-cost solution, poised to find applications across diverse industries seeking both cost-efficiency and sustainable materials.

1.10 Research objectives

1.10.1 Problem statement

In today’s industries, there's a noticeable rise in material wastage due to the limited lifetimes of various devices, instruments, equipment, and furniture. This excessive waste generation triggers a chain of ecological, economic, and societal issues. The urgency to tackle this growing problem is underscored by the need for sustainable alternatives that protect both the planet and humanity. It's crucial to move away from traditional practices to reduce the increasing use of plastics and expensive metals and the resulting harm to the environment. Recycling waste contributes to the economy by conserving valuable resources, reducing the need for raw material extraction, and lowering energy consumption. This sustainable practice fosters environmental stewardship while generating economic opportunities through the creation of jobs in recycling industries and the development of innovative technologies.

At the same time, the excessive use of limited energy resources, especially fossil fuels, is worsened by the inefficiencies arising from heavy and suboptimal structural elements that require excessive energy consumption to excavate more materials and considerable utilization of energy during the operation of these materials/structures. This negative trend worsens the challenges posed by global climate change and environmental pollution caused by inefficient utilization of materials and energy sources. Clearly, an innovative and environmentally conscious approach is necessary to reduce mass across various industries. This mass reduction is essential to improve energy efficiency, lower fossil fuel consumption, and advance our shared pursuit to develop a more

sustainable future.

Within this context, the importance of isotropic mechanical properties in different industrial sectors like automotive, energy, aerospace, and construction becomes evident. These properties lead to consistent material behavior in all directions, simplifying design and manufacturing, enhancing structural strength, and ensuring effective and reliable performance in applications ranging from aircraft parts and satellite structures to medical implants and high-performance sports equipment.

Adding to these challenges is the matter of waste management in Canada, as exemplified by the presence of unrecovered wood debris in municipal solid waste (MSW) and construction, renovation, and demolition (CR&D) waste streams. This issue underscores a significant disparity between current waste management practices and the goals of sustainability. According to estimates from Natural Resources Canada (NRCan, 2013 report), around 1.75 million metric tons of unrecovered wood debris accumulate annually, constituting approximately 7 percent of the total unrecovered waste.

Moreover, contemporary research has demonstrated that incorporating short fibers into man-made materials, such as composite laminates [121], enhances the mechanical performance of these materials. However, limited attention has been devoted to exploring the potential of short fibers in enhancing the mechanical and thermal properties of cellular solids. Utilizing wood fibers – a by-product of the timber industry – as reinforcement in cellular composites can substantially mitigate the environmental impact of composite materials. Furthermore, the prevalent practice of recycling waste wood through burning emits harmful carbon dioxide into the environment, necessitating the identification of sustainable alternatives. Notably, there is an evident research gap concerning the utilization of wood fibers in the fabrication of architected cellular composites.

Given the multifaceted challenges described above, there's a clear need to develop innovative approaches that surpass existing limitations. A comprehensive exploration of sustainable materials, advanced manufacturing techniques, and holistic waste management strategies is warranted. This research endeavor aims to leverage the collaborative potential of different fields, propelling the development of eco-conscious solutions that harmonize industrial requirements with ecological balance. By delving into the principles of material science, engineering, and waste management, this study seeks to chart a transformative path toward a regenerative industrial ecosystem that reconciles performance demands with environmental concerns, ultimately benefiting current and future generations.

1.10.2 Contributions of this research

In the current thesis, strategies are introduced to improve the mechanical functionalities (in tension and bending) of cellular lattice structures by putting forward the idea of adding short fibers to the cellular structure and architecting the geometry of cells for improving and engineering the cellular structure responses while reducing the mass. In addition, the design of cells is engineered to have members with different fiber volume fractions distributed rationally, which can also enhance cellular structures' mechanical performance. Furthermore, the potential of waste wood fiber as a reinforcement material in cellular composites to create sustainable and environmentally friendly materials is explored. This research addresses the increasing demand for eco-friendly alternatives in various industries, particularly in the search for cost-effective and renewable options to traditional synthetic fiber-reinforced composites. In this thesis, theoretical (strain energy and Euler–Bernoulli beam theory) and numerical (homogenization and finite element analysis) techniques are used to examine the response of the engineered fiber-reinforced cellular structures. In order to verify this thesis’s theoretical and computational predictions using AM technologies,

samples out of wood fiber-PLA filaments have been manufactured and tensile and bending tests have been implemented. To provide a thorough overview of the performed study, a short summary of the following chapters of this thesis is given below.

Chapter 2 introduces a low-cost additive manufacturing strategy for developing sustainable high-performance advanced materials. Architected wood fiber-reinforced polymeric (WF-PLA) cellular composites are designed and fabricated, offering controllable properties and significant structural mass reduction. Mechanical tests show an increase in modulus of elasticity by 18% and tensile strength by up to 9% with the addition of recycled wood fibers. The thermal conductivity of the WF-PLA composites is also found to be higher than pure PLA. A lightweight sheet of high-performance quasi-isotropic cellular architecture is prototyped (*Isomixed*) to outperform conventional hexagonal cells. Optimization of cell architecture and material composition enhances the stiffness-to-mass and strength-to-mass ratios by up to 91% and 48%, respectively. The introduced design and manufacturing strategy can offer a paradigm shift in the fabrication of man-made green biocomposites for applications in various sectors.

Chapter 3 proposes a new computational method to determine the effective thermomechanical properties of architected cellular fiber-reinforced composites. The method analyzes the effects of fiber length, orientation, and volume fraction and introduces a multi-level method to obtain effective properties of cellular composites. Validity is examined through computational methodologies, and the method is found to be accurate as long as fibers are shorter than half of the minimum wall thickness. Novel 2D rectangular and 3D cuboid cells are designed to show isotropic effective mechanical properties. Experimental tests on 3D printed samples show the accuracy of proposed conditions for isotropy. This thesis offers advanced development in 3D printing and opens new avenues for smart lightweight material design.

Chapter 4 introduces a low-cost additive manufacturing strategy that uses recycled wood fibers and biopolymers to develop sustainable advanced materials with enhanced and controllable flexural properties and significant structural mass reduction. Mechanical tests show that adding 15 *wt%* recycled wood fibers to the polymeric composite leads to a 60% increase in flexural rigidity, and adding 5 *wt%* wood fibers increases flexural strength by up to 39%. Optimizing cell architecture and material composition can enhance the effective flexural isotropicity and rigidity-to-mass ratio by up to 130% and 99%, respectively. This approach can potentially be tailored towards additive manufacturing of a wide range of eco-friendly and application-specific multifunctional materials for various sectors such as aerospace, automotive, construction and machinery.

Finally, **Chapter 5** summarizes the points of this dissertation and suggests possible directions for further research.

1.11 References

[1] Landel, R.F. and L.E. Nielsen, *Mechanical properties of polymers and composites*. 1993: CRC press.
[2] Carter, C.B. and M.G. Norton, *Ceramic materials: science and engineering*. Vol. 716. 2007: Springer.
[3] Reed, R.C., *The superalloys: fundamentals and applications*. 2008: Cambridge university press.
[4] Ricotti, L. and A. Menciassi, *Nanotechnology in biorobotics: opportunities and challenges.* Journal of Nanoparticle Research, 2015. 17(2): p. 1-10.
[5] Stupp, S.I. and P.V. Braun, *Molecular manipulation of microstructures: biomaterials, ceramics, and semiconductors.* Science, 1997. 277(5330): p. 1242-8.
[6] Aly, A.A., *Heat treatment of polymers: a review*. Int. J. Materials Chemistry and Physics, 2015. 1(2): p. 132-140.
[7] Abdollahiparsa, H., A. Shahmirzaloo, P. Teuffel, and R. Blok, *A review of recent developments in structural applications of natural fiber-Reinforced composites (NFRCs).* Composites and Advanced Materials, 2023. 32: p. 26349833221147540.
[8] Gibson, L.J., *Cellular solids.* Mrs Bulletin, 2003. 28(4): p. 270-271.
[9] Solórzano, E. and M.A. Rodriguez-Perez, *Cellular materials.* Structural Materials and Processes in Transportation, 2013: p. 371-374.
[10] Benedetti, M., A. du Plessis, R.O. Ritchie, M. Dallago, N. Razavi, and F. Berto, *Architected cellular materials: A review on their mechanical properties towards fatigue-tolerant design and fabrication.* Materials Science and Engineering: R: Reports, 2021. 144: p. 100606.
[11] Gibson, L.J. and M.F. Ashby, *Cellular solids: structure and properties*. 1999: Cambridge university press.
[12] Bedell, R., A. Hassan, A.J. Tinet, J. Arrieta-Escobar, D. Derrien, M.F. Dignac, V. Boly, S. Ouvrard, and J.M. Pearce, *Open-Source Script for Design and 3D Printing of Porous Structures for Soil Science.* Technologies, 2021. 9(3): p. 67.
[13] Kim, D.H., H.G. Kim, and H.S. Kim, *Design optimization and manufacture of hybrid glass/carbon fiber reinforced composite bumper beam for automobile vehicle.* Composite Structures, 2015. 131: p. 742-752.
[14] Tsantilis, A.V. and T.C. Triantafillou, *Innovative seismic isolation of masonry infills using cellular materials at the interface with the surrounding RC frames.* Engineering Structures, 2018. 155: p. 279-297.
[15] Thomsen, O.T., E. Bozhevolnaya, and A. Lyckegaard, *Sandwich Structures 7: Advancing with Sandwich Structures and Materials: Proceedings of the 7th International Conference on Sandwich Structures, Aalborg University, Aalborg, Denmark, 29-31 August 2005*. 2005: Springer Science & Business Media.
[16] Evans, A.G., M.Y. He, V.S. Deshpande, J.W. Hutchinson, A.J. Jacobsen, and W.B. Carter, *Concepts for enhanced energy absorption using hollow micro-lattices.* International Journal of Impact Engineering, 2010. 37(9): p. 947-959.
[17] Rincón, A., M. Marangoni, S. Cetin, and E. Bernardo, *Recycling of inorganic waste in monolithic and cellular glass-based materials for structural and functional applications.* Journal of Chemical Technology & Biotechnology, 2016. 91(7): p. 1946-1961.

[18] Zhang, Z.H., J.L. Provis, A. Reid, and H. Wang, *Mechanical, thermal insulation, thermal resistance and acoustic absorption properties of geopolymer foam concrete.* Cement & Concrete Composites, 2015. 62: p. 97-105.
[19] Ahmed, M., O. Meade, and M.A. Medina, *Reducing heat transfer across the insulated walls of refrigerated truck trailers by the application of phase change materials.* Energy Conversion and Management, 2010. 51(3): p. 383-392.
[20] Araki, K. and J.W. Halloran, *Porous ceramic bodies with interconnected pore channels by a novel freeze casting technique.* Journal of the American Ceramic Society, 2005. 88(5): p. 1108-1114.
[21] Urgun-Demirtas, M., P.L. Benda, P.S. Gillenwater, M.C. Negri, H. Xiong, and S.W. Snyder, *Achieving very low mercury levels in refinery wastewater by membrane filtration.* J Hazard Mater, 2012. 215-216: p. 98-107.
[22] Kuku, R., N. Raji, and T. Bello, *Development and performance evaluation of sound proof enclosure for portable generators.* Res J of Appl Sci, 2012. 4: p. 2600-3.
[23] Banhart, J., *Manufacture, characterisation and application of cellular metals and metal foams.* Progress in Materials Science, 2001. 46(6): p. 559-U3.
[24] Smith, B., S. Szyniszewski, J. Hajjar, B. Schafer, and S. Arwade, *Steel foam for structures: A review of applications, manufacturing and material properties.* Journal of Constructional Steel Research, 2012. 71: p. 1-10.
[25] Park, C. and S.R. Nutt, *PM synthesis and properties of steel foams.* Materials Science and Engineering a-Structural Materials Properties Microstructure and Processing, 2000. 288(1): p. 111-118.
[26] Friedl, O., C. Motz, H. Peterlik, S. Puchegger, N. Reger, and R. Pippan, *Experimental investigation of mechanical properties of metallic hollow sphere structures.* Metallurgical and Materials Transactions B-Process Metallurgy and Materials Processing Science, 2008. 39(1): p. 135-146.
[27] Ikeda, T., T. Aoki, and H. Nakajima, *Fabrication of Lotus-type porous stainless steel by continuous zone melting technique and mechanical property.* Metallurgical and Materials Transactions a-Physical Metallurgy and Materials Science, 2005. 36a(1): p. 77-86.
[28] Rupani, S.V., G. Acharya, and S.S. Jani, *Design, modelling and manufacturing aspects of honeycomb sandwich structures: a review.* 2017.
[29] Gauthier, M.M., *Engineered materials handbook.* Vol. 1. 1995: ASM International.
[30] Wadley, H.N.G., N.A. Fleck, and A.G. Evans, *Fabrication and structural performance of periodic cellular metal sandwich structures.* Composites Science and Technology, 2003. 63(16): p. 2331-2343.
[31] Mezzadri, F., V. Bouriakov, and X.P. Qian, *Topology optimization of self-supporting support structures for additive manufacturing.* Additive Manufacturing, 2018. 21: p. 666-682.
[32] Zhang, L., S. Feih, S. Daynes, S. Chang, M.Y. Wang, J. Wei, and W.F. Lu, *Energy absorption characteristics of metallic triply periodic minimal surface sheet structures under compressive loading.* Additive Manufacturing, 2018. 23: p. 505-515.
[33] Gross, A., P. Pantidis, K. Bertoldi, and S. Gerasimidis, *Correlation between topology and elastic properties of imperfect truss-lattice materials.* Journal of the Mechanics and Physics of Solids, 2019. 124: p. 577-598.
[34] Ngo, T.D., A. Kashani, G. Imbalzano, K.T.Q. Nguyen, and D. Hui, *Additive manufacturing (3D printing): A review of materials, methods, applications and challenges.* Composites Part B-Engineering, 2018. 143: p. 172-196.

[35] Bonatti, C. and D. Mohr, *Smooth-shell metamaterials of cubic symmetry: Anisotropic elasticity, yield strength and specific energy absorption.* Acta Materialia, 2019. 164: p. 301-321.
[36] Jandyal, A., I. Chaturvedi, I. Wazir, A. Raina, and M.I.U. Haq, *3D printing–A review of processes, materials and applications in industry 4.0.* Sustainable Operations and Computers, 2022. 3: p. 33-42.
[37] Zhang, X. and H. Zhang, *Theoretical and numerical investigation on the crush resistance of rhombic and kagome honeycombs.* Composite Structures, 2013. 96: p. 143-152.
[38] Dharmasena, K.P., H.N.G. Wadley, Z.Y. Xue, and J.W. Hutchinson, *Mechanical response of metallic honeycomb sandwich panel structures to high-intensity dynamic loading.* International Journal of Impact Engineering, 2008. 35(9): p. 1063-1074.
[39] Burton, H.E., N.M. Eisenstein, B.M. Lawless, P. Jamshidi, M.A. Segarra, O. Addison, D.E.T. Shepherd, M.M. Attallah, L.M. Grover, and S.C. Cox, *The design of additively manufactured lattices to increase the functionality of medical implants.* Mater Sci Eng C Mater Biol Appl, 2019. 94: p. 901-908.
[40] Jhaver, R. and H.V. Tippur, *Processing, compression response and finite element modeling of syntactic foam based interpenetrating phase composite (IPC).* Materials Science and Engineering a-Structural Materials Properties Microstructure and Processing, 2009. 499(1-2): p. 507-517.
[41] Xiao, D.B., Z.C. Dong, Y. Li, W.W. Wu, and D.N. Fang, *Compression behavior of the graded metallic auxetic reentrant honeycomb: Experiment and finite element analysis.* Materials Science and Engineering a-Structural Materials Properties Microstructure and Processing, 2019. 758: p. 163-171.
[42] Zhang, J.J., G.X. Lu, D. Ruan, and Z.H. Wang, *Tensile behavior of an auxetic structure: Analytical modeling and finite element analysis.* International Journal of Mechanical Sciences, 2018. 136: p. 143-154.
[43] Sun, G.Y., X.T. Huo, D.D. Chen, and Q. Li, *Experimental and numerical study on honeycomb sandwich panels under bending and in-panel compression.* Materials & Design, 2017. 133: p. 154-168.
[44] Zhao, C.Y., *Review on thermal transport in high porosity cellular metal foams with open cells.* International Journal of Heat and Mass Transfer, 2012. 55(13-14): p. 3618-3632.
[45] Hassani, B. and E. Hinton, *A review of homogenization and topology optimization I - homogenization theory for media with periodic structure.* Computers & Structures, 1998. 69(6): p. 707-717.
[46] Hassani, B. and E. Hinton, *A review of homogenization and topology optimization III - topology optimization using optimality criteria.* Computers & Structures, 1998. 69(6): p. 739-756.
[47] Wang, C., K.R. Ramakrishnan, K. Shankar, E. Morozov, H. Wang, and A. Fien, *Homogenized shell element-based modeling of low-velocity impact response of stainless-steel wire mesh.* Mechanics of Advanced Materials and Structures, 2021. 28(18): p. 1932-1947.
[48] Hundley, J.M., E.C. Clough, and A.J. Jacobsen, *The low velocity impact response of sandwich panels with lattice core reinforcement.* International Journal of Impact Engineering, 2015. 84: p. 64-77.
[49] El Nady, K., F. Dos Reis, and J. Ganghoffer, *Computation of the homogenized nonlinear elastic response of 2D and 3D auxetic structures based on micropolar continuum models.* Composite Structures, 2017. 170: p. 271-290.

[50] Cheng, P., Y. Peng, S. Li, Y. Rao, A. Le Duigou, K. Wang, and S. Ahzi, *3D printed continuous fiber reinforced composite lightweight structures: A review and outlook.* Composites Part B: Engineering, 2023. 250: p. 110450.
[51] Pandey, J.K., S.H. Ahn, C.S. Lee, A.K. Mohanty, and M. Misra, *Recent Advances in the Application of Natural Fiber Based Composites.* Macromolecular Materials and Engineering, 2010. 295(11): p. 975-989.
[52] Bakis, C.E., L.C. Bank, V.L. Brown, E. Cosenza, J.F. Davalos, J.J. Lesko, A. Machida, S.H. Rizkalla, and T.C. Triantafillou, *Fiber-reinforced polymer composites for construction-state-of-the-art review.* Journal of Composites for Construction, 2002. 6(2): p. 73-87.
[53] Rajak, D.K., D.D. Pagar, P.L. Menezes, and E. Linul, *Fiber-Reinforced Polymer Composites: Manufacturing, Properties, and Applications.* Polymers (Basel), 2019. 11(10): p. 1667.
[54] Tarfaoui, M., O.R. Shah, and M. Nachtane, *Design and Optimization of Composite Offshore Wind Turbine Blades.* Journal of Energy Resources Technology-Transactions of the Asme, 2019. 141(5).
[55] Li, Z.P., T. Ma, J.X. Zhao, A.T. Song, and Y.D. Cheng, *Experimental study and performance analysis on solar photovoltaic panel integrated with phase change material.* Energy, 2019. 178: p. 471-486.
[56] Liu, H.Y., H.S. Du, T. Zheng, K. Liu, X.X. Ji, T. Xu, X.Y. Zhang, and C.L. Si, *Cellulose based composite foams and aerogels for advanced energy storage devices.* Chemical Engineering Journal, 2021. 426: p. 130817.
[57] Li, C.S., C. Vannabouathong, S. Sprague, and M. Bhandari, *The Use of Carbon-Fiber-Reinforced (CFR) PEEK Material in Orthopedic Implants: A Systematic Review.* Clin Med Insights Arthritis Musculoskelet Disord, 2015. 8: p. 33-45.
[58] Krishnakumar, S. and T. Senthilvelan, *Polymer composites in dentistry and orthopedic applications-a review.* Materials Today-Proceedings, 2021. 46: p. 9707-9713.
[59] Huijing, P.A., *Muscle as a collagen fiber reinforced composite: a review of force transmission in muscle and whole limb.* J Biomech, 1999. 32(4): p. 329-45.
[60] Nazarenko, L., H. Stolarski, and H. Altenbach, *Effective properties of short-fiber composites with Gurtin-Murdoch model of interphase.* International Journal of Solids and Structures, 2016. 97-98: p. 75-88.
[61] Tekinalp, H.L., V. Kunc, G.M. Velez-Garcia, C.E. Duty, L.J. Love, A.K. Naskar, C.A. Blue, and S. Ozcan, *Highly oriented carbon fiber-polymer composites via additive manufacturing.* Composites Science and Technology, 2014. 105: p. 144-150.
[62] Duschlbauer, D., H.J. Bohm, and H.E. Pettermann, *Computational simulation of composites reinforced by planar random fibers: Homogenization and localization by unit cell and mean field approaches.* Journal of Composite Materials, 2006. 40(24): p. 2217-2234.
[63] Sanjay, M.R., G.R. Arpitha, and B. Yogesha, *Study on Mechanical Properties of Natural - Glass Fibre Reinforced Polymer Hybrid Composites: A Review.* Materials Today-Proceedings, 2015. 2(4-5): p. 2959-2967.
[64] Hyun, S. and S. Torquato, *Optimal and manufacturable two-dimensional, Kagome-like cellular solids.* Journal of Materials Research, 2002. 17(1): p. 137-144.
[65] Bertoldi, K., P.M. Reis, S. Willshaw, and T. Mullin, *Negative Poisson's ratio behavior induced by an elastic instability.* Adv Mater, 2010. 22(3): p. 361-6.
[66] Fernandes, M.C., J. Aizenberg, J.C. Weaver, and K. Bertoldi, *Mechanically robust lattices inspired by deep-sea glass sponges.* Nat Mater, 2021. 20(2): p. 237-241.

[67] Tubío, C.R., A. Rama, M. Gómez, F. del Río, F. Guitián, and A. Gil, *3D-printed graphene-Al2O3 composites with complex mesoscale architecture.* Ceramics International, 2018. 44(5): p. 5760-5767.
[68] Jungst, T., W. Smolan, K. Schacht, T. Scheibel, and J. Groll, *Strategies and Molecular Design Criteria for 3D Printable Hydrogels.* Chem Rev, 2016. 116(3): p. 1496-539.
[69] Chen, Z., Z. Li, J. Li, C. Liu, C. Lao, Y. Fu, C. Liu, Y. Li, P. Wang, and Y. He, *3D printing of ceramics: A review.* Journal of the European Ceramic Society, 2019. 39(4): p. 661-687.
[70] Thomas, D.S. and S.W. Gilbert, *Costs and cost effectiveness of additive manufacturing.* NIST special publication, 2014. 1176: p. 12.
[71] Ning, F.D., W.L. Cong, J.J. Qiu, J.H. Wei, and S.R. Wang, *Additive manufacturing of carbon fiber reinforced thermoplastic composites using fused deposition modeling.* Composites Part B-Engineering, 2015. 80: p. 369-378.
[72] Popescu, D., A. Zapciu, C. Amza, F. Baciu, and R. Marinescu, *FDM process parameters influence over the mechanical properties of polymer specimens: A review.* Polymer Testing, 2018. 69: p. 157-166.
[73] Shofner, M.L., K. Lozano, F.J. Rodriguez-Macias, and E.V. Barrera, *Nanofiber-reinforced polymers prepared by fused deposition modeling.* Journal of Applied Polymer Science, 2003. 89(11): p. 3081-3090.
[74] Takagi, H. and A. Asano, *Effects of processing conditions on flexural properties of cellulose nanofiber reinforced "green" composites.* Composites Part a-Applied Science and Manufacturing, 2008. 39(4): p. 685-689.
[75] Zhao, X., K. Copenhaver, L. Wang, M. Korey, D.J. Gardner, K. Li, M.E. Lamm, V. Kishore, S. Bhagia, M. Tajvidi, H. Tekinalp, O. Oyedeji, S. Wasti, E. Webb, A.J. Ragauskas, H. Zhu, W.H. Peter, and S. Ozcan, *Recycling of natural fiber composites: Challenges and opportunities.* Resources, Conservation and Recycling, 2022. 177: p. 105962.
[76] Zhao, D., Y. Zhu, W. Cheng, W. Chen, Y. Wu, and H. Yu, *Cellulose-Based Flexible Functional Materials for Emerging Intelligent Electronics.* Adv Mater, 2021. 33(28): p. e2000619.
[77] Oliveux, G., L.O. Dandy, and G.A. Leeke, *Current status of recycling of fibre reinforced polymers: Review of technologies, reuse and resulting properties.* Progress in Materials Science, 2015. 72: p. 61-99.
[78] Lotfi, A., H.Z. Li, D.V. Dao, and G. Prusty, *Natural fiber-reinforced composites: A review on material, manufacturing, and machinability.* Journal of Thermoplastic Composite Materials, 2021. 34(2): p. 238-284.
[79] Iwatake, A., M. Nogi, and H. Yano, *Cellulose nanofiber-reinforced polylactic acid.* Composites Science and Technology, 2008. 68(9): p. 2103-2106.
[80] Jensen, J.P. and K. Skelton, *Wind turbine blade recycling: Experiences, challenges and possibilities in a circular economy.* Renewable & Sustainable Energy Reviews, 2018. 97: p. 165-176.
[81] Cousins, D.S., Y. Suzuki, R.E. Murray, J.R. Samaniuk, and A.P. Stebner, *Recycling glass fiber thermoplastic composites from wind turbine blades.* Journal of Cleaner Production, 2019. 209: p. 1252-1263.
[82] Yao, S.S., F.L. Jin, K.Y. Rhee, D. Hui, and S.J. Park, *Recent advances in carbon-fiber-reinforced thermoplastic composites: A review.* Composites Part B-Engineering, 2018. 142: p. 241-250.
[83] Liu, P., F.R. Meng, and C.Y. Barlow, *Wind turbine blade end-of-life options: An eco-audit comparison.* Journal of Cleaner Production, 2019. 212: p. 1268-1281.

[84] Chandrasekaran, S., E.B. Duoss, M.A. Worsley, and J.P. Lewicki, *3D printing of high performance cyanate ester thermoset polymers.* Journal of Materials Chemistry A, 2018. 6(3): p. 853-858.
[85] Awal, A., M. Rana, and M. Sain, *Thermorheological and mechanical properties of cellulose reinforced PLA bio-composites.* Mechanics of Materials, 2015. 80: p. 87-95.
[86] Rouison, D., M. Sain, and M. Couturier, *Resin transfer molding of natural fiber reinforced composites: cure simulation.* Composites Science and Technology, 2004. 64(5): p. 629-644.
[87] Mulinari, D.R., H.J.C. Voorwald, M.O.H. Cioffi, M.L.C.P. da Silva, T.G. da Cruz, and C. Saron, *Sugarcane bagasse cellulose/HDPE composites obtained by extrusion.* Composites Science and Technology, 2009. 69(2): p. 214-219.
[88] Shimazaki, Y., Y. Miyazaki, Y. Takezawa, M. Nogi, K. Abe, S. Ifuku, and H. Yano, *Excellent thermal conductivity of transparent cellulose nanofiber/epoxy resin nanocomposites.* Biomacromolecules, 2007. 8(9): p. 2976-8.
[89] Wang, S., A. Lu, and L.N. Zhang, *Recent advances in regenerated cellulose materials.* Progress in Polymer Science, 2016. 53: p. 169-206.
[90] Ashori, A., *Wood–plastic composites as promising green-composites for automotive industries!* Bioresource technology, 2008. 99(11): p. 4661-4667.
[91] Das, M., S. Sahu, and D.R. Parhi, *Composite materials and their damage detection using AI techniques for aerospace application: A brief review.* Materials Today: Proceedings, 2021. 44: p. 955-960.
[92] Asim, M., N. Saba, M. Jawaid, and M. Nasir, *12 - Potential of natural fiber/biomass filler-reinforced polymer composites in aerospace applications*, in *Sustainable Composites for Aerospace Applications*, M. Jawaid and M. Thariq, Editors. 2018, Woodhead Publishing. p. 253-268.
[93] Puttegowda, M., S.M. Rangappa, M. Jawaid, P. Shivanna, Y. Basavegowda, and N. Saba, *15 - Potential of natural/synthetic hybrid composites for aerospace applications*, in *Sustainable Composites for Aerospace Applications*, M. Jawaid and M. Thariq, Editors. 2018, Woodhead Publishing. p. 315-351.
[94] Dahy, H., *Natural fibre-reinforced polymer composites (NFRP) fabricated from lignocellulosic fibres for future sustainable architectural applications, case studies: segmented-shell construction, acoustic panels, and furniture.* Sensors, 2019. 19(3): p. 738.
[95] Asyraf, M.R.M., M. Rafidah, A. Azrina, and M.R. Razman, *Dynamic mechanical behaviour of kenaf cellulosic fibre biocomposites: a comprehensive review on chemical treatments.* Cellulose, 2021. 28(5): p. 2675-2695.
[96] Chung, T.J., J.W. Park, H.J. Lee, H.J. Kwon, H.J. Kim, Y.K. Lee, and W.T.Y. Tze, *The Improvement of Mechanical Properties, Thermal Stability, and Water Absorption Resistance of an Eco-Friendly PLA/Kenaf Biocomposite Using Acetylation.* Applied Sciences-Basel, 2018. 8(3): p. 376.
[97] Malek, S., J.R. Raney, J.A. Lewis, and L.J. Gibson, *Lightweight 3D cellular composites inspired by balsa.* Bioinspir Biomim, 2017. 12(2): p. 026014.
[98] Thybring, E.E. and M. Fredriksson, *Wood Modification as a Tool to Understand Moisture in Wood.* Forests, 2021. 12(3): p. 372.
[99] Lee, S.M., *International encyclopedia of composites*. 1989: VCH.
[100] Bouafif, H., A. Koubaa, P. Perre, and A. Cloutier, *Effects of fiber characteristics on the physical and mechanical properties of wood plastic composites.* Composites Part a-Applied Science and Manufacturing, 2009. 40(12): p. 1975-1981.

[101] Kayaks, Y.A., B.N. Bulmanis, S.A. Reikhmane, and M.G. Tsiprin, *Effect of the composition and concentration of fibrous wastes from linen yarn production on the physicomechanical properties of polyolefin composites.* Mechanics of Composite Materials, 1997. 33(3): p. 293-298.
[102] Keunecke, D., T. Merz, W. Sonderegger, T. Schnider, and P. Niemz, *Stiffness moduli of various softwood and hardwood species determined with ultrasound.* Wood Material Science & Engineering, 2011. 6(3): p. 91-94.
[103] Nazrin, A., S.M. Sapuan, M.Y.M. Zuhri, R.A. Ilyas, R. Syafiq, and S.F.K. Sherwani, *Nanocellulose Reinforced Thermoplastic Starch (TPS), Polylactic Acid (PLA), and Polybutylene Succinate (PBS) for Food Packaging Applications.* Front Chem, 2020. 8: p. 213.
[104] Devaux, E., C. Aubry, C. Campagne, and M. Rochery, *PLA/Carbon Nanotubes Multifilament Yarns for Relative Humidity Textile Sensor.* Journal of Engineered Fibers and Fabrics, 2011. 6(3): p. 13-24.
[105] Tanase, C.E. and I. Spiridon, *PLA/chitosan/keratin composites for biomedical applications.* Mater Sci Eng C Mater Biol Appl, 2014. 40: p. 242-7.
[106] Pozo Morales, A., A. Guemes, A. Fernandez-Lopez, V. Carcelen Valero, and S. De La Rosa Llano, *Bamboo-Polylactic Acid (PLA) Composite Material for Structural Applications.* Materials (Basel), 2017. 10(11): p. 1286.
[107] Kumar, N. and D. Das, *Fibrous biocomposites from nettle (Girardinia diversifolia) and poly(lactic acid) fibers for automotive dashboard panel application.* Composites Part B-Engineering, 2017. 130: p. 54-63.
[108] Turner, B.N. and S.A. Gold, *A review of melt extrusion additive manufacturing processes: II. Materials, dimensional accuracy, and surface roughness.* Rapid Prototyping Journal, 2015. 21(3): p. 250-261.
[109] Compton, B.G. and J.A. Lewis, *3D-printing of lightweight cellular composites.* Adv Mater, 2014. 26(34): p. 5930-5.
[110] Tao, Y., H. Wang, Z. Li, P. Li, and S.Q. Shi, *Development and Application of Wood Flour-Filled Polylactic Acid Composite Filament for 3D Printing.* Materials (Basel), 2017. 10(4): p. 339.
[111] *Canadian Forest Industries*. 2023; Available from: https://www.woodbusiness.ca/.
[112] Sarı, A., G. Hekimoğlu, and V.V. Tyagi, *Low cost and eco-friendly wood fiber-based composite phase change material: Development, characterization and lab-scale thermoregulation performance for thermal energy storage.* Energy, 2020. 195: p. 116983.
[113] *Filabot*. 2023; Available from: https://www.filabot.com/.
[114] Canessa, E., C. Fonda, M. Zennaro, and N. Deadline, *Low-cost 3D printing for science, education and sustainable development.* Low-Cost 3D Printing, 2013. 11(1).
[115] Li, Y., B.S. Linke, H. Voet, B. Falk, R. Schmitt, and M. Lam, *Cost, sustainability and surface roughness quality – A comprehensive analysis of products made with personal 3D printers.* CIRP Journal of Manufacturing Science and Technology, 2017. 16: p. 1-11.
[116] Ellringmann, T., C. Wilms, M. Warnecke, G. Seide, and T. Gries, *Carbon fiber production costing: a modular approach.* Textile Research Journal, 2016. 86(2): p. 178-190.
[117] Peijs, T., R. Kirschbaum, and P.J. Lemstra, *Chapter 5: A critical review of carbon fiber and related products from an industrial perspective.* Advanced Industrial and Engineering Polymer Research, 2022. 5(2): p. 90-106.
[118] Akhshik, M., S. Panthapulakkal, J. Tjong, and M. Sain, *Life cycle assessment and cost analysis of hybrid fiber-reinforced engine beauty cover in comparison with glass fiber-reinforced counterpart.* Environmental Impact Assessment Review, 2017. 65: p. 111-117.

[119] Kuo, C.-C. and J.-Q. Wu, *Development of a low-cost epoxy resin mold with high cooling efficiency.* The International Journal of Advanced Manufacturing Technology, 2021. 113(7): p. 2065-2086.
[120] Witik, R.A., F. Gaille, R. Teuscher, H. Ringwald, V. Michaud, and J.-A.E. Månson, *Economic and environmental assessment of alternative production methods for composite aircraft components.* Journal of Cleaner Production, 2012. 29-30: p. 91-102.
[121] Draiche, K., A.A. Bousahla, A. Tounsi, A.S. Alwabli, A. Tounsi, and S.R. Mahmoud, *Static analysis of laminated reinforced composite plates using a simple first-order shear deformation theory.* Computers and Concrete, 2019. 24(4): p. 369-378.

2 Chapter two: 3D Printed Wood Fiber-reinforced Architected Cellular Composite[1]

Abstract

Enhancing thermomechanical properties of bio-based polymers by the introduction of cellulose-based (wood) compounds not only paves the way for developing sustainable materials but also opens new opportunities in low-cost additive manufacturing. This thesis provides a novel methodology for integrating waste-wood fibers, a versatile renewable resource of cellulose, into polylactic-acid (PLA) polymers to produce sustainable wood fiber-reinforced PLA (WF-PLA) filaments and then to 3D print high-performance architected cellular composites. The experimental results demonstrate increased stiffness (18%), ultimate strength (9%), fracture strain (15%), toughness (44%), thermal conductivity (23%) and reduced overall density (10%) for 3D printed composite dogbones made of optimum wood fiber contents, compared to the PLA counterpart. Following the growing interest in architected cellular solids, a rising class of advanced materials with superior multifunctional properties, WF-PLA filaments are used to 3D print two quasi-isotropic cellular materials, hexagonal and novel mixed square (*Isomixed*) microarchitectures. The WF-PLA *Isomixed* cell exhibits considerably enhanced stiffness (91%) and ultimate strength (48%) compared to the PLA hexagonal honeycombs. The WF-PLA architected composites offer a first-of-a-kind strategy to additively manufacture sustainable

[1]*Reproduced with permission from Estakhrianhaghighi, E., Mirabolghasemi, A., Zhang, Y., Lessard, L. & Akbarzadeh, A. 3D-Printed Wood-Fiber Reinforced Architected Cellular Composites. Advanced Engineering Materials 22, 2000565, (2020).*

advanced materials with enhanced thermomechanical properties out of low-cost waste materials through an optimized material composition and the rational design of underlying microarchitectures.

2.1 Introduction

One class of state-of-the-art lightweight, energy-efficient materials with enhanced material properties is *architected cellular solids*. Their exotic properties (e.g., high strength-to-mass ratio, high energy absorption capability and tunable multiphysical properties) mainly stem from their rationally-designed underlying architectures (e.g., cell topology and cell connectivity) and partially from the properties of their constituent materials [1-4]. Cellular solids, so-called cellular-based *metamaterials*, upon showing unprecedented properties, have recently received considerable attention due to their potential applications in aerospace, automotive, energy, robotics and biomedical sectors as high-performance lightweight panels, energy absorbers, morphing structures, noise reduction, waveguide devices, programmable battery electrodes and bio-implantable medical devices [5-12].

Recently, advances in *3D printing*, interchangeably called *additive manufacturing* (AM), have shed light on strategies for design and realization of advanced materials (including *cellular solids* and *architected metamaterials*) with controlled material composition and architectural complexity. A large number of studies have been carried out to investigate the correlation between specific mechanical properties and the architecture of 3D printed advanced materials [13-19]. Fast prototyping, material saving, waste minimization, design freedom and the capability to manufacture complex architectures are the main 3D printing advantages [20-23]. 3D printing is a fabrication process for constructing free-form materials and structures from a CAD model. The printing process typically involves layer-upon-layer fabrication that enables the production of

complex geometries that would be impossible by conventional manufacturing processes [24-31]. Several methods can be adopted for 3D printing: Direct Metal Laser Sintering (DMLS), Selective Laser Melting (SLM) and Electron Beam Melting (EBM) for printing metallic powders; Selective Laser Sintering (SLS) for printing polymeric and metallic powders; Laminated Object Manufacturing (LOM), Direct Foam Writing, 3D Extrusion Freeforming of Ceramics (EFF) and Lithography-based Ceramic Manufacturing (LCM) for Ceramic-Based Materials; Stereolithography apparatus (SLA) and Digital Light Projection (DLP) for printing photopolymeric resins; and Fused Deposition Modeling (FDM) for printing thermoplastic polymers [32-35]. The simplicity, reliability, affordability (minimal waste, low processing and operational cost), multi-material (multi-nozzle) printing capability and adaptability to new materials and composites have made FDM one of the most commonly used 3D printing technologies [36-39]. However, several factors may affect the properties of the FDM 3D printed parts, including the filament material and manufacturing process such as nozzle diameter and temperature, printing speed, filament feeding rate and bed temperature [40, 41].

Thermoplastic polylactic acid (PLA) and acrylonitrile butadiene styrene (ABS) are the most commonly used filaments as feedstock for the FDM process. However, due to their inherent brittleness, FDM 3D printed parts suffer from relatively low strength, stiffness and toughness [42, 43]. Recent advances in 3D printing technologies offer new opportunities for reinforcing thermoplastic polymers by new or recycled biomaterials to manufacture sustainable composites with enhanced mechanical properties [36, 44-48]. In addition, the interest has been growing in the development of natural-based compounds as ecologically benign, recyclable and renewable 3D printing process feedstock [49-52]. The renewable and sustainable natural fibers obtained from wood and plants (e.g., bamboo, flax and jute) are commonly compatible with bio-based matrices;

as a result, they can potentially be considered as reinforcements of 3D printing materials. Several researchers have investigated the mechanical properties (e.g., stiffness and strength) of the complex microstructure of different wood types (e.g., hardwood and softwood) through different techniques, including homogenization and computational multiscale modeling [53-60]. As one of the most common organic polymers [61], cellulose is used for green biocomposite manufacturing and also is mechanically robust [62], renewable, inexpensive and biodegradable. Therefore, cellulose-based natural composites have found a wide range of applications in thermal management [63, 64], electronics [65], construction and packaging [66-68]. Moreover, some cellulose derivatives, such as water-soluble methyl cellulose and carboxymethyl cellulose, are being used in construction materials, pharmaceuticals and cosmetics [69]. Cellulose and its derivatives may well serve as a sustainable additive for the reinforcement of thermoplastic polymers used in FDM 3D printing [70]. Several conventional processing methods, including compression [71], injection [72, 73], resin transfer [74] and extrusion [75], have already been used to process such natural composites.

Considering the bio-based nature of PLA, combining it with recycled wood or wood waste to fabricate natural composite filaments is potentially a promising strategy to produce sustainable filaments with enhanced material properties, to improve the multifunctionality and sustainability of 3D printed materials and to reduce the cost of 3D printed parts. Despite a great deal of attention and studies on the 3D printing of conventional and advanced materials, the number of studies on the additive manufacturing of bio-based reinforced composites is limited [76, 77]. The fabrication of lightweight cellular structures with enhanced mechanical properties, which are 3D printed by fiber-reinforced composite filaments, is the result of recent advances in additive manufacturing technology [58, 78-80]. Producing architected cellular composites out of biological resources (i.e.,

bio-based PLA) and waste materials (i.e., wood fibers) with enhanced multifunctional properties, including stiffness and ultimate strength, can be a turning point in sustainable design and fabrication of advanced materials.

In this thesis, sustainable, load-bearable and low-cost architected natural composites with controllable thermomechanical properties are developed by exploiting produced biocomposite filaments. This thesis aims at introducing and evaluating the properties of new bio-based 3D printing filaments, composed of PLA and wood waste, for developing engineered lightweight materials with optimized microarchitectures in two different steps: *first*, by investigating the effect of adding wood fibers to PLA on the properties (i.e., stiffness, ultimate strength, fracture strain, toughness and thermal conductivity) of 3D printed samples, and *second*, by developing a new isotropic cellular material with an engineered cell topology to surpass the stiffness and ultimate strength of conventional hexagonal cellular solids.

The process of producing wood fiber-reinforced polylactic acid (WF-PLA) composite filaments is illustrated in Section 2.2. PLA as a bio-based matrix is combined with wood fibers of various weight percentages (i.e., 2.5, 5, 10 and 15%) to produce the biocomposite filaments, which are used to feed the FDM 3D printer to fabricate dogbone and architected cellular specimens. In Section 2.3, the mechanical and thermal properties of the 3D printed sustainable composites are determined through tensile and thermal conductivity tests to evaluate their performance compared to the pristine PLA. Section 2.4 provides a systematic design procedure for a novel isotropic 2D cellular architecture and the comparison between its properties and those of the hexagonal honeycomb. Detailed finite element modeling (FEM) and multiscale homogenization are conducted on these isotropic cellular solids to further support the experimental results. In Supporting Information, using TGA and DSC tests, the thermal behavior of WF-PLA filaments is

examined to better understand the effect of wood fiber contents on their crystallinity, thermal stability and degradation, which are important parameters that influence the FDM process.

This research reveals that an optimum wood fiber content can increase stiffness, ultimate strength, toughness, durability and thermal conductivity of the WF-PLA material while it can simultaneously decrease the material density leading to the design and fabrication of lightweight advanced materials with enhanced thermomechanical properties. Furthermore, an isotropic cellular architecture is designed that demonstrates higher stiffness and ultimate strength compared to hexagonal honeycomb, for relative densities smaller than 0.6 (the relative density (ρ_r) is expressed as the ratio of the cellular material's density to the density of the material of which the cellular structure is made). This thesis can lead a paradigm shift in developing high-performance renewable advanced materials by using low-cost and scrap materials through a reticulated microarchitectural design.

2.2 Materials and methods

2.2.1 Materials

The feedstock used in this thesis is pulverized PLA-4043D (supplied by *FILABOT,* Barre VT, USA) (Detailed specifications on PLA-4043D are provided in **Table 2-S1**, Supporting Information) and wood fibers are obtained from a recycled woodblock (supplied by *CANAWICK,* Saint-Quentin NB, Canada, more information is given in Section 2.5.1.3 of Supporting Information). It is worth mentioning that the properties of this thesis's WF-PLA composites (filament and architected cellular materials) are compared in this thesis with a commercial wood-like thermoplastic composite named "Wood+" (*SUNLU Industry Park,* Xiangzhou, Zhuhai, China), which unlike this thesis's developed WF-PLA filament, is comprised of polymeric binders in addition to PLA and wood fibers (Detailed specifications on Wood+ are given in **Table 2-**S2,

Supporting Information).

2.2.2 Experimental setup and methods

2.2.2.1 Processing of WF-PLA Composite Filament

As illustrated in **Figure 2-1**, a single screw extruder Filabot EX2 (*FILABOT*, Barre VT, USA) is used to produce WF-PLA composite filaments with alternative wood fiber contents for FDM 3D printing. The woodblock is hammered, repeatedly ground by a grinder, and sieved by a 0.25 mm sieve to produce wood fibers with a maximum diameter of 0.25 mm. It is expected that the increased surface area of fiber-matrix interface, due to the grinding process, would lead to better bonding between the matrix and rough surface of fibers and consequently enhance the stiffness and strength of the composite filament.

Pulverized PLA is first blended with 2.5, 5, 10 and 15 *wt%* wood fibers, previously dried in an oven at 80° C for half an hour, and then poured into the extruder to get heated and extruded in the form of composite filaments. The extruded filament is then cooled by a fan system and guided to a spool to be used for FDM 3D printing (further information about the extruder is given in **Table 2-S3**, Supporting Information). No additional binding material is used during the filament making process. The wood fiber weight percentage is calculated by:

$$wt\% = \frac{M_w}{M_w + M_{PLA}} \tag{2.1}$$

where M_w and M_{PLA} represent the weight of wood fibers and pulverized PLA, respectively. Pure PLA filament is also produced to provide a baseline for comparison of thermomechanical properties of wood fiber-reinforced composites. In the filament making process, a 1.75mm diameter nozzle is used, and the extrusion temperature is set at 165°C. The average 1.75mm filament diameter is achieved by tuning the extrusion and spooler pulling speed (**Table 2-S3**,

Supporting Information). The produced filaments are then used in an FDM 3D printer to fabricate the composite specimens.

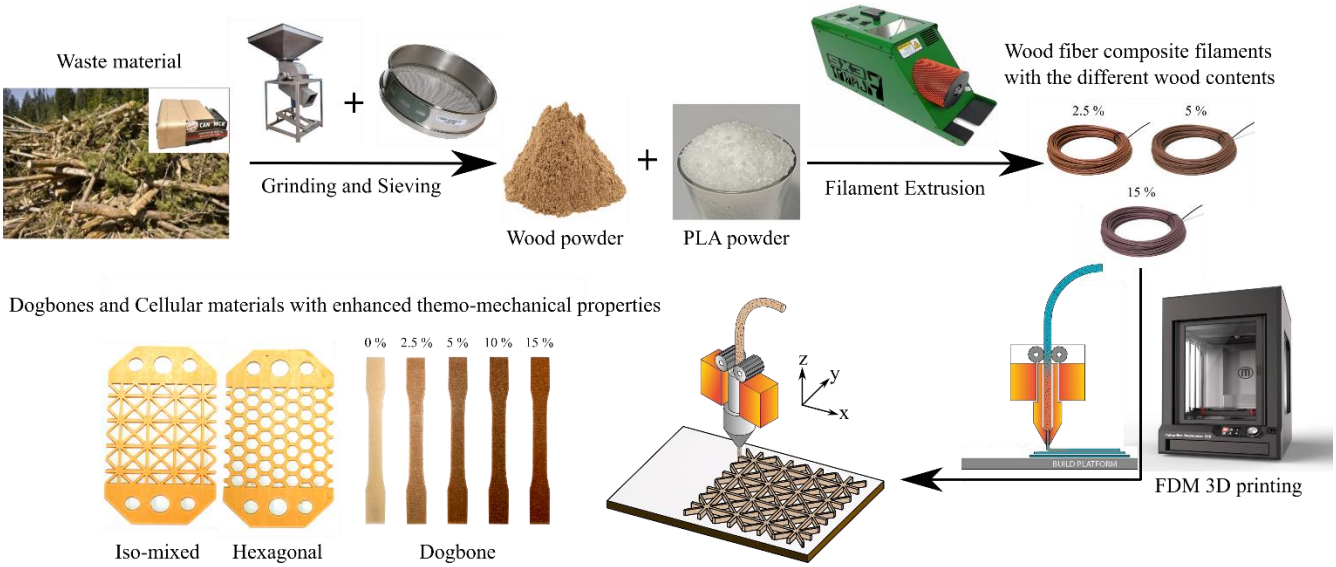

Figure 2 - 1: Flowchart of WF-PLA composite filament making and fabrication of FDM 3D printed architected specimens.

2.2.2.2 3D Printing and Testing Setup of WF-PLA Composite Samples

3D models are created in SolidWorks and imported to be 3D printed by MakerBot Replicator Z18 (*MakerBot Industries*, Brooklyn, NY, USA). A variety of 3D printing settings (e.g., extruding and chamber temperatures, layer thickness, printing speed and nozzle diameter) are tuned to optimize the quality of the extruded filaments and 3D printed parts. Different wood fiber contents absorb and dissipate heat differently within the extruder. As a result, the viscosity of the molten composite material is influenced by the wood fiber content. A higher wood fiber content can lead to increased viscosity, making it more challenging for the material to flow through the extruder. Increasing the extruder temperature for higher wood fiber content can help optimize the material's viscosity, flow behavior, and energy transfer to the composite material, thereby ensuring proper extrusion. A summary of the final settings is provided in **Table 2-S5** (Supporting Information). Although manufacturing parameters are shown to play an important role in the structural behavior

of the FDM 3D printed parts, in this thesis, the effect of material composition and cell topology on the structural properties of 3D printed composite parts is mainly investigated. Therefore, after tuning, all the manufacturing parameters are kept identical for the 3D printing of all specimens.

Following ASTM D638 standard, at least five dogbone samples are 3D printed with linear (0/90 in-plane orientation) infill pattern for each type of the considered filaments (i.e., pure PLA, WF-PLA with 2.5, 5, 10, 15 *wt%* and Wood+ for comparison) as shown schematically in **Figure 2-1** and **Figure 2-S3** (Supporting Information). In addition to the 3D printing of dogbone samples that are printed flat on the build plate (*in-plane configuration*), designed dogbone samples are also oriented so that the printed layers are perpendicular to the direction of the tensile load (*out-of-plane configuration*). Tensile tests are then conducted using an ADMET tensile test machine with an MTESTQuattro (*ADMET*, Norwood MA, USA) testing control system, equipped with a 20 KN load cell. An EX-3542 extensometer (*ADMET*, Norwood MA, USA) is attached to the gauge length of the 3D printed dogbone samples to accurately measure the axial strains. Dogbone samples are stored under a standard laboratory atmosphere condition (23°C and 50% relative humidity) for 40 hours before testing, and tests are performed with a 3N preload under a 5mm/min test speed condition.

The thermal conductivity of the 3D printed WF-PLA composites is measured by C-Therm TCi thermal analyzer (*C-Therm Technologies*, Fredericton NB, Canada) that works based on a modified transient plane source (MTPS) technique [81, 82]. Following the procedure provided by TCi thermal analyzer, three cuboids, with dimensions of 1.27 cm × 1.27 cm × 2.54 cm, are 3D printed for each wood fiber content. Furthermore, water droplets have been added to the interface of the sensor and the specimen to reduce the thermal contact resistance [83]. A small amount of heat is given to the specimen by applying a known current to the sensor's spiral heating element.

The thermal conductivity (κ) of the specimens is determined by monitoring the changes in the voltage drop of the sensor element caused by a temperature increase at the interface of the sensor and the specimen (factory-calibrated).

2.2.2.3 Architected Cellular WF-PLA Composite

Previous sections introduced a feasible and low-cost methodology for improving the sustainability, and thermomechanical properties of 3D printed PLA products by utilizing WF-PLA filaments. Inheriting from anomalous properties exhibited by cellular-based *mechanical metamaterials* (e.g., negative Poisson's ratio [84], negative incremental stiffness [85] and ultrahigh multifunctional figures of merits [86]), in this section, the architectural topology of wood fiber-reinforced composite matter is controlled to further enhance the mechanical properties of the medium with respect to its mass. Hexagonal honeycomb with isotropic in-plane properties, commonly used in lightweight structures, is selected to be compared with an *Isomixed* cell, this thesis's proposed isotropic cellular architecture. After a brief review of the adopted methodology for designing the novel *Isomixed* cellular architecture, the cellular composites are 3D printed out of WF-PLA, and a series of experimental tests and numerical studies are conducted to elicit the effect of the rationally-designed cell microarchitecture on optimizing the performance of cellular composites.

As thoroughly discussed in [87, 88], a hexagonal honeycomb is a bending-dominated structure at small relative densities; hence, its Young's modulus is significantly smaller than a 2D hollow square cell along its wall/strut directions $\theta = 0^{o}$ or 90^{o}. As shown in **Figure 2-2a**, the hollow square cell is mechanically anisotropic, and its stiffness is considerably reduced, to even smaller than the hexagonal honeycomb, by changing the angle towards the diagonals, whilst the shear modulus shows an opposite trend.

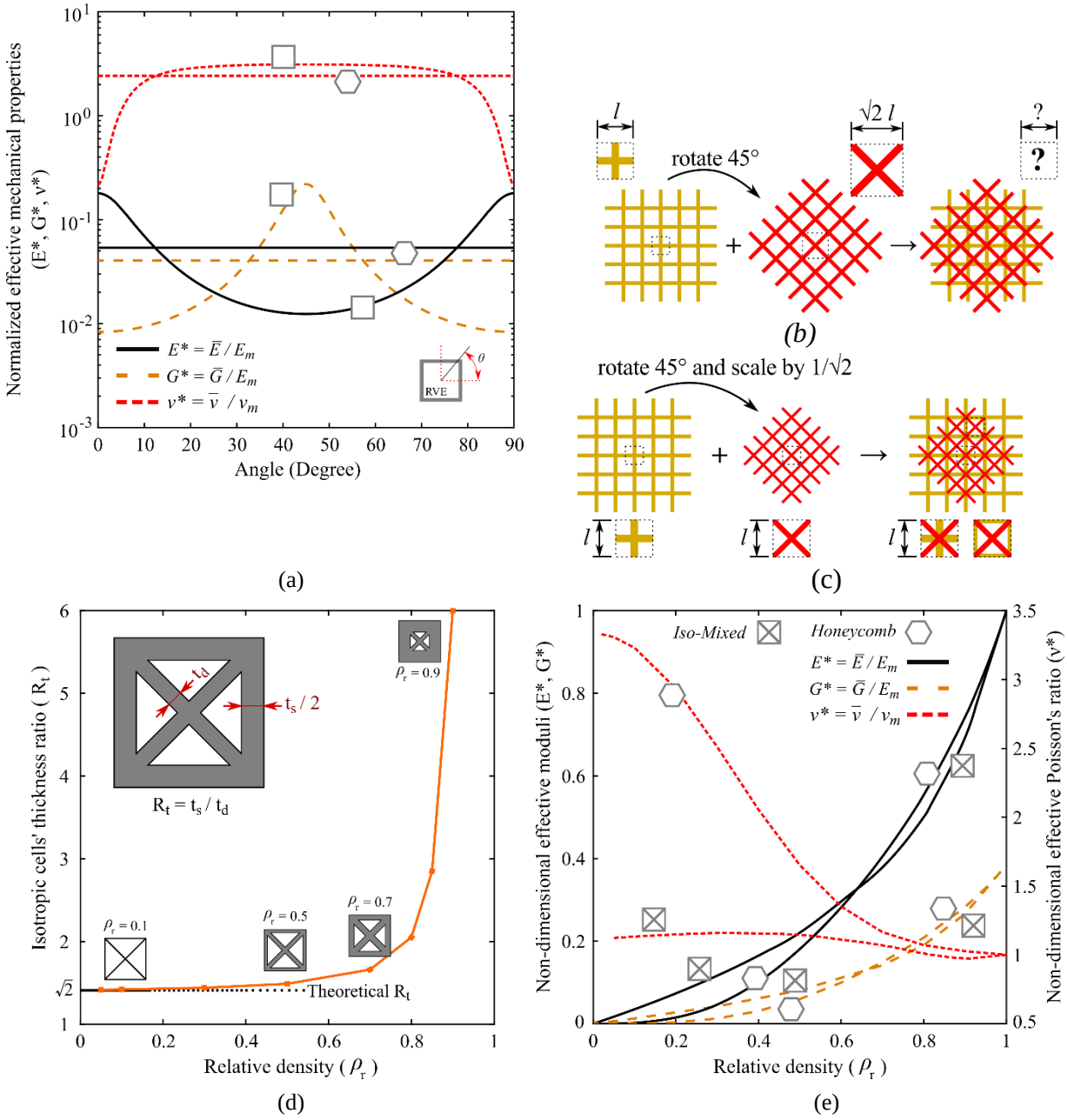

Figure 2 - 2: a) Angle dependency of mechanical properties of square and hexagonal cellular architectures at an arbitrary relative density of 0.32 (2D architectures are under plane stress and the Poisson's ratio of the isotropic matrix ν_m is assumed 0.3). b,c) An intuitive methodology for creating *Isomixed* architecture, inspired by the quasi-isotropic laminate: (b) a quasi-isotropic laminate and (c) an isotropic *Isomixed* lattice. d) Thickness ratios at which an *Isomixed* cell possesses isotropic effective mechanical properties. e) Effective mechanical properties of the *Isomixed* cell, compared to those of the honeycomb counterpart.

Considering the low in-plane stiffness of the hexagonal cells and the anisotropic behavior of

square cells, a 2D cellular architecture with isotropic effective mechanical (and thermal) properties is designed here based on the square cell. The idea is developed by introducing diagonal bracing members and tuning the wall thickness of the hollow square cell (t_s) and thickness of the diagonal members (t_d) to reduce the directionality of mechanical properties of the square cell, as presented in **Figure 2-2c**. Using the cell's effective Young's and shear moduli ($\bar{E}$ and $\bar{G}$) and Poisson's ratio ($\bar{\nu}$) determined by standard mechanics homogenization [89], the mechanical isotropy of the new cellular architecture (*Isomixed*) is assessed by calculating the Zener anisotropic ratio[90] ($\alpha = 2\bar{G}(1+\bar{\nu})/\bar{E}$), which is unity for isotropic materials. To study the mechanical properties of cellular architectures at low relative densities, it is common to idealize cell walls by links/struts connected by frictionless joints [87, 88], a model whose validity has been confirmed for highly porous cellular materials. For the *Isomixed* architecture, the idealized cell model with non-extensible links has zero degree-of-freedom, and it is rigid and statically indeterminate. Therefore, this cell is not bending-dominated, and cell struts deform mainly under tension/compression modes. In order to design a mixed square cell with the effective Young's modulus ($\bar{E}$), shear modulus ($\bar{G}$) and Poisson's ratio ($\bar{\nu}$) satisfying the unit Zener ratio ($\alpha = 1$), the strain energy density of the idealized cell under three loading cases (uni-axial, bi-axial and shear strains) are compared to those of an isotropic material under the same loading condition (**Table 2-S6**, Supporting Information). A similar approach has recently been exploited to design a 3D isotropic cellular architecture, that can reach the theoretical upper bound of elastic stiffness for isotropic materials [91]. It is worth mentioning that the cell is assumed to be under a plane stress condition since the considered cellular plate in this thesis is thin. Moreover, in the idealized cell model, the struts of this stretching-dominated architecture are simplified as independent two-force members, and the small portions of the cell that are common between the members are deemed negligible.

Table 2 - 1: The strain energy density (U) over the entire cell for different loading cases for plane stress condition.

			$\leftarrow\square\rightarrow \begin{bmatrix}\varepsilon_x\\ \varepsilon_y\\ \gamma_{xy}\end{bmatrix}=\begin{bmatrix}\varepsilon_1\\ 0\\ 0\end{bmatrix}$	$\leftarrow\square\rightarrow \begin{bmatrix}\varepsilon_x\\ \varepsilon_y\\ \gamma_{xy}\end{bmatrix}=\begin{bmatrix}\varepsilon_2\\ \varepsilon_2\\ 0\end{bmatrix}$	$\begin{bmatrix}\varepsilon_x\\ \varepsilon_y\\ \gamma_{xy}\end{bmatrix}=\begin{bmatrix}0\\ 0\\ \gamma\end{bmatrix}$
			$U^{(1)}=\frac{1}{4}E_m{\varepsilon_1}^2\rho_s$	$U^{(1)}=\frac{1}{4}E_m{\varepsilon_2}^2\rho_s$	$U^{(1)}=0$
			$U^{(2)}=0$	$U^{(2)}=\frac{1}{4}E_m{\varepsilon_2}^2\rho_s$	$U^{(2)}=0$
			$U^{(3)}=\frac{1}{16}E_m{\varepsilon_1}^2\rho_d$	$U^{(3)}=\frac{1}{4}E_m{\varepsilon_2}^2\rho_d$	$U^{(3)}=\frac{1}{16}E_m\gamma^2\rho_d$
			$U^{(4)}=\frac{1}{16}E_m{\varepsilon_1}^2\rho_d$	$U^{(4)}=\frac{1}{4}E_m{\varepsilon_2}^2\rho_d$	$U^{(4)}=\frac{1}{16}E_m\gamma^2\rho_d$
Total strain energy density			$U_{tot}=\frac{1}{4}E_m{\varepsilon_1}^2(\rho_s+{\rho_d}/{2})$	$U_{tot}=\frac{1}{2}E_m{\varepsilon_2}^2(\rho_s+\rho_d)$	$U_{tot}=\frac{1}{8}E_m\gamma^2\rho_d$
Strain energy density of Isotropic materials			$U=\frac{1}{2(1-\nu^2)}E{\varepsilon_1}^2$	$U=\frac{1}{1-\nu}E{\varepsilon_2}^2$	$U=\frac{1}{4(1+\nu)}E\gamma^2$

*E_m: Young's modulus of the underlying isotropic solid material; ρ_s and ρ_d: Relative density of the simple square cell and the diagonal members, respectively.

By comparing the strain energy densities of the idealized *Isomixed* cell and the isotropic material (given in **Table 2-1**), and solving for the relative densities of the square (ρ_s) and diagonal (ρ_d) members, it turns out that with equal relative densities of the two underlying architectures, the low-density *Isomixed* cells can show isotropic mechanical properties. Furthermore, under the aforementioned assumptions, equal ρ_s and ρ_d translates to $R_t = t_s/t_d = \sqrt{2}$, indicating that at small relative densities, an *Isomixed* cell in which the thickness of the square cell is $\sqrt{2}$ times of the diagonal members shall be isotropic.

Isomixed architectures can also be intuitively designed by considering the 2D struts of the low-density square cell as fibers and treating the cellular architecture similar to a laminated composite. It is commonly known that utilizing a [0/±45/90] stacking sequence results in a quasi-isotropic laminate (i.e., in-plane stiffness isotropy). Hence, mixing a low relative density square cell (corresponding to [0/90] stacking) and its 45° rotated cell (corresponding to [±45] stacking), could also produce an isotropic architecture. However, this combination is not made of repeated identical cells since the ratio of the square cell sizes of the underlying architectures is an irrational

number ($l/l\sqrt{2}$) rather than a simple fraction (see **Figure 2-2b**). In addition, knowing that scaling a periodic cellular architecture does not change its effective linear mechanical properties in classical continuum mechanics, it is possible to scale the rotated cell before the combining process in order to develop an isotropic lattice architecture (**Figure 2-2c**). Finally, because scaling preserves the relative density of cells, ρ_s and ρ_d are equal, and the thickness ratio R_t is equal to the inverse of the scaling factor (i.e. $R_t = \frac{1}{1/\sqrt{2}} = \sqrt{2}$), further validating the abovementioned theoretical findings.

To further investigate the isotropy of the proposed *Isomixed* architecture, computational standard mechanics homogenization is used to obtain the effective cell properties subjected to periodic boundary conditions to design isotopic lattice architectures for higher relative densities, the thickness ratio of an *Isomixed* cell is tuned to achieve the Zener anisotropic ratio of unity. **Figure 2-2d** shows that the numerically tuned thickness ratio converges to the theoretically derived value of $\sqrt{2}$ by decreasing the cell's relative density, and the actual thickness ratio is less than 1% greater than the theoretical value for relative densities up to 0.2. It is worth mentioning that by increasing the thicknesses of the cell members (hence increasing the relative density), the behavior of *Isomixed* cell architectures deviates from the assumed ideal scaffold of two-force members and stretching-dominated deformation mechanism. However, the thickness ratio of the *Isomixed* architecture for relative densities up to 0.5 is only slightly more than the theoretical ratio; for example, less than 2% and about 5% deviations for 0.3 and 0.5 relative densities, respectively. Finally, the effective mechanical properties of the *Isomixed* architecture are compared with those of the hexagonal cell in **Figure 2-2e**. As expected, the introduced stretching-dominated *Isomixed* architecture performs significantly better than hexagonal cells at relative densities smaller than 0.6, around which the two architectures exhibit almost the same modulus of elasticity.

Interestingly, above 0.7 relative density, it is the honeycomb that marginally outperforms the *Isomixed*, which is a result of better load and material distribution in the honeycomb architecture yielding a cellular architecture that is not bending-dominated at higher relative densities. It is worth mentioning that in addition to being mechanically isotropic, the *Isomixed* is thermally-isotropic due to the inherent symmetry of its architecture.

2.2.2.4 3D Printing and Testing Setup of Architected Cellular WF-PLA Composite Samples

To characterize the in-plane mechanical properties of the developed architected cellular materials, cellular specimens for tensile tests (**Figure 2-S3**, Supporting Information) are 3D printed according to the process demonstrated in **Figure 2-1**. Due to the limitation of the FDM 3D printer, the minimum allowable wall thickness of the specimens is selected as 1 mm. Four unit cells with a 20 mm length are printed along the 80 mm width of the architected cellular specimen. The selected number of unit cells is justified by comparing the calculated modulus of elasticity through standard mechanics homogenization on periodic unit cells and a detailed finite element analysis of the cellular samples for different relative densities, as shown in **Figure 2-S4** (Supporting Information). At least, three replicas, with relative density ρ_r = 0.32 and out-of-plane thickness $t_{out\text{-}of\text{-}plane}$ = 3.5mm (*as-designed*), are 3D printed for both honeycomb and *Isomixed* cellular architectures, out of the pure PLA, and 2.5, 5 and 10 *wt%* WF-PLA and Wood+ filaments. According to the relative density of ρ_r = 0.32, the wall thickness of the hexagonal cell is 2.03 mm, and the diagonal member (t_d) and wall thickness (t_s) of the *Isomixed* cell are 1.23 mm and 1.77 mm, respectively (**Figure 2-2d**). Due to the variations in the filament diameter and other FDM 3D printing deficiencies, the relative density and out-of-plane thickness of *as-built* architected specimens vary from the *as-designed* values leading ρ_r = 0.31 ~ 0.33 and $t_{out\text{-}of\text{-}plane}$ = 3.5 ~ 4mm. Similar to the dogbone samples, the 3D printing parameters are chosen based on **Table 2-S5**

(Supporting Information), and test settings similar to Section 2.2.2.2 are used to perform the tensile tests and measure the stiffness and strength of the cellular specimens.

It should also be considered that unlike the 3D models, the corners of the 3D printed parts are inevitably filleted, which can play an important role in the discrepancy between the relative densities of *as-built* and *as-designed* parts. The discrepancy caused by filleted corners is more pronounced for the *Isomixed* architecture because of the acute angles between the struts.

2.2.2.5 Detailed Finite Element Modeling

While FEM has been used for the implementation of multiscale homogenization and determination of effective properties of ideally periodic cellular materials, this research also resorts to nonlinear finite element analysis (implemented by Abaqus Ver.2019) to conduct a detailed numerical simulation on the as-designed model of 3D printed WF-PLA cellular structures in order to examine their elasto-plastic and fracture behavior. The relative density, Poisson's ratio and thickness of the model for finite element analysis are chosen as 0.32, 0.33 and 3.5mm, respectively. The material properties of WF-PLA composite constituting the cellular structure are defined using the experimentally-determined stress-strain curves of WF-PLA dogbones under tension. FEM is performed using the explicit dynamic solver on the cellular structure geometry discretized by 8-node linear brick elements. The loading and boundary conditions are defined to resemble the experimental test setup. A tensile load is applied using the uniaxial extension of the cellular structure at a strain rate of 5 mm/min, similar to the condition used during the experiments, and the stress-strain curves generated through FEM on the as-designed model are compared with the experimental results on the as-built cellular composites.

2.3 Result and discussion

2.3.1 Microstructure of WF-PLA filament

As shown in **Figure 2-3a**, an SEM image of wood fibers, the shape of wood fibers can deviate from an ideal cylinder, especially for the smaller pieces, which is mainly caused by the implemented grinding procedure and the inherent property of hardwood sawdust used here as a filler in the PLA matrix. Although using a grinder to reduce the overall wood size is convenient, it may result in the formation of wood fibers that look more like wood chips, with relatively irregular shapes and a wide range of sizes. To better understand the size distribution of wood fibers, three SEM images of the sieved wood fiber samples, taken at 60x magnification, are analyzed using ImageJ software. The idealized length and diameter of 150 randomly selected fibers in each image, 450 fibers in total, are measured, and the results are shown in **Figure 2-3a**, b. As shown in **Figure 2-3a**, 44.6% of fibers have lengths between 0.1mm and 0.2mm and 75.9% and 92.6% of the fibers' lengths are less than 0.25 mm and 0.4mm, respectively. These results verify the effectiveness of the grinding and sieving process for reducing the overall fiber size. **Figure 2-3b** shows that the length-to-diameter ratio distribution of wood fibers lies mainly in the range of 2 to 8. The 76% of length-to-diameter ratio of the evaluated wood fibers is larger than 3, indicating relatively slender wood fibers.

The morphology of the cross-sectional area of WF-PLA filaments with 5, 10 and 15 *wt%* wood fiber contents is elicited by scanning electron microscopy (SEM) images shown respectively in **Figure 2-3c**, **d**, **e**. According to these figures, the reinforced filaments feature more and larger internal voids with increasing wood fiber content, which is likely the result of more vaporized moisture and also trapped air remaining in the medium while mixing wood fibers with PLA. For example, the average voids' diameter of spherical pores on 5, 10 and 15 *wt%* WF-PLA filaments

are 36.27±8.42 µm, 47.30±11.20 µm and 48.76±14.03 µm, respectively. Furthermore, the high porosity of wood fibers can provide some possibility for trapped air to get inside the system, forming void regions during the extruding process.

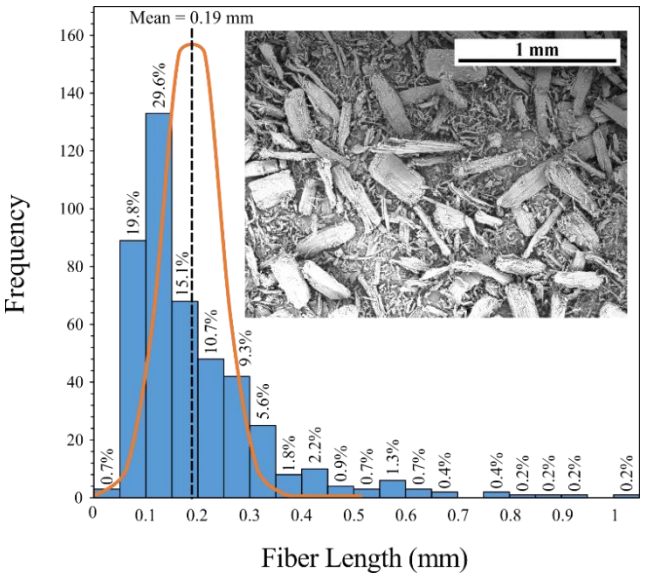

(a)

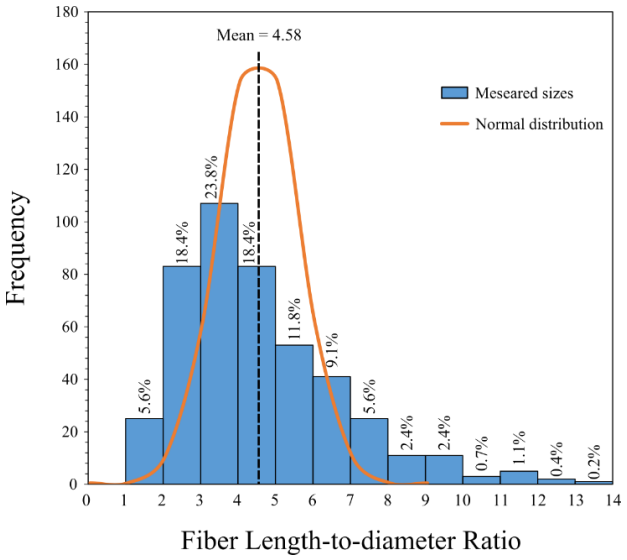

(b)

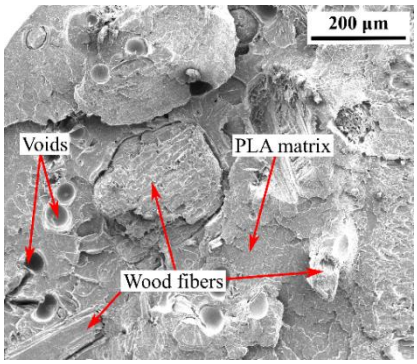

(c)

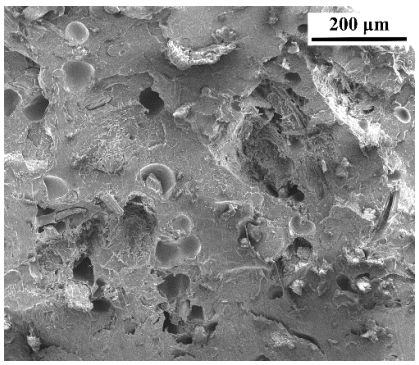

(d)

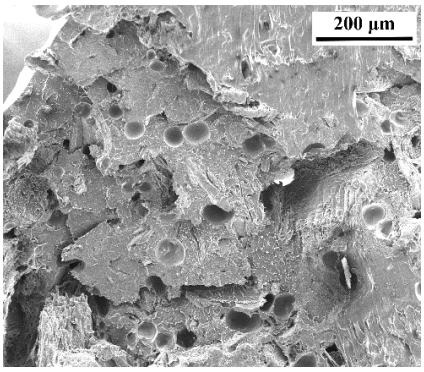

(e)

Figure 2 - 3: a) SEM image of sieved wood fibers at 60× magnification and fiber length distribution. b) Fiber length-to-diameter ratio distribution. c, d, e) SEM images of WF-PLA filament cross-section at 145× magnification: (c) 5, (d) 10 and (e) 15 *wt%* WF-PLA.

2.3.2 Thermomechanical properties of WF-PLA composite

Figure 2-4 presents the experimental data for Young's modulus, ultimate strengths, fracture strain and toughness for all of 3D printed dogbones (6 types × (at least) 5 replicas). The stress-strain curves of all samples are presented in **Figure 2-S5** (Supporting Information).

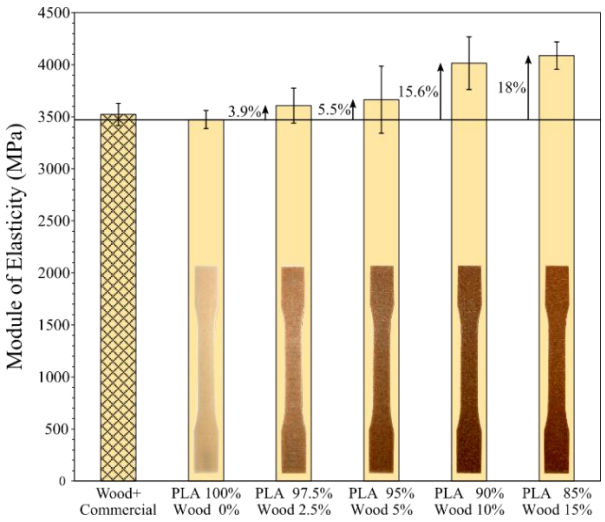

(a)

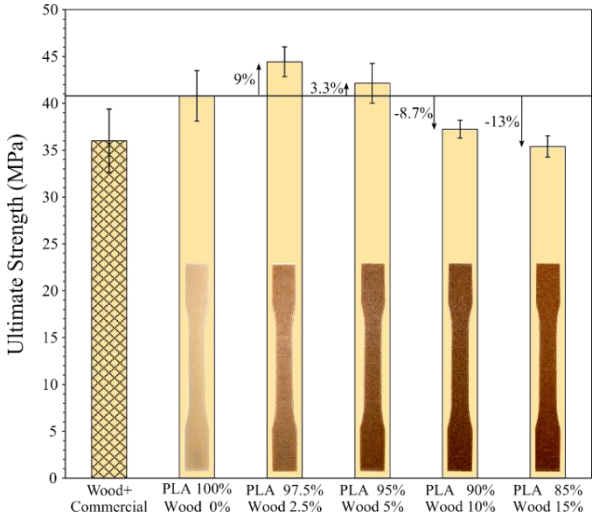

(b)

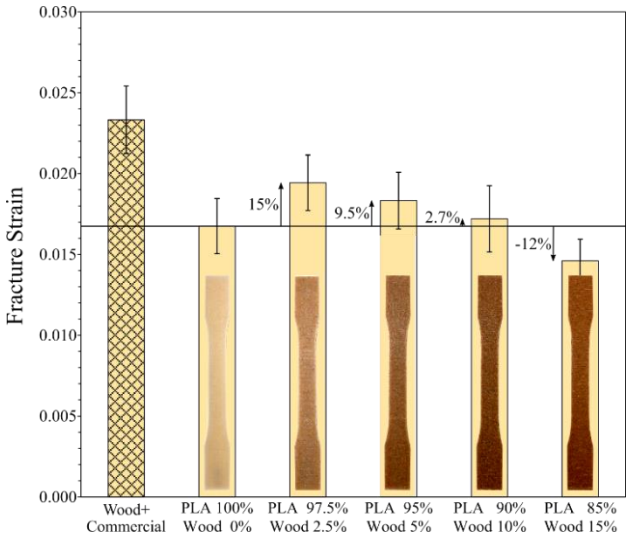

(c)

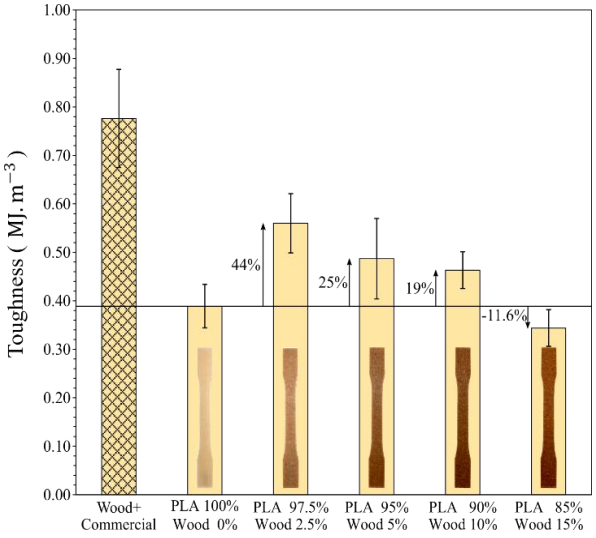

(d)

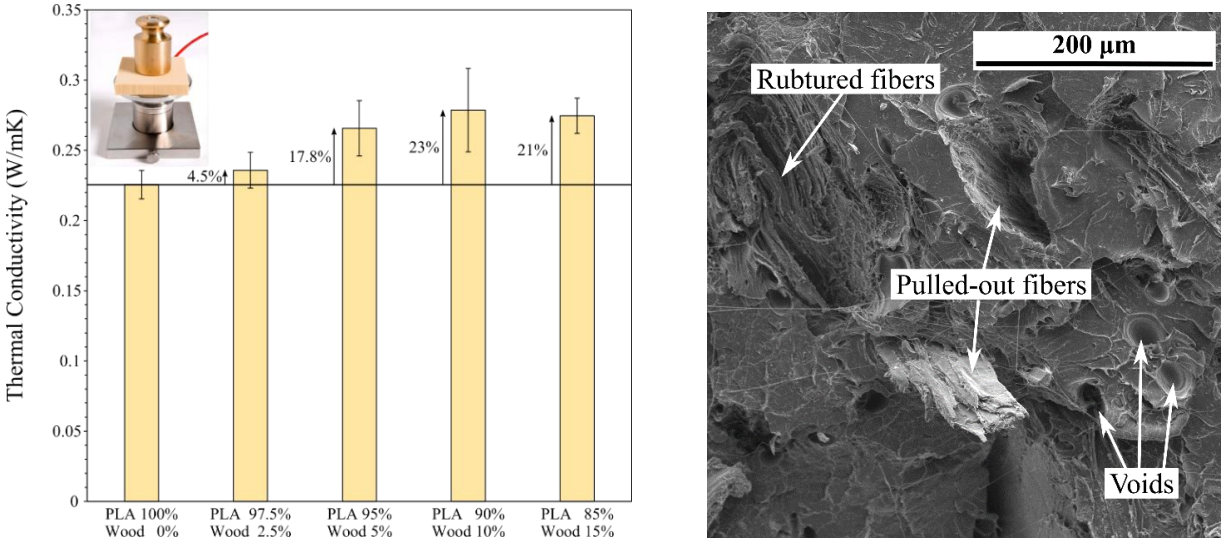

(e) (f)

Figure 2 - 4: Comparing thermomechanical properties of 3D printed composites: a) Young's Modulus, b) Ultimate strength, c) Fracture strain, d) Toughness and e) Thermal conductivity. f) SEM image of the fracture surface for 10 *wt%* 3D printed WF-PLA dogbone samples.

As the experimental results show, increasing the wood fiber content enhances Young's modulus of WF-PLA. The Young's modulus of 15 *wt%* WF-PLA is 18% greater than the pure PLA; however, it is only 2.4% higher than 10 *wt%* WF-PLA, suggesting that Young's modulus of WF-PLA composite does not noticeably change beyond 10 *wt%* wood fiber content (**Figure 2-4a**). This is thought to be the result of inferior wood fiber dispersion in the samples for composites with higher wood fiber contents that causes agglomeration and plays an important role in the reduction of composite stiffness [92]. The results of ultimate strength presented in **Figure 2-4b** suggest that a percentage of wood fiber around 2.5 *wt%* maximizes the ultimate strength of WF-PLA composite and can surpass the strength of pure PLA. Beyond this optimum value, the ultimate strength decreases by increasing the wood fiber content. The decreasing trend might be associated with the separation of wood fibers from the PLA matrix at stresses above elastic limit due to the insufficient bonding of wood fibers and PLA, as no plasticizer has been used in this thesis for the low-cost manufacturing of composite filaments, creating gaps at the interface of matrix and wood

fibers. Considering that wood fibers possess a higher strength than PLA [93, 94], the increased strength of PLA with added wood fibers is more than the weakening effect of the imperfections; as the amount of wood fibers increases, introduced imperfect bonds and agglomeration surpass the strengthening effect of fibers. When the fiber content is about 2.5 *wt%* (**Figure 2-4c**, **d**), the fracture strain and toughness are both increased, respectively, by 14% and 44% compared to the pure PLA. As opposed to commonly-found *performance trade-off* [95] in monolithic materials, where the enhancement of a specific material property commonly deteriorates another material performance (e.g., trade-offs between material density and stiffness, strength and toughness, and stiffness and energy absorption), WF-PLA offers a new strategy to not only unravel the selected performance trade-offs to simultaneously enhance strength/stiffness-to-density and toughness-to-density ratios (e.g., for 2.5 *wt%* of WF-PLA composite) but to also fabricate sustainable and recyclable advanced materials. If these WF-PLA composites are exploited to develop *architected materials*, a new class of advanced materials, i.e. *biocomposite metamaterials*, with unprecedented multifunctional properties (e.g. ultrahigh stiffness, programmable stiffness, geometrical reconfiguration and negative permittivity) [96-98] can be developed that inherits their exotic properties from both their architectural design and material composition of their constituents. **Table 2-2** reports the density, mechanical properties and thermal conductivity of the 3D printed WF-PLA composites. As presented, while reducing mass, the methodology reported in this thesis manages to enhance the stiffness, ultimate strength, fracture strain and toughness. The corresponding empirical equations correlating the thermomechanical properties to the mass fraction of wood fibers (W_f) is presented in **Table 2-S7** (Supporting Information) using the experimental data.

Table 2 - 2: Material density and thermomechanical properties of Wood+, pure PLA and WF-PLA composites.

	Wood+ (Commercial)	**PLA 100% Wood 0%**	**PLA 97.5% Wood 2.5%**	**PLA 95% Wood 5%**	**PLA 90% Wood 10%**	**PLA 85% Wood 15%**
Density [gcm^{-3}]	1.30 ± 0.01	1.24 ± 0.01	1.21 ± 0.00	1.20 ± 0.00	1.19 ± 0.00	1.18 ± 0.00
Modulus of elasticity [MPa]	3523 ± 107	3474 ± 87	3608 ± 167	3664 ± 322	4015 ± 252	4088 ± 132
Ultimate strength [MPa]	36.0 ± 3.4	40.8 ± 2.7	44.4 ± 1.6	42.1 ± 2.1	37.3 ± 1.0	35.4 ± 1.1
Fracture strain(×10)	0.233 ± 0.021	0.168 ± 0.017	0.194 ± 0.017	0.183 ± 0.018	0.172 ± 0.020	0.146 ± 0.013
Toughness [MJm^{-3}]	0.776 ± 0.101	0.389 ± 0.045	0.560 ± 0.061	0.487 ± 0.083	0.463 ± 0.038	0.343 ± 0.038
Thermal conductivity [$Wm^{-1}K^{-1}$]	0.304 ± 0.007	0.226 ± 0.010	0.236 ± 0.012	0.266 ± 0.019	0.279 ± 0.029	0.275 ± 0.012

Figure 2-S6 (Supporting Information) shows the comparison of tensile test results on dogbone samples 3D printed at *in-plane configuration* and *out-of-plane configuration*. Dogbone samples with printed layers oriented perpendicular to the loading direction show a lower overall stiffness and ultimate strength than samples printed with the in-plane configuration due to weak bonding between the 3D printed layers. The effect of printing direction on strength is more significant compared to stiffness which is associated with increased stress concentration between the layers. The effect of wood fiber content on mechanical properties is also almost the same for samples 3D printed in both in-plane and out-of-plane configurations. As shown in **Figure 2-S6** (Supporting Information), the stiffness and ultimate strength of the samples with 2.5 *wt%* WF-PLA are higher than the pure PLA for both in-plane and out-of-plane configurations; specifically, the out-of-plane 3D printed samples with 2.5 *wt%* WF-PLA have 50% higher strength than the pure PLA. Increasing the wood fiber content beyond 2.5 *wt%* decreases the stiffness and ultimate strength of 3D printed samples in out-of-plane configurations due to the fiber agglomeration and weak bonding between the 3D printed layers.

Figure 2-4e shows the variation of thermal conductivity of 3D printed composites that have various wood fiber contents. Thermal conductivity mainly exhibits an increasing trend with the increase of wood fiber content due to the greater thermal conductivity of wood fiber compared to

the PLA [99]; for example, a 23% increase in the thermal conductivity is seen in WF-PLA composite with 10 *wt%* compared to a pure PLA specimen. Further increase of wood fiber content, beyond 10 *wt%*, leads to a decrease in the thermal conductivity. This is believed to be the result of the increase of the void volume fraction in the 3D printed WF-PLA composite since the thermal conductivity should decrease by the increase of porosity [100, 101].

Figure 2-4f shows an SEM image of the fractured surface of the 3D printed WF-PLA material for 10 *wt%* WF-PLA. As shown in this figure, the reinforced composite PLA features internal voids, which are due to the vaporized moisture in the wood as well as nozzle clogging due to the existence of longer fibers relative to the diameter of the nozzle. The ruptured fibers found in the cross-sectional images indicate effective load transfer between wood fibers and PLA matrix. The SEM image also demonstrates a few pulled-out wood fibers from the PLA matrix due to the insufficient interfacial strength between the fiber and matrix.

2.3.3 Mechanical properties of architected cellular WF-PLA composite

To better elucidate the effects of exploiting optimized material composition (traditional approach for enhancing material properties of base materials) and architected geometry (architected material approach for enhancing material properties by tuning spatial distribution of base materials) for controlling the mechanical performance of WF-PLA composites, experimental and FEM results of uniaxial tensile tests for WF-PLA cellular composites containing hexagonal or *Isomixed* cells are presented in **Figure 2-5**. **Figure 2-5a** shows that cellular composites, 3D printed out of WF-PLA filament, possess Young's modulus greater than the pure PLA cellular specimens. For example, the elastic modulus of hexagonal and *Isomixed* cellular WF-PLA composites with 10 *wt%* wood fiber is, respectively, 26% and 28% higher than their counterparts made of pure PLA biopolymer. **Table 2-S8** (Supporting Information) compares the modulus of elasticity of cellular

specimens with different wood fiber contents determined by conducting experimental testing (3 replicas) and numerical simulation through homogenization (implemented on periodic cells with $\rho_r = 0.32$, which is the relative density of the as-designed specimen) and detailed FEM. Increasing the weight fraction of wood fiber in WF-PLA cellular composites monotonically increases the elastic stiffness, a phenomenon aligned with findings in **Figure 2-4a** for the constitutive wood fiber-reinforced composites (traditional approach). Considering the reduction of material density of WF-PLA composite by increasing the wood fiber content, the traditional approach presents a strategy for enhancing the stiffness/strength-to-mass ratio of cellular solids by using an optimized material composition.

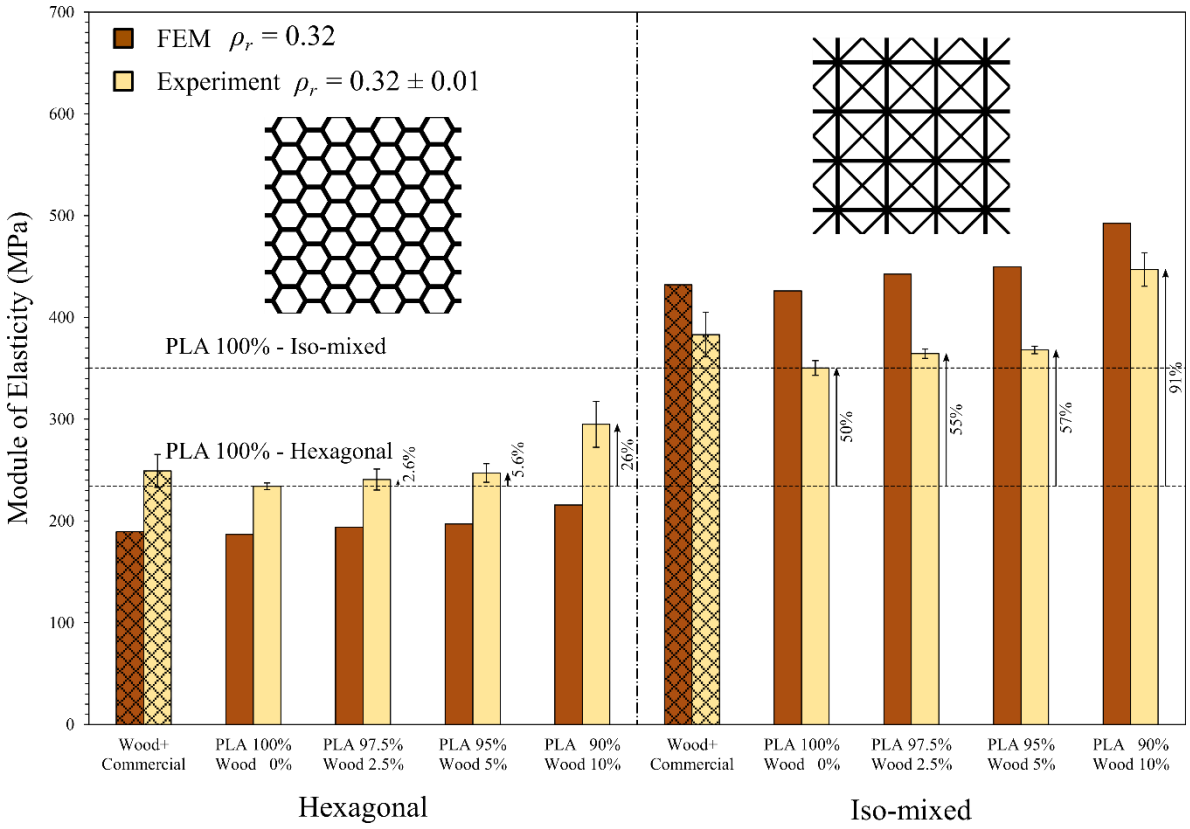

(a)

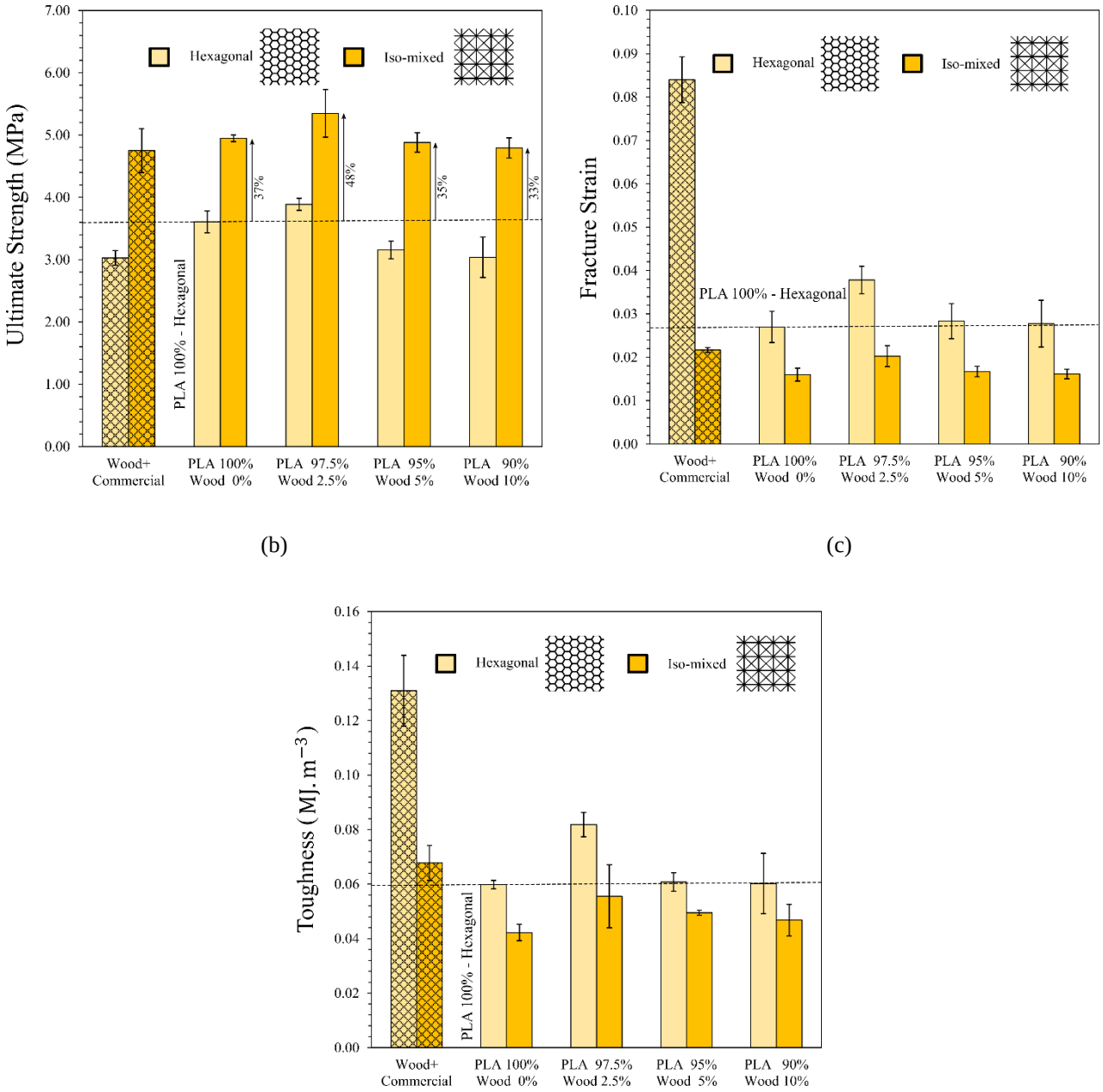

Figure 2 - 5: Comparison of mechanical properties for alternative wood fiber contents and cell topologies: a) Module of elasticity, b) Ultimate strength, c) Fracture strain (ductility) and d) Toughness.

In addition, engineering the architecture offers a unique strategy for programming the material properties of cellular solids by controlling their underlying geometry and, consequently, by tuning their effective properties. The experimental results in **Figure 2-5a**, **b** indicate that 3D printed

Isomixed cellular specimens have significantly higher stiffness and ultimate strength than the 3D printed hexagonal honeycombs; for example, 49% and 52% enhancement in elastic modulus and 55% and 58% increase in the ultimate strength are, respectively, found in the *Isomixed* cellular WF-PLA composites with 5 *wt%* and 10 *wt%* of the wood fiber, all with respect to the hexagonal cells with the same wood fiber content. However, aligned with the long-standing dilemma of the strength–ductility trade-off [102], the increase in stiffness and strength of *Isomixed* cellular solids leads to a slight decrease in the fracture strain (ductility) and toughness with respect to the hexagonal cell (**Figure 2-5c**, **d**). Hexagonal cells are bending-dominated and more ductile (lower strength and higher ductility), while *Isomixed* cells are stretching-dominated and commonly more brittle (higher strength and lower ductility). This trade-off can be potentially counteracted with an optimum material composition to design lightweight cellular materials.

As expected from the tests on dogbone samples, the ultimate strength, fracture strain and toughness of the *Isomixed* specimens are all maximized in 2.5 *wt%* WF-PLA specimens, indicating 9%, 31% and 32% improvement compared to the pure PLA *Isomixed* specimens. As opposed to the enhancement offered by the architected approach (cellular design), these material-based enhancements show no selected performance trade-offs, which is aligned with results from the dogbone samples. Increasing the wood fiber content beyond 2.5 *wt%* can lead to increased fiber agglomeration. In addition, compared to the dogbone samples, manufacturing defects are more likely to be formed during the 3D printing process of cellular solids due to the complexity of their microarchitecture and the need for sharp changes in 3D printing tool path. This phenomenon is more intensive for filaments with higher wood fiber content. For example, comparing 5 *wt%* WF-PLA with the pure PLA counterparts, while WF-PLA dogbone samples show an improvement in all mechanical properties, WF-PLA cellular samples show an improvement in stiffness, slight

improvement in fracture strain and toughness, and no improvement in ultimate strength (**Figure 2-4** and **Figure 2-5**). **Figure 2-5a** shows that experimental results on the 3D printed cellular samples with 5 *wt%* WF-PLA do not show improved stiffness compared to Wood+, unlike the observed trend in **Figure 2-4a** for dogbone samples. Since FEM results of cellular solids (**Figure 2-5**a) are aligned with findings in **Figure 2-4a**, the discrepancy is thought to be stemmed from the better printability of Wood+ filament as it contains some binding polymers.

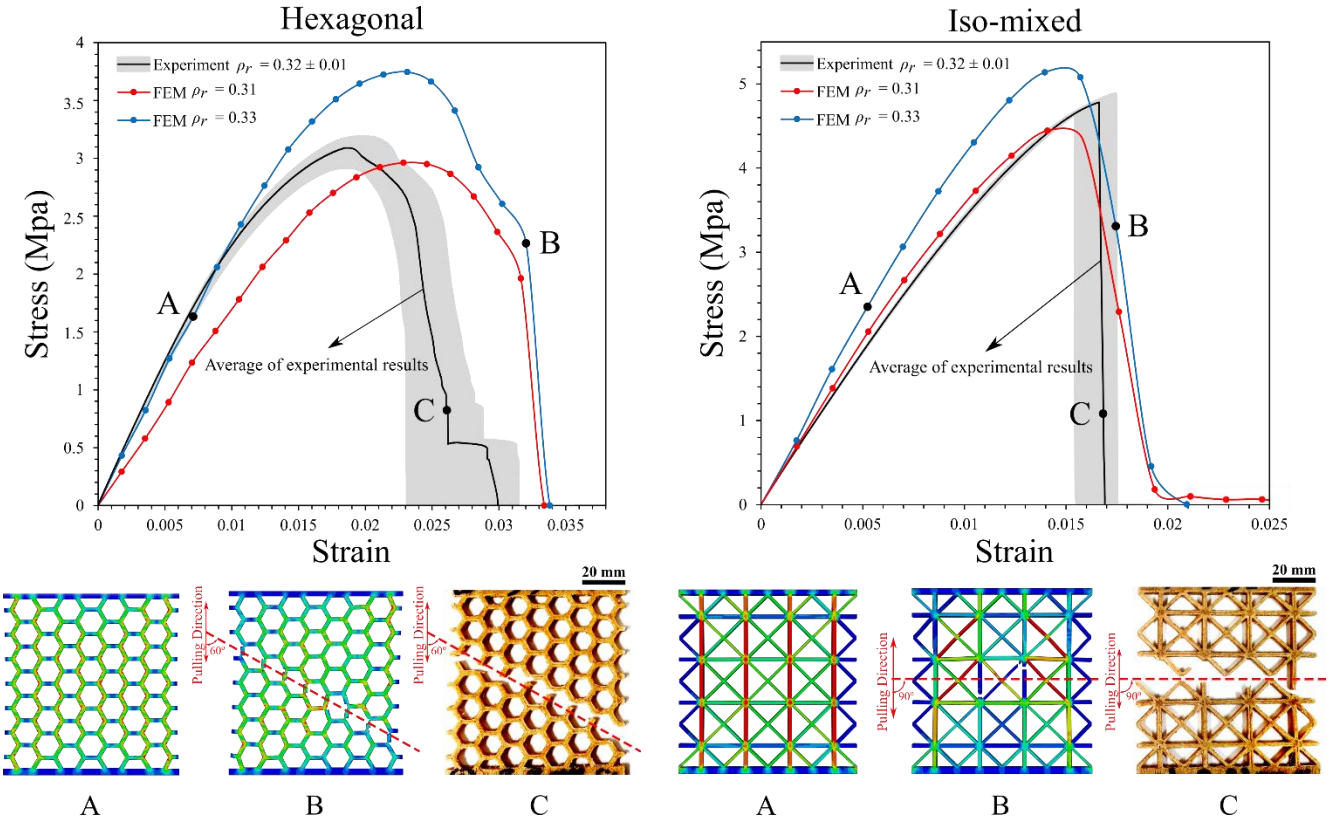

Figure 2 - 6: Comparison of the results of FEM and experimental tensile test on 3D printed architected cellular composites made out of 5 *wt%* WF-PLA: Stress-strain curve and Fracture behavior.

Figure 2-6 compares the stress-strain curves of cellular specimens 3D printed out of 5 *wt%* WF-PLA reinforced filaments under tension, determined by experimental testing and FEM (implemented on cellular samples with ρ_r = 0.31 and 0.33, selected based on the relative densities of the as-built specimens). The crack propagation through the 3D printed cellular composites and

the failure modes are also shown in this figure. Considering the bending dominated nature of the hexagonal cell, maximum stress within the cell occurs at the intersection of the cell walls with sharp edges, causing stress concentration and initiation and propagation of failure along the inclined fracture path of $\pm 60^{o}$ with respect to the loading direction. On the other hand, for stretching-dominated *Isomixed* cellular architectures, cell walls parallel to the tensile loading direction experience stress twice as high as the stress in the bracing members. This, combined with the stress concentration at sharp corners, determines the location of failure initiation and its corresponding brittle-like fracture mode (fracture path at 90^{o} with respect to the loading direction). As discussed in Section 2.3.1, differences between mechanical properties determined by numerical simulation and experimental testing in **Figure 2-6** can emanate from the shortcomings of 3D printing process. For hexagonal cells, the experimental results on the as-built specimens show a higher modulus of elasticity than the finite element anticipation analyses on as-designed specimens with $\rho_r = 0.32$, which can be attributed to the reduced stress concentration in the as-built 3D printed specimens, where instead of sharp corners, the 3D printed cells contain filleted corners due to the limited resolution of the FDM 3D printer and the finite acceleration/deceleration of the printing head as it marches the toolpath associated with the complex architecture of cellular solids. Corner fillets are shown to reduce stress concentration and consequently affect the effective mechanical properties of cellular architectures such as hexagonal honeycombs [103, 104]. As opposed to the hexagonal architecture, the stiffness obtained by FEM is greater than the experimental results for the *Isomixed* architecture. Since the wall thickness of *Isomixed* architecture is smaller than the hexagonal one, the limited resolution of FDM 3D printer may cause more pronounced deviation on the size of the cell walls, especially on those parallel to the loading direction, which leads to the relatively lower performance of the as-built specimens compared to the as-designed one.

2.4 Conclusions

This research introduces a low-cost additive manufacturing strategy for developing sustainable high-performance advanced materials. By integrating recycling and FDM 3D printing with a rational design of architected materials, architected wood fiber-reinforced polymeric (WF-PLA) cellular composites are designed and fabricated. While the sustainable cellular composite simultaneously benefits from recyclability and biodegradability of wood and biopolymers, and the high mechanical performances of wood fibers, it also offers controllable properties and significant structural mass reduction. Mechanical tests on 3D printed WF-PLA composites show the enhanced modulus of elasticity compared to pure PLA samples, e.g., 15 *wt%* addition of recycled wood fibers leads to an 18% increase in modulus of elasticity. The tensile strength can also be increased up to 9% when 2.5 *wt%* wood fiber is used for the fabrication of WF-PLA. In addition, the thermal conductivity of the WF-PLA composites is found to be higher than pure PLA, which would be an advantage in the various heat-sink and heat-dissipating applications such as electronics, housings or automotive parts [105-107]. To investigate the underlying failure mechanisms of the WF-PLA, the fractured surfaces of the 3D printed composite samples are studied using SEM micrographs, demonstrating the existence of ruptured fibers that confirms an effective load transfer between the wood fibers and the PLA matrix.

By exploiting the controllability of properties of lightweight cellular materials through tuning their underlying architecture and improving their constituent solid materials, a rational procedure is introduced, and a lightweight sheet of high-performance quasi-isotropic cellular architecture (*Isomixed*) is prototyped using FDM 3D printing to outperform the linear mechanical properties of the conventional hexagonal cells in a wide range of relative density. To explore the efficacy of wood fiber addition to the pure PLA, WF-PLA filaments with various wood fiber contents are used

to 3D print tensile test samples of these 2D cellular architectures. In addition to the experimental tensile tests, their effective mechanical properties are investigated using both detailed nonlinear finite element modeling and linear standard mechanics homogenization adopted on their unit cells under periodic boundary conditions. The results demonstrate the possibility of simultaneous enhancement of the stiffness-to-mass and strength-to-mass ratios (up to 91% and 48%, respectively) by optimizing cell architecture and material composition; showcasing a new dimension to engineering design and optimization, where lightweighting and multifunctionality are achieved by multi-level engineering of the constitutive material and its underlying structure. The introduced design and manufacturing strategy results in the development of high-performance sustainable advanced materials, made of cost-effective, versatile, renewable and biodegradable constituents free of hazardous ingredients, and can offer a paradigm shift in the fabrication of manmade green biocomposites for applications in aerospace, automotive, construction and machinery sectors. The introduced approaches can potentially be tailored towards additive manufacturing of a wide range of biocomposite materials and structures out of other bio-compatible source materials, with controlled architecture and thermomechanical properties, delivering eco-friendly and application-specific multifunctional properties.

2.5 S-Supporting information

2.5.1 S-Materials and equipment

2.5.1.1 S-PLA pellets-4043D

Table 2-S1 shows the PLA pellets-4043D specifications purchased from *FILABOT* Company.

Table 2-S1: PLA pellets-4043D specification.

Parameter	Value
Density [g.cm^{-3}]	1.24
Tensile strength [Mpa]	110-145
Tensile modulus [MPa]	3300-3860
Melting temp. [^{o}C]	210 ± 8

2.5.1.2 S-Wood fibers

The wood fibers are prepared by grinding the hardwood (e.g., beech, northern red oak, black cherry and white ash trees) sawdust (supplied by *CANAWICK*, Saint-Quentin, NB, Canada). There is no additional chemical in the wood fiber. The mechanical properties of various types of hardwoods have been reported in the literature [93].

2.5.1.3 S-Wood+ filament

Wood+ filament was purchased from Amazon about a year ago, and the manufacturing company is "*SUNLU*". Based on the provided information on the time of purchase, the filament is made of 30% wood, PLA and polymer binders. However, the supplied did not provide detailed information about the weight percentage of each component. All other information about Wood+ filament is provided in **Table 2-S2**.

Table 2-S2: Specifications of Wood+ filament.

Parameter	Value
Filament diameter [mm]	1.75 ± 0.02
Spool mass [kg]	1
Wood fiber [%]	30
Printing temperature	185 - 230
Print speed[mm/s]	20 - 40

2.5.1.4 S-Extruder specifications:

Filabot EX2 extruder has been purchased from *FILABOT* Company (Barre VT, USA), and the extruder specifications are given in **Table 2-S3**.

Table 2-S3: Specifications of extruder.

Parameter	Value
Extruder length [cm]	22
Extrusion temp. [^{o}C]	165
Spooler pulling speed [mm.s^{-1}]	28 ± 1
Feed screw driver speed [rpm]	17 ± 2

2.5.2 S-Thermal analysis of WF-PLA composite filament

2.5.2.1 S-Thermogravimetric analysis (TGA)

To evaluate the effect of wood fiber addition on the thermal stability and degradation temperature of WF-PLA composite, thermogravimetric analysis (TGA) is carried out on a series of filaments made out of pure (unreinforced) PLA, and 2.5, 5 and 10 *wt%* WF-PLA and wood fibers. The tests are conducted using a Q500 analyzer (TA Instruments, New Castle, DE, USA) at 5°C/min from 0°C to 500°C under a nitrogen atmosphere, and the results are shown in **Figure 2-S1**, indicating that the degradation temperature shifts slightly to lower values with the increase of wood fiber content, which is consistent with the performance of WF-PLA composites [77, 108]. The observed decrease of thermal stability is proportional to the amount of added wood fiber content whose onset degradation temperature is significantly lower than the pure PLA. However, wood fiber content is found to not significantly alter the thermal stability of the WF-PLA composite.

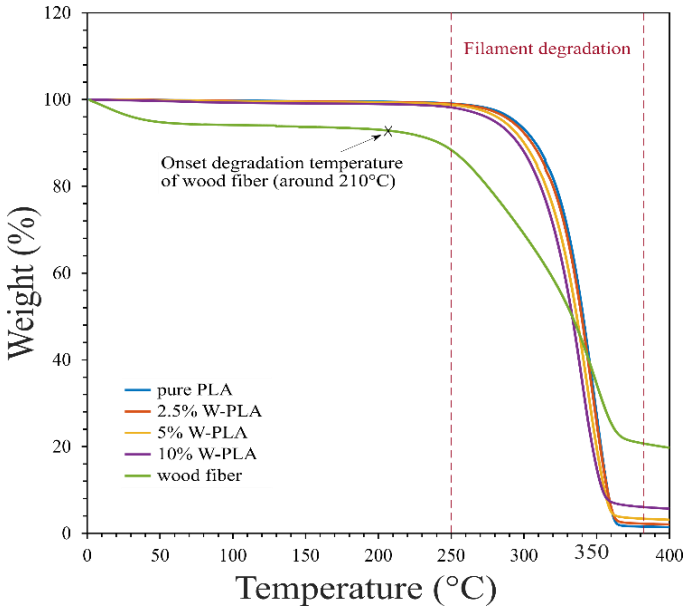

Figure 2-S1: TGA curve for pure PLA, and 2.5, 5 and 10 *wt%* WF-PLA and wood fibers.

2.5.2.2 S-Differential scanning calorimetry (DSC)

In order to assess crystallinity and thermal behavior of PLA matrices combined with different amounts of wood fiber contents, differential scanning calorimetry (DSC) is carried out on the extruded filaments using a Q200 analyzer (TA Instruments, New Castle, DE, USA) under nitrogen atmosphere conditions (50ml/min). The applied thermal cycle includes an initial cooling to 0°C, maintained for 10 minutes (isothermal), then heating up at 5°C /min from 0°C to 215°C, followed by an isothermal step at 215°C for 10min, cooling to 25°C and finally reheating to 215°C at the same rate. The DSC thermograms of each thermal cycle are shown in **Figure 2-S2**, and the thermal parameters are listed in **Table 2-S4.** To verify the reliability of the result, tests are repeated three times, and the average and standard deviation of the data are reported in **Table 2-S4**. As shown in **Figure 2-S2a**, adding wood fiber content does not significantly change the glass transition (T_g) and melting (T_m) temperatures of WF-PLA filaments, which are around 56°C and 162°C, respectively. **Figure 2-S2b** shows the corresponding cooling cycle where the cold crystallization temperature (T_c) is observed. For all of the samples, cold crystallization temperature (T_c) is close

to 96°C.

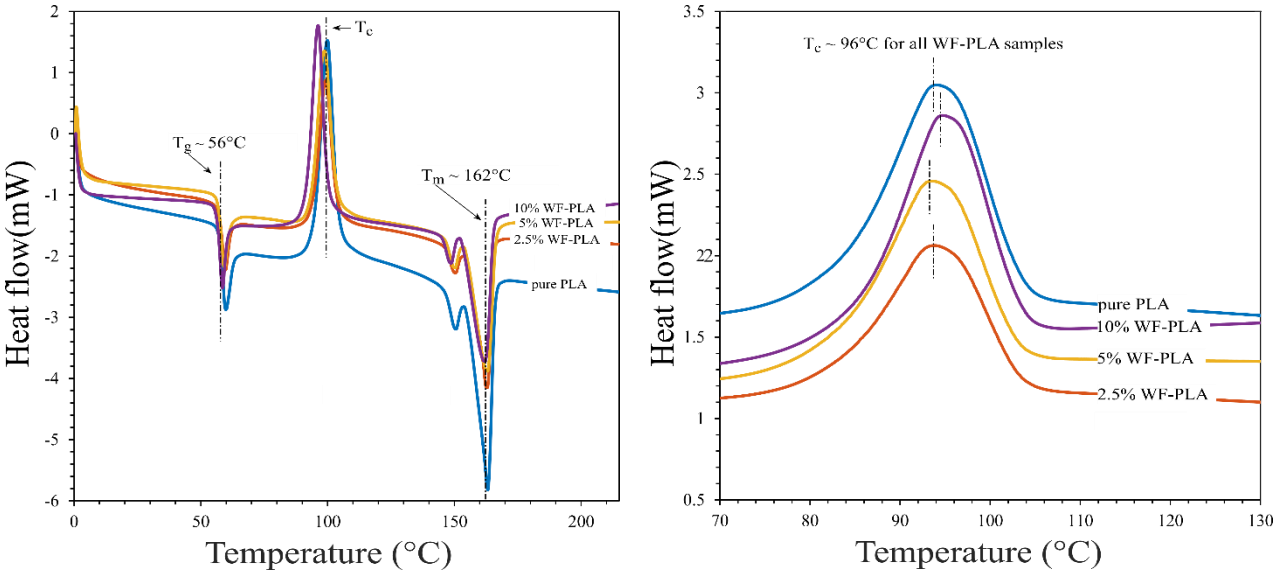

(a) (b)

Figure 2-S2: a) First heating and b) Corresponding cooling cycles of the filaments of pure PLA, and 2.5, 5 and *10 wt%* WF-PLA and wood fibers.

To further study the effect of adding wood fibers on the physical performance of WF-PLA filaments, the degree of crystallinity is also computed by [109]:

$$\lambda_c(\%) = \frac{\Delta H_m - \Delta H_{cc}}{\Delta H_f(1-W_f)} \times 100 \qquad \text{(S1)}$$

where ΔH_m is the melting enthalpy, ΔH_{cc} is the cold crystallization enthalpy. ΔH_f is a reference value that represents the enthalpy of 100% crystalline PLA (equal to 93Jg^{-1}) [110], and W_f is the weight percentage of the wood fibers. The degree of crystallinity has a significant influence on the hardness and density of the material, and it is also an important index for the potential energy absorption behavior of materials. With a higher degree of crystallinity, more lamellae (ordered regions), which are less amorphous, are formed in the material, leading to higher hardness, higher density and lower potential for energy absorption. As **Table 2-S4** shows, the degree of crystallinity of all filaments containing wood fibers is lower than pure PLA filament. The pronounced decrease

of crystallinity with the increase of wood fiber content indicates that wood fibers act as a barrier to the crystallinity of PLA.

Table 2-S4: Thermal parameters and crystallinity for WF-PLA filaments with alternative wood fiber contents.

Specimen	Tg [°C]	Tm [°C]	ΔHm [Jg^{-1}]	Tc [C]	ΔHcc [Jg^{-1}]	λc [%]
Pure PLA	56.1 ± 0.4	162.0 ± 0.4	30.0 ± 0.7	96.2 ± 0.7	20.3 ± 1.0	10.5 ± 1.1
2.5% WF-PLA	56.0 ± 0.2	161.6 ± 0.8	30.8 ± 1.8	96.3 ± 1.1	21.9 ± 2.0	9.8 ± 2.0
5% WF-PLA	55.9 ± 1.1	162.0 ± 0.4	27.8 ± 1.7	96.1 ± 1.1	19.8 ± 2.2	9.1 ± 0.7
10% WF-PLA	54.9 ± 0.7	161.5 ± 0.5	27.0 ± 0.6	96.5 ± 0.9	20.6 ± 0.8	7.6 ± 0.8

2.5.3 S-Manufacturing parameters

Table 2-S5: Manufacturing parameters for specimen 3D printing.

Filament type	Extruding temperature [˚C]	FDM 3D printing parameter	Value
Wood+	210	Layer height [mm]	0.2
Pure PLA	190	Chamber temperature [˚C]	45
2.5% WF-PLA	190	Maximum print speed [mm/min]	35
5% WF-PLA	185	Nozzle diameter [mm]	0.6
10% WF-PLA	180	Filament diameter [mm]	1.75
15% WF-PLA	180	Infill (%)	100

2.5.4 S-Photos of 3D printed WF-PLA samples

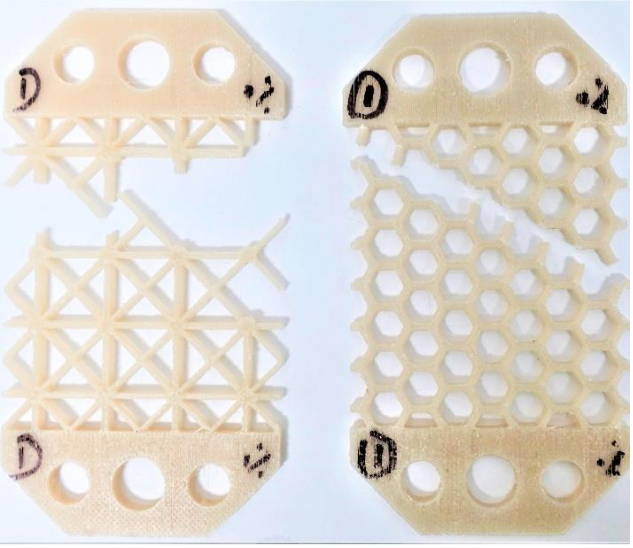

(a) (b)

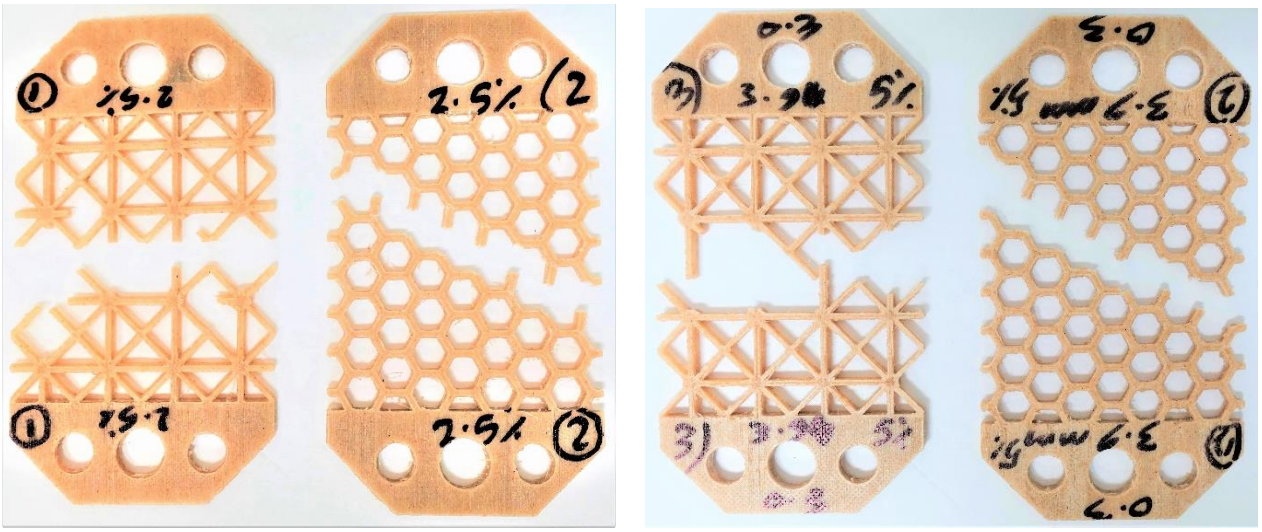

(c) (d)

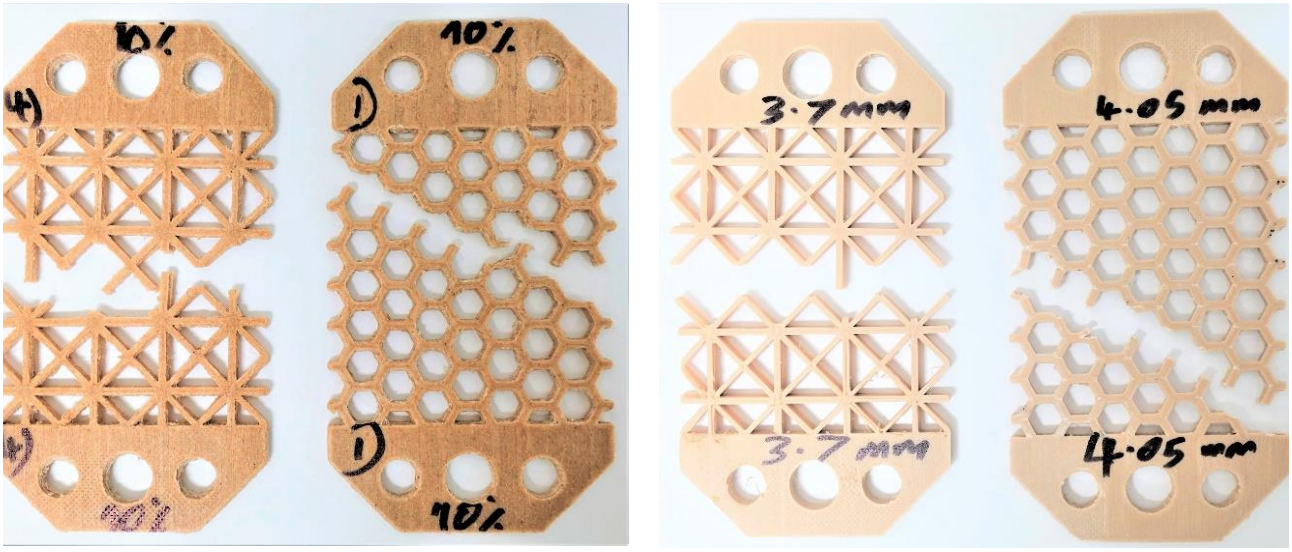

(e) (f)

Figure 2-S3: 3D printed WF-PLA samples: a) Dogbones with 0, 2.5, 5, 10, 15 *wt%* WF-PLA from left to right, respectively; and b, c, d, e, f) Cellular samples, *Isomixed* (left) and hexagonal (right), respectively, made out of (b) 0, (c) 2.5, (d) 5, (e) 10 *wt%* WF-PLA and (f) Wood+ filament.

2.5.5 S-Comparison of homogenization and FEM results

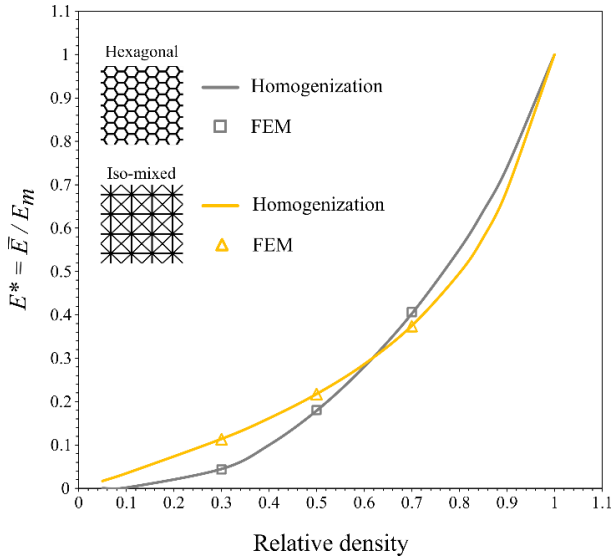

Figure 2-S4: Comparison of the stiffness of architected cellular materials for different relative densities and cell topologies.

2.5.6 S-Stress-Strain curves of WF-PLA dogbone samples

Figure 2-S5 presents the experimental stress-strain curves obtained from the tensile test for all 3D printed dogbone samples (6 types × (at least) 5 replicas). The shaded area in each figure shows the results' range, and the black curve is the stress-strain curve of one of the dogbone samples for each wood fiber content.

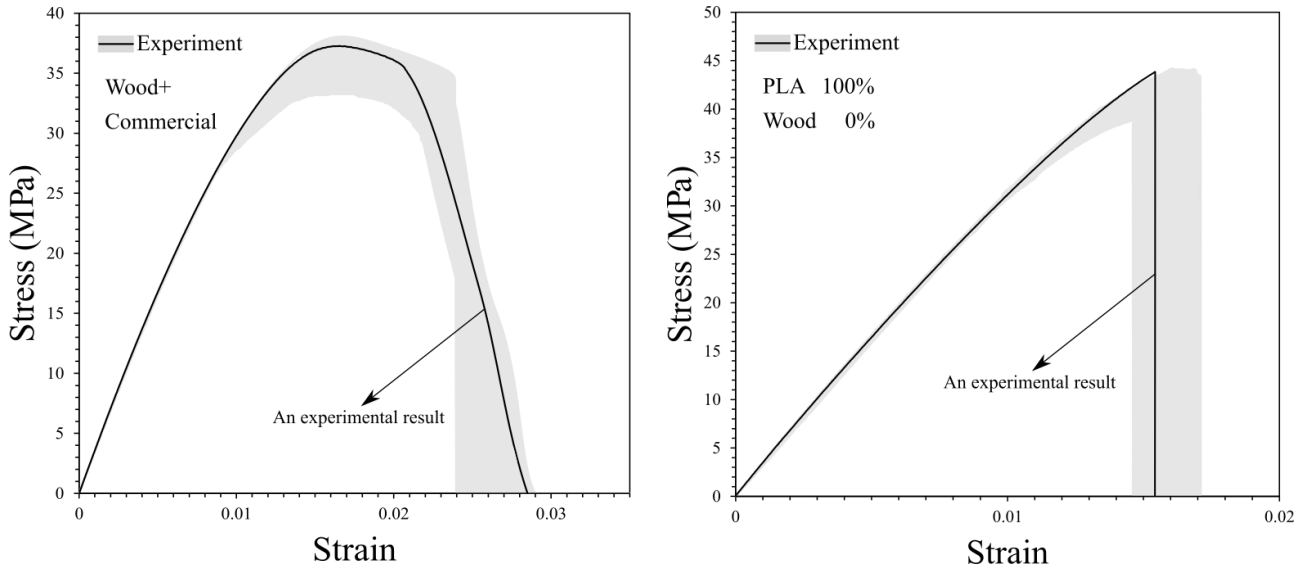

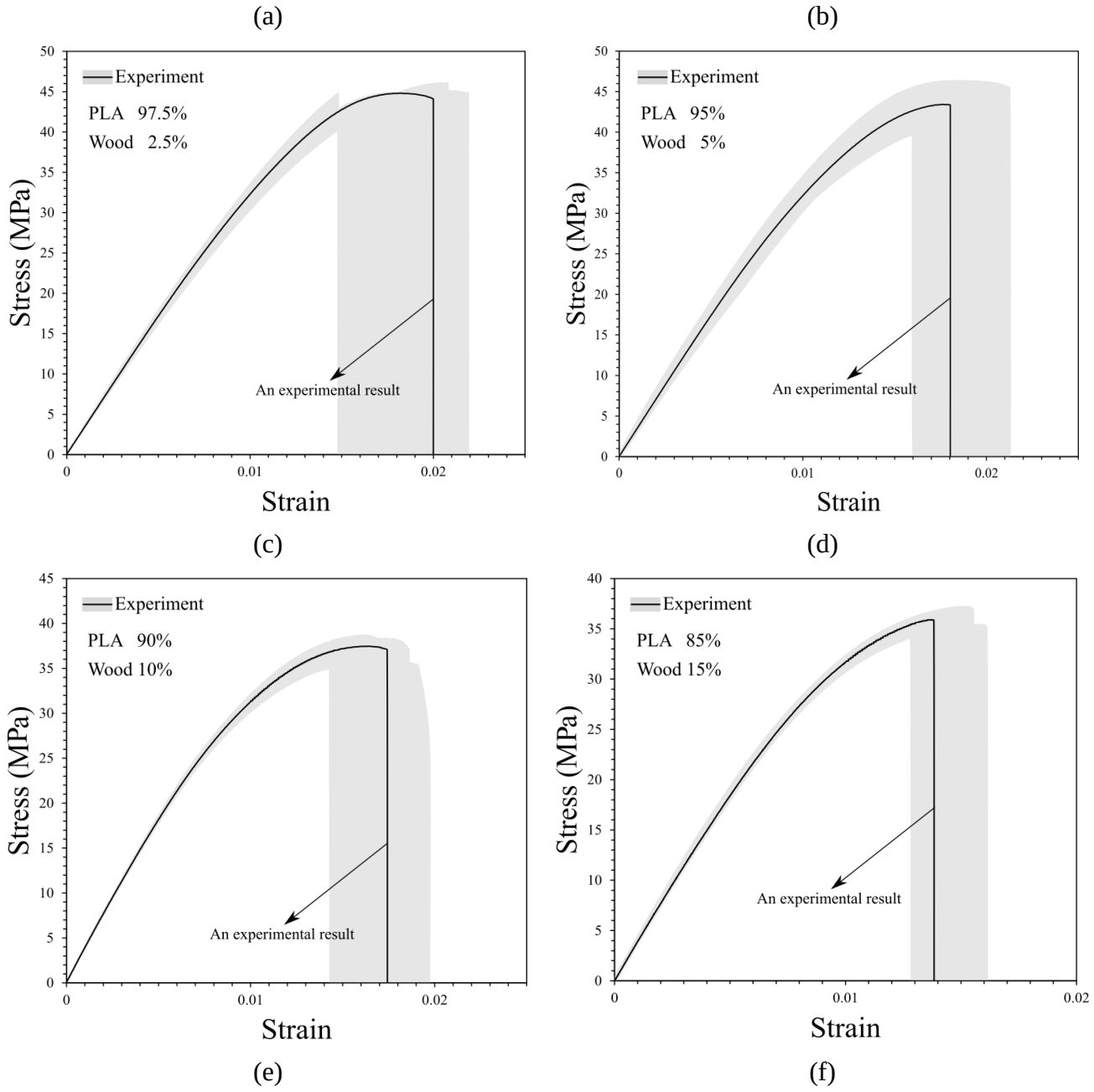

Figure 2-S5: Stress-strain curves of tested WF-PLA dogbone samples.

2.5.7 S-Out-of-plane 3D printed WF-PLA dogbone samples

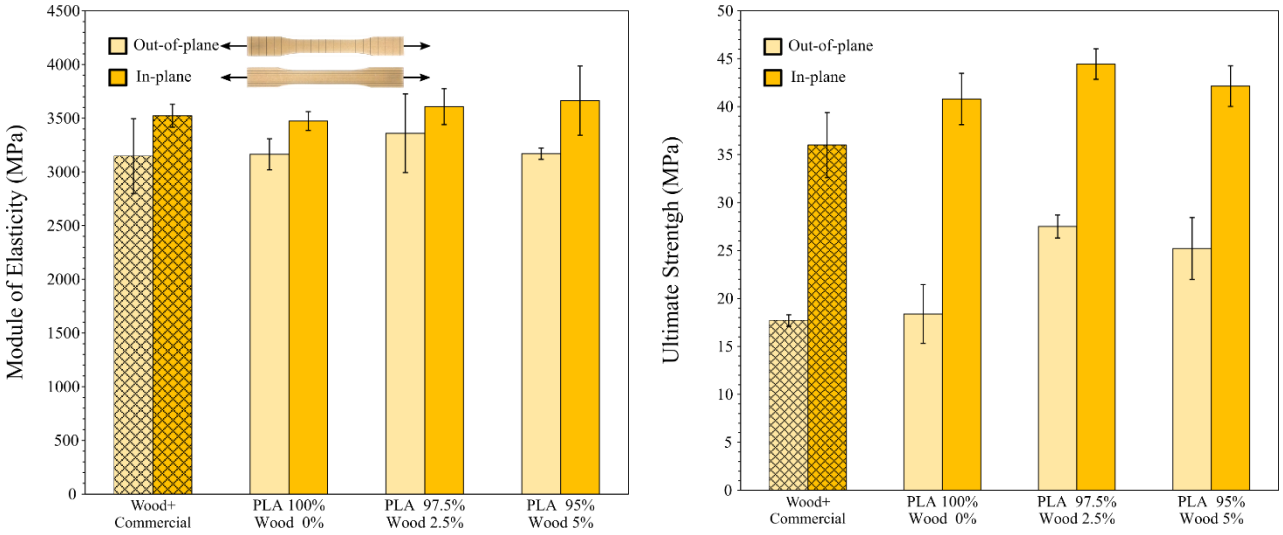

(a) (b)

Figure 2-S6: Comparison of mechanical properties of WF-PLA dogbone samples 3D printed in in-plane and out-of-plane configurations: a) Stiffness and b) Ultimate tensile strength.

2.5.8 S-*Isomixed* architecture design

To estimate the total stored strain energy density in the idealized mixed cell at small relative densities, horizontal, vertical and diagonal 2-force members are separately put under the same loading condition, and their stored energy densities are summed up (as presented in **Table 2-S6**).

Table 2-S6: Calculating the strain energy density (U) over the entire cell for different loading cases, under plane stress condition.

Loading on the cell	Cell	Link's strain (ε)	Strain energy density in the link ($\frac{1}{2}E\varepsilon^2$)	Cell's Relative density (ρ)	Strain energy density over the entire cell ($\frac{1}{2}E\varepsilon^2\rho$)
$\begin{bmatrix}\varepsilon_x\\ \varepsilon_y\\ \gamma_{xy}\end{bmatrix}=\begin{bmatrix}\varepsilon_1\\ 0\\ 0\end{bmatrix}$ 		ε_1	$\frac{1}{2}E_m{\varepsilon_1}^2$	$\frac{\rho_s}{2}$	$U^{(1)}=\frac{1}{4}E_m{\varepsilon_1}^2\rho_s$
		0	0	$\frac{\rho_s}{2}$	$U^{(2)}=0$
		$\frac{\varepsilon_1}{2}$	$\frac{1}{8}E_m{\varepsilon_1}^2$	$\frac{\rho_d}{2}$	$U^{(3)}=\frac{1}{16}E_m{\varepsilon_1}^2\rho_d$
		$\frac{\varepsilon_1}{2}$	$\frac{1}{8}E_m{\varepsilon_1}^2$	$\frac{\rho_d}{2}$	$U^{(4)}=\frac{1}{16}E_m{\varepsilon_1}^2\rho_d$
			Total strain energy density ($=\sum U^{(i)}$)		$U_{tot1}=\frac{1}{4}E_m{\varepsilon_1}^2(\rho_s+{\rho_d}/{2})$
$\begin{bmatrix}\varepsilon_x\\ \varepsilon_y\\ \gamma_{xy}\end{bmatrix}=\begin{bmatrix}\varepsilon_2\\ \varepsilon_2\\ 0\end{bmatrix}$ 		ε_2	$\frac{1}{2}E_m{\varepsilon_2}^2$	$\frac{\rho_s}{2}$	$U^{(1)}=\frac{1}{4}E_m{\varepsilon_2}^2\rho_s$
		ε_2	$\frac{1}{2}E_m{\varepsilon_2}^2$	$\frac{\rho_s}{2}$	$U^{(2)}=\frac{1}{4}E_m{\varepsilon_2}^2\rho_s$
		ε_2	$\frac{1}{2}E_m{\varepsilon_2}^2$	$\frac{\rho_d}{2}$	$U^{(3)}=\frac{1}{4}E_m{\varepsilon_2}^2\rho_d$
		ε_2	$\frac{1}{2}E_m{\varepsilon_2}^2$	$\frac{\rho_d}{2}$	$U^{(4)}=\frac{1}{4}E_m{\varepsilon_2}^2\rho_d$
			Total strain energy density ($=\sum U^{(i)}$)		$U_{tot2}=\frac{1}{2}E_m{\varepsilon_2}^2(\rho_s+\rho_d)$
$\begin{bmatrix}\varepsilon_x\\ \varepsilon_y\\ \gamma_{xy}\end{bmatrix}=\begin{bmatrix}0\\ 0\\ \gamma\end{bmatrix}$ 		0	0	$\frac{\rho_s}{2}$	$U^{(1)}=0$
		0	0	$\frac{\rho_s}{2}$	$U^{(2)}=0$
		$\frac{\gamma}{2}$	$\frac{1}{8}E_m\gamma^2$	$\frac{\rho_d}{2}$	$U^{(3)}=\frac{1}{16}E_m\gamma^2\rho_d$
		$-\frac{\gamma}{2}$	$\frac{1}{8}E_m\gamma^2$	$\frac{\rho_d}{2}$	$U^{(4)}=\frac{1}{16}E_m\gamma^2\rho_d$
			Total strain energy density ($=\sum U^{(i)}$)		$U_{tot3}=\frac{1}{8}E_m\gamma^2\rho_d$

*E_m: Young's modulus of the underlying isotropic solid material; ρ_s and ρ_d: Relative density of the simple square cell and the diagonal members, respectively.

Strain energy densities are then compared to those of an Isotropic material (with ρ, E, ν and $G=E/(2(1+\nu))$ as unknown material properties) under the same loading conditions as follows:

$$U_{tot1}=\frac{1}{4}E_m{\varepsilon_1}^2\left(\rho_s+{\rho_d}/{2}\right)=\frac{1}{2(1-\nu^2)}E{\varepsilon_1}^2\ \rightarrow\ E_m\left(\rho_s+{\rho_d}/{2}\right)=\frac{2}{1-\nu^2}E \qquad \text{(S2a)}$$

$$U_{tot2}=\frac{1}{2}E_m{\varepsilon_2}^2(\rho_s+\rho_d)=\frac{1}{1-\nu}E{\varepsilon_2}^2\ \rightarrow\ \frac{1}{2}E_m(\rho_s+\rho_d)=\frac{1}{1-\nu}E \qquad \text{(S2b)}$$

$$U_{tot3}=\frac{1}{8}E_m\gamma^2\rho_d=\frac{1}{2}G\gamma^2\xrightarrow{G=E/(2(1+\nu))}\frac{1}{2}E_m\rho_d=\frac{1}{1+\nu}E \qquad \text{(S2c)}$$

To find the relationship between the two unknown relative densities (i.e., ρ_s and ρ_d), left-hand sides and right-hand sides of equations II and III are subtracted from the corresponding sides of equation I, which results in $E_m\left({}^{\rho_s}/_{2} - {}^{\rho_d}/_{2}\right) = 0$, and since E_m is not zero, it yields $\rho_s = \rho_d$ which itself requires that $R_t = t_s/t_d = \sqrt{2}$. Additionally, noting that $\rho = \rho_{s+}\ \rho_d$, other material parameters are obtained as $\nu = 1/3$ and $E = \frac{1}{3}\rho E_m$.

2.5.9 S-Proposed equations for mechanical properties of 3D printed composite samples

Table 2-S7: Empirical equations for thermomechanical properties of wood fiber-reinforced

Modulus of elasticity [MPa]	$E = -0.1477w_f^4 + 3.8467w_f^3 - 28.627w_f^2 + 103.43w_f + 3474$
Ultimate strength [MPa]	$UTS = -0.0028w_f^4 + 0.0952w_f^3 - 1.0647w_f^2 + 3.55w_f + 40.8$
Fracture strain	$\varepsilon_f = -2(10^{-6})w_f^4 + 8(10^{-5})w_f^3 - 0.0008w_f^2 + 0.0025w_f + 0.0168$
Toughness [MJm^{-3}]	$U_T = -0.0002w_f^4 + 0.0054w_f^3 - 0.0523w_f^2 + 0.1681w_f + 0.389$
Thermal conductivity [$Wm^{-1}K^{-1}$]	$\kappa = 2(10^{-5})w_f^4 - 0.0007w_f^3 + 0.0057w_f^2 - 0.0063w_f + 0.2256$

* E, UTS, ε_f, U_T: Module of elasticity, Ultimate strength, Fracture strain and Toughness, respectively; w_f: WF-PLA weight percentage ratio.

2.5.10 S-Comparison of results determined by homogenization, FEM and experiment for modulus of elasticity of cellular samples

Table 2-S8: Numerical results (homogenization and finite element simulation) versus experimental data for modulus of elasticity [MPa].

	Hexagonal				*Isomixed*			
	Wood+ commercial	PLA 100% Wood 0%	PLA 95% Wood 5%	PLA 90% Wood 10%	Wood+ commercial	PLA 100% Wood 0%	PLA 95% Wood 5%	PLA 90% Wood 10%
Homogenization	189.2	186.6	196.8	215.7	432.1	426.1	449.4	492.4
FEM	187.9	185.2	195.4	214.1	427.4	421.5	444.6	487.1
Experiment	249±16	234±3.2	247±9.1	295±22	383±22	350±7.2	368±3.7	447±16
Discrepancy (%)	24.0	20.2	20.3	26.8	-12.7	-21.6	-22.1	-10.1

*$\rho_r = 0.32$ for homogenization; $\rho_r = 0.32 \pm 0.01$ for FEM; The discrepancy is between FEM and experimental results.

2.6 References

[1] Ashby, M.F., *The properties of foams and lattices.* Philos Trans A Math Phys Eng Sci, 2006. 364(1838): p. 15-30.
[2] Raney, J.R. and J.A. Lewis, *Printing mesoscale architectures.* Mrs Bulletin, 2015. 40(11): p. 943-950.
[3] Mirabolghasemi, A., A.H. Akbarzadeh, D. Rodrigue, and D. Therriault, *Thermal conductivity of architected cellular metamaterials.* Acta Materialia, 2019. 174: p. 61-80.
[4] Shi, J. and A.H. Akbarzadeh, *Architected cellular piezoelectric metamaterials: Thermo-electro-mechanical properties.* Acta Materialia, 2019. 163: p. 91-121.
[5] Zok, F.W., H. Rathbun, M. He, E. Ferri, C. Mercer, R.M. McMeeking, and A.G. Evans, *Structural performance of metallic sandwich panels with square honeycomb cores.* Philosophical Magazine, 2005. 85(26-27): p. 3207-3234.
[6] Yazdani Sarvestani, H., A.H. Akbarzadeh, H. Niknam, and K. Hermenean, *3D printed architected polymeric sandwich panels: Energy absorption and structural performance.* Composite Structures, 2018. 200: p. 886-909.
[7] Li, M., L.Z. Wu, L. Ma, B. Wang, and Z.X. Guan, *Mechanical Response of All-composite Pyramidal Lattice Truss Core Sandwich Structures.* Journal of Materials Science & Technology, 2011. 27(6): p. 570-576.
[8] Wadley, H.N., *Multifunctional periodic cellular metals.* Philos Trans A Math Phys Eng Sci, 2006. 364(1838): p. 31-68.
[9] Sajadi, S.M., P.S. Owuor, S. Schara, C.F. Woellner, V. Rodrigues, R. Vajtai, J. Lou, D.S. Galvao, C.S. Tiwary, and P.M. Ajayan, *Multiscale Geometric Design Principles Applied to 3D Printed Schwarzites.* Adv Mater, 2018. 30(1): p. 1704820.
[10] Hammetter, C.I., R.G. Rinaldi, and F.W. Zok, *Pyramidal Lattice Structures for High Strength and Energy Absorption.* Journal of Applied Mechanics-Transactions of the Asme, 2013. 80(4): p. 11.
[11] Wang, P., Y. Zheng, M.C. Fernandes, Y. Sun, K. Xu, S. Sun, S.H. Kang, V. Tournat, and K. Bertoldi, *Harnessing Geometric Frustration to Form Band Gaps in Acoustic Channel Lattices.* Phys Rev Lett, 2017. 118(8): p. 084302.
[12] Xia, X., A. Afshar, H. Yang, C.M. Portela, D.M. Kochmann, C.V. Di Leo, and J.R. Greer, *Electrochemically reconfigurable architected materials.* Nature, 2019. 573(7773): p. 205-213.
[13] Yuan, S.Q., F. Shen, J.M. Bai, C.K. Chua, J. Wei, and K. Zhou, *3D soft auxetic lattice structures fabricated by selective laser sintering: TPU powder evaluation and process optimization.* Materials & Design, 2017. 120: p. 317-327.
[14] Lei, M., C.M. Hamel, C. Yuan, H.B. Lu, and H.J. Qi, *3D printed two-dimensional periodic structures with tailored in-plane dynamic responses and fracture behaviors.* Composites Science and Technology, 2018. 159: p. 189-198.
[15] Habib, F.N., P. Iovenitti, S.H. Masood, and M. Nikzad, *Cell geometry effect on in-plane energy absorption of periodic honeycomb structures.* International Journal of Advanced Manufacturing Technology, 2018. 94(5-8): p. 2369-2380.
[16] Moini, M., J. Olek, J.P. Youngblood, B. Magee, and P.D. Zavattieri, *Additive Manufacturing and Performance of Architectured Cement-Based Materials.* Adv Mater, 2018. 30(43): p. e1802123.

[17] Sugiyama, K., R. Matsuzaki, M. Ueda, A. Todoroki, and Y. Hirano, *3D printing of composite sandwich structures using continuous carbon fiber and fiber tension.* Composites Part a-Applied Science and Manufacturing, 2018. 113: p. 114-121.
[18] Yang, Y., X. Song, X. Li, Z. Chen, C. Zhou, Q. Zhou, and Y. Chen, *Recent Progress in Biomimetic Additive Manufacturing Technology: From Materials to Functional Structures.* Adv Mater, 2018. 30(36): p. e1706539.
[19] Yazdani Sarvestani, H., A.H. Akbarzadeh, A. Mirbolghasemi, and K. Hermenean, *3D printed meta-sandwich structures: Failure mechanism, energy absorption and multi-hit capability.* Materials & Design, 2018. 160: p. 179-193.
[20] Tubío, C.R., A. Rama, M. Gómez, F. del Río, F. Guitián, and A. Gil, *3D-printed graphene-Al2O3 composites with complex mesoscale architecture.* Ceramics International, 2018. 44(5): p. 5760-5767.
[21] Dawood, A., B. Marti Marti, V. Sauret-Jackson, and A. Darwood, *3D printing in dentistry.* Br Dent J, 2015. 219(11): p. 521-9.
[22] Shao, H., X. Ke, A. Liu, M. Sun, Y. He, X. Yang, J. Fu, Y. Liu, L. Zhang, G. Yang, S. Xu, and Z. Gou, *Bone regeneration in 3D printing bioactive ceramic scaffolds with improved tissue/material interface pore architecture in thin-wall bone defect.* Biofabrication, 2017. 9(2): p. 025003.
[23] Wei, G. and P.X. Ma, *Partially nanofibrous architecture of 3D tissue engineering scaffolds.* Biomaterials, 2009. 30(32): p. 6426-34.
[24] Mueller, B., *Additive Manufacturing Technologies – Rapid Prototyping to Direct Digital Manufacturing.* Assembly Automation, 2012. 32(2).
[25] Wong, K.V. and A. Hernandez, *A review of additive manufacturing.* ISRN Mechanical Engineering, 2012. 2012.
[26] Stampfl, J. and M. Hatzenbichler, *Additive Manufacturing Technologies*, in *CIRP Encyclopedia of Production Engineering*, L. Laperrière and G. Reinhart, Editors. 2014, Springer Berlin Heidelberg: Berlin, Heidelberg. p. 20-27.
[27] Henke, K. and S. Treml, *Wood based bulk material in 3D printing processes for applications in construction.* European Journal of Wood and Wood Products, 2013. 71(1): p. 139-141.
[28] Horn, T.J. and O.L. Harrysson, *Overview of current additive manufacturing technologies and selected applications.* Sci Prog, 2012. 95(Pt 3): p. 255-82.
[29] Jungst, T., W. Smolan, K. Schacht, T. Scheibel, and J. Groll, *Strategies and Molecular Design Criteria for 3D Printable Hydrogels.* Chem Rev, 2016. 116(3): p. 1496-539.
[30] Håkansson, K.M.O., I.C. Henriksson, C. de la Peña Vázquez, V. Kuzmenko, K. Markstedt, P. Enoksson, and P. Gatenholm, *Solidification of 3D Printed Nanofibril Hydrogels into Functional 3D Cellulose Structures.* Advanced Materials Technologies, 2016. 1(7).
[31] Bourell, D.L., *Perspectives on Additive Manufacturing.* Annual Review of Materials Research, Vol 46, 2016. 46(1): p. 1-18.
[32] Noorani, R., *3D Printing : Technology, Applications, and Selection*. 2017, CRC Press: Boca Raton, FL.
[33] Wong, K., *K.V. Wong, A.Hernandez, "A Review of Additive Manufacturing," ISRN Mechanical Engineering, Vol 2012 (2012), Article ID 208760, 10 pages*. Vol. 2012. 2012.
[34] Travitzky, N., A. Bonet, B. Dermeik, T. Fey, I. Filbert-Demut, L. Schlier, T. Schlordt, and P. Greil, *Additive Manufacturing of Ceramic-Based Materials.* Advanced Engineering Materials, 2014. 16(6): p. 729-754.

[35] Chen, Z., Z. Li, J. Li, C. Liu, C. Lao, Y. Fu, C. Liu, Y. Li, P. Wang, and Y. He, *3D printing of ceramics: A review.* Journal of the European Ceramic Society, 2019. 39(4): p. 661-687.
[36] Ning, F.D., W.L. Cong, J.J. Qiu, J.H. Wei, and S.R. Wang, *Additive manufacturing of carbon fiber reinforced thermoplastic composites using fused deposition modeling.* Composites Part B-Engineering, 2015. 80: p. 369-378.
[37] Gray, R.W., D.G. Baird, and J.H. Bohn, *Effects of processing conditions on short TLCP fiber reinforced FDM parts.* Rapid Prototyping Journal, 1998. 4(1): p. 14-25.
[38] Gray, R.W., D.G. Baird, and J.H. Bohn, *Thermoplastic composites reinforced with long fiber thermotropic liquid crystalline polymers for fused deposition modeling.* Polymer Composites, 1998. 19(4): p. 383-394.
[39] Novakova-Marcincinova, L., J. Novak-Marcincin, J. Barna, and J. Torok. *Special materials used in FDM rapid prototyping technology application*. in *2012 IEEE 16th International Conference on Intelligent Engineering Systems (INES)*. 2012.
[40] Popescu, D., A. Zapciu, C. Amza, F. Baciu, and R. Marinescu, *FDM process parameters influence over the mechanical properties of polymer specimens: A review.* Polymer Testing, 2018. 69: p. 157-166.
[41] Rodriguez-Panes, A., J. Claver, and A.M. Camacho, *The Influence of Manufacturing Parameters on the Mechanical Behaviour of PLA and ABS Pieces Manufactured by FDM: A Comparative Analysis.* Materials (Basel), 2018. 11(8): p. 1333.
[42] Turner, B.N. and S.A. Gold, *A review of melt extrusion additive manufacturing processes: II. Materials, dimensional accuracy, and surface roughness.* Rapid Prototyping Journal, 2015. 21(3): p. 250-261.
[43] A. Gold, S., R. Strong, and B. N. Turner, *A review of melt extrusion additive manufacturing processes: I. Process design and modeling.* Rapid Prototyping Journal, 2014. 20(3): p. 192-204.
[44] Rahimizadeh, A., J. Kalman, K. Fayazbakhsh, and L. Lessard, *Recycling of fiberglass wind turbine blades into reinforced filaments for use in Additive Manufacturing.* Composites Part B-Engineering, 2019. 175: p. 107101.
[45] Matsuzaki, R., M. Ueda, M. Namiki, T.K. Jeong, H. Asahara, K. Horiguchi, T. Nakamura, A. Todoroki, and Y. Hirano, *Three-dimensional printing of continuous-fiber composites by in-nozzle impregnation.* Sci Rep, 2016. 6: p. 23058.
[46] Shofner, M.L., K. Lozano, F.J. Rodriguez-Macias, and E.V. Barrera, *Nanofiber-reinforced polymers prepared by fused deposition modeling.* Journal of Applied Polymer Science, 2003. 89(11): p. 3081-3090.
[47] Tekinalp, H.L., V. Kunc, G.M. Velez-Garcia, C.E. Duty, L.J. Love, A.K. Naskar, C.A. Blue, and S. Ozcan, *Highly oriented carbon fiber-polymer composites via additive manufacturing.* Composites Science and Technology, 2014. 105: p. 144-150.
[48] Zhong, W.H., F. Li, Z.G. Zhang, L.L. Song, and Z.M. Li, *Short fiber reinforced composites for fused deposition modeling.* Materials Science and Engineering a-Structural Materials Properties Microstructure and Processing, 2001. 301(2): p. 125-130.
[49] Khaled, S.A., J.C. Burley, M.R. Alexander, and C.J. Roberts, *Desktop 3D printing of controlled release pharmaceutical bilayer tablets.* Int J Pharm, 2014. 461(1-2): p. 105-11.
[50] Gladman, A.S., E.A. Matsumoto, R.G. Nuzzo, L. Mahadevan, and J.A. Lewis, *Biomimetic 4D printing.* Nat Mater, 2016. 15(4): p. 413-8.
[51] Chandrasekaran, S., E.B. Duoss, M.A. Worsley, and J.P. Lewicki, *3D printing of high performance cyanate ester thermoset polymers.* Journal of Materials Chemistry A, 2018. 6(3): p. 853-858.

[52] Le Duigou, A., M. Castro, R. Bevan, and N. Martin, *3D printing of wood fibre biocomposites: From mechanical to actuation functionality.* Materials & Design, 2016. 96: p. 106-114.
[53] Hofstetter, K., C. Hellmich, and J. Eberhardsteiner, *Development and experimental validation of a continuum micromechanics model for the elasticity of wood.* European Journal of Mechanics a-Solids, 2005. 24(6): p. 1030-1053.
[54] Hofstetter, K. and E.K. Gamstedt, *Hierarchical modelling of microstructural effects on mechanical properties of wood. A review COST Action E35 2004–2008: Wood machining – micromechanics and fracture,* in *Holzforschung*. 2009. p. 130.
[55] Qing, H. and L. Mishnaevsky, *3D hierarchical computational model of wood as a cellular material with fibril reinforced, heterogeneous multiple layers.* Mechanics of Materials, 2009. 41(9): p. 1034-1049.
[56] Qing, H. and L. Mishnaevsky, *3D multiscale micromechanical model of wood: From annual rings to microfibrils.* International Journal of Solids and Structures, 2010. 47(9): p. 1253-1267.
[57] Shishkina, O., S.V. Lomov, I. Verpoest, and L. Gorbatikh, *Structure-property relations for balsa wood as a function of density: modelling approach.* Archive of Applied Mechanics, 2014. 84(6): p. 789-805.
[58] Malek, S., J.R. Raney, J.A. Lewis, and L.J. Gibson, *Lightweight 3D cellular composites inspired by balsa.* Bioinspir Biomim, 2017. 12(2): p. 026014.
[59] Gereke, T., S. Malekmohammadi, C. Nadot-Martin, C. Dai, F. Ellyin, and R. Vaziri. *A numerical multiscale approach for stiffness predictions of wood composite*. in *Proceedings of the American Society for Composites: twenty-sixth technical conference*. 2011.
[60] Malek, S. and L.J. Gibson, *Multi-scale modelling of elastic properties of balsa.* International Journal of Solids and Structures, 2017. 113: p. 118-131.
[61] Klemm, D., B. Heublein, H.P. Fink, and A. Bohn, *Cellulose: fascinating biopolymer and sustainable raw material.* Angew Chem Int Ed Engl, 2005. 44(22): p. 3358-93.
[62] Zhu, H., S. Zhu, Z. Jia, S. Parvinian, Y. Li, O. Vaaland, L. Hu, and T. Li, *Anomalous scaling law of strength and toughness of cellulose nanopaper.* Proc Natl Acad Sci U S A, 2015. 112(29): p. 8971-6.
[63] Frydrych, I., G. Dziworska, and J. Bilska, *Comparative analysis of the thermal insulation properties of fabrics made of natural and man-made cellulose fibres.* Fibres & Textiles in Eastern Europe, 2002. 10(4): p. 40-44.
[64] Shimazaki, Y., Y. Miyazaki, Y. Takezawa, M. Nogi, K. Abe, S. Ifuku, and H. Yano, *Excellent thermal conductivity of transparent cellulose nanofiber/epoxy resin nanocomposites.* Biomacromolecules, 2007. 8(9): p. 2976-8.
[65] Zhao, D., Y. Zhu, W. Cheng, W. Chen, Y. Wu, and H. Yu, *Cellulose-Based Flexible Functional Materials for Emerging Intelligent Electronics.* Adv Mater, 2021. 33(28): p. e2000619.
[66] Wang, S., A. Lu, and L.N. Zhang, *Recent advances in regenerated cellulose materials.* Progress in Polymer Science, 2016. 53: p. 169-206.
[67] Agnarsson, I., M. Kuntner, and T.A. Blackledge, *Bioprospecting finds the toughest biological material: extraordinary silk from a giant riverine orb spider.* PLoS One, 2010. 5(9): p. e11234.
[68] Adusumali, R.B., M. Reifferscheid, H. Weber, T. Roeder, H. Sixta, and W. Gindl. *Mechanical properties of regenerated cellulose fibres for composites*. in *Macromolecular Symposia*. 2006. Wiley Online Library.
[69] Pattinson, S.W. and A.J. Hart, *Additive Manufacturing of Cellulosic Materials with Robust Mechanics and Antimicrobial Functionality.* Advanced Materials Technologies, 2017. 2(4): p. 1600084.

[70] Gibson, L.J., *The hierarchical structure and mechanics of plant materials.* J R Soc Interface, 2012. 9(76): p. 2749-66.
[71] Iwatake, A., M. Nogi, and H. Yano, *Cellulose nanofiber-reinforced polylactic acid.* Composites Science and Technology, 2008. 68(9): p. 2103-2106.
[72] Awal, A., M. Rana, and M. Sain, *Thermorheological and mechanical properties of cellulose reinforced PLA bio-composites.* Mechanics of Materials, 2015. 80: p. 87-95.
[73] Panthapulakkal, S., A. Zereshkian, and M. Sain, *Preparation and characterization of wheat straw fibers for reinforcing application in injection molded thermoplastic composites.* Bioresour Technol, 2006. 97(2): p. 265-72.
[74] Rouison, D., M. Sain, and M. Couturier, *Resin transfer molding of natural fiber reinforced composites: cure simulation.* Composites Science and Technology, 2004. 64(5): p. 629-644.
[75] Mulinari, D.R., H.J.C. Voorwald, M.O.H. Cioffi, M.L.C.P. da Silva, T.G. da Cruz, and C. Saron, *Sugarcane bagasse cellulose/HDPE composites obtained by extrusion.* Composites Science and Technology, 2009. 69(2): p. 214-219.
[76] Montalvo Navarrete, J.I., M.A. Hidalgo-Salazar, E. Escobar Nunez, and A.J. Rojas Arciniegas, *Thermal and mechanical behavior of biocomposites using additive manufacturing.* International Journal on Interactive Design and Manufacturing (IJIDeM), 2017. 12(2): p. 449-458.
[77] Tao, Y., H. Wang, Z. Li, P. Li, and S.Q. Shi, *Development and Application of Wood Flour-Filled Polylactic Acid Composite Filament for 3D Printing.* Materials (Basel), 2017. 10(4): p. 339.
[78] Compton, B.G. and J.A. Lewis, *3D-printing of lightweight cellular composites.* Adv Mater, 2014. 26(34): p. 5930-5.
[79] Sang, L., S.F. Han, X.S. Peng, X.G. Jian, and J.Y. Wang, *Development of 3D-printed basalt fiber reinforced thermoplastic honeycombs with enhanced compressive mechanical properties.* Composites Part a-Applied Science and Manufacturing, 2019. 125: p. 105518.
[80] Jiang, Y.J. and J.R. Raney, *3D Printing of Amylopectin-Based Natural Fiber Composites.* Advanced Materials Technologies, 2019. 4(11): p. 1900521.
[81] Harris, A., S. Kazachenko, R. Bateman, J. Nickerson, and M. Emanuel, *Measuring the thermal conductivity of heat transfer fluids via the modified transient plane source (MTPS).* Journal of Thermal Analysis and Calorimetry, 2014. 116(3): p. 1309-1314.
[82] Kuvandykova, D. and R. St-Laurent, *Application of the modified transient plane source technique in testing the thermal conductivity of concrete.* C-Therm Technol, 2010. 18: p. 1-7.
[83] Technologies, C.-T. *TCi Thermal Conductivity Analyzer*. 2020 [cited 2020 January]; Available from: https://ctherm.com/products/tci_thermal_conductivity/.
[84] Bertoldi, K., P.M. Reis, S. Willshaw, and T. Mullin, *Negative Poisson's ratio behavior induced by an elastic instability.* Adv Mater, 2010. 22(3): p. 361-6.
[85] Rafsanjani, A., A. Akbarzadeh, and D. Pasini, *Snapping mechanical metamaterials under tension.* Adv Mater, 2015. 27(39): p. 5931-5.
[86] Shi, J. and A.H. Akbarzadeh, *3D Hierarchical lattice ferroelectric metamaterials.* International Journal of Engineering Science, 2020. 149: p. 103247.
[87] Deshpande, V.S., M.F. Ashby, and N.A. Fleck, *Foam topology bending versus stretching dominated architectures.* Acta Materialia, 2001. 49(6): p. 1035-1040.
[88] Guest, S.D. and J.W. Hutchinson, *On the determinacy of repetitive structures.* Journal of the Mechanics and Physics of Solids, 2003. 51(3): p. 383-391.
[89] Hollister, S.J. and N. Kikuchi, *A comparison of homogenization and standard mechanics analyses for periodic porous composites.* Computational Mechanics, 1992. 10(2): p. 73-95.

[90] Zener, C., *Contributions to the Theory of Beta-Phase Alloys.* Physical Review, 1947. 71(12): p. 846-851.
[91] Berger, J.B., H.N. Wadley, and R.M. McMeeking, *Mechanical metamaterials at the theoretical limit of isotropic elastic stiffness.* Nature, 2017. 543(7646): p. 533-537.
[92] Lusti, H.R., I.A. Karmilov, and A.A. Gusev, *Effect of Particle Agglomeration on the Elastic Properties of Filled Polymers.* Soft Materials, 2002. 1(1): p. 115-120.
[93] Green, D., J. Winandy, and D. Kretschmann, *Mechanical properties of wood, Chapter 4.* Wood Handbook–Wood as an Engineered Material, FPL-GTR-113, USDA Forest Service, Forest Products Laboratory, Madison WI, USA, 1999.
[94] Sudamrao Getme, A. and B. Patel, *A Review: Bio-fiber's as reinforcement in composites of polylactic acid (PLA).* Materials Today: Proceedings, 2020. 26: p. 2116-2122.
[95] Jia, Z., Y. Yu, and L.F. Wang, *Learning from nature: Use material architecture to break the performance tradeoffs.* Materials & Design, 2019. 168: p. 107650.
[96] Cabuz, A.I., D. Felbacq, and D. Cassagne, *Homogenization of negative-index composite metamaterials: a two-step approach.* Phys Rev Lett, 2007. 98(3): p. 037403.
[97] Zheng, X., H. Lee, T.H. Weisgraber, M. Shusteff, J. DeOtte, E.B. Duoss, J.D. Kuntz, M.M. Biener, Q. Ge, J.A. Jackson, S.O. Kucheyev, N.X. Fang, and C.M. Spadaccini, *Ultralight, ultrastiff mechanical metamaterials.* Science, 2014. 344(6190): p. 1373-7.
[98] Overvelde, J.T., T.A. de Jong, Y. Shevchenko, S.A. Becerra, G.M. Whitesides, J.C. Weaver, C. Hoberman, and K. Bertoldi, *A three-dimensional actuated origami-inspired transformable metamaterial with multiple degrees of freedom.* Nat Commun, 2016. 7(1): p. 10929.
[99] MacLean, J., *Thermal conductivity of wood.* Heating, piping & air conditioning. Madison, USA, 1941. Vol. 13, no. 6: p. 380-391.
[100] Takagi, H., S. Kako, K. Kusano, and A. Ousaka, *Thermal conductivity of PLA-bamboo fiber composites.* Advanced Composite Materials, 2007. 16(4): p. 377-384.
[101] Chung, S.Y., D. Stephan, M. Abd Elrahmana, and T.S. Han, *Effects of anisotropic voids on thermal properties of insulating media investigated using 3D printed samples.* Construction and Building Materials, 2016. 111: p. 529-542.
[102] Wei, Y., Y. Li, L. Zhu, Y. Liu, X. Lei, G. Wang, Y. Wu, Z. Mi, J. Liu, H. Wang, and H. Gao, *Evading the strength-ductility trade-off dilemma in steel through gradient hierarchical nanotwins.* Nat Commun, 2014. 5(1): p. 3580.
[103] Ronan, W., V.S. Deshpande, and N.A. Fleck, *The tensile tensile ductility of cellular Solids: The role of imperfections.* International Journal of Solids and Structures, 2016. 102: p. 200-213.
[104] Sarac, B., J. Ketkaew, D.O. Popnoe, and J. Schroers, *Honeycomb Structures of Bulk Metallic Glasses.* Advanced Functional Materials, 2012. 22(15): p. 3161-3169.
[105] Lebedev, S.M., O.S. Gefle, E.T. Amitov, D.Y. Berchuk, and D.V. Zhuravlev, *Poly(lactic acid)-based polymer composites with high electric and thermal conductivity and their characterization.* Polymer Testing, 2017. 58: p. 241-248.
[106] Smith, M., S. Kim, A. Lambert, M. Walde, J. Lindahl, K. Mungale, T. Bougher, A.A. Hassen, and V. Kunc. *Maximizing the Performance of a 3D Printed Heat Sink by Accounting for Anisotropic Thermal Conductivity During Filament Deposition*. in *2019 18th IEEE Intersociety Conference on Thermal and Thermomechanical Phenomena in Electronic Systems (ITherm)*. 2019.
[107] Ibrahim, Y., A. Elkholy, J.S. Schofield, G.W. Melenka, and R. Kempers, *Effective thermal conductivity of 3D-printed continuous fiber polymer composites.* Advanced Manufacturing-Polymer & Composites Science, 2020. 6(1): p. 17-28.

[108] Lee, S.Y., I.A. Kang, G.H. Doh, H.G. Yoon, B.D. Park, and Q.L. Wu, *Thermal and mechanical properties of wood flour/talc-filled polylactic acid composites: Effect of filler content and coupling treatment.* Journal of Thermoplastic Composite Materials, 2008. 21(3): p. 209-223.
[109] Kong, Y. and J.N. Hay, *The measurement of the crystallinity of polymers by DSC.* Polymer, 2002. 43(14): p. 3873-3878.
[110] Davoodi, S., E. Oliaei, S.M. Davachi, I. Hejazi, J. Seyfi, B.S. Heidari, and H. Ebrahimi, *Preparation and characterization of interface-modified PLA/starch/PCL ternary blends using PLLA/triclosan antibacterial nanoparticles for medical applications.* RSC Advances, 2016. 6(46): p. 39870-39882.

Link between Chapter 2 and Chapter 3

Chapter 2 of this thesis (Paper 1) focused on investigating the thermomechanical advantages obtained by incorporating wood short fibers into PLA. Additionally, the influence of engineering cell geometry on achieving desired mechanical properties is examined in this paper. However, further analysis is required to determine the impact of short fiber specifications on the thermomechanical properties of short fiber-reinforced composites. Such detailed understanding is crucial for effectively engineering the thermomechanical properties of the cells through appropriate selection of fiber percentage, size, orientation, and other factors. Furthermore, the potential for enhancing and engineering the mechanical properties of architected fiber-reinforced composites is needed to be explored, particularly by utilizing multi-materials with the same matrix but varying fiber percentages to enhance bonding between cell members. Chapter 3 of this thesis presents Paper 2, in which the above-mentioned further investigations have been accomplished.

3 Chapter three: Architected Cellular Fiber-reinforced Composites[2]

Abstract

Advances in 3D printing have enabled fabrication of rationally-designed cellular architectures out of fiber-reinforced composites, offering a new class of low-density high-performance materials with multifunctional properties unattainable with either of their constituent composites or the underlying cellular architectures. In this thesis, efficacy of the hierarchical material design approach is investigated by creating various periodic fiber-reinforced representative cells and evaluating effects of fiber volume fraction, fiber length, fiber orientation and cell topology on their effective thermomechanical properties using multiscale standard mechanics homogenization with periodic boundary conditions. The incorporated approach is finally corroborated by comparing the numerical and experimental data for the Young's moduli of cellular metamaterials with tunable isotropic/anisotropic thermomechanical properties, 3D printed out of pure and carbon-fiber-reinforced PETG polymer.

[2] *Reproduced with permission from Estakhrianhaghighi, E., Mirabolghasemi, A., Shi, J., Lessard, L. & Akbarzadeh, A. H. Architected cellular fiber-reinforced composite. Composites Part B: Engineering 238, 109894, (2022).*

3.1 Introduction

Among alternative composite materials [1-3], the most commonly used is the fiber-reinforced composite (FRC) (containing short or long fibers and a polymer/metallic matrix) owing to its high specific strength/stiffness/toughness, outstanding fatigue behavior and low cost [4, 5]. Cellular FRC (CFRC), an emerging class of high-performance structural material, offers several advantages since they benefit from the properties of both FRC and lightweight and tunable cellular solids. CFRCs have recently found applications in lightweight sandwich panels, energy absorbers and vibration dampers [6-8].

Exploring their complex periodic microarchitectures and potential superior multifunctional properties solicits detailed numerical and experimental analysis techniques. Although studies on CFRCs have been mainly focused on their mechanical performance [9-12], a few research studies have recently been devoted to the connection between cell microarchitecture and their effective thermal conductivity [13-18] as well as material composition and their thermal expansion coefficient [19, 20]. The substantial progress in the design and fabrication of cellular microarchitectures is mainly due to the recent advances in manufacturing techniques such as additive manufacturing (3D printing) and laser cutting. These advances have led to improved thermomechanical properties of the CFRCs [14, 21-35]. A possible procedure for measuring and optimizing the thermomechanical properties of cellular materials and fiber-reinforced composites is fabricating various samples and experimentally determining their properties [36-40]. Considering that the method is time-consuming and costly, different analytical micromechanics models approached [41-47] and numerical techniques (e.g., Random Sequential Adsorption (RSA) implemented by finite element method (FEM)[48-50] and Monte Carlo Algorithm [51]) have been developed to computationally explore the effective properties of CFRC.

In addition to the properties of their individual constituents, the effective properties of multi-material CFRC are derived by a multitude of material and architectural parameters including the inclusion/fiber volume fraction (the percentage of inclusion/fiber volume in the entire volume of the fiber-reinforced composite), the relative density of the cellular composite (the volume fraction of solid in the cellular material), fiber specifications (i.e., fiber location, dimension, orientation and aspect ratio), adhesion of fibers to matrix, surface roughness of fibers, defects (e.g., voids and bubbles in the matrix or in the interface of the fibers and matrix) and cell topology [12, 52]. Although detailed modeling of all the aforementioned features is possible, the vast number of attainable variations (material compositions and architectural designs) and the limitations of the detailed analysis methods pose a challenge in multiscale prediction of effective properties for CFRCs; thus, a feasible strategy is required to reduce the complexity of the analysis while keeping the predictions accurate. To the best of the authors' knowledge, no study in the literature has reported the relationship among the fiber characteristics and the effective thermomechanical properties of architected cellular fiber-reinforced composites.

In this thesis, a new multi-level approach (i.e., first obtaining the effective properties of the composite, and then use those effective properties as the equivalent properties of the composite solid to analyze the meso/macro scale effective properties of cellular composite material) is introduced and implemented based on standard mechanics homogenization (SMH) with periodic boundary conditions [53]. The effect of relative density, fiber volume fraction, relative fiber size, fiber orientation and cell topology is investigated on the effective thermomechanical properties of CFRC with complex architectures. Among different existing techniques to find the effective elastic properties [54], the introduced approach is independent of the RVE size for a specific range of fiber relative size. The RSA method is used to disperse random fibers in a periodic RVE;

homogenization technique is then adopted to numerically determine the effective thermomechanical properties of randomly distributed CFRC [55-59]. 3D RVEs, instead of 2D ones [60], are used to account for the interaction effects among fibers more accurately. Under the assumption that a periodic building block can closely mimic CFRCs, a single cell is used to analyze their effective thermomechanical properties [53]. The efficiency of the proposed multi-level approach is justified by comparing its results with a detailed multiscale analysis for a variety of cell topologies, fiber volume fraction, fiber length and fiber orientations. Following the distinctive properties offered by cellular-based mechanical metamaterials (e.g., negative Poisson's ratio, negative incremental stiffness and ultrahigh multifunctional Figures of merits [61-64]), novel thermomechanically quasi-isotropic composite cells, called 2D and 3D *Isomixed*, are designed through developing an analytical method. By comparing the strain energy density of the cells under various loading conditions with those of isotropic materials, multi-material rectangular (2D) and cuboid (3D) strut-based cells with isotropic elastic stiffness and thermal conductivity are rationally designed. Previous studies have mainly focused on 2D square and 3D cubic cells without considering more general cell architectures with isotropic properties [65]. In addition to the numerical evaluation of their effective properties using the multi-level method, the quasi-isotropic cellular metamaterials are 3D printed and their effective Young's moduli are experimentally assessed.

The RVE modeling process with periodic boundary conditions is presented in Section 3.2. Two different cell topologies (closed simple cube and open simple cube) are considered in this thesis to obtain the thermomechanical properties of CFRCs. In Section 3.3, the fundamentals of the standard mechanics homogenization for determining effective properties of an RVE are summarized. Section 3.4 provides a multiscale thermomechanical finite element analysis. Section

3.5 presents a systematic design methodology for developing new 2D and 3D *Isomixed* composite cellular architectures. Detailed finite element analyses along with experimental tests have been performed on the 2D *Isomixed* biomaterial composite cellular solids to further corroborate analytical results (Section 3.6). This thesis provides a multi-level strategy and evaluates its underlying assumptions for finding the effective properties of architected cellular fiber-reinforced composites through a periodic RVE. The developed strategy is used to tailor the cell architecture and material composition in order to devise cellular metamaterials with controllable isotopy/anisotropy of thermomechanical properties that also take advantage of the excellent properties of fibers inside the composite constituents.

Material properties and structural design play critical roles in the engineering of optimized and multifunctional structural elements. Due to limited material and energy resources, economical constraints and environmental concerns, demands are growing for the development of advanced lightweight and durable materials and structures with programmable properties for applications in aerospace, automotive, energy and medical sectors. In an effort to meet such demands, various materials have been designed, among which engineered cellular composite materials are one of the cutting-edge solutions for developing lightweight and optimized materials and structures. The architected cellular composites can simultaneously satisfy multiple functionalities, from high structural stiffness-to-mass ratio to thermal insulation and energy harvesting [12, 66]. In addition, these materials have received considerable attention for their high strength-to-mass ratios, high energy absorption, excellent crashworthiness performance and programmability of their energy dissipation and structural configuration [66-69].

3.2 RVE modeling

A microstructure model, capable of accurate predictions of the CFRCs' effective properties,

is crucial to exploit their multifunctional potentials. To apply the standard mechanics homogenization and explore the effects of fiber reinforcement characteristics, pore topology and relative density on the effective thermomechanical properties of cellular composite metamaterials, 2D and 3D RVEs that statistically represent the real microstructure are examined.

3.2.1 Generation of periodic RVEs with random fibers

This thesis considers that the RVE of a fiber-reinforced composite consists of randomly distributed fibers throughout the whole RVE, in which each fiber is a straight cylinder with length *l*, radius *r*, center C(X, Y, Z) and two angles (Φ and Θ) that determine its in-plane and out-of-plane orientations, respectively (**Figure 3-1a**). One of the widely used techniques to generate fiber-reinforced composites with randomly dispersed fibers and to study their effective properties is the Random Sequential Adsorption (RSA) technique [50] (**Figure 3-1b**). In this technique, random fibers (discrete in the form of ones in a 3D matrix of zeros) are sequentially added to the cell (a $500 \times 500 \times 500$ matrix of zeros and ones, in which ones represent the occupied positions by fibers) and kept if there is no overlap between the fibers. This process repeats until the desired fiber volume fraction is met. To avoid high-stress gradient and stress concentrations, a minimum distance of 0.002 times the side length of RVE is considered in this thesis between two adjacent fibers.

In this thesis's modified RSA method, periodic geometry is one of this thesis's assumptions of RVE generation. The geometric periodicity of boundaries means that the fibers penetrating through the walls reappear at opposite sides. All faces, edges and corners of the RVE shall conform to this continuity criterion. In the case of periodicity across the faces, parts of a fiber that cross the faces of the RVE and are shared by the adjacent cells are copied to occupy the same position in the initial RVE. These fibers are shown in grey in **Figure 3-1a**, while fibers that do not cross the

cell boundary are shown in cyan and red.

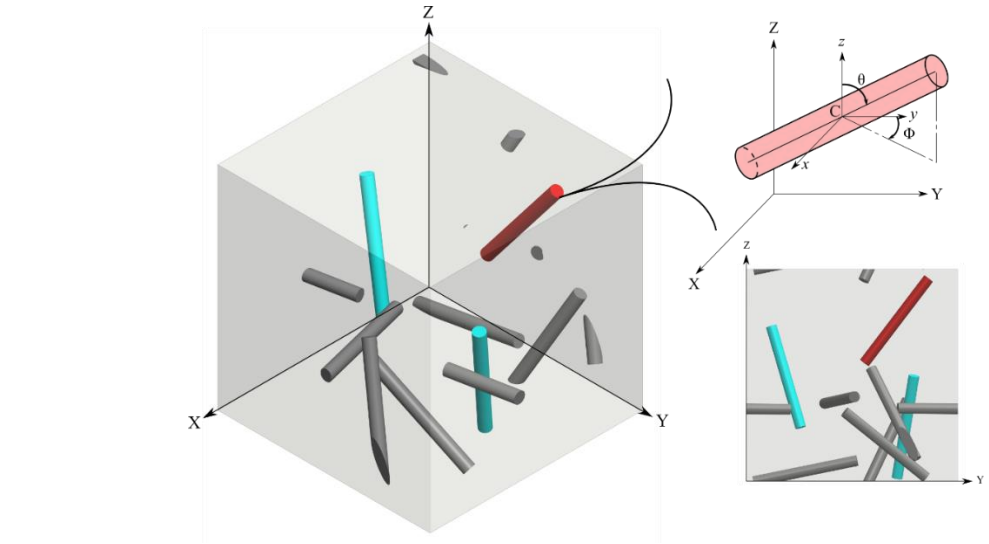

(a)

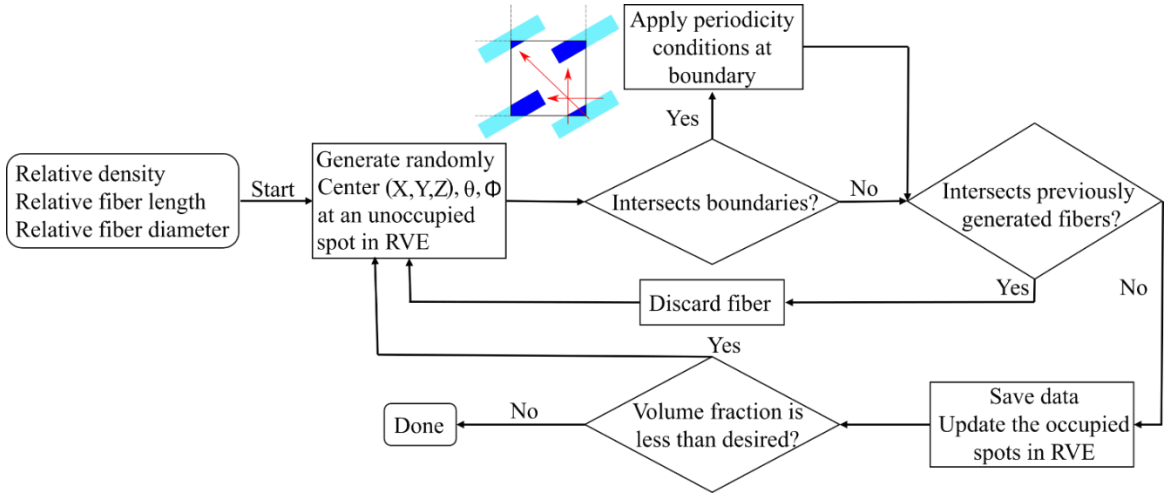

(b)

Figure 3 - 1: (a) Fiber and RVE modeling at global (XYZ) and local (xyz) coordinates: Grey fibers are intersecting the RVE walls, and cyan/red fibers are all inside the RVE; (b) Modified Random sequential adsorption (RSA) flowchart.

3.2.2 Cellular fiber-reinforced composite metamaterials

This thesis investigates one closed- and one open-cell geometry for the cellular fiber-reinforced composite metamaterials: closed simple cube (*CSC*) cell type and b) open simple cube (*OSC*) cell type. The *CSC* cell is a simple $L \times L \times L$ cell with a $\frac{L}{2} \times \frac{L}{2} \times \frac{L}{2}$ cubic void at its center.

The *OSC* cell consists of a simple cube that is cut by three $\frac{L}{2} \times \frac{L}{2} \times L$ cuboids at its center along X, Y and Z directions. Periodicity on the RVE faces, edges and corners for the fibers touching the boundaries and a perfectly bonded interface between the matrix and fibers are assumed. The details of the cell topology of each type are presented in **Figure 3 - 2**.

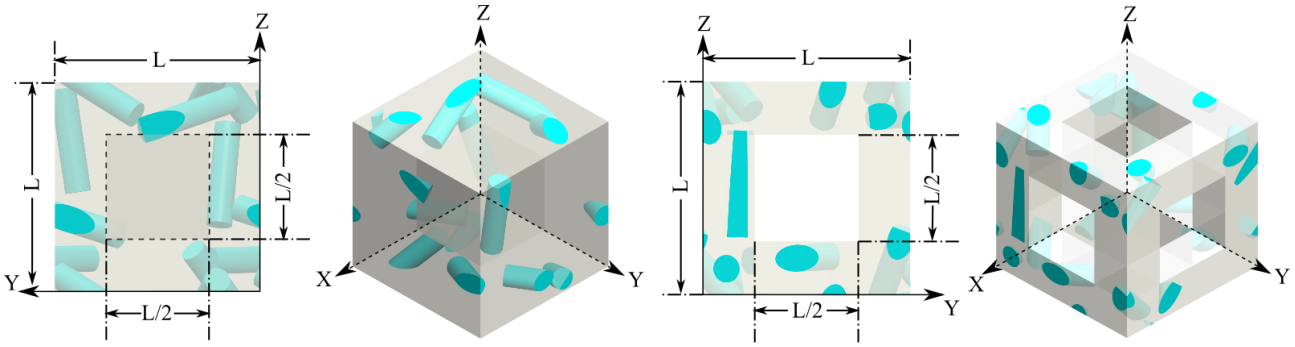

(a) CSC (b) OSC

Figure 3 - 3: RVE of fiber-reinforced composite metamaterials with two different lattice topologies: (a) closed simple cube (CSC) cell and (b) open simple cube (OSC) cell.

3.3 Standard mechanics homogenization technique for obtaining effective thermomechanical properties of cellular composite materials

Since detailed numerical simulation of structures comprising many cells made of composites is a complicated and expensive task, an efficient and accurate approach is desired to simplify this design process. One of the most effective solutions is to obtain effective properties of cellular composites by analyzing their representative volume elements (RVE) through homogenization techniques [70, 71], such as Asymptotic Homogenization (AH) [70] and Standard Mechanics Homogenization (SMH) [72]. The SMH method with periodic boundary conditions is used here to evaluate the effective thermomechanical properties of the architected cellular material.

3.3.1 Constitutive and governing equations for thermomechanical effective properties

The RVE of a periodic cellular material is assumed to be repeated in all three directions.

Under this assumption, to determine the properties of an equivalent homogeneous medium that accurately represents the response of the microscopically heterogeneous material at the macroscopic level (i.e., the RVE, in this thesis), six independent unit strain loadings together with the periodic boundary conditions are applied on the cell boundaries [70]. The equivalent macro scale stress and strain, $\bar{\sigma}$ and $\bar{\varepsilon}$, are then defined as the volumetric mean values of the respective fields in the RVE [73]:

$$\bar{\sigma}_{ij} = \frac{1}{V} \int_V \sigma_{ij}(m)\, dV, \bar{\varepsilon}_{ij} = \frac{1}{V} \int_V \varepsilon_{ij}(m)\, dV,\ i,j = 1,2,3, \quad m \in V \tag{3.1}$$

where σ and ε are micro-scale stress and strain and V is the RVE volume. The following linear constitutive equation can then define the effective elastic constants of the equivalent homogeneous material:

$$\bar{\sigma}_{ij} = \bar{C}_{ijkl}\bar{\varepsilon}_{kl} \tag{3.2}$$

The components of the stiffness tensor of the equivalent homogeneous material ($\bar{C}_{ijkl}$) can be entirely determined by solving the state equilibrium solution for six independent loading cases that, in this thesis's case, correspond to three pure axial and three pure shear deformations of the RVE [74]. The effective linear elastic properties are deduced from the coefficients obtained from the compliance tensors, the inverse of stiffness tensors. To check if the overall material behavior is isotropic, a non-dimensional parameter A (isotropic ratio) is employed, for which, when it approaches 1.00 ± 0.01, the material is said to be isotropic. The isotropic ratio A is defined on the basis of the stiffness entries relation for typical mechanically isotropic material and is expressed as [59]:

$$A = \frac{2(\bar{C}_{44}+\bar{C}_{55}+\bar{C}_{66})}{(\bar{C}_{44}+\bar{C}_{55}+\bar{C}_{66})-(\bar{C}_{12}+\bar{C}_{23}+\bar{C}_{31})} \tag{3.3}$$

where C_{ij} are the components of the effective stiffness tensor.

Once the coefficients of the effective stiffness tensor are determined, the corresponding effective thermal expansion matrix coefficients ($\bar{\alpha}_{ij}$) are calculated by employing the homogenized constitutive equations as [75, 76]:

$$\bar{\sigma}_{ij} = \bar{C}_{ijkl}(\bar{\varepsilon}_{kl} - \bar{\alpha}_{kl}\Delta T) \tag{3.4}$$

where ΔT is the temperature change. Average stresses in the periodic unit cell under zero macroscopic strain ($\bar{\varepsilon}$) and a unit temperature change (ΔT) value are then numerically obtained and subsequently used for calculating the homogenized coefficient of thermal expansion matrix using:

$$\bar{\alpha}_{ij} = -\bar{C}^{-1}_{ijkl}\,\bar{\sigma}_{kl} \tag{3.5}$$

3.3.2 Constitutive and governing equations for effective thermal conductivity

Via a thermal conductivity tensor ($\bar{k}$), Fourier's law indicates the following linear relation between the heat flux ($\vec{q}$) and the temperature gradient ($\vec{\nabla}T$):

$$\vec{q} = -\bar{k}\,\vec{\nabla}T \tag{3.6}$$

The thermal conductivity tensor for 3D materials can be written as a symmetric 3×3 matrix *k*, where $k_{ij} = k_{ji}$. While the $\bar{k}$ tensor simplifies to (*kI*) for thermally isotropic homogenous solid materials, where (*I*) is the identity tensor and *k* is the isotropic thermal conductivity, the overall thermal conductivity of cellular materials is typically anisotropic and relies on the cell's micro-architectural parameters [77].

The effective thermal conductivity of the cellular materials can be determined by applying independent periodic unit thermal gradients [77] and measuring the volumetric average of the resulting heat fluxes based on the standard mechanics homogenization as [78]:

$$\overline{k}_{ij} = \frac{1}{V_{RVE}} \int k_{ik} M^{T}_{kj} dV_{RVE} \; (i,j,k = 1,2,3) \tag{3.7}$$

where $\overline{k}_{ij}$ and k_{ik}, are the effective and local thermal conductivity tensors and the M_{kj}^{T} tensor represents the average and local temperature gradient relation ($\nabla \mathrm{T} = M^{T}\,\overline{\nabla \mathrm{T}}$).

3.4 Methodology for thermomechanical analyses

Using a Python finite-element script in Abaqus CAE, a homogenization scheme is implemented to calculate the effective material properties. For each case, due to the fibers' randomness, at least five RVEs with specific random parameters are generated based on the presented RSA algorithm. The homogenization method is first verified by comparing the obtained effective properties of periodic composite cubic RVEs containing random fibers with those found in the literature, the summary of which is provided in **Table 3-S1** (Supplementary Information), demonstrating good agreement between this thesis's numerical results with those reported in Ref. [59]. Accordingly, following Ref. [12, 59], 3501-6 epoxy matrix and AS4 carbon fibers are chosen, fiber positions in all RVE are assumed to be random, and their length-to-diameter ratio is four.

3.4.1 Fiber-reinforced composites (FRC)

This section investigates the effects of fiber length, fiber volume fraction and fiber orientation on the overall effective thermomechanical properties of fiber-reinforced composites. The thermomechanical properties of the constituent carbon fibers and epoxy matrix are given in **Table 3-1**.

Table 3 - 1: Material properties of 3501-6 epoxy matrix and AS4 carbon fibers [79].

	E_L (GPa)	E_T (GPa)	G_{LT} (GPa)	G_T (GPa)	ν_{LT}	k_L ($\mathrm{W.m^{-1}.K^{-1}}$)	k_T ($\mathrm{W.m^{-1}.K^{-1}}$)	α_L ($10^{-6} \times \mathrm{K^{-1}}$)	α_T ($10^{-6} \times \mathrm{K^{-1}}$)
Fiber	225	15	15	7	0.2	10	1.55	15	-0.5
Matrix	4.2		1.567		0.35	0.256		45	

* *L* and *T* indices show the longitudinal and transverse properties of fibers, respectively.

3.4.1.1 Effect of fiber length

This section discusses the dependency of the effective thermomechanical properties on the relative fiber length (L_R, fiber length to RVE side length). The fiber volume fraction is kept constant as (15 ± 0.5) % for all cases, and the assumption is made that fiber orientations and their positions are distributed uniformly randomly throughout the matrix. The variations of effective linear elastic mechanical properties (**Figure 3-3a**) and thermal properties (**Figure 3-3b**) with respect to the RVE side-to-fiber length ratio ($R = \frac{1}{L_R}$) are shown. The values obtained for the isotropic ratio parameter (A) show that isotropic mechanical behavior is more evident in the fiber-reinforced composites with their R greater than two (**Figure 3-3a**). In addition, as the error bars in **Figure 3-3b** show, the variations in the effective thermal conductivity and thermal expansion coefficients decrease as the fibers get shorter with respect to the RVE (i.e., R value increases from 1 to 4). Increasing R leads to more fibers inside the RVE (for example, for R = 1, 2, 3 and 4, there are 3, 24, 82 and 195 fibers, respectively), which enhances randomness, isotropy and reduces the possibility of effective property variation. The homogenized thermomechanical properties are given in **Table 3-S2** (Supplementary Information).

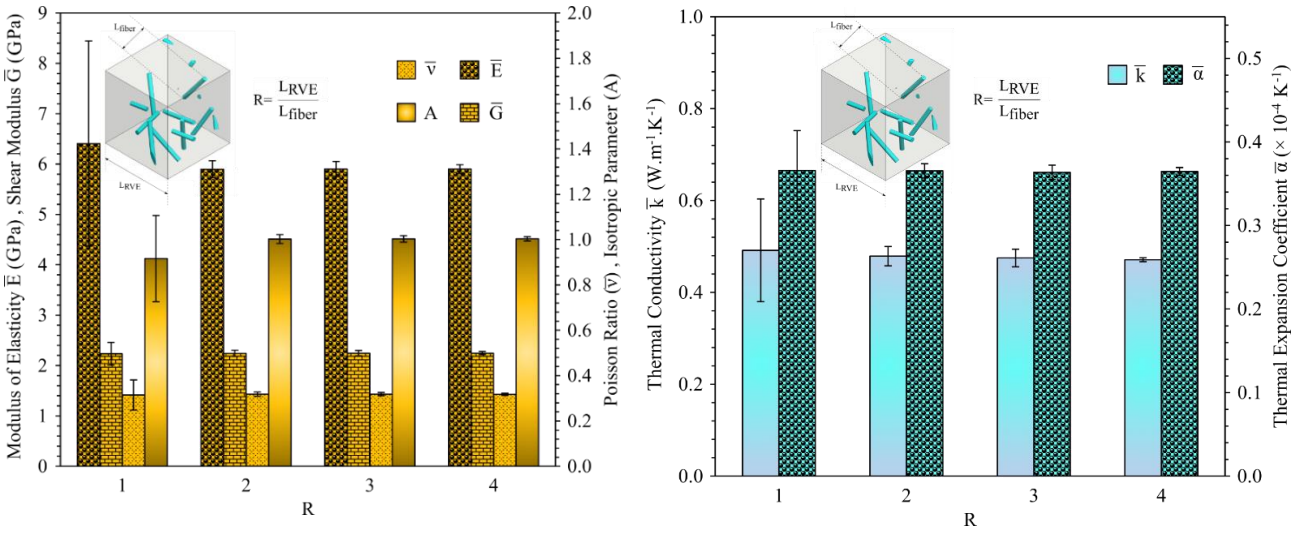

Figure 3 - 4: Comparison of the effective thermomechanical properties of random FRC for different fiber relative lengths for 15% fiber volume fraction.

3.4.1.2 Effect of fiber volume fraction

To show the effect of fiber (inclusion) volume fraction (the percentage of fiber volume in the solid material volume), effective thermomechanical properties of RVEs with various fiber volume fractions are obtained in this section. The position and the orientation of fibers are assumed random and $R = 4$ (Section 3.4.1.1). As shown in **Figure 3-4a**, by increasing the fiber volume fraction, effective modulus of elasticity ($\bar{E}$), shear modulus ($\bar{G}$) and thermal conductivity ($\bar{k}$) of the carbon fiber-reinforced epoxy composite increase since the fibers are stiffer and more conductive than the matrix (**Table 3-1**). However, the thermal expansion coefficient ($\bar{\alpha}$) and Poisson's ratio ($\bar{v}$) show a decreasing trend consistent with the lower value of these properties in the fibers compared to the matrix. (**Figure 3-4a** and **4b**). The isotropic ratio parameter *A* remains unchanged and close to one, which confirms the isotropic mechanical properties of random FRC (**Figure 3-4a**). The results demonstrate that fiber volume fraction is one of the dominant parameters that influence the effective properties of random FRCs. The numerically obtained effective thermomechanical properties are given in **Table 3-S3** (Supplementary Information).

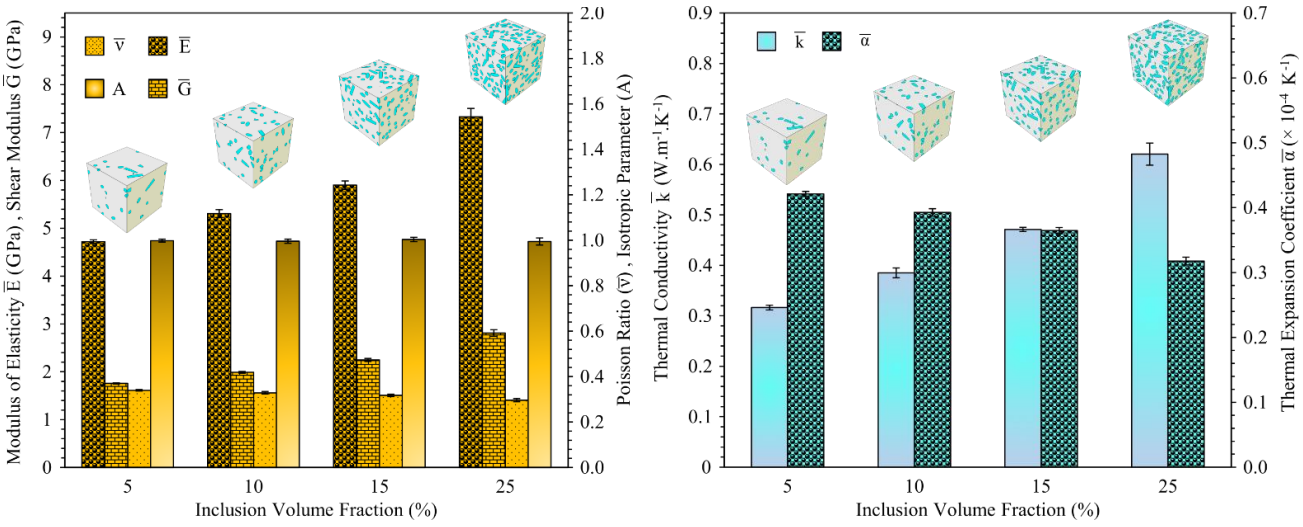

(a) (b)

Figure 3 - 5: Comparison of effective thermomechanical properties for different fiber volume fractions.

3.4.1.3 Effect of fibers' orientation

In this section, the position of the fibers is assumed random, and the effect of fiber orientations on the overall effective properties are investigated while keeping the fiber volume fraction and R constant (i.e., 15% and 4, respectively). **Figure 3-5** illustrates how effective thermomechanical properties change by increasing the fiber angles with respect to direction 3 (θ) (Directions 1, 2 and 3 can represent x, y and z directions), while the fiber angles with the other two directions are assumed to be random. It can be seen that by increasing θ, E_{33} and k_{33} decrease, whereas E_{11}, E_{22}, k_{11} and k_{22} increase (**Figure 3-5**). This observable trend is justified by the greater modulus of elasticity and thermal conductivity of the fibers along their axial direction when compared to their radial direction.

By increasing θ, the stiffer longitudinal direction of the fibers orients away from direction 3, which increases the effective thermal expansion coefficient of the composite along this direction. As fibers get closer to perpendicular to direction 3, more fibers will effectively act along directions 1 and 2, leading to a decreasing trend in the thermal expansion coefficient along these two

directions (**Figure 3-5**). The shear modulus in the 1-2 plane (G_{12}) is increasing due to the assumption that as θ is increased, there are more fibers on the 1-2 plane, resulting in a higher G_{12}. If the fibers are in the 2-3 plane and have a 45-degree angle with either direction 2 or 3, G_{23} has the highest value, since shear in 2-3 direction is equivalent to compression and tension along the 45 degree angles directions. As a result, G_{23} has a higher value at θ = 30 degrees than at θ = 0 and 90 degrees. As the angle θ increases, the Poisson's ratio ν_{13} also rises until it approaches to that of the matrix material (**Figure 3-5a**), which can be justified by the reorientation of the inclined fibers towards the loading axis when the composite is stretched or compressed along direction 3, the so-called "scissoring effect". This reorientation process gets weaker as the fibers get closer to laying on the 1-2 plane, leading to the lower sensitivity of this ratio with the change in angles above 60º. The Poisson's ratio ν_{12} (**Figure 3-5a**) has higher value at θ = 0 since at this angle, the fibers are aligned with direction 3 and have the least effect on ν_{12}. By increasing θ, the stiff fibers have more effect and cause less deformation in directions 1 and 2. The numerical values of the thermo-mechanical properties of FRC for different fibers' orientations are provided in **Table 3-S4** (Supplementary Information).

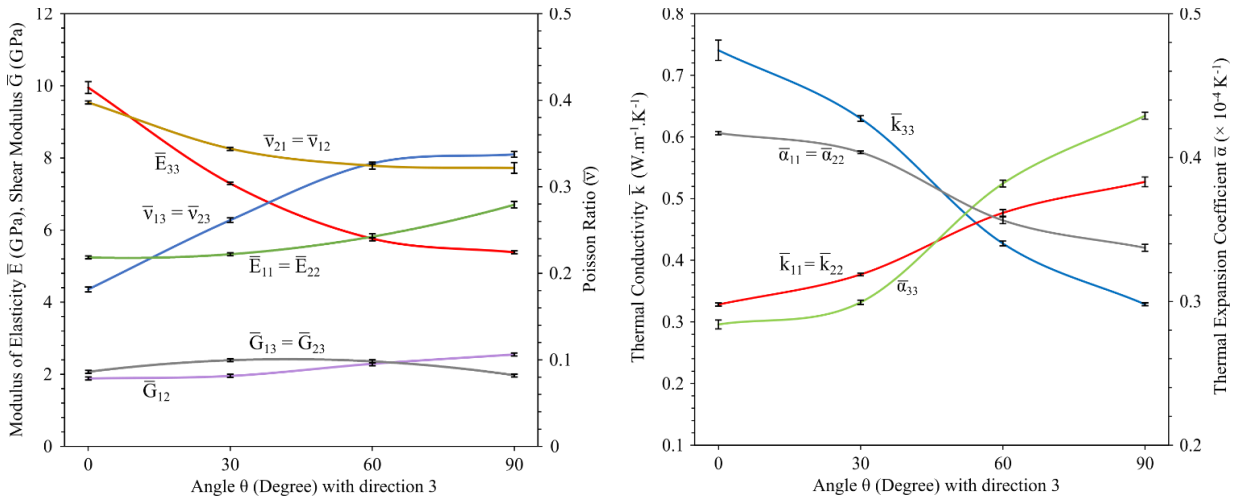

(a) (b)

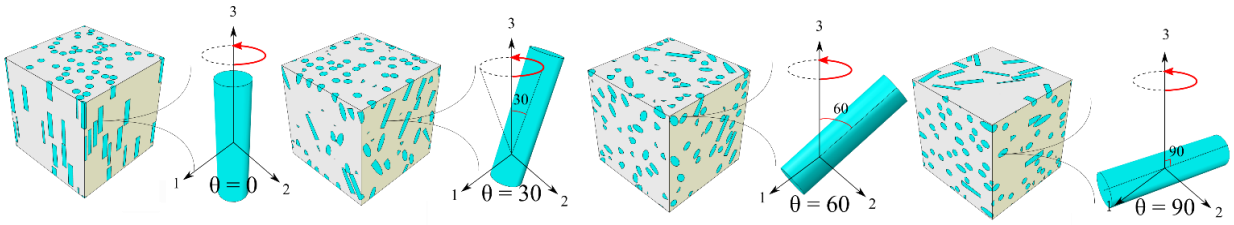

(c)

Figure 3 - 6: Comparison of effective thermomechanical properties for different fiber angles with respect to the direction 3.

3.4.2 Cellular fiber-reinforced composites

In this section, a comprehensive investigation is conducted via two different methods (namely *detailed multiscale analysis* and *multi-level* methods) to evaluate the effective properties of cellular composite metamaterials for the two cell types (open- and closed-cell, presented in **Figure 3-2**). Comparing the results, the conditions under which each method can be used and their advantages and disadvantages are evaluated.

3.4.2.1 Detailed multiscale analysis method

In this method, it is considered that the RVE consists of three different phases: matrix, fibers and voids (**Figure 3-6a**). Under this assumption, effective thermomechanical properties of cellular fiber-reinforced composites (CFRC) are obtained by standard mechanics homogenization. In this case, the fibers are not allowed to be cut by the void boundary to be compatible with real structures.

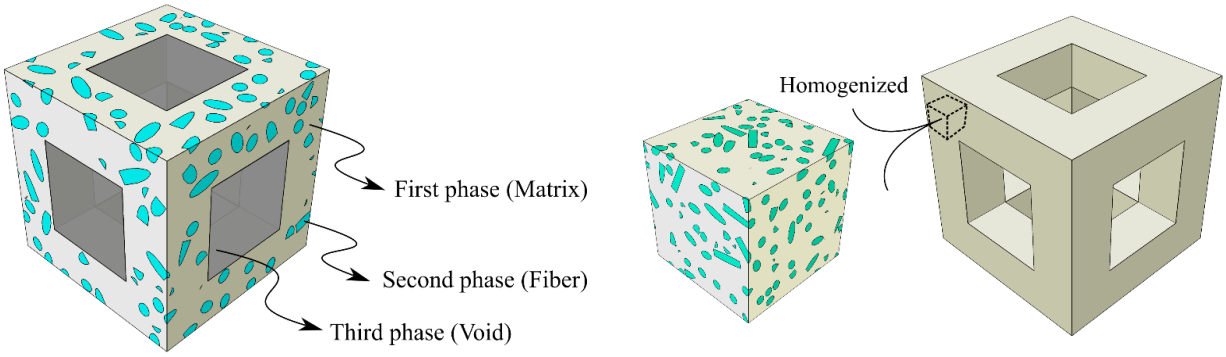

(a) (b)

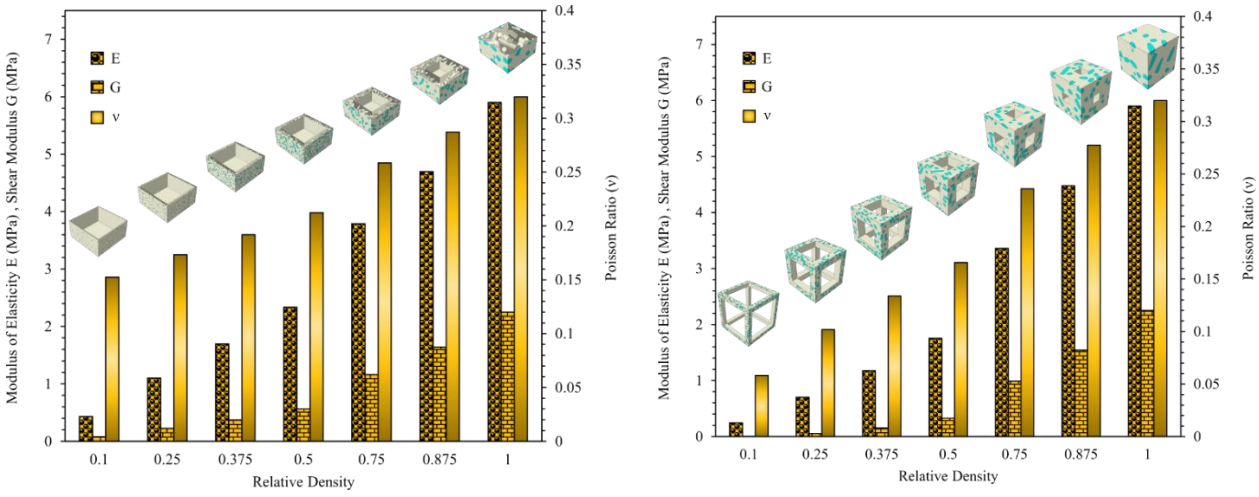

(c) (d)

Figure 3 - 7: RVE based on (a) detailed multiscale analysis method; (b) multi-level method and (c, d) Effective mechanical properties of CFRC obtained from the multi-level methods for metamaterials with (c) closed simple cube (CSC) cell type and (d) open simple cube (OSC) cell type.

3.4.2.2 Multi-level method

In this method, the effective properties of CFRC are evaluated in two steps, as illustrated in **Figure 3-6b**. First, the effective properties of FRC material with no voids are calculated. Then, the CFRCs are modeled as one homogeneous cellular solid with the effective material properties that are obtained in the first step. As shown in **Figure 3-3a** and **Table 3-S2** (Supplementary Information), for $R \geq 2$, the effective properties of FRC are approximately the same with less than 1% difference and therefore, the multi-level method gives the same results for the effective properties of CFRCs.

Table 3 - 2: Comparison of the effective thermomechanical properties of CFRC obtained from the multi-level and detailed multiscale analysis methods.

Cell Type	Property	Multi-level ($R \geq 2$)	Detailed multiscale analysis	|Difference %|	Detailed multiscale analysis	|Difference %|	Detailed multiscale analysis	|Difference %|	Detailed multiscale analysis	|Difference %|
			R_C = 0.5		R_C = 1		R_C = 1.5		R_C = 2	
CSC	$\overline{E}$ (GPa)	4.71	5.27 ± 1.65	10	4.76 ± 0.03	1	4.69 ± 0.16	< 1	4.72 ± 0.08	< 1
	$\overline{\nu}$	0.28	0.26 ± 0.06	8	0.28 ± 0.00	2	0.28 ± 0.01	1	0.28 ± 0.00	< 1
	$\overline{G}$ (GPa)	1.65	1.44 ± 0.13	13	1.62 ± 0.01	2	1.64 ± 0.05	< 1	1.64 ± 0.02	< 1
	$\overline{k}$ ($\frac{W}{m.K}$)	0.38	0.36 ± 0.09	9	0.37 ± 0.01	5	0.38 ± 0.02	3	0.38 ± 0.00	< 2
	$\overline{\alpha}$ ($\times\frac{10^{-5}}{k}$)	3.65	3.78 ± 0.58	4	3.58 ± 0.04	3	3.61 ± 0.13	1	3.62 ± 0.10	< 1
OSC	$\overline{E}$ (GPa)	1.77	1.95 ± 0.31	9	1.91 ± 0.11	7	1.82 ± 0.10	2	1.77 ± 0.05	< 1
	$\overline{\nu}$	0.17	0.14 ± 0.03	13	0.15 ± 0.00	6	0.16 ± 0.01	5	0.16 ± 0.00	1
	$\overline{G}$ (GPa)	0.34	0.27 ± 0.04	26	0.31 ± 0.01	7	0.31 ± 0.01	6	0.33 ± 0.00	< 4
	$\overline{k}$ ($\frac{W}{m.K}$)	0.15	0.13 ± 0.03	12	0.14 ± 0.01	6	0.15 ± 0.01	3	0.15 ± 0.00	< 1
	$\overline{\alpha}$ ($\times\frac{10^{-5}}{k}$)	3.29	3.66 ± 0.51	11	3.43 ± 0.13	6	3.55 ± 0.17	3	3.60 ± 0.07	< 2

* R_C: Minimum cell-wall-thickness to the fiber-length ratio; Fiber volume fraction is 15% for all cases; Difference percentage is calculated by $\frac{|\text{Detailed multiscale value} - \text{multi-level value}|}{\text{Detailed multiscale value}} \times 100\%$

3.4.2.3 Strategy to choose between the detailed multiscale analysis and multi-level method

RVEs with CSC and OSC cell topologies (**Figure 3-2**) are considered to compare the results of the detailed multiscale analysis and multi-level methods. **Table 3-2** provides the effective thermomechanical properties evaluated via these two approaches for different fiber lengths with the same material properties, as given in **Table 3-1**. The effective properties obtained from the detailed multiscale analysis and multi-level methods are almost identical as long as the ratio of the

cellular material's minimum wall-thickness to the fiber-length (R_C) is more than two, with a maximum difference of 4% (**Table 3-2**), suggesting that for CFRC materials with the minimum wall thickness at least twice the length of the fibers, their effective thermomechanical properties can be accurately obtained through the multi-level method. Although the detailed multiscale analysis approach is a more precise representation of the actual cellular composite models; dealing with the extra complexity is costly and requires more computational power and time. Therefore, under correct conditions (i.e., the appropriate R_C range), the multi-level method, which is accurate and significantly faster, can be alternatively adopted to reduce the cost and time associated with the detailed multiscale analysis approach. The effective mechanical properties of CSC and OSC for different relative densities are shown in **Figure 3-6c**, **d**. Through the multi-level method, the influence of pore topology, fiber orientation, and fiber volume fraction on the effective properties of RVE with complex cell geometries can be investigated.

3.5 Engineered cellular fiber-reinforced composite

To design efficient, multifunctional programmable cellular materials, cell members might need different rigidities. While a member's rigidity can be engineered by changing its base material, modifying the stiffness by controlling fiber characteristics (e.g., fiber volume fraction and orientation) has the merit of better adhesion between cell parts/layers that are practically made out of the same material (i.e., same matrix with different fiber characteristics), which in turns helps with better overall mechanical properties and manufacturability. Additionally, this approach puts forward the strategy to increase the effective stiffness without increasing the relative density. Following these advantages, in this section, 2D and 3D cellular architectures are designed to show isotropic mechanical properties, in which the required different stiffnesses of the struts are achieved by tuning their fiber content.

Considering that cellular architectures generally have complex geometries that are not manufacturable using conventional methods, fused deposition modeling (FDM) 3D printing using fiber-reinforced materials based on the same matrix medium offers a feasible approach for fabricating these complex architectures. Considering the multi-level method introduced in Section 3.4.2.2, in this section, it is assumed that each cell member is made out of a homogenous material with a module of elasticity similar to the effective module of elasticity of fiber-reinforced composites discussed in Section 3.4. An analytical methodology is adopted to develop novel mechanically isotropic cellular architectures [12] by engineering cell topology and members' constituent materials (**Figure 3-7a** and **Figure 3-8**). In the idealized cell model, with high slenderness ratios for the struts of these stretching-dominated architectures at low relative densities, struts are simplified as independent two-force members with negligible overlaps. The isotropic conditions are derived by comparing the strain energy densities of the idealized *Isomixed* cells with an isotropic material and then solving for Young's moduli and the thicknesses of the members.

3.5.1 2D rectangular *Isomixed* cell

Section 3.4.1 showed that different moduli of elasticity could be achieved by changing fiber contents and orientations. In this section, a cell, named 2D rectangular *Isomixed* cell, with three different moduli of elasticity and thickness for the horizontal, vertical and diagonal members is considered (**Figure 3-7a**). This cellular architecture is mechanically isotropic in the low-relative-density limit when:

$$E_h t_h = \frac{3n-n^3}{(n^2+1)^{\frac{3}{2}}} E_d t_d \; and \; E_v t_v = \frac{3n^2-1}{(n^2+1)^{\frac{3}{2}}} E_d t_d \; ; \; for \; 1/\sqrt{3} < n < \sqrt{3} \tag{3.8}$$

where t_v, t_h and t_d are the thicknesses and E_v , E_h and E_d are Young's modulus of the underlying

isotropic solid material of vertical, horizontal and diagonal members, respectively, and n is the horizontal-to-vertical member length ratio. It is worth noting that the slender struts do not have to be made out of isotropic materials since the mechanical behavior of these two-force members is mainly governed by the effective Young's moduli of their constituent solids along their length; therefore, in the analysis here, hypothetical isotropic mechanical behaviors can be assumed instead of anisotropic properties, without losing generality and accuracy. **Figure 3-7b** shows the required relations between Young's modulus and thickness of members for a 2D rectangular *Isomixed* cell. For $1/\sqrt{3} < n < \sqrt{3}$, the analytical closed-form formulas for the effective mechanical properties are:

$$\bar{E} = \rho \frac{\frac{8}{3}E_d n^2}{\left(1-\frac{E_d}{E_h}\right)n^4+\left(3\frac{E_d}{E_v}+3\frac{E_d}{E_h}+2\right)n^2+1-\frac{E_d}{E_v}} \text{ , and } \quad \rho = 2\frac{nt_h + t_\mathrm{v} + t_\mathrm{d}\sqrt{n^2+1}}{nL}$$
$$\bar{G} = \rho \frac{E_d n^2}{\left(1-\frac{E_d}{E_h}\right)n^4+\left(3\frac{E_d}{E_v}+3\frac{E_d}{E_h}+2\right)n^2+1-\frac{E_d}{E_v}} \text{ , and } \quad \bar{\nu} = \frac{1}{3} \tag{3.9}$$

where L and ρ are the width and relative density of unit cell. It can be seen that in the case of $n = 1$ (square cell, **Figure 3-7c**), $E_h t_h$ is equal to $E_v t_v$ and equation 3.8 reduces to $E_h t_h = E_v t_v = (\frac{1}{\sqrt{2}})E_d t_d$, aligned with this thesis's previous finding [12].

The steps to derive equation 3.8 for a specific case where all members have the same thickness are presented in **Table 3-3**. The 2D cellular architecture is assumed to be thin and without any out-of-plane restrictions; therefore, plane stress condition is adopted to calculate the strain energy density (U) over the entire *Isomixed* cell under various loading conditions.

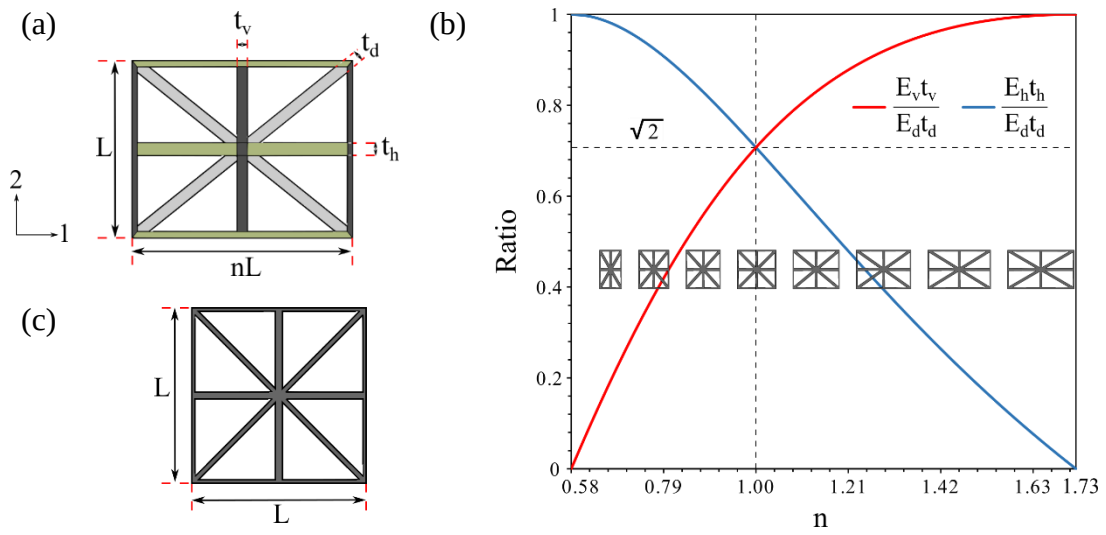

Figure 3 - 8: (a) 2D rectangular *Isomixed* composite cell with n=1.25: different colors represent different materials. (b) Ratios to achieve isotropic elastic modulus. (c) 2D square *Isomixed* cell (n = 1) made of a single material with $\frac{t_v}{t_d} = \frac{t_h}{t_d} = \sqrt{2}$.

Table 3 - 3: Calculating the strain energy density (U) over the entire cell for different loading cases under plane stress conditions.

Loading on the cell	Cell	Magnitude of Link's strain (ε)	Strain energy density in the links ($\frac{1}{2}E\varepsilon^2$) shown in red	Relative density of the links (ρ)	Strain energy density over the entire cell ($\frac{1}{2}E\varepsilon^2\rho$)
$\begin{bmatrix}\varepsilon_x\\ \varepsilon_y\\ \gamma_{xy}\end{bmatrix} = \begin{bmatrix}\varepsilon_1\\ 0\\ 0\end{bmatrix}$ $\leftarrow\square\rightarrow$		ε_1	$\frac{1}{2}E_h{\varepsilon_1}^2$	$\rho_h = n\rho_v$	$U^{(1)} = \frac{n}{2}E_h{\varepsilon_1}^2\rho_v$
		0	0	ρ_v	$U^{(2)} = 0$
		$\frac{\varepsilon_1 n^2}{n^2+1}$	$\frac{n^4}{2(n^2+1)^2}E_d{\varepsilon_1}^2$	$\rho_d = \sqrt{1+n^2}\rho_v$	$U^{(3)} = \frac{n^4}{2(n^2+1)^{\frac{3}{2}}}E_d{\varepsilon_1}^2\rho_v$
	Total strain energy density (=$\sum U^{(i)}$)				$U_{tot1} = \frac{n}{2}\rho_v{\varepsilon_1}^2[E_h + \frac{n^3}{(n^2+1)^{\frac{3}{2}}}E_d]$

$\begin{bmatrix}\varepsilon_x\\ \varepsilon_y\\ \gamma_{xy}\end{bmatrix} = \begin{bmatrix}0\\ \varepsilon_2\\ 0\end{bmatrix}$		0	0	$\rho_h = n\rho_v$	$U^{(1)} = 0$
		ε_2	$\frac{1}{2}E_v{\varepsilon_2}^2$	ρ_v	$U^{(3)} = \frac{1}{2}E_v{\varepsilon_2}^2\rho_v$
		$\frac{\varepsilon_2}{n^2+1}$	$\frac{1}{2(n^2+1)^2}E_d{\varepsilon_2}^2$	$\rho_d = \sqrt{1+n^2}\rho_v$	$U^{(3)} = \frac{1}{2(n^2+1)^{\frac{3}{2}}}E_d{\varepsilon_2}^2\rho_v$
	Total strain energy density $(=\sum U^{(i)})$				$U_{tot2} = \frac{1}{2}\rho_v{\varepsilon_2}^2[E_v + \frac{1}{(n^2+1)^{\frac{3}{2}}}E_d]$
$\begin{bmatrix}\varepsilon_x\\ \varepsilon_y\\ \gamma_{xy}\end{bmatrix} = \begin{bmatrix}\varepsilon_3\\ \varepsilon_3\\ 0\end{bmatrix}$		ε_3	$\frac{1}{2}E_h{\varepsilon_3}^2$	$\rho_h = n\rho_v$	$U^{(1)} = \frac{n}{2}E_h{\varepsilon_3}^2\rho_v$
		ε_3	$\frac{1}{2}E_v{\varepsilon_3}^2$	ρ_v	$U^{(3)} = \frac{1}{2}E_v{\varepsilon_3}^2\rho_v$
		ε_3	$\frac{1}{2}E_d{\varepsilon_3}^2$	$\rho_d = \sqrt{1+n^2}\rho_v$	$U^{(3)} = \frac{\sqrt{1+n^2}}{2}E_d{\varepsilon_3}^2\rho_v$
	Total strain energy density (=$\sum U^{(i)}$)				$U_{tot3} = \frac{1}{2}\rho_v{\varepsilon_3}^2[nE_h + E_v + \sqrt{1+n^2}E_d]$
$\begin{bmatrix}\varepsilon_x\\ \varepsilon_y\\ \gamma_{xy}\end{bmatrix} = \begin{bmatrix}0\\ 0\\ \gamma\end{bmatrix}$		0	0	$\rho_h = n\rho_v$	$U^{(1)} = 0$
		0	0	ρ_v	$U^{(2)} = 0$
		$\frac{\gamma n}{1+n^2}$	$\frac{n^2}{2(1+n^2)^2}E_d\gamma^2$	$\rho_d = \sqrt{1+n^2}\rho_v$	$U^{(3)} = \frac{n^2}{2(1+n^2)^{\frac{3}{2}}}E_d\gamma^2\rho_v$
	Total strain energy density (=$\sum U^{(i)}$)				$U_{tot4} = \frac{n^2}{2(1+n^2)^{\frac{3}{2}}}\gamma^2\rho_v(E_d)$

*E_h, E_v and E_d: Young's modulus of the underlying isotropic solid material of the horizontal, vertical and diagonal members; ρ_h, ρ_v and ρ_d: Relative density of the horizontal, vertical and diagonal members, respectively; n: Horizontal-to-vertical member length ratio.

Assuming the same thickness for all members, the relationships between the relative densities

are approximated as follows:

$$\rho_d = \sqrt{1+n^2}\rho_v \text{ and } \rho_h = n\rho_v \tag{3.10}$$

where ρ_h, ρ_v and ρ_d are the relative densities of the horizontal, vertical and diagonal members, respectively. The strain energy densities are then compared to those of an isotropic material (with ρ, E, ν and $G = E/(2(1+\nu))$ as unknown material properties) under the same loading conditions as follows:

$$U_{tot1} = \frac{n}{2}\rho_v {\varepsilon_1}^2 \left[E_h + \frac{n^3}{(n^2+1)^{\frac{3}{2}}}E_d\right] = \frac{1}{2(1-\nu^2)}E{\varepsilon_1}^2 \tag{3.11a}$$

$$U_{tot2} = \frac{1}{2}\rho_v {\varepsilon_2}^2 \left[E_v + \frac{1}{(n^2+1)^{\frac{3}{2}}}E_d\right] = \frac{1}{2(1-\nu^2)}E{\varepsilon_2}^2 \tag{3.11b}$$

$$U_{tot3} = \frac{1}{2}\rho_v {\varepsilon_3}^2 \left[nE_h + E_v + \sqrt{1+n^2}E_d\right] = \frac{1}{1-\nu}E{\varepsilon_3}^2 \tag{3.11c}$$

$$U_{tot4} = \frac{n^2}{2(1+n^2)^{\frac{3}{2}}}\gamma^2\rho_v[E_d] = \frac{1}{2}G\gamma^2 \xrightarrow{G=E/(2(1+\nu))} \frac{2n^2}{(1+n^2)^{\frac{3}{2}}}\rho_v[E_d] = \frac{1}{1+\nu}E \tag{3.11d}$$

Solving these equations results in the following relations between the Young's moduli of the horizontal/vertical members with the diagonal struts in a rectangular *Isomixed* cell with isotropic effective mechanical properties:

$$E_h = \frac{3n-n^3}{(n^2+1)^{\frac{3}{2}}}E_d \text{ , and } E_v = \frac{3n^2-1}{(n^2+1)^{\frac{3}{2}}}E_d \tag{3.12}$$

The analytical closed-form formulas for the effective thermal properties for $1/\sqrt{3} < n < \sqrt{3}$ are also derived and presented in equation 3.13. The thermal expansion coefficients are derived using equation 3.5 (section 3.8.5, Supplementary Information), while the thermal circuit modelling [80] is used to derive closed-form formulas for the thermal conductivity of 2D rectangular *Isomixed* cell using the similarity between thermal and electric fields. In this method, the thermal gradient corresponds to electric voltage, the heat flow is analogous to electric current, and the thermal resistance (reciprocal of thermal conductivity for a unit cell) is associated with the electric

resistance. wherein equation 3.13 (k_v, α_v), (k_h, α_h) and (k_d, α_d) are the thermal conductivity and thermal expansion coefficient of vertical, horizontal and diagonal members.

$$\bar{k}_{11} = \frac{2}{L}\left(\frac{t_h k_h \sqrt{n^2+1} + n k_d t_d}{\sqrt{n^2+1}}\right), \bar{k}_{22} = \frac{2}{nL}\left(\frac{t_v k_v \sqrt{n^2+1} + k_d t_d}{\sqrt{n^2+1}}\right), \bar{k}_{12} = 0 \tag{3.13a}$$

$$\bar{\alpha}_{11} = \frac{2E_d t_d}{L\bar{E}\sqrt{n^2+1}}\left[\alpha_h \frac{3n-n^3}{(n^2+1)} - \alpha_v \frac{3n^2-1}{3n(n^2+1)} + \alpha_d\left(n - \frac{1}{3n}\right)\right],$$

$$\bar{\alpha}_{22} = \frac{2E_d t_d}{L\bar{E}\sqrt{n^2+1}}\left[\alpha_v \frac{3n^2-1}{n(n^2+1)} - \alpha_h \frac{3n-n^3}{3(n^2+1)} + \alpha_d\left(\frac{1}{n} - \frac{n}{3}\right)\right], \tag{3.13b}$$

$$\bar{\alpha}_{12} = 0$$

This thesis engineered the cell architectures and material compositon to be make the cell show mechanical isotropic properties, while they can be thermally isotropic or anisotropic as shown by equation 3.13. It is also possible to design a cell that is thermally isotropic while it is mechanically anisotropic by modifying the derived equations. The analytical approach allows to program the isotropy/anisotropy of elastic stiffness, thermal conductivity and thermal expansion coefficients in composite cellular metamaterials. In Section 3.6, the above analytical results for 2D rectangular *Isomixed* composite cells are verified with detailed numerical and experimental analysis.

3.5.2 3D cuboid *Isomixed* cell

In another investigation, two types of 3D *Isomixed* cells are designed, and following the same strategy, the conditions that make these cellular architectures mechanically isotropic are found. This thesis assumes a cuboid cell in which the cylindrical cuboid and diagonal members have different diameters and constituent materials that can be achieved by changing fiber specifications in their base composite material, as discussed in Section 3.4.1.

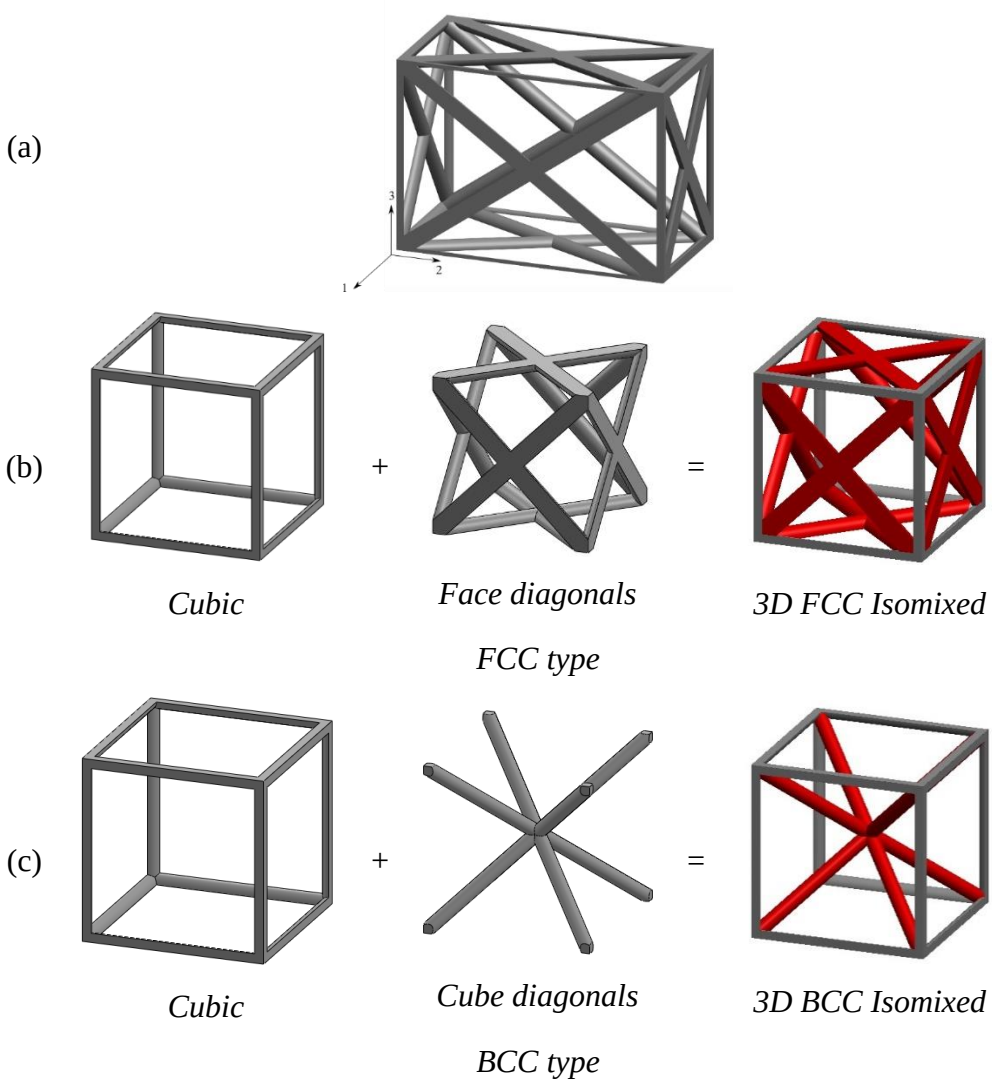

Figure 3 - 9: 3D *Isomixed* cell: (a) 3D cuboid multi-material *Isomixed*; (b) 3D FCC bimaterial *Isomixed*; and (c) 3D BCC bimaterial *Isomixed*.

3.5.2.1 3D FCC Isomixed cell

We find that the low-density 3D *Isomixed FCC type* cells can show isotropic effective mechanical properties if the following conditions are met (**Figure 3-8a**):

$$E_2 t_2^2 = E_1 t_1^2 n_{12} \frac{3-n_{12}^2-\frac{n_{12}^2}{n_{13}^2}}{3n_{12}^2-1-\frac{n_{12}^2}{n_{13}^2}},\ E_3 t_3^2 = E_1 t_1^2 \frac{3n_{12}^2-n_{12}^2 n_{13}^2-n_{13}^2}{n_{13}(3n_{12}^2-1-\frac{n_{12}^2}{n_{13}^2})},\ E_{12} t_{12}^2 = E_1 t_1^2 \frac{(1+n_{12}^2)^{1.5}}{2(3n_{12}^2-1-\frac{n_{12}^2}{n_{13}^2})},$$

$$E_{13} t_{13}^2 = E_1 t_1^2 \frac{n_{12}^2(1+n_{13}^2)^{1.5}}{2n_{13}^2(3n_{12}^2-1-\frac{n_{12}^2}{n_{13}^2})},\ E_{23} t_{23}^2 = E_1 t_1^2 \frac{(n_{12}^2+n_{13}^2)^{1.5}}{2n_{13}^2(3n_{12}^2-1-\frac{n_{12}^2}{n_{13}^2})} \quad (3.14)$$

where $n_{12} = \frac{L_2}{L_1}$, $n_{13} = \frac{L_3}{L_1}$, and the other parameters are defined as follows:

L_1 , E_1 , t_1 : Length, module of elasticity, and diameters of the struts Parallel to direction 1; L_2 , E_2 , t_2 : Length, module of elasticity, and diameters of the struts Parallel to direction 2; L_3 , E_3 , t_3 : Length, module of elasticity, and diameters of the struts Parallel to direction 3; E_{12} , t_{12} : Module of elasticity and Diameters of the diagonal struts located on planes parallel to 1-2 plane; E_{13} , t_{13} : Module of elasticity and Diameters of the diagonal struts located on planes parallel to 1-3 plane; E_{23} , t_{23} : Module of elasticity and Diameters of the diagonal struts located on planes parallel to 2-3 plane; where i-j plane is the plane containing edge i and j. Considering that Young's moduli of the members are greater than zero, the abovementioned equations are valid when $(3n_{12}^2 - 1 - \frac{n_{12}^2}{n_{13}^2}) > 0$, $(3 - n_{12}^2 - \frac{n_{12}^2}{n_{13}^2}) > 0$ and $(3n_{12}^2 - n_{12}^2 n_{13}^2 - n_{13}^2) > 0$ (with the admissible range for both n_{12} and n_{13} between $\frac{1}{\sqrt{2}}$ and $\sqrt{2}$). Under these conditions, the closed-form expressions for the effective thermomechanical properties of cuboid FCC *Isomixed* material with slender cylindrical struts are obtained by:

$$\bar{E} = \frac{5\pi n_{12} E_1 t_1^2}{8 n_{13} L_1^2 \left(3n_{12}^2 - 1 - \frac{n_{12}^2}{n_{13}^2}\right)}, \bar{G} = \frac{\pi n_{12} E_1 t_1^2}{4 n_{13} L_1^2 \left(3n_{12}^2 - 1 - \frac{n_{12}^2}{n_{13}^2}\right)}, \bar{\nu} = \frac{1}{4}, \tag{3.15a}$$

$$\bar{k}_{11} = \frac{\pi}{4L_1^2 n_{12} n_{13}} \left(\frac{2k_{13}t_{13}^2}{\sqrt{1+n_{13}^2}} + \frac{2k_{12}t_{12}^2}{\sqrt{1+n_{12}^2}} + k_1 t_1^2\right), \bar{k}_{22} = \frac{\pi}{4L_1^2 n_{13}} \left(\frac{2k_{23}t_{23}^2}{\sqrt{1+\left(\frac{n_{13}}{n_{12}}\right)^2}} + \frac{2k_{12}t_{12}^2}{\sqrt{1+\left(\frac{1}{n_{12}}\right)^2}} + k_2 t_2^2 \right), \bar{k}_{33} = \frac{\pi}{4L_1^2 n_{12}} \left(\frac{2k_{13}t_{13}^2}{\sqrt{1+\left(\frac{1}{n_{13}}\right)^2}} + \frac{2k_{23}t_{23}^2}{\sqrt{1+\left(\frac{n_{12}}{n_{13}}\right)^2}} + k_3 t_3^2 \right) \tag{3.15b}$$

$$\bar{\alpha}_{11} = \frac{2}{5n_{12}^2} \left(\alpha_1 \left(3n_{12}^2 - 1 - \frac{n_{12}^2}{n_{13}^2}\right) - \alpha_2 \frac{n_{12}^2}{4} \left(3 - n_{12}^2 - \frac{n_{12}^2}{n_{13}^2}\right) - \frac{\alpha_3}{4} (3n_{12}^2 - n_{12}^2 n_{13}^2 - n_{13}^2) + \alpha_{12} \left(1 - \frac{n_{12}^2}{4}\right)(1 + n_{12}^2) + \alpha_{13} \frac{n_{12}^2}{n_{13}^2} \left(1 - \frac{n_{13}^2}{4}\right)(1 + n_{13}^2) - \alpha_{23} \frac{\left(n_{12}^2 + n_{13}^2\right)^2}{4n_{13}^2} \right), \tag{3.15c}$$

$$\bar{\alpha}_{22} = \frac{2}{5n_{12}^2}\left(-\frac{\alpha_1}{4}\left(3n_{12}^2 - 1 - \frac{n_{12}^2}{n_{13}^2}\right) + \alpha_2 n_{12}^2\left(3 - n_{12}^2 - \frac{n_{12}^2}{n_{13}^2}\right) - \frac{\alpha_3}{4}(3n_{12}^2 - n_{12}^2 n_{13}^2 - n_{13}^2) + \alpha_{12}\left(n_{12}^2 - \frac{1}{4}\right)(1 + n_{12}^2) - \alpha_{13}\frac{n_{12}^2}{4n_{13}^2}(1 + n_{13}^2)^2 + \alpha_{23}(n_{12}^2 + n_{13}^2)(\frac{n_{12}^2}{n_{13}^2} - \frac{1}{4})\right),$$

$$\bar{\alpha}_{33} = \frac{2}{5n_{12}^2}\left(-\frac{\alpha_1}{4}\left(3n_{12}^2 - 1 - \frac{n_{12}^2}{n_{13}^2}\right) - \alpha_2\frac{n_{12}^2}{4}\left(3 - n_{12}^2 - \frac{n_{12}^2}{n_{13}^2}\right) + \alpha_3(3n_{12}^2 - n_{12}^2 n_{13}^2 - n_{13}^2) - \frac{\alpha_{12}}{4}(1 + n_{12}^2)^2 + \alpha_{13}\frac{n_{12}^2}{n_{13}^2}\left(n_{13}^2 - \frac{1}{4}\right)(1 + n_{13}^2) + \alpha_{23}(n_{13}^2 - \frac{n_{12}^2}{4})(\frac{n_{12}^2}{n_{13}^2} + 1)\right)$$

where: k_1 , α_1: Thermal conductivity and thermal expansion coefficient of the struts parallel to direction 1; k_2 , α_2: Thermal conductivity and thermal expansion coefficient of the struts parallel to direction 2; k_3 , α_3: Thermal conductivity and thermal expansion coefficient of the struts parallel to direction 3; k_{12} , α_{12}: Thermal conductivity and thermal expansion coefficient of the diagonal struts located on planes parallel to 1-2 plane; k_{13} , α_{13}: Thermal conductivity and thermal expansion coefficient of the diagonal struts located on planes parallel to 1-3 plane; k_{23} , α_{23} : Thermal conductivity and thermal expansion coefficient of the diagonal struts located on planes parallel to 2-3 plane.

It is worth mentioning that the struts should be slender and the shape of their cross-section is not important. For any arbitrary cross-section area (A_i) the value of t_i for each strut to be substituted in equation (3.14, 3.15) can be obtained from $t_i = \sqrt{\frac{4A_i}{\pi}}$.

In the case of cubic cells, the conditions equation 3.14 can be simplified to $E_c t_c^2 = \frac{1}{\sqrt{2}} E_d t_d^2$ (**Figure 3-8b**), where t_d, t_c and E_d, E_c are the diameters and Young's moduli of the underlying isotropic solid material of the diagonal and cubic part members, accordingly. The steps for obtaining this relationship for a particular case of the same diameter for all members are provided in **Table 3-4**.

Table 3 - 4: Calculating the strain energy density (U) over the entire cell for different loading cases for FCC type 3D *Isomixed* cell.

Loading on the cell	Cell	Magnitude of Link's strain (ε)	Strain energy density in the links ($\frac{1}{2}E\varepsilon^2$) shown in red	Relative density of the links (ρ)	Strain energy density over the entire cell ($\frac{1}{2}E\varepsilon^2\rho$)
$\begin{bmatrix}\varepsilon_x\\ \varepsilon_y\\ \varepsilon_z\\ \gamma_{xy}\\ \gamma_{xz}\\ \gamma_{yz}\end{bmatrix}=\begin{bmatrix}\varepsilon_1\\ 0\\ 0\\ 0\\ 0\\ 0\end{bmatrix}$		ε_1	$\frac{1}{2}E_c{\varepsilon_1}^2$	$\frac{4\,\rho_c}{12}$	$U^{(1)}=\frac{1}{6}E_c{\varepsilon_1}^2\rho_c$
	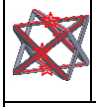	$\frac{\varepsilon_1}{2}$	$\frac{1}{8}E_d{\varepsilon_1}^2$	$\frac{8\,\rho_d}{12}$	$U^{(3)}=\frac{1}{12}E_d{\varepsilon_1}^2\rho_d$
	Total strain energy density (=$\sum U^{(i)}$)				$U_{tot1}=\frac{1}{12}{\varepsilon_1}^2(2E_c\rho_c+E_d\rho_d)$
$\begin{bmatrix}\varepsilon_x\\ \varepsilon_y\\ \varepsilon_z\\ \gamma_{xy}\\ \gamma_{xz}\\ \gamma_{yz}\end{bmatrix}=\begin{bmatrix}\varepsilon_2\\ \varepsilon_2\\ \varepsilon_2\\ 0\\ 0\\ 0\end{bmatrix}$		ε_2	$\frac{1}{2}E_c{\varepsilon_2}^2$	ρ_c	$U^{(1)}=\frac{1}{2}E_c{\varepsilon_2}^2\rho_c$
		ε_2	$\frac{1}{2}E_d{\varepsilon_2}^2$	ρ_d	$U^{(3)}=\frac{1}{2}E_d{\varepsilon_2}^2\rho_d$
	Total strain energy density (=$\sum U^{(i)}$)				$U_{tot2}=\frac{1}{2}{\varepsilon_2}^2(E_c\rho_c+E_d\rho_d)$
$\begin{bmatrix}\varepsilon_x\\ \varepsilon_y\\ \varepsilon_z\\ \gamma_{xy}\\ \gamma_{xz}\\ \gamma_{yz}\end{bmatrix}=\begin{bmatrix}0\\ 0\\ 0\\ \gamma\\ 0\\ 0\end{bmatrix}$ 		0	0	ρ_c	$U^{(1)}=0$
		$\frac{\gamma}{2}$	$\frac{1}{8}E_d\gamma^2$	$\frac{4\,\rho_d}{12}$	$U^{(3)}=\frac{1}{24}E_d\gamma^2\rho_d$
	Total strain energy density (=$\sum U^{(i)}$)				$U_{tot3}=\frac{1}{24}E_d\gamma^2\rho_d$

* E_c and E_d : Young's modulus of the underlying isotropic solid material of the cubic part and the diagonal members, respectively; ρ_c and ρ_d: Relative density of the simple cubic cell and the diagonal members, respectively.

Table 3-4 shows the calculation of strain energy densities for the *FCC type* of 3D *Isomixed* cell with the same diameter for all members. Strain energy densities are then compared to those of an isotropic material (with $\rho, E, \nu,$ and $G = E/(2(1+\nu))$ as unknown material properties) under the same loading conditions as follows:

$$U_{tot1}=\frac{1}{12}{\varepsilon_1}^2(2E_c\rho_c+E_d\rho_d)=\frac{1-\nu}{2(1+\nu)(1-2\nu)}E{\varepsilon_1}^2 \tag{3.16a}$$

$$U_{tot2}=\frac{1}{2}{\varepsilon_2}^2(E_c\rho_c+E_d\rho_d)=\frac{3}{2(1-2\nu)}E{\varepsilon_2}^2 \tag{3.16b}$$

$$U_{tot3}=\frac{1}{24}E_d\gamma^2\rho_d=\frac{1}{2}G\gamma^2\xrightarrow{G=E/(2(1+\nu))}E_d\rho_d=\frac{6}{1+\nu}E \tag{3.16c}$$

at low relative densities, having the same diameter for all members leads to $\frac{\rho_c}{\rho_d} = \frac{1}{2\sqrt{2}}$ (where ρ_c and ρ_d are the relative densities of the simple cubic cell and the diagonal members, respectively). While determining the relation between the two unknown Young's moduli, it is found that with $E_c = \frac{1}{\sqrt{2}} E_d$, the low-density cubic *Isomixed* cells can show isotropic effective mechanical properties. As shown in Section 3.4.1, that ratio between the two moduli can be achieved by playing with fiber volume fraction and fibers' orientation.

3.5.2.2 3D BCC Isomixed cell

Following the same methodology and assumptions used to design the *FCC type* 3D *Isomixed* cell, it is determined that the at small relative densities, the 3D *Isomixed BCC type* cell can only be mechanically isotropic if it is a cubic cell (**Figure 3-8c**) and if $E_i t_i^2 = \frac{8}{3\sqrt{3}} E_d t_d^2$ for $i = 1, 2, 3$. The closed-form expressions for the effective thermomechanical properties of the cubic BCC *Isomixed* material with slender cylindrical struts are derived as:

$$\bar{E} = \frac{5\pi E_1 t_1^2}{16L^2}, \bar{G} = \frac{\pi E_1 t_1^2}{8L^2}, \bar{\nu} = \frac{1}{4}, \tag{3.17a}$$

$$\bar{k}_{ii} = \frac{\pi}{L^2}\left(\frac{k_i t_i^2}{4} + \frac{k_d t_d^2}{\sqrt{3}}\right), \bar{k}_{ij} = 0 \quad i, j = 1,2,3\ , i \neq j \tag{3.17b}$$

$$\bar{\alpha}_{ii} = \alpha_i - \frac{\alpha_1 + \alpha_2 + \alpha_3 - 3\alpha_d}{5}\ , \bar{\alpha}_{ij} = 0 \quad i, j = 1,2,3\ , i \neq j \tag{3.17c}$$

where L is the cell width; E_i , t_i , k_i and α_i are Young's modulus, diameter, thermal conductivity and thermal expansion coefficient of the struts parallel to direction i ($i = 1, 2, 3$), and, E_d , t_d , k_d and α_d represent the corresponding material property of the diagonal struts. For non-cylindrical slender members, equivalent diameter $t = \sqrt{\frac{4A}{\pi}}$ can be used where A is the cross-section area of the corresponding member.

For the case of the same diameters for all members ($t_i = t_d$), the discussed condition for

mechanical isotropy results in $E_i = \frac{8}{3\sqrt{3}} E_d$; hence, the same Young's modulus E_C is used for the cubic struts. **Table 3-5** shows the calculation for the strain energy of the 3D *Isomixed BCC type* cell with the same diameter for all members.

Table 3 - 5: Calculating the strain energy density (U) over the entire cell for different BCC type 3D *Isomixed* cell loading cases.

Loading on the cell	Cell	Magnitude of Link's strain (ε)	Strain energy density in the links ($\frac{1}{2}E\varepsilon^2$) shown in red	Relative density of the red links (ρ)	Strain energy density over the entire cell ($\frac{1}{2}E\varepsilon^2\rho$)
$\begin{bmatrix}\varepsilon_x\\ \varepsilon_y\\ \varepsilon_z\\ \gamma_{xy}\\ \gamma_{xz}\\ \gamma_{yz}\end{bmatrix} = \begin{bmatrix}\varepsilon_1\\ 0\\ 0\\ 0\\ 0\\ 0\end{bmatrix}$		ε_1	$\frac{1}{2}E_c{\varepsilon_1}^2$	$\frac{4\,\rho_c}{12}$	$U^{(1)} = \frac{1}{6}E_c{\varepsilon_1}^2\rho_c$
		$\frac{\varepsilon_1}{3}$	$\frac{1}{18}E_d{\varepsilon_1}^2$	ρ_d	$U^{(3)} = \frac{1}{18}E_d{\varepsilon_1}^2\rho_d$
	Total strain energy density (=$\sum U^{(i)}$)				$U_{tot1} = \frac{1}{18}{\varepsilon_1}^2(3E_c\rho_c + E_d\rho_d)$
$\begin{bmatrix}\varepsilon_x\\ \varepsilon_y\\ \varepsilon_z\\ \gamma_{xy}\\ \gamma_{xz}\\ \gamma_{yz}\end{bmatrix} = \begin{bmatrix}\varepsilon_2\\ \varepsilon_2\\ \varepsilon_2\\ 0\\ 0\\ 0\end{bmatrix}$		ε_2	$\frac{1}{2}E_c{\varepsilon_2}^2$	ρ_c	$U^{(1)} = \frac{1}{2}E_c{\varepsilon_2}^2\rho_c$
		ε_2	$\frac{1}{2}E_d{\varepsilon_2}^2$	ρ_d	$U^{(3)} = \frac{1}{2}E_d{\varepsilon_2}^2\rho_d$
	Total strain energy density (=$\sum U^{(i)}$)				$U_{tot2} = \frac{1}{2}{\varepsilon_2}^2(E_c\rho_c + E_d\rho_d)$
$\begin{bmatrix}\varepsilon_x\\ \varepsilon_y\\ \varepsilon_z\\ \gamma_{xy}\\ \gamma_{xz}\\ \gamma_{yz}\end{bmatrix} = \begin{bmatrix}0\\ 0\\ 0\\ \gamma\\ 0\\ 0\end{bmatrix}$ 		0	0	ρ_c	$U^{(1)} = 0$
		$\frac{\gamma}{3}$	$\frac{1}{18}E_d\gamma^2$	ρ_d	$U^{(3)} = \frac{1}{18}E_d\gamma^2\rho_d$
	Total strain energy density (=$\sum U^{(i)}$)				$U_{tot3} = \frac{1}{18}E_d\gamma^2\rho_d$

* E_c and E_d : Young's modulus of the underlying isotropic solid material of the cubic part and the diagonal members, respectively; ρ_c and ρ_d: Relative density of the simple cubic cell and the diagonal members, respectively.

Strain energy densities are then compared to those of an isotropic material (with ρ, E, ν and $G = E/(2(1+\nu))$ as unknown material properties) under the same loading conditions as follows:

$$U_{tot1} = \frac{1}{18}{\varepsilon_1}^2(3E_c\rho_c + E_d\rho_d) = \frac{1-\nu}{2(1+\nu)(1-2\nu)}E{\varepsilon_1}^2 \tag{3.18a}$$

$$U_{tot2} = \frac{1}{2}{\varepsilon_2}^2(E_c\rho_c + E_d\rho_d) = \frac{3}{2(1-2\nu)}E{\varepsilon_2}^2 \quad (3.18b)$$

$$U_{tot3} = \frac{1}{18}E_d\gamma^2\rho_d = \frac{1}{2}G\gamma^2 \xrightarrow{G=E/(2(1+\nu))} E_d\rho_d = \frac{9}{2(1+\nu)}E \quad (3.18c)$$

The same diameter for all members translates to $\frac{\rho_c}{\rho_d} = \frac{\sqrt{3}}{4}$. It is found that at low relative density, the 3D *Isomixed BCC type* cells with $E_c = \frac{8}{3\sqrt{3}}E_d$ can demonstrate isotropic mechanical properties.

Equations 3.15 and 3.17 demonstrate the possibility of designing low-density thermally anisotropic, yet mechanically isotropic cellular metamaterials with cubic BCC and cuboid FCC architecture for which the effective thermal conductivity and thermal expansion along different directions can be tuned by changing base material and diameter of the struts, while keeping the mechanical properties in different directions unchanged.

3.6 Numerical simulation and experimental tests of the 2D rectangular *Isomixed* composite

3.6.1 Assessing the homogeneity assumption of fiber-reinforced PETG-C

PETG-S (Polyethylene terephthalate glycol) and PETG-C (Carbon fiber-reinforced Polyethylene terephthalate glycol) are the materials chosen for 3D printing, experimental testing, and associated finite element analysis. Scanning electron microscope (SEM) imaging is used to analyze the fiber characteristics of PTEG-C, a short fiber-reinforced composite filament (**Figure 3-9**). As shown, fibers are randomly oriented (**Figure 3-9a**) and they are generally shorter than 85 μm (**Figure 3-9b**), which is significantly smaller than the filament diameter (i.e., 2.85 mm) and the thinnest feature of the 3D printed cellular samples. Moreover, the aspect ratio of the majority of the fibers is closed to 4 (**Figure 3-9c**). These fiber characteristics comply with the discussed conditions in Section 3.4 on fiber orientation, length and aspect ratio, under which the composite

base material of a CFRC can be regarded as a homogeneous isotropic material; therefore, without losing precision, the PETG-C in this thesis is treated as a homogenous mechanically and thermally isotropic base material, while this assumption loses its accuracy at smaller cell and feature sizes.

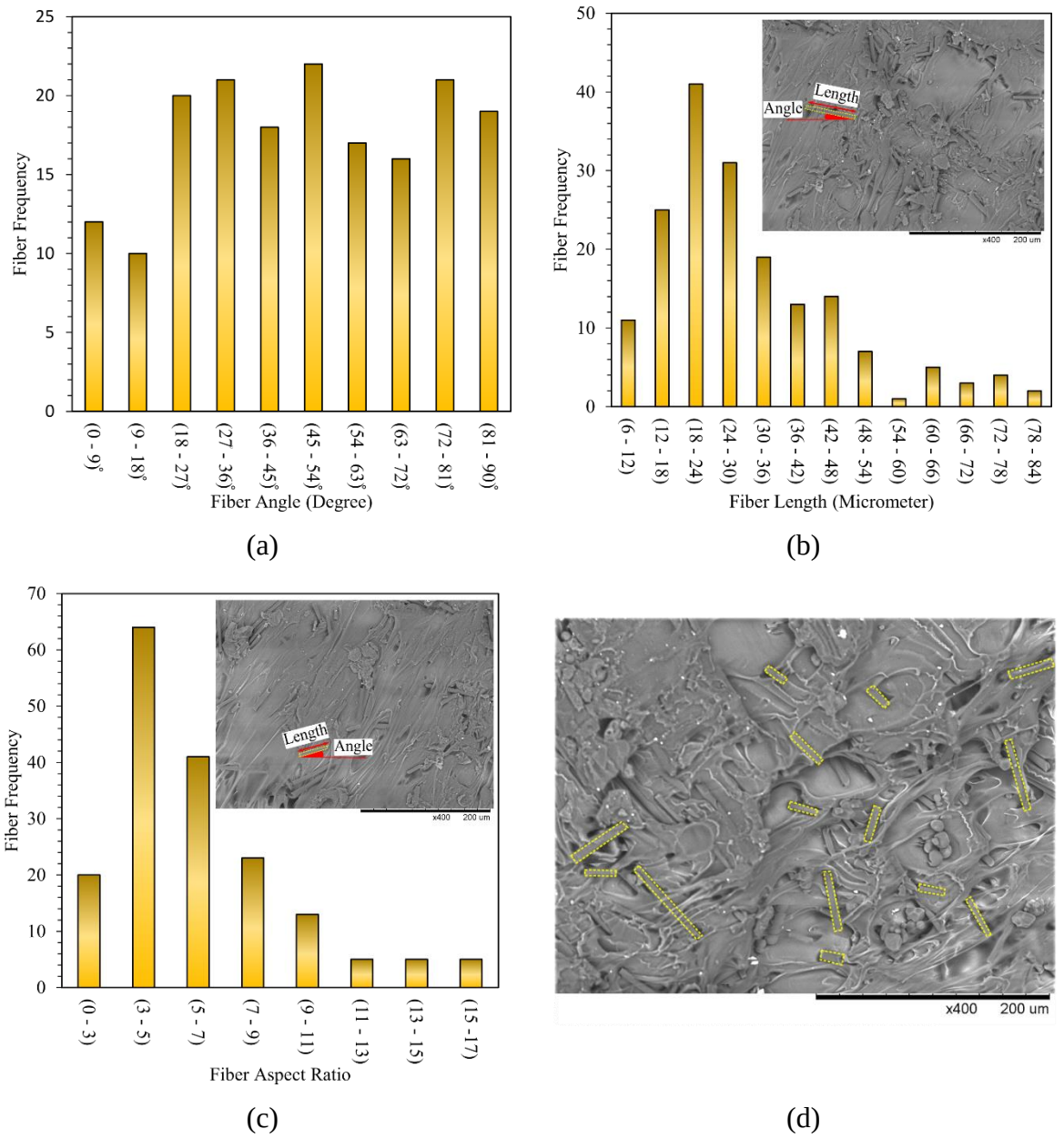

Figure 3 - 10: Carbon fibers characteristic in PTEG-C: (a) Fiber angles, (b) Fiber length, (c) Fiber aspect ratio and (d) SEM image of longitudinal cross-section of filament (yellow dash lines show some fibers boundaries).

3.6.2 Numerical simulation

To numerically verify the discussed analytical findings, cellular parts based on the 2D rectangular *Isomixed* architecture with n = 1.2 are modeled using SolidWorks. While the porosity of all parts is kept constant, five models (containing at least three cells along all in-plane directions with the overall size of 133.2 mm × 133.2 mm × 3.5 mm) along different rotation angles (0, 15, 30, 45 and 90 degrees) are considered to analyze the anisotropy of the stiffness (**Figure 3-10a**). Three different unit cells are considered (**Figure 3-10b**): Type I) 2D rectangular *Isomixed* composite cell designed based on equation 3.8 made out of two materials that are PETG-S and PETG-C. Vertical and diagonal members are made out of PETG-C, and horizontal members are made out of PETG-S. The mechanical properties of the based materials are imported in ABAQUS from **Table 3-S5** (Supplementary Information) that are obtained from the tensile tests on the 3D printed dogbone samples (**Figure 3-11b**), explained in the following section (Section 3.6.2). The member's in-plane thicknesses are chosen based on equation 3.8 for n=1.2 and the ratio of PETG-C to PETG-S modulus of elasticity (i.e., $E_v = E_d = 1.67\, E_h$, obtained from the experiment) as following: $t_h = 1.6\, mm$, $t_v = 1.7\, mm$ and $t_d = 1.9\, mm$, Type II) Cell with the same materials of the first group but having the same thickness for all members (i.e., 1.6 mm, the horizontal members thickness of the first group) and Type III) Cell with the same geometry of the first group but made out of single material (i.e., PETG-S).

Tensile test simulations with load along the Y-axis are completed using a stress analysis (Finite Element Analysis) tool in ABAQUS (version 2019). Loads and constraints are first assigned on the bottom and top of cellular samples resembling the real tensile test (i.e., the bottom of the sample is assumed to be fixed and the displacement load at the rate of 5 $mm.min^{-1}$ is applied to the top of the sample). The reaction force of the cellular structure along the Y direction is then

obtained, and finally, the tensile stiffnesses of the samples are calculated using the stress-strain curve. Considering this thesis's goal of obtaining only stiffness, no large deformation is considered in the simulation, and only the linear elastic response is studied. The stiffness contours based on detailed FE analysis and stiffness rotational transformation (section 3.8.6, Supplementary Information) are provided in (**Figure 3-10c**). The isotropic mechanical properties can be seen only in 2D rectangular *Isomixed* composite samples (Type I), which confirms the accuracy of equation 3.8. As discussed in Section 3.4.1, this design is possible by choosing different fiber contents along vertical and diagonal directions.

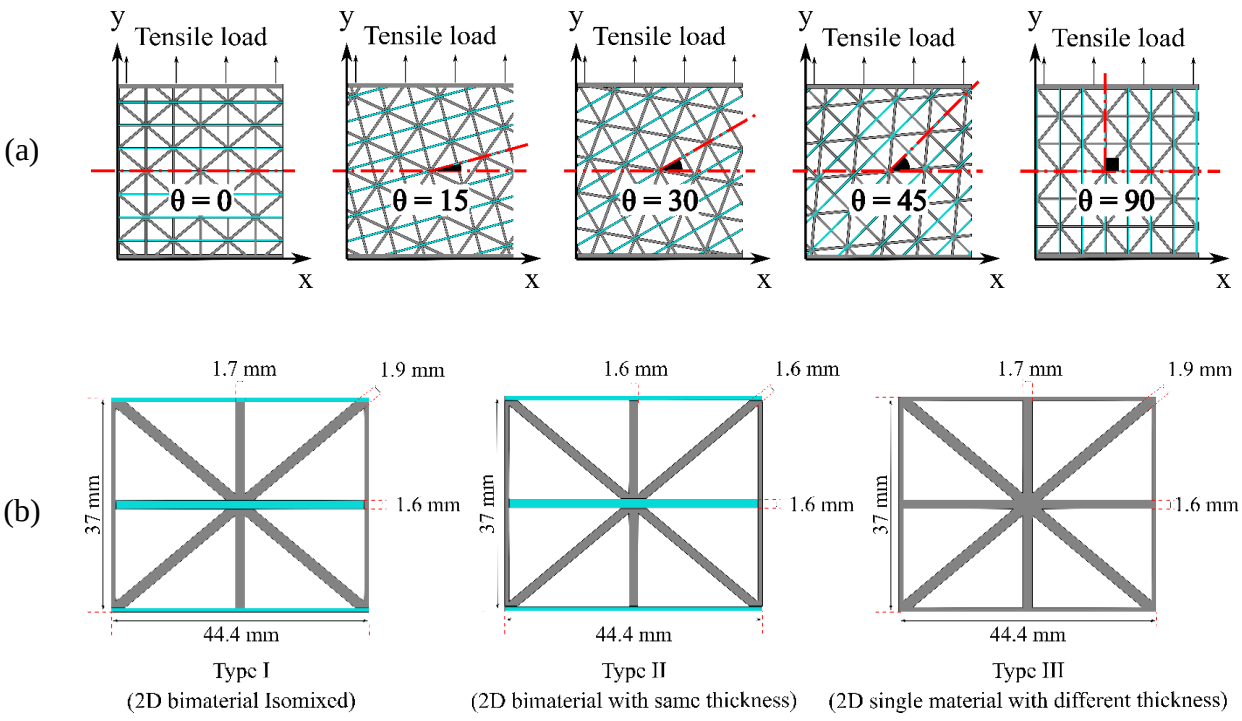

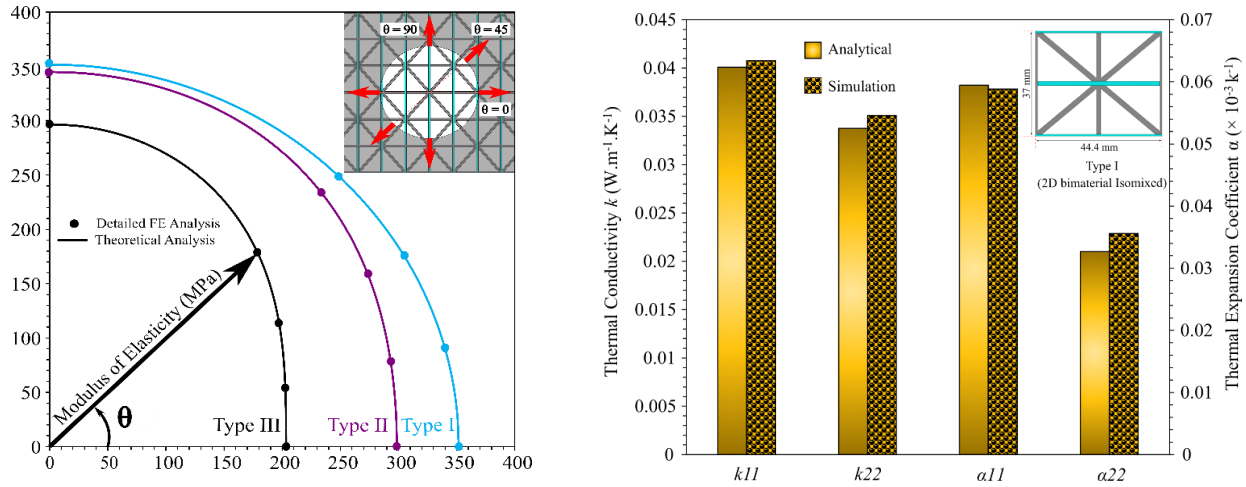

(c) (d)

Figure 3 - 11: (a) CAD models for the specimens with different cell orientations; (b) Three different unit cells; (c) Module of elasticity for the samples with different cell orientations based on FEA and theoretical rotational transformation: Type I) 2D rectangular bi-material *Isomixed* cell, Type II) bi-material samples with same members' thickness and Type III) samples with different member's thicknesses made out of single material [Red arrows show the tensile load direction at each angle. Members made out of PETG-S and PETG-C material are shown in cyan and grey, respectively] and (d) Comparison of the results obtained from analytical equations and numerical simulation for the thermal conductivity and thermal expansion coefficient of 2D rectangular *Isomixed* cell.

In addition to mechanical properties, the thermal properties of 2D rectangular *Isomixed* cell are calculated and compared using the analytical approach (equation 3.13) and finite element detailed analysis (simulation) to verify the derived closed-form expressions, as illustrated in **Figure 3-10d**. The thermal properties of the base material are measured by TCi Thermal Conductivity Analyzer and Thermal Mechanical Analyzer (TMA) device (**Table 3-6**). The maximum discrepancy between the analytical approach and detailed finite element analysis for the thermal expansion coefficient and thermal conductivity is 8% and 3%, respectively, as shown in **Figure 3-10d**. This can be attributed to the fact that the analytical equations are derived for low relative density, whereas the relative density of 2D rectangular *Isomixed* cell is 0.29.

Table 3 - 6: Thermal properties of PETG-S and PTEG-C

	Thermal conductivity k ($W.m^{-1}.K^{-1}$)	*Thermal expansion coefficient (K^{-1})*
PETG-S	0.229	7.39×10^{-5}
PETG-C	0.257	3.93×10^{-5}

3.6.3 Experimental tests

The specimens for the tensile test are 3D printed using an open-source fused deposition modelling (FDM) 3D printer (Ultimaker 3). The CAD models for the dogbone and 2D rectangular *Isomixed* samples are first designed in SOLIDWORKS and then imported into the CURA software (Version 4.8.0, developed by Ultimaker) to set the printer parameters (**Table 3-7**). PETG-S and Carbon fiber-reinforced PETG-C (Kimya, Armor USA Inc.) filaments are used to print the samples in this experiment.

Table 3 - 7: Filament and Printer parameters.

Parameter	PETG-S	PETG-C	Parameter	PETG-S	PETG-C
Nozzle diameter (mm)	0.4		Filament diameter (mm)	2.8	
Layer height (mm)	0.1		Printing speed (mm/s)	60	
Line width (mm)	0.35	0.3	Printing temperature (ºC)	240	255
Wall thickness (mm)	0.35	0.3	Bed temperature (ºC)	70	
Filling density	100%		Mesh Overlaps (mm)	0.3	

To keep the same condition, all printed specimens are stored at room temperature for approximately 24 h before conducting experiments. Tensile tests are conducted using an ADMET tensile test machine with an MTESTQuattro (ADMET, Norwood MA, USA) testing control system, equipped with a 20 kN load cell, under a constant strain rate of 5 $mm.min^{-1}$. The axial stiffness of the samples is then calculated using the extracted stress-strain curves (**Figure 3-11**). Videos of sample tests are provided in Supplementary information. Following the recommendation of ASTM D638 standard for the dogbone samples, five replicates are printed and tested for each sample (i.e., PETG-S dogbone, PETG-C dogbone and composite 2D rectangular *Isomixed*) to

minimize the experimental uncertainties. The elastic moduli of PETG-S and PETG-C are measured as 2215 ± 59 MPa and 3708 ± 67 MPa, respectively, which are used in the detailed numerical simulations in the previous section. As shown in **Figure 3-12**, experimental results for the selected 2D rectangular *Isomixed* are consistent with the detailed analysis results, confirming the in-plane isotropic mechanical properties; however, due to printing defects, imperfect bonding and dependency of the material properties with the printing direction, the experiment test results show lower values. In addition, analytically calculated Young's moduli (obtained from equation 3.9 for n = 1.2) are compared with the experimental and numerical results for n = 1.2; the analytical results underpredict the moduli by 2% when compared to the experimental data. Besides the 3D printing defects, the discrepancy may emanate from the simplifying assumptions made for derivation of closed-form expression (e.g., two-force members connected by frictionless joints and neglecting the common areas among neighboring struts).

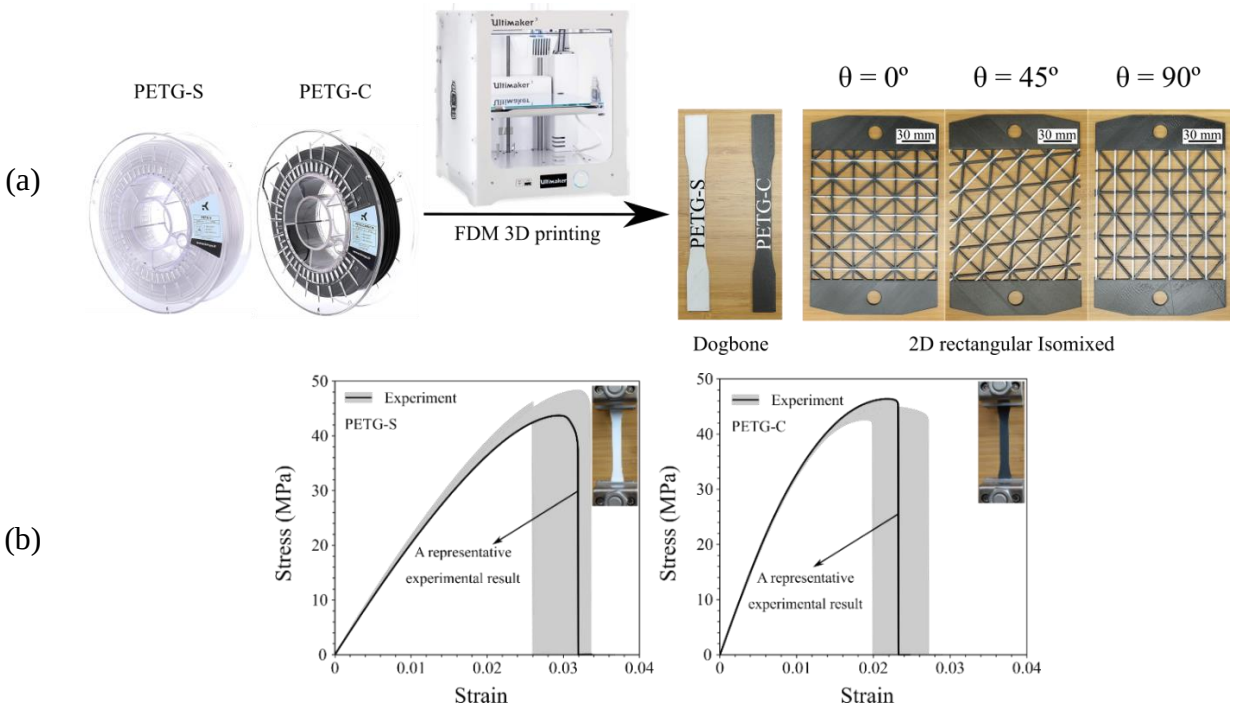

(c)

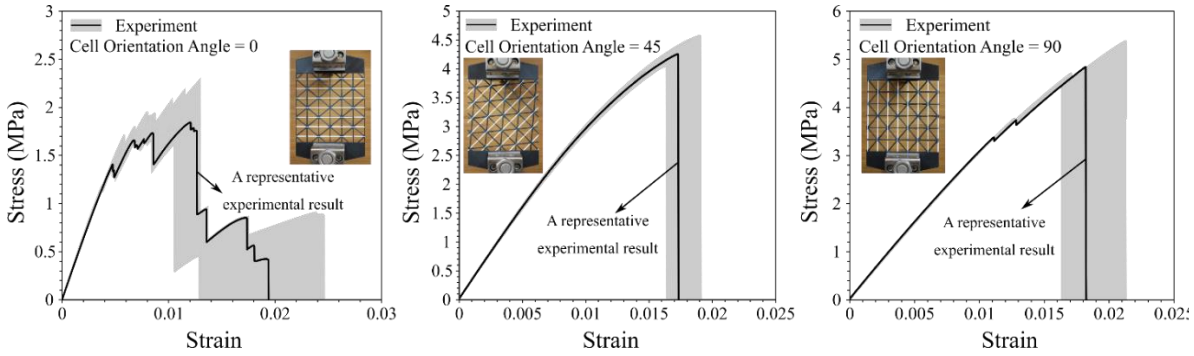

Figure 3 - 12: Experimental tests process: **(**a) 3D printing samples; **(**b) Stress-strain curves of dogbones and **(**c) 2D rectangular *Isomixed* samples.

To determine the source of discrepancies between simulation and experimental results, the printing process of specimens is studied, revealing that the walls of the outside contour and the walls of the cellular holes of the model are printed first, followed by the walls of the infill zone, and finally, the filling lines in the infill zone. Even though the infill density is set at 100% for this experiment, this printing sequence leaves tiny holes or gaps between the contour wall lines and the infill zone wall lines. The printing settings are optimized to reduce this imperfection (**Table 3-7**).

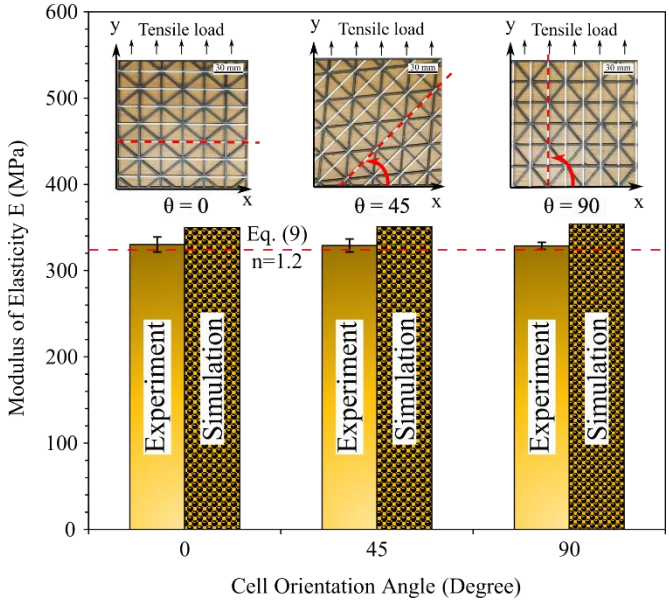

Figure 3 - 13: Comparison of the detailed analysis (simulation) and experiment results on 3D printed samples with results analytically predicted for n=1.2: 3D printed specimens with cell orientations of 0, 45 and 90 degrees are shown for experimental tests.

3.7 Conclusions

This thesis introduces a new computationally-efficient methodology to find the effective thermomechanical properties of architected cellular fiber-reinforced composites. First, an analysis is conducted to investigate the effects of fiber length fiber orientation, and fiber volume fraction on effective thermomechanical properties of fiber-reinforced composite materials using numerical standard mechanics homogenization. Then, a multi-level method is introduced to obtain the effective material properties of cellular composites. Furthermore, the validity of the method is examined by conducting computational methodologies (i.e., detailed analysis combined with homogenization technique) to predict the effective thermomechanical properties of closed-cell and open-cell cellular composite metamaterials. These properties are scrutinized in terms of the fiber relative size, and different pore shapes. Comparison of the predictions of multi-level method with detailed multiscale analysis method reveals that they are in good agreement as long as the fibers are shorter than half of the minimum wall thickness of the cellular architecture.

Additionally, by tuning the cross-section and the underlying solid medium of cell members, novel 2D rectangular and 3D cuboid cells are systematically designed to show isotropic effective mechanical properties, while they lack certain rotational symmetries of 2D square cells with 4-fold symmetries and 3D cells with cubic crystal symmetries. Finally, mechanical isotropy of selected engineered cellular architectures and the accuracy of the proposed conditions under which these cellular materials are isotropic are assessed through detailed numerical simulation and experimental tests on the 3D printed samples out of simple and carbon fiber-reinforced PETG.

A wide variety of material properties can be achieved by fabricating the isotropic 2D and 3D *Isomixed* material using composite constituents that have valuable properties. Although there is room for designing at higher relative densities, the present work introduces an advanced

development in 3D printing that opens new avenues in additive manufacturing and smart lightweight material design. With the continued development of manufacturing technology and light material systems, the use of complex cellular structural materials will inevitably become as common in engineered systems as those found in nature.

3.8 Supporting information

3.8.1 S-Verification of the numerical code

The code is verified by a comparison of the obtained result with the results provided in reference [59]. The length and the diameters of the fibers are chosen based on Ref. [59] and the effective properties of randomly distributed short fiber composites are predicted in four different cases for the fibers' orientation. Table.S1 shows the present and Ref. [59] numerical results; as shown, the maximum difference is 4%. This difference could be associated with the fact that the fiber distributions are random and therefore, they are not identical for the current thesis and Ref. [1].

Table 3-S1: Comparison of the effective mechanical properties obtained from the current thesis and Ref. [59].

Case	*Property*	$\overline{E}_{11}$ *(GPa)*	$\overline{E}_{22}$ *(GPa)*	$\overline{E}_{33}$ *(GPa)*	$\overline{\nu}_{12}$	$\overline{\nu}_{13}$	$\overline{\nu}_{23}$	$\overline{G}_{12}$ *(GPa)*	$\overline{G}_{13}$ *(GPa)*	$\overline{G}_{23}$ *(GPa)*
	Ref. [59]	9.4 ± 0.4	5.26 ± 0.03	5.26 ± 0.04	0.33 ± 0.01	0.33 ± 0.01	0.37 ± 0.00	2.10 ± 0.03	2.12 ± 0.02	1.90 ± 0.01
	Current thesis	9.6 ± 0.3	5.26 ± 0.02	5.27 ± 0.02	0.34± 0.00	0.34 ± 0.00	0.39 ± 0.00	2.08 ± 0.01	2.09 ± 0.03	1.89 ± 0.00
	Difference %	< 3	< 0.1	< 0.2	< 4	< 3	< 4	< 2	< 2	< 2
I	Ref. [59]	6.7 ± 0.3	6.3 ± 0. 3	5.4 ± 0.1	0.33 ± 0.03	0.32 ± 0.01	0.33 ± 0.01	2.54 ± 0.16	2.02 ± 0.02	1.99 ± 0.01
	Current thesis	6.5 ± 0.4	6.5 ± 0. 4	5.3 ± 0.1	0.33 ± 0.02	0.33 ± 0.00	0.33 ± 0.00	2.6 ± 0.03	1.98 ± 0.03	1.98 ± 0.01
	Difference %	< 4	< 4	< 0.5	< 0.6	< 4	< 0.3	< 4	< 3	< 2
II	Ref. [59]	6.67 ± 0.2	6.5 ± 0.5	5.4 ± 0.03	0.31 ± 0.04	0.33 ± 0.02	0.33 ± 0.01	2.46 ± 0.12	2.01 ± 0.02	2.00 ± 0.02
	Current thesis	6.67 ± 0.4	6.8 ± 0.4	5.4 ± 0.02	0.34 ± 0.00	0.33 ± 0.01	0.33 ± 0.01	2.50 ± 0.07	2.00 ± 0.02	2.00 ± 0.02
	Difference %	< 0.1	< 4	< 1	< 2	< 4	< 3	< 4	< 1	< 0.1
V	Ref. [59]	5.53 ± 0.06	5.56 ± 0.11	5.77 ± 0.09	0.31 ± 0.01	0.31 ± 0.01	0.29 ± 0.00	2.10 ± 0.03	2.11 ± 0.05	2.08 ± 0.03
	Current thesis	5.80 ± 0.13	5.83 ± 0.24	5.82 ± 0.18	0.32 ± 0.01	0.32 ± 0.01	0.32 ± 0.01	2.19 ± 0.03	2.16 ± 0.07	2.17 ± 0.07
	Difference %	< 4	< 4	< 1	< 3	< 4	< 4	< 4	< 3	< 4

*Fiber volume fraction is 15.23% for all cases. Aspect ratio is 3.5; Case I (In-plane aligned fibers): Fibers orient in the X-direction (direction 1); Case II (In-plane randomly oriented fibers): Fibers are randomly oriented in XY-plane (12-plane) located at different positions; Case III (In-plane randomly oriented and out of plane partial randomly oriented fibers): This is the same as case 2 and further allowing orientations of the fibers by ± 10° in XZ-plane. (23-plane); Case IV (Completely random oriented fibers): Fibers orient randomly in all planes.

3.8.2 S-Influence of fiber length on thermomechanical properties of fiber-reinforced composites

Table 3-S2 shows the numerical values of effective thermomechanical properties at various fiber lengths for fiber-reinforced composites.

Table 3-S2: Comparison of effective thermomechanical properties for different fiber lengths.

Property	**R = 1**	**R = 2**	**R = 3**	**R = 4**
$\overline{E}$ (GPa)	6.41 ± 2.04	5.90 ± 0.17	5.90 ± 0.15	5.90 ± 0.09
$\overline{\nu}$	0.31 ± 0.07	0.32 ± 0.01	0.32 ± 0.01	0.32 ± 0.01
$\overline{G}$ (GPa)	2.23 ± 0.22	2.24 ± 0.06	2.24 ± 0.05	2.25 ± 0.03
$\overline{k}$ ($\frac{W}{m^2.K}$)	0.49 ± 0.11	0.48 ± 0.02	0.47 ± 0.02	0.47 ± 0.00
$\overline{\alpha}$ ($\times\frac{10^{-4}}{K}$)	0.37 ± 0.05	0.37 ± 0.01	0.36 ± 0.01	0.36 ± 0.00
A	0.91 ± 0.19	1.01 ± 0.02	1.00 ± 0.01	1.00 ± 0.00

* R: RVE side-to-fiber length ratio; The bar notation is used for the effective properties of the cellular material; Fiber volume fraction is approximately 15% for all cases. 15.43%.

3.8.3 S-Influence of fiber volume fraction on thermomechanical properties of fiber-reinforced composites

Table 3-S3 shows the numerical values of effective thermomechanical properties at various inclusion volume fractions for fiber-reinforced composites.

Table 3-S3: Comparison of effective thermomechanical properties for different inclusion volume fractions.

Property	V_f = 5 %	V_f = 10 %	V_f = 15 %	V_f = 25 %
$\overline{E}$ (GPa)	4.71 ± 0.04	5.30 ± 0.08	5.90 ± 0.09	7.33 ± 0.17
$\overline{\nu}$	0.33 ± 0.00	0.33 ± 0.01	0.32 ± 0.01	0.30 ± 0.01
$\overline{G}$ (GPa)	1.76 ± 0.01	1.98 ± 0.02	2.25 ± 0.03	2.81 ± 0.07
$\overline{k}$ ($\frac{W}{m^2.K}$)	0.31 ± 0.00	0.38 ± 0.01	0.47 ± 0.00	0.62 ± 0.02
$\overline{\alpha}$ ($\times\frac{10^{-4}}{K}$)	0.42 ± 0.01	0.39 ± 0.00	0.36 ± 0.00	0.32 ± 0.01
A	0.99 ± 0.01	1.00 ± 0.01	1.00 ± 0.00	1.00 ± 0.01

* V_f: Inclusion volume fraction; the bar notation is used for the effective properties of the cellular material; Fiber lengths are one-fourth of RVE side for all cases.

3.8.4 S-Influence of fibers orientation on thermomechanical properties fiber-reinforced composites

Table 3-S4 shows the numerical values of effective thermomechanical properties at various fiber orientations for fiber-reinforced composites.

Table 3-S4: Comparison of effective thermomechanical properties for different fiber angles with direction 3.

Property	$\theta = 0$	$\theta = 30$	$\theta = 60$	$\theta = 90$	Property	$\theta = 0$	$\theta = 30$	$\theta = 60$	$\theta = 90$
$\overline{E}_{11} = \overline{E}_{22}$ (GPa)	5.27 ± 0.01	5.41 ± 0.01	5.89 ± 0.05	6.67 ± 0.09	$\overline{E}_{33}$ (GPa)	9.95 ± 0.16	7.29 ± 0.03	5.76 ± 0.02	5.38 ± 0.02
$\overline{G}_{13} = \overline{G}_{23}$ (GPa)	2.07 ± 0.00	2.39 ± 0.02	2.35 ± 0.02	1.97 ± 0.01	$\overline{G}_{12}$ (GPa)	1.88 ± 0.00	1.95 ± 0.00	2.29 ± 0.01	5.55 ± 0.04
$\overline{\nu}_{12} = \overline{\nu}_{21}$	0.39 ± 0.00	0.34 ± 0.00	0.33 ± 0.00	0.32 ± 0.01	$\overline{\nu}_{13} = \nu_{23}$	0.18 ± 0.00	0.26 ± 0.00	0.32 ± 0.00	0.34 ± 0.00
$\overline{k}_{11} = \overline{k}_{22}$ $(\frac{W}{m^2.K})$	0.33 ± 0.00	0.38 ± 0.00	0.47 ± 0.01	0.53 ± 0.01	$\overline{k}_{33}$ $(\frac{W}{m^2.K})$	0.74 ± 0.01	0.63 ± 0.00	0.42 ± 0.00	0.33 ± 0.00
$\overline{\alpha}_{11} = \overline{\alpha}_{22}$ $(\times\frac{10^{-4}}{K})$	0.42 ± 0.00	0.40 ± 0.00	0.35 ± 0.00	0.34 ± 0.00	$\overline{\alpha}_{33}$ $(\times\frac{10^{-4}}{K})$	0.28 ± 0.00	0.30 ± 0.00	0.38 ± 0.00	0.43 ± 0.00

*θ: Angle of fiber axis with direction 3; The bar notation is used for the effective properties of the cellular material; Fiber lengths are one-fourth of RVE side for all cases; Fiber volume fraction is approximately 15% for all cases.

3.8.5 S-Analytical analysis for thermal expansion coefficient of 2D rectangular *Isomixed*

To find the thermal expansion coefficient ($\bar{\alpha}$), it is started with equation $\bar{\sigma}_{ij} = \bar{C}_{ijkl}(\bar{\varepsilon}_{kl} - \bar{\alpha}_{kl}\Delta T)$ and all boundaries are fixed to make the overall stain zero **(**$\bar{\varepsilon} = 0$), then the thermal load of ΔT=1 is applied to determine the effective stress ($\bar{\sigma}$). Then the effective thermal expansion coefficient can be calculated by using the effective stiffness matrix and equation $\bar{\alpha}_{ij} = -\bar{C}^{-1}_{ijkl}\,\bar{\sigma}_{kl}$.

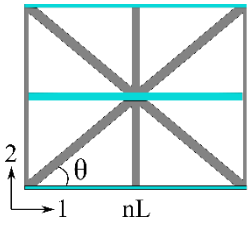

Effective stress in direction 1	Effective stress in direction 2
$\bar{\sigma}_1 = \frac{-2}{L}(\alpha_h E_h t_h + \frac{n\alpha_d E_d t_d}{\sqrt{1+n^2}})$	$\bar{\sigma}_2 = \frac{-2}{nL}(\alpha_v E_v t_v + \frac{\alpha_d E_d t_d}{\sqrt{1+n^2}})$
Effective thermal expansion in direction 1	Effective thermal expansion in direction 2
$\bar{\alpha}_1 = \frac{-\bar{\sigma}_1}{\bar{E}} + \frac{\nu\bar{\sigma}_2}{\bar{E}}$	$\bar{\alpha}_2 = \frac{-\bar{\sigma}_2}{\bar{E}} + \frac{\nu\bar{\sigma}_1}{\bar{E}}$

Having $E_h t_h = \frac{3n-n^3}{(n^2+1)^{\frac{3}{2}}} E_d t_d$, $E_v t_v = \frac{3n^2-1}{(n^2+1)^{\frac{3}{2}}} E_d t_d$, and $\nu = \frac{1}{3}$ results in:

$$\bar{\alpha}_{11} = \frac{2E_d t_d}{L\bar{E}\sqrt{n^2+1}}\left[\alpha_h \frac{3n-n^3}{(n^2+1)} - \alpha_v \frac{3n^2-1}{3n(n^2+1)} + \alpha_d\left(n - \frac{1}{3n}\right)\right]$$

$$\bar{\alpha}_{22} = \frac{2E_d t_d}{L\bar{E}\sqrt{n^2+1}}\left[\alpha_v \frac{3n^2-1}{n(n^2+1)} - \alpha_h \frac{3n-n^3}{3(n^2+1)} + \alpha_d\left(\frac{1}{n} - \frac{n}{3}\right)\right]$$

3.8.6 S-Analytical analysis for modulus of elasticity in different directions

Table 3-S5 shows the On-Axis and Off-Axis "strain-stress" relations in 2D dimensions. equation 3.S1 [81] shows off-axis and on-axis compliance relation.

$$S_{11} = m^4 S_{xx} + n^4 S_{yy} + m^2 n^2 (2S_{xy} + S_{ss}) \quad (3.S1)$$

where $m = \cos\theta$ and $n = \sin\theta$. The value of S_{xx} at $\theta = 0^o$, S_{yy} at $\theta = 90^o$ and S11 at $\theta = 45^o$ are obtained via detailed analysis simulation (Section 3.6.1) and given in **Table 3-S5**.

Table 3-S5: On-Axis and Off-Axis compliance matrix components for the three cell types:

$\begin{bmatrix}\varepsilon_x\\ \varepsilon_y\\ \varepsilon_s\end{bmatrix} = \begin{bmatrix}S_{xx} & S_{xy} & S_{xs}\\ S_{xy} & S_{yy} & S_{ys}\\ S_{xs} & S_{ys} & S_{ss}\end{bmatrix}\begin{bmatrix}\sigma_x\\ \sigma_y\\ \sigma_s\end{bmatrix}$	$\begin{bmatrix}\varepsilon_1\\ \varepsilon_2\\ \varepsilon_6\end{bmatrix} = \begin{bmatrix}S_{11} & S_{12} & S_{16}\\ S_{12} & S_{22} & S_{26}\\ S_{16} & S_{26} & S_{66}\end{bmatrix}\begin{bmatrix}\sigma_1\\ \sigma_2\\ \sigma_6\end{bmatrix}$	2D rectangular *Isomixed* cell	Cell made out of single material	Cell with same members' thickness
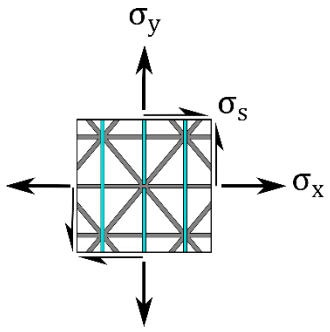 **On-Axis**	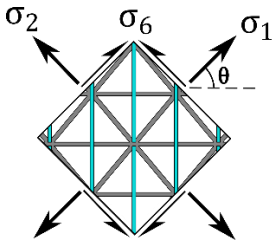 **Off-Axis**			
$S_{xx} \times 10^{-3}$ (MPa)$^{-1}$		2.856	4.917	3.348
$S_{yy} \times 10^{-3}$ (MPa)$^{-1}$		2.825	3.370	2.796
$S_{11} \times 10^{-3}$ (MPa)$^{-1}$ at $\theta = 45^o$		2.851	3.956	3.026
$(2S_{xy} + S_{ss}) \times 10^{-3}$ (MPa)$^{-1}$		5.724	7.538	5.958

By substitution of these values in equation 3.S1, the value of $(2S_{xy} + S_{ss})$ could be found for each cell. Then, S11 is found as a function of θ by equation 3.S2 (**Table 3-S6**). Module of elasticity E_{11} can be found by inversing S_{11}.

Table 3-S6: S_{11} ($\times 10^{-3}$ $(MPa)^{-1}$) as a function of θ for the three cell types ($m = \cos\theta$ and $n = \sin\theta$):

2D rectangular *Isomixed* cell	$2.856\ m^4 + 2.825\ n^4 + 5.724\ m^2n^2$
Cell made out of single material	$4.917\ m^4 + 3.370\ n^4 + 7.538\ m^2n^2$
Cell with same members' thickness	$3.348\ m^4 + 2.796\ n^4 + 5.958\ m^2n^2$

Experimental tests of 2D rectangular *Isomixed* samples and their failure behavior for different cell orientations, as discussed in Section 3.6.2, are presented in a Video clip.

3.9 References

[1] Ling, C., A. Cernicchi, M.D. Gilchrist, and P. Cardiff, *Mechanical behaviour of additively-manufactured polymeric octet-truss lattice structures under quasi-static and dynamic compressive loading.* Materials & Design, 2019. 162: p. 106-118.

[2] Askarinejad, S., H.A. Choshali, C. Flavin, and N. Rahbar, *Effects of tablet waviness on the mechanical response of architected multilayered materials: Modeling and experiment.* Composite Structures, 2018. 195: p. 118-125.

[3] Imbalzano, G., S. Linforth, T.D. Ngo, P.V.S. Lee, and P. Tran, *Blast resistance of auxetic and honeycomb sandwich panels: Comparisons and parametric designs.* Composite Structures, 2018. 183: p. 242-261.

[4] Harris, B., *Engineering composite materials*. Vol. 1. 1999: The Institute of Materials, London. 33-193.

[5] Fu, S.Y., X.Q. Feng, B. Lauke, and Y.W. Mai, *Effects of particle size, particle/matrix interface adhesion and particle loading on mechanical properties of particulate-polymer composites.* Composites Part B-Engineering, 2008. 39(6): p. 933-961.

[6] Sorrentino, L., L. Cafiero, M. D'Auria, and S. Iannace, *Cellular thermoplastic fibre reinforced composite (CellFRC): A new class of lightweight material with high impact properties.* Composites Part a-Applied Science and Manufacturing, 2014. 64: p. 223-227.

[7] Duan, S.Y., Y.R. Tao, X. Han, X.J. Yang, S.J. Hou, and Z.P. Hu, *Investigation on structure optimization of crashworthiness of fiber reinforced polymers materials.* Composites Part B-Engineering, 2014. 60: p. 471-478.

[8] Harizi, W., S. Chaki, G. Bourse, and M. Ourak, *Mechanical damage assessment of Glass Fiber-Reinforced Polymer composites using passive infrared thermography*. Composites Part B-Engineering, 2014. 59: p. 74-79.

[9] Yu, Y.L., X.N. Huang, and W.J. Yu, *A novel process to improve yield and mechanical performance of bamboo fiber reinforced composite via mechanical treatments.* Composites Part B-Engineering, 2014. 56: p. 48-53.

[10] Dong, K., H.Z. Ke, M. Panahi-Sarmad, T.T. Yang, X.Y. Huang, and X.L. Xiao, *Mechanical properties and shape memory effect of 4D printed cellular structure composite with a novel continuous fiber-reinforced printing path.* Materials & Design, 2021. 198: p. 109303.

[11] Kabir, S.F., K. Mathur, and A.-F.M. Seyam, *Impact resistance and failure mechanism of 3D printed continuous fiber-reinforced cellular composites.* The Journal of The Textile Institute, 2021. 112(5): p. 752-766.

[12] Estakhrianhaghighi, E., A. Mirabolghasemi, Y.N. Zhang, L. Lessard, and A. Akbarzadeh, *3D-Printed Wood-Fiber Reinforced Architected Cellular Composites.* Advanced Engineering Materials, 2020. 22(11): p. 2000565.

[13] Yazdani Sarvestani, H., A.H. Akbarzadeh, D. Therriault, and M. Lévesque, *Engineered bi-material lattices with thermomechanical programmability.* Composite Structures, 2021. 263: p. 113705.

[14] Belova, I.V., C. Veyhl, T. Fiedler, and G.E. Murch, *Analysis of anisotropic behaviour of thermal conductivity in cellular metals.* Scripta Materialia, 2011. 65(5): p. 436-439.

[15] Abueidda, D.W., R.K. Abu Al-Rub, A.S. Dalaq, D.W. Lee, K.A. Khan, and I. Jasiuk, *Effective conductivities and elastic moduli of novel foams with triply periodic minimal surfaces.* Mechanics of Materials, 2016. 95: p. 102-115.

[16] Park, G., S. Kang, H. Lee, and W. Choi, *Tunable Multifunctional Thermal Metamaterials: Manipulation of Local Heat Flux via Assembly of Unit-Cell Thermal Shifters.* Sci Rep, 2017. 7: p. 41000.
[17] Zhang, C.Y., A. Akbarzadeh, W. Kang, J.X. Wang, and A. Mirabolghasemi, *Nano-architected metamaterials: Carbon nanotube-based nanotrusses.* Carbon, 2018. 131: p. 38-46.
[18] Romano, G., K. Esfarjani, D.A. Strubbe, D. Broido, and A.M. Kolpak, *Temperature-dependent thermal conductivity in silicon nanostructured materials studied by the Boltzmann transport equation.* Physical Review B, 2016. 93(3): p. 035408.
[19] Xu, H., A. Farag, and D. Pasini, *Routes to program thermal expansion in three-dimensional lattice metamaterials built from tetrahedral building blocks.* Journal of the Mechanics and Physics of Solids, 2018. 117: p. 54-87.
[20] Li, Y.B., Y.Y. Chen, T.T. Li, S.Y. Cao, and L.F. Wang, *Hoberman-sphere-inspired lattice metamaterials with tunable negative thermal expansion.* Composite Structures, 2018. 189: p. 586-597.
[21] Abueidda, D.W., M. Elhebeary, C.S. Shiang, S.Y. Pang, R.K. Abu Al-Rub, and I.M. Jasiuk, *Mechanical properties of 3D printed polymeric Gyroid cellular structures: Experimental and finite element study.* Materials & Design, 2019. 165: p. 107597.
[22] Sugiyama, K., R. Matsuzaki, M. Ueda, A. Todoroki, and Y. Hirano, *3D printing of composite sandwich structures using continuous carbon fiber and fiber tension.* Composites Part a-Applied Science and Manufacturing, 2018. 113: p. 114-121.
[23] Lubombo, C. and M.A. Huneault, *Effect of infill patterns on the mechanical performance of lightweight 3D-printed cellular PLA parts.* Materials Today Communications, 2018. 17: p. 214-228.
[24] Bates, S.R.G., I.R. Farrow, and R.S. Trask, *Compressive behaviour of 3D printed thermoplastic polyurethane honeycombs with graded densities.* Materials & Design, 2019. 162: p. 130-142.
[25] Compton, B.G. and J.A. Lewis, *3D-printing of lightweight cellular composites.* Adv Mater, 2014. 26(34): p. 5930-5.
[26] Matsuzaki, R., M. Ueda, M. Namiki, T.K. Jeong, H. Asahara, K. Horiguchi, T. Nakamura, A. Todoroki, and Y. Hirano, *Three-dimensional printing of continuous-fiber composites by in-nozzle impregnation.* Sci Rep, 2016. 6: p. 23058.
[27] Gibson, L.J. and M.F. Ashby, *Cellular solids: structure and properties*. 1999: Cambridge university press.
[28] Öchsner, A. and T. Fiedler, *Effective thermal properties of hollow-sphere structures: a finite element approach.* Cellular and Porous Materials: Thermal Properties Simulation and Prediction, 2008: p. 31-72.
[29] Baillis, D. and R. Coquard, *Radiative and conductive thermal properties of foams.* Cellular and Porous Materials: Thermal Properties Simulation and Prediction, 2008: p. 343-384.
[30] Belova, I.V. and G.E. Murch, *Thermal properties of composite materials and porous media: lattice-based Monte Carlo approaches.* Cellular and Porous Materials: Thermal Properties Simulation and Prediction, 2008: p. 73-96.
[31] Fiedler, T., M.A. Sulong, M. Vesenjak, Y. Higa, I.V. Belova, A. Ochsner, and G.E. Murch, *Determination of the thermal conductivity of periodic APM foam models.* International Journal of Heat and Mass Transfer, 2014. 73: p. 826-833.

[32] Gasia, J., L. Miro, and L.F. Cabeza, *Materials and system requirements of high temperature thermal energy storage systems: A review. Part 2: Thermal conductivity enhancement techniques.* Renewable & Sustainable Energy Reviews, 2016. 60: p. 1584-1601.
[33] Kumar, P., F. Topin, and J. Vicente, *Determination of effective thermal conductivity from geometrical properties: Application to open cell foams.* International Journal of Thermal Sciences, 2014. 81: p. 13-28.
[34] Montazerian, H., E. Davoodi, M. Asadi-Eydivand, J. Kadkhodapour, and M. Solati-Hashjin, *Porous scaffold internal architecture design based on minimal surfaces: A compromise between permeability and elastic properties.* Materials & Design, 2017. 126: p. 98-114.
[35] Wang, W.B., X.H. Yang, B. Han, Q.C. Zhang, X.F. Wang, and T.J. Lu, *Analytical design of effective thermal conductivity for fluid-saturated prismatic cellular metal honeycombs.* Theoretical and Applied Mechanics Letters, 2016. 6(2): p. 69-75.
[36] Lei, M., C.M. Hamel, C. Yuan, H.B. Lu, and H.J. Qi, *3D printed two-dimensional periodic structures with tailored in-plane dynamic responses and fracture behaviors.* Composites Science and Technology, 2018. 159: p. 189-198.
[37] Habib, F.N., P. Iovenitti, S.H. Masood, and M. Nikzad, *Cell geometry effect on in-plane energy absorption of periodic honeycomb structures.* International Journal of Advanced Manufacturing Technology, 2018. 94(5-8): p. 2369-2380.
[38] Sarvestani, H.Y., A.H. Akbarzadeh, H. Niknam, and K. Hermenean, *3D printed architected polymeric sandwich panels: Energy absorption and structural performance.* Composite Structures, 2018. 200: p. 886-909.
[39] Moini, M., J. Olek, J.P. Youngblood, B. Magee, and P.D. Zavattieri, *Additive Manufacturing and Performance of Architectured Cement-Based Materials.* Adv Mater, 2018. 30(43): p. e1802123.
[40] George, T., V.S. Deshpande, and H.N.G. Wadley, *Hybrid carbon fiber composite lattice truss structures.* Composites Part a-Applied Science and Manufacturing, 2014. 65: p. 135-147.
[41] McCartney, L.N., *Analytical Methods of Predicting Performance of Composite Materials*, in *Failure and Damage Analysis of Advanced Materials*, H. Altenbach and T. Sadowski, Editors. 2015, Springer Vienna: Vienna. p. 191-254.
[42] Mori, T. and K. Tanaka, *Average Stress in Matrix and Average Elastic Energy of Materials with Misfitting Inclusions.* Acta Metallurgica, 1973. 21(5): p. 571-574.
[43] Halpin, J.C., *Stiffness and Expansion Estimates for Oriented Short Fiber Composites.* Journal of Composite Materials, 1969. 3(4): p. 732-&.
[44] Benveniste, Y., *A new approach to the application of Mori-Tanaka's theory in composite materials.* Mechanics of materials, 1987. 6(2): p. 147-157.
[45] Chow, T., *Effect of particle shape at finite concentration on the elastic moduli of filled polymers.* Journal of Polymer Science: Polymer Physics Edition, 1978. 16(6): p. 959-965.
[46] Ionita, A. and Y.J. Weitsman, *On the mechanical response of randomly reinforced chopped-fibers composites: Data and model.* Composites Science and Technology, 2006. 66(14): p. 2566-2579.
[47] Nazarenko, L., H. Stolarski, and H. Altenbach, *Effective properties of short-fiber composites with Gurtin-Murdoch model of interphase.* International Journal of Solids and Structures, 2016. 97-98: p. 75-88.
[48] Jain, A., S.V. Lomov, Y. Abdin, I. Verpoest, and W. Van Paepegem, *Pseudo-grain discretization and full Mori Tanaka formulation for random heterogeneous media: Predictive*

abilities for stresses in individual inclusions and the matrix. Composites Science and Technology, 2013. 87: p. 86-93.
[49] Böhm, H.J., A. Eckschlager, and W. Han, *Multi-inclusion unit cell models for metal matrix composites with randomly oriented discontinuous reinforcements.* Computational materials science, 2002. 25(1-2): p. 42-53.
[50] Pan, Y., L. Lorga, and A.A. Pelegri, *Analysis of 3D random chopped fiber reinforced composites using FEM and random sequential adsorption.* Computational Materials Science, 2008. 43(3): p. 450-461.
[51] Duschlbauer, D., H.J. Bohm, and H.E. Pettermann, *Computational simulation of composites reinforced by planar random fibers: Homogenization and localization by unit cell and mean field approaches.* Journal of Composite Materials, 2006. 40(24): p. 2217-2234.
[52] Tekinalp, H.L., V. Kunc, G.M. Velez-Garcia, C.E. Duty, L.J. Love, A.K. Naskar, C.A. Blue, and S. Ozcan, *Highly oriented carbon fiber-polymer composites via additive manufacturing.* Composites Science and Technology, 2014. 105: p. 144-150.
[53] Berger, H., S. Kari, U. Gabbert, R.R. Ramos, J.B. Castillero, and R.G. Diaz, *Evaluation of effective material properties of randomly distributed short cylindrical fiber composites using a numerical homogenization technique.* Journal of Mechanics of Materials and Structures, 2007. 2(8): p. 1561-1570.
[54] Saenger, E.H., *Numerical methods to determine effective elastic properties.* International Journal of Engineering Science, 2008. 46(6): p. 598-605.
[55] Kari, S., H. Berger, and U. Gabbert, *Numerical evaluation of effective material properties of randomly distributed short cylindrical fibre composites.* Computational materials science, 2007. 39(1): p. 198-204.
[56] Velmurugan, R., G. Srinivasulu, and S. Jayasankar, *Influence of fiber waviness on the effective properties of discontinuous fiber reinforced composites.* Computational Materials Science, 2014. 91: p. 339-349.
[57] Doghri, I. and L. Tinel, *Micromechanical modeling and computation of elasto-plastic materials reinforced with distributed-orientation fibers.* International Journal of Plasticity, 2005. 21(10): p. 1919-1940.
[58] Ogierman, W. and G. Kokot, *A study on fiber orientation influence on the mechanical response of a short fiber composite structure.* Acta Mechanica, 2016. 227(1): p. 173-183.
[59] Babu, K.P., P.M. Mohite, and C.S. Upadhyay, *Development of an RVE and its stiffness predictions based on mathematical homogenization theory for short fibre composites.* International Journal of Solids and Structures, 2018. 130: p. 80-104.
[60] Sukiman, M.S., T. Kanit, F. N'Guyen, A. Imad, A. El Moumen, and F. Erchiqui, *Effective thermal and mechanical properties of randomly oriented short and long fiber composites.* Mechanics of Materials, 2017. 107: p. 56-70.
[61] Bertoldi, K., P.M. Reis, S. Willshaw, and T. Mullin, *Negative Poisson's ratio behavior induced by an elastic instability.* Adv Mater, 2010. 22(3): p. 361-6.
[62] Rafsanjani, A., A. Akbarzadeh, and D. Pasini, *Snapping mechanical metamaterials under tension.* Adv Mater, 2015. 27(39): p. 5931-5.
[63] Shi, J. and A.H. Akbarzadeh, *3D Hierarchical lattice ferroelectric metamaterials.* International Journal of Engineering Science, 2020. 149: p. 103247.
[64] Shi, J., H. Mofatteh, A. Mirabolghasemi, G. Desharnais, and A. Akbarzadeh, *Programmable Multistable Perforated Shellular.* Adv Mater, 2021. 33(42): p. e2102423.

[65] Berger, J.B., H.N. Wadley, and R.M. McMeeking, *Mechanical metamaterials at the theoretical limit of isotropic elastic stiffness.* Nature, 2017. 543(7646): p. 533-537.
[66] Shi, J. and A.H. Akbarzadeh, *Architected cellular piezoelectric metamaterials: Thermo-electro-mechanical properties.* Acta Materialia, 2019. 163: p. 91-121.
[67] Sajadi, S.M., P.S. Owuor, S. Schara, C.F. Woellner, V. Rodrigues, R. Vajtai, J. Lou, D.S. Galvao, C.S. Tiwary, and P.M. Ajayan, *Multiscale Geometric Design Principles Applied to 3D Printed Schwarzites.* Adv Mater, 2018. 30(1): p. 1704820.
[68] Sun, G.Y., H. Jiang, J.G. Fang, G.Y. Li, and Q. Li, *Crashworthiness of vertex based hierarchical honeycombs in out-of-plane impact.* Materials & Design, 2016. 110: p. 705-719.
[69] Yang, Y., X. Song, X. Li, Z. Chen, C. Zhou, Q. Zhou, and Y. Chen, *Recent Progress in Biomimetic Additive Manufacturing Technology: From Materials to Functional Structures.* Adv Mater, 2018. 30(36): p. e1706539.
[70] Hassani, B. and E. Hinton, *A review of homogenization and topology optimization I - homogenization theory for media with periodic structure.* Computers & Structures, 1998. 69(6): p. 707-717.
[71] Hassani, B. and E. Hinton, *A review of homogenization and topology opimization II—analytical and numerical solution of homogenization equations.* Computers & Structures, 1998. 69(6): p. 719-738.
[72] Hollister, S.J. and N. Kikuchi, *A comparison of homogenization and standard mechanics analyses for periodic porous composites.* Computational Mechanics, 1992. 10(2): p. 73-95.
[73] Guedes, J.M. and N. Kikuchi, *Preprocessing and Postprocessing for Materials Based on the Homogenization Method with Adaptive Finite-Element Methods.* Computer Methods in Applied Mechanics and Engineering, 1990. 83(2): p. 143-198.
[74] Iorga, L., Y. Pan, and A. Pelegri, *Numerical Characterization of Material Elastic Properties for Random Fiber Composites.* Journal of Mechanics of Materials and Structures, 2008. 3(7): p. 1279-1298.
[75] Sigmund, O. and S. Torquato, *Design of materials with extreme thermal expansion using a three-phase topology optimization method.* Journal of the Mechanics and Physics of Solids, 1997. 45(6): p. 1037-1067.
[76] Andreassen, E. and C.S. Andreasen, *How to determine composite material properties using numerical homogenization.* Computational Materials Science, 2014. 83: p. 488-495.
[77] Mirabolghasemi, A., A.H. Akbarzadeh, D. Rodrigue, and D. Therriault, *Thermal conductivity of architected cellular metamaterials.* Acta Materialia, 2019. 174: p. 61-80.
[78] Akbarzadeh, A.H., J.W. Fu, L. Liu, Z.T. Chen, and D. Pasini, *Electrically conducting sandwich cylinder with a planar lattice core under prescribed eigenstrain and magnetic field.* Composite Structures, 2016. 153: p. 632-644.
[79] Soden, P.D., M.J. Hinton, and A.S. Kaddour, *Lamina properties, lay-up configurations and loading conditions for a range of fibre-reinforced composite laminates.* Composites Science and Technology, 1998. 58(7): p. 1011-1022.
[80] Bergman, T.L., T.L. Bergman, F.P. Incropera, D.P. Dewitt, and A.S. Lavine, *Fundamentals of heat and mass transfer*. 2011: John Wiley & Sons.
[81] Reddy, J.N., *Mechanics of laminated composite plates : theory and analysis*. 1997, Boca Raton: CRC Press.

Link between Chapter 3 and Chapter 4

Chapter 3 of this thesis (Paper 2) provided a comprehensive understanding of the thermomechanical properties of short fiber-reinforced composites and offered valuable insights for enhancing architected fiber-reinforced composite properties through the use of multi-materials. However, in order to fully comprehend the impact of incorporating short fibers, particularly wood fibers, on the flexural properties of beams (as a structural demonstrator), additional investigations are required. Furthermore, it is crucial to explore the potential of employing the methodology introduced in Chapter 3 to design and fabricate cells using multi-materials, with the aim of achieving tailored mechanical properties to enhance the flexural characteristics of beams. The outcomes of these further investigations are presented in Paper 3, which is detailed in Chapter 4 of this thesis.

4 Chapter Four: 3D Printed Wood Fiber-reinforced Architected Cellular Composite Beams with Engineered Flexural Properties[3]

Abstract

Enhancing the flexural-mechanical properties of bio-based polymers by the introduction of cellulose-based (wood) compounds paves the way for developing sustainable materials with better properties. In this thesis, linear elastic flexural properties of sustainable (3D) printed polylactic-acid (PLA) composites reinforced with different amounts of waste wood fiber are investigated. First, wood fiber-reinforced filaments (WF-PLA) with a variety of waste wood fiber weight percentages (2.5, 5, 10 and 15%) are produced, and then test samples are 3D printed using a dual extruder FDM printer. The experimental results demonstrate the possibility of achieving increased flexural modulus (60%), flexural rigidity (72%), flexural strength (39%), flexural failure strain (21%) and reduced overall density (4.5%) of the composite coupons with the addition of wood fiber into the neat PLA polymer. In addition, following the growing interest in architected cellular solids, 2D architected composite cells with only one or two reflection symmetries consisting of composites members with different fiber contents are designed to show not only enhanced flexural rigidity but also engineered quasi-isotropic flexural rigidity. The isotropicity ratio (EI_{yy}/EI_{xx}) of the designed cell beam in bending is investigated by analytical and numerical analysis as well as experimental tests. The resulting numerical simulation indicates a 30% increase in the isotropicity

[3]*Reproduced with permission from Ehsan Estakhrianhaghighi, Armin Mirabolghasemi, Larry Lessard, Abdolhamid Akbarzadeh, Engineered Flexural Properties of 3D Printed Wood-fiber Reinforced Architected Cellular Composite, Submitted to Additive Manufacturing, June 2023.*

ratio. WF-PLA filaments are used to 3D print the engineered quasi-isotropic cellular beams (*Isoflex*) consisting of members made using different wood fiber percentages. WF-PLA *Isoflex* cell exhibits an enhanced specific flexural rigidity (bending rigidity-to-mass ratio) of 30% to 130% and bending isotropicity ratio increases by 96% to 99% compared to the pure PLA. Wood fiber-reinforced engineered cellular composites offer a sustainable strategy to additively manufacture materials with enhanced and rationally engineered mechanical properties.

4.1 Introduction

Architected cellular solids are one of the novel classes of lightweight, energy-efficient materials with advanced properties. Their unique properties (such as high strength-to-mass ratio, high energy absorption capability and tunable multiphysics properties) stem from their logically designed underlying architectures (such as cell topology and cell connectivity) and the properties of their constituent materials [1, 2]. Cellular solids, also known as cellular metamaterials, have lately been identified for their prospective applications in the aerospace, automotive, energy, robotics and biomedical industries as high-performance noise reduction panels, energy absorbers, cores of sandwich beams and lightweight morphing structures, to name a few [3].

With the increasing demand and rising manufacturing costs of synthetic polymers and the growing advances in 3D printing, interchangeably called additive manufacturing (AM), scientists have recently focused on the 3D printing of low-cost and sustainable materials, as well as enhancing the quality of these materials. The key advantages of 3D printing include fast prototyping, material savings, waste minimization, design flexibility, and the ability to fabricate complicated architectures [4]. 3D printing is a manufacturing technology that uses a CAD model and is capable of creating free-form materials and structures. Several studies have been conducted to study the relationships between different mechanical properties and 3D-printed architected

materials [5]. The majority of these investigations have been on biodegradable Polylactic Acid (PLA) polymer [6, 7] due to its ease of manufacture, low production costs and biodegradability [8]. Recent advances in 3D printing technology have created potential for reinforcing PLA with fibers to 3D print fiber-reinforced composites with improved mechanical properties [9]. Furthermore, there has been a rising interest in the development of natural-based composites as recyclable, biodegradable and renewable materials [10, 11]. The sustainable natural fibers derived from wood and plants (e.g., bamboo, flax and jute) are compatible with bio-based matrices and thus can potentially be considered as fiber reinforcement for such matrix materials.

Recent studies on WF-PLA composite materials, produced by combining low-cost waste wood fiber into a thermoplastic polymer matrix (PLA), have shed light on strategies for designing and realizing advanced materials with controlled material composition and architectural complexity [6]. The addition of readily available waste wood fibers leads to lower material manufacturing costs and improved thermomechanical properties (such as elasticity, ultimate strength and thermal conductivity) of the plain polymer [6, 12]. While wood waste is commonly utilized for heating applications with inefficient combustion, using these residues in polymer composite manufacturing would broaden their application area and value [13]. The WF-PLA composite material can be transformed into 3D printing filament and used for additive manufacturing methods, such as fused deposition modeling (FDM), as an alternative to traditional composite manufacturing methods such as injection molding and hot pressing [14]. FDM is one of the most widely used 3D printing methods owing to its simplicity, reliability, affordability (low waste, low processing and operational costs), multi-material (multi-nozzle) printing potential and adaptation to new materials and composites [15]. Developing studies are being conducted to improve the printing performance of 3D-printed WF-PLA composites. Recent research has

concluded that the type and proportion of wood fibers in the filaments have a substantial impact on the performance of the printed composites [16]. It is also shown that WF-PLA composites containing certain amounts of wood fibers significantly offset the drawbacks of the PLA polymer (such as inherent brittleness, low strength, stiffness and toughness) while reducing final production costs and providing 3D printed products with a sustainable aspect [6].

Producing architected cellular composites with controllable flexural properties using biological resources (i.e., bio-based PLA) and waste materials (i.e., wood fibers) can be a critical step in the development of sustainable design and manufacturing of high-performance materials. Despite a great deal of attention, there are limited studies on the development of 3D printed natural fiber-reinforced PLA composite [17]; hence, more research on the effect of type of filler and additive proportions on the thermomechanical properties of the 3D printed parts is required. Furthermore, to the best of the author, no research has been conducted on the application of waste wood fiber on the rational design of 3D-printed WF-PLA composite beams with desired flexural properties. On the other hand, recent advances in additive manufacturing technology have resulted in the fabrication of lightweight fiber-reinforced cellular composite with enhanced mechanical properties [18-20].

This thesis aims to introduce sustainable, load-bearable and low-cost architected natural-based composites with controllable flexural mechanical properties. This is done *first* by investigating the effect of adding wood fibers to PLA on the flexural properties (i.e., flexural modulus, rigidity, strength and failure strain) of 3D printed samples and *second* by developing novel multi-material quasi-isotropic cellular beams with engineered cell topology and engineered material composition distribution (i.e., different wood-to-PLA weight percentage for different members of the cell) to surpass the single material cellular beam counterpart and exhibit isotropic

flexural modulus. Section 4.2 presents the manufacturing process for wood fiber-reinforced polylactic acid (WF-PLA) composite filaments, in which PLA powder, a bio-based matrix, is mixed with wood fibers in various weight percentages (2.5, 5, 10 and 15%) and extruded through a single filament extruder to make biocomposite filaments that are fed into the double extruder FDM 3D printer to fabricate test samples. Section 4.3 analyzes the flexural mechanical properties of 3D printed sustainable composite samples using three-point bending tests to compare their performance with that of pure PLA and describes a systematic approach for designing multi-material cellular beams with isotropic bending behavior based on 2D cellular architectures with only one or two reflection symmetries, as well as a comparison of their properties to those made out of single material. Finally, the designed multi-material cells are 3D printed by filament made of different percentages of wood with double extruder FDM 3D printers to be examined through experimental testing. Detailed finite element modeling (FEM) is performed to supplement the experimental results on these quasi-isotropic cellular solids.

This research reveals that an optimum wood fiber content can increase flexural modulus, rigidity, strength and failure strain of the WF-PLA material, while simultaneously decreasing the material density leading to the design and fabrication of lightweight advanced materials with enhanced flexural mechanical properties. Furthermore, the engineered cellular beams made using multi-wood-to-PLA percentages demonstrate enhanced bending rigidity and present isotropic flexural properties compared to those made out of pure PLA. This thesis showcases the possibility of developing high-performance renewable advanced materials by using low-cost and scrap materials through an engineered microarchitectural design.

4.2 Experimental section

4.2.1 Material specification and processing of WF-PLA composite filament

In this thesis, WF-PLA composite filaments are made using pulverized PLA-4043D (supplied by FILABOT, Barre VT, USA) (Detailed specifications on PLA-4043D are provided in **Table 4-S1,** Section 4.5.1, Supporting Information) and wood fibers extracted from a recycled woodblock (supplied by CANAWICK, Saint-Quentin NB, Canada, more information is given in Section 4.5.1, Supporting Information). It is worth mentioning that the properties of this thesis's WF-PLA composites (filament and architected cellular materials) are compared with those made out of pure PLA-4043D and a commercial white PLA filament (supplied by *Shop3D.Ca*, detailed specifications on white PLA filament are given in **Table 4-S1**, Section 4.5.1, Supporting Information). A single screw extruder Filabot EX2 (*FILABOT, Barre VT, USA*, detailed specifications are given in **Table 4-S2**, Section 4.5.2, Supporting Information) is utilized in this research to produce WF-PLA composite filaments with different weight percentages 2.5, 5, 10 and 15 *wt%*, following Ref. [6], where the wood fiber weight percentage is calculated by:

$$wt\% = \frac{M_w}{M_w + M_{PLA}} \tag{4.1}$$

The 2.8 ± 0.1 mm filament diameter is achieved by adjusting the extrusion and spooler pulling speed of the Filabot extruder to make the filament compatible with the Ultimaker S3 double extruder FDM printer (*Ultimaker B.V, Massachusetts 01701, USA*, detailed specifications are given in **Table 4-S2**, Section 4.5.2, Supporting Information). This process is schematically shown in **Figure 4-1**.

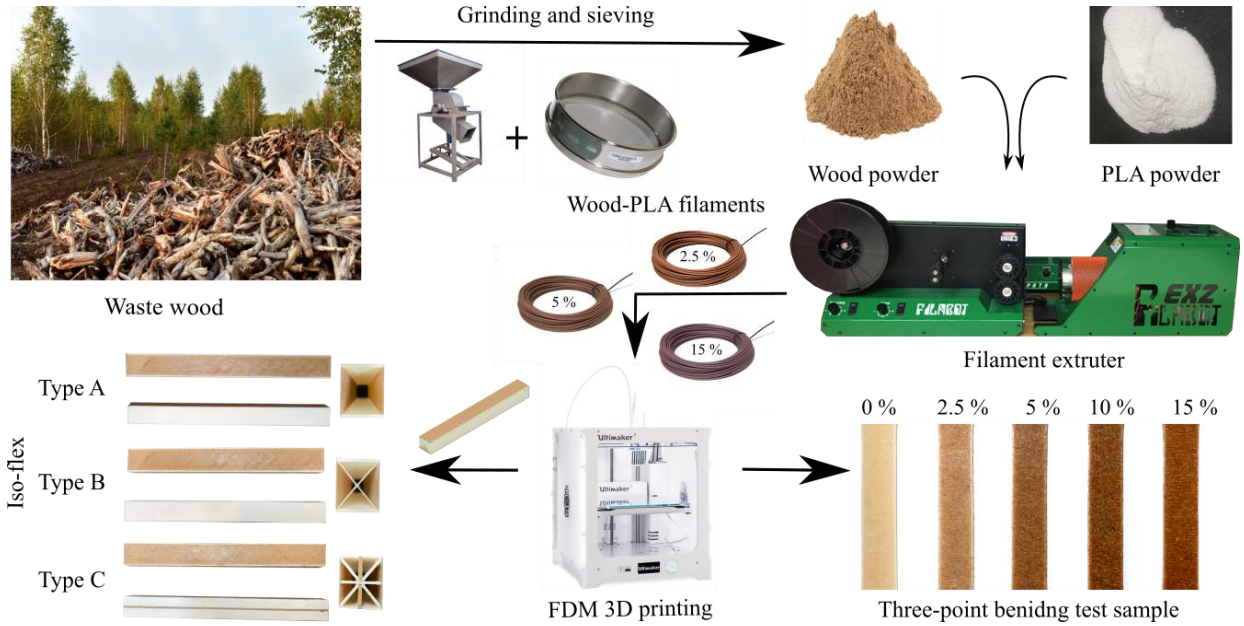

Figure 4 - 1: WF-PLA filament fabrication process and FDM 3D printed three-point bending test specimens.

4.2.2 3D printing and testing setup of WF-PLA composite samples

3D models are created in SolidWorks and imported to UltiMaker Cura (version 5.2.2) to be 3D printed by Ultimaker S3. A variety of 3D printing settings (e.g., extruding and bed temperatures, layer thickness, printing speed and nozzle diameter) are tuned to optimize the quality of the 3D printed parts. A summary of the final settings is provided in **Table 4-1**. Different temperatures are employed for filament extrusion due to the varying viscosities of wood and molten PLA mixtures with different wood percentages. Although manufacturing parameters are shown to play an important role in the structural behavior of the FDM 3D printed parts [21, 22], in this thesis, the investigation focuses on the effect of material composition and cell topology on the structural properties of 3D printed composite parts. Therefore, all manufacturing parameters are kept identical for the 3D printing of all specimens.

Following ASTM D790 standard, at least five cuboids samples ($3.2\times12.7\times64$ mm^3) are 3D printed with linear (0/±45/90 in-plane orientation) infill pattern for each type of the considered

filaments (i.e., pure PLA, WF-PLA with 2.5, 5, 10, 15 *wt%* and commercial white PLA for comparison) as shown schematically in **Figure 4-1**. Three-point bending tests are then conducted using an ADMET mechanical test machine with an MTESTQuattro (*ADMET, Norwood, MA, USA*) testing control system equipped with a 20 KN load cell. Samples are stored under a standard laboratory atmosphere condition (23°C and 50% relative humidity) for 40 hours before testing, and tests are performed with a 3N preload under a 5mm/min test speed condition.

Table 4 - 1: Manufacturing parameters for specimen 3D printing.

Filament type	Printing temperature [˚C]	FDM 3D printing parameter	Value
Commercial White PLA	210	Layer height [mm]	0.2
Pure PLA	190	Bed temperature [˚C]	70
2.5% WF-PLA	190	Maximum print speed [mm/min]	35
5% WF-PLA	185	Nozzle diameter [mm]	0.8
10% WF-PLA	180	Filament diameter [mm]	2.8 ± 0.1
15% WF-PLA	180	Infill (%)	100

The flexural stress, strain at outer surface and modulus and rigidity of the samples are calculated using the extracted force-displacement curves and the following equations for a simply supported beam with rectangular ($b \times d$) cross-section [23]:

Flexural stress at outer surface (MPa) $$\sigma_f = \frac{3Fl}{2bd^2} \quad (4.2a)$$

Flexural strain at outer surface (mm/mm) $$\varepsilon_f = \frac{6\delta d}{l^2} \quad (4.2b)$$

Flexural modulus (MPa) $$E_f = \frac{\sigma_f}{\varepsilon_f} = \frac{l^3}{4bd^3}\, m \quad (4.2c)$$

Flexural rigidity (N.mm2) $$(EI)_f = \frac{l^3}{48}\, m \quad (4.2d)$$

where F and δ are the load (N) and deflection (mm) at the middle of the beam, $m = \frac{F}{\delta}$ is the slope of the initial linear elastic portion of the load-deflection curve (N/mm) and l, b and d are the beams' support span, width and depth or thickness in (mm), respectively. The flexural strength and failure

strain of the outer surface can be determined by applying the maximum force (F_{max}), and the corresponding deflection (δ), into Eq. (4.2a) and (4.2b), respectively.

4.2.3 Engineered cellular WF-PLA composite

Previous sections introduced a feasible and low-cost methodology for improving the sustainability and flexural properties of 3D-printed PLA products by utilizing WF-PLA filaments. Taking cellular-based *mechanical metamaterials* with anomalous properties (e.g., negative Poisson's ratio [24], negative incremental stiffness [25] and ultrahigh multifunctional figures of merits [26-30]) as a model, the architectural topology and material composition of wood fiber-reinforced composite matter can be engineered to further tune and enhance the flexural properties of a WF-PLA beam with respect to its mass.

To achieve efficient and multifunctional controllable cellular materials, it is critical to optimize and potentially differentiate the rigidity of cell members. While manipulating a member's rigidity can be achieved by changing its base material and thickness, controlling the stiffness by modifying fiber characteristics such as fiber volume fraction and orientation offers benefits, including improved adhesion between cell parts/layers constructed from the same matrix with differing fiber characteristics, ultimately resulting in superior overall mechanical properties and manufacturability [31]. Additionally, this approach puts forward the strategy to increase the effective flexural rigidity without increasing the relative density or mass. Following these advantages, in this section, multi-material cellular beams based on 2D cellular architectures with only one or two reflection symmetries are designed to show isotropic flexural rigidity, in which the required different rigidity of cell members is achieved by tuning their fiber content and thickness. Considering that cellular architectures generally have complex geometries that are not manufacturable using conventional methods, fused deposition modeling (FDM) 3D printing using

fiber-reinforced materials based on the same matrix medium offers a feasible approach for fabricating these complex architectures.

This thesis adopts an analytical methodology to develop novel multi-material cellular architectures with isotropic bending rigidity (*Isoflex*) by engineering cell topology and members' material composition. **Figure 4-2** shows the four types of multi-material *Isoflex* cells investigated in this thesis as follows:

Type A: Rectangular *Isoflex* composite cell made out of two material compositions.

Type B: Rectangular *Isoflex* composite cell with two additional diagonal members made out of three material compositions.

Type C: Rectangular *Isoflex* composite cell with two additional horizontal, vertical and diagonal members made out of three material compositions.

Type D: *Isoflex* composite cell with only one reflection symmetry made out of two material compositions.

The isotropic bending conditions are derived by equalizing the flexural rigidity of the idealized *Isoflex* cells in *x* and *y* directions and solving for the members' thicknesses and modules of elasticities. After a brief review of the adopted methodology, in the next sections, the *Isoflex* cellular composites are 3D printed out of WF-PLA, and a series of experimental tests and numerical studies are conducted to elicit the effect of the rationally designed cell microarchitecture and material composition on optimizing the bending performance of cellular composite beams.

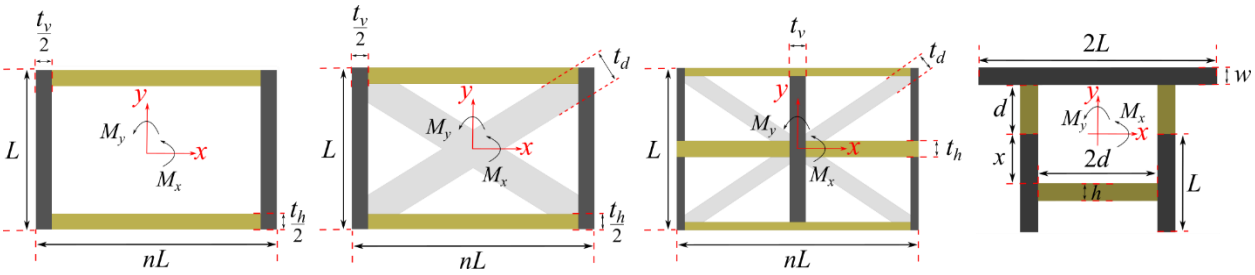

Figure 4 - 2: Non-square *Isoflex* composite cell with n = 1.5: different colors represent different materials (Type *A* to *D*).

Considering the anisotropic behavior of non-square cells and cells with only one reflection symmetry in bending, a 2D cellular architecture with isotropic flexural rigidity properties is designed here based on those cells. The idea is developed by tuning the wall thickness and the material (wood fiber content percentage) of the members and introducing additional horizontal, vertical and diagonal bracing members to reduce the directionality of flexural rigidity properties of the cell (mathematically expressed by $I_{xx} = I_{yy}$ and $I_{xy} = 0$). The conditions for the designed multi-material cellular architecture to have isotropic flexural rigidity are given in **Table 4-2**.

Table 4 - 2: Calculating the Flexural Rigidity of an *Isoflex* cell.

Flexural Rigidity		**Cell Type A**
EI_{xx}	$(EI_{xx})_h$	$E_h \frac{t_h\left(\frac{1}{3}{t_h}^2 + (L+L_1)^2\right)L_2}{16}$
	$(EI_{xx})_v$	$n_{vh}E_h\frac{t_v L^3}{12}$
EI_{yy}	$(EI_{yy})_h$	$E_h\frac{t_h(L_2)^3}{12}$
	$(EI_{yy})_v$	$n_{vh}E_h\frac{Lt_v\left(\frac{1}{3}{t_v}^2 + (nL+L_2)^2\right)}{16}$
If $EI_{xx} = EI_{yy}$ then $(I_{xx})_h + n_{vh}(I_{xx})_v - (I_{yy})_h - n_{vh}(I_{yy})_h = 0$		

Flexural Rigidity	**Cell Type B**

EI_{xx}	$(EI_{xx})_h$	$E_h \frac{t_h L_2}{16}\left(\frac{{t_h}^2}{3} + (L + L_1)^2\right)$
	$(EI_{xx})_v$	$n_{vh} E_h \frac{L^3 t_v}{12}$
	$(EI_{xx})_d$	$\frac{n_{dh}E_h}{18L_1(L_2)^4}\Big\{1.5(L_1)^4(L_2)^5 - 0.25\Big(td\sqrt{(L_1)^2 + (L_2)^2} - L_1L_2\Big)^3\Big(t_dL_2\sqrt{(L_1)^2 + (L_2)^2} - L_1(L_2)^2\Big) - 0.25\Big(t_d\sqrt{(L_1)^2 + (L_2)^2} - L_1L_2\Big)\Big(t_dL_2\sqrt{(L_1)^2 + (L_2)^2} - L_1(L_2)^2\Big)\Big(\Big(t_d\sqrt{(L_1)^2 + (L_2)^2} - L_1L_2\Big)^2 + \Big(t_d\sqrt{(L_1)^2 + (L_2)^2} + 2L_1L_2\Big)^2\Big)\Big\}$
EI_{yy}	$(EI_{yy})_h$	$E_h \frac{t_h (L_2)^3}{12}$
	$(EI_{yy})_v$	$n_{vh} E_h L t_v \frac{\frac{{t_v}^2}{3} + (nL + L_2)^2}{16}$
	$(EI_{yy})_d$	$\frac{n_{dh}E_h}{18(L_1)^3(L_2)^4}\Big\{1.5(L_1)^4(L_2)^7 - 0.25\Big(t_d\sqrt{(L_1)^2 + (L_2)^2} - L_1L_2\Big)\Big((L_2)^2\Big(t_d\sqrt{(L_1)^2 + (L_2)^2} + 2L_1L_2\Big)^2 + \Big(t_dL_2\sqrt{(L_1)^2 + (L_2)^2} - L_1(L_2)^2\Big)^2\Big)\Big(t_dL_2\sqrt{(L_1)^2 + {L_2}^2} - L_1(L_2)^2\Big) - 0.25\Big(t_d\sqrt{(L_1)^2 + (L_2)^2} - L_1L_2\Big)\Big(t_dL_2\sqrt{(L_1)^2 + (L_2)^2} - L_1(L_2)^2\Big)^3\Big\}$

If $EI_{xx} = EI_{yy}$ then $(I_{xx})_h + n_{vh}(I_{xx})_v + n_{dh}(I_{xx})_d - (I_{yy})_h - n_{vh}(I_{yy})_v - n_{dh}(I_{yy})_d = 0$

Flexural Rigidity		**Cell Type C**
EI_{xx}	$(EI_{xx})_h$	$E_h \frac{th\left(\frac{5}{3}{t_h}^2 + (L + L_1)^2\right)L_2}{16}$
	$(EI_{xx})_v$	$n_{vh}E_h \frac{t_v(L_1)\left(\frac{5}{3}(L_1)^2 + (L + t_h)^2\right)}{16}$
	$(EI_{xx})_d$	$n_{dh}E_h \frac{-(n^2+1)^{\frac{3}{2}}}{144n^3}\Bigg(-n^3(L_1 - t_h)\frac{9L^2(L_2 - t_v) + (L_1 - t_h)^2(3nL - 6t_v)}{(n^2+1)^{\frac{3}{2}}} + 2\Big(\Big(t_d + \frac{t_v}{\sqrt{n^2+1}} + 2n\frac{L_1}{\sqrt{n^2+1}}\Big)^2 + \Big(t_d + t_v\frac{1}{\sqrt{n^2+1}} - n\frac{L + 2t_h}{\sqrt{n^2+1}}\Big)^2\Big)\Big(t_d + \frac{t_v}{\sqrt{n^2+1}} - \frac{nL_1}{\sqrt{n^2+1}}\Big)\Big(-nL_1 + t_d\sqrt{n^2+1} + t_v\Big) + 2\Big(t_d + \frac{t_v}{\sqrt{n^2+1}} - \frac{nL_1}{\sqrt{n^2+1}}\Big)^3\Big(-nL_1 + t_d\sqrt{n^2+1} + t_v\Big)\Bigg)$
EI_{yy}	$(EI_{yy})_h$	$E_h \frac{t_h L_2\left(\frac{5}{3}(L_2)^2 + (nL + t_v)^2\right)}{16}$
	$(EI_{yy})_v$	$n_{vh}E_h \frac{t_v L_1\left(\frac{5}{3}{t_v}^2 + (nL + L_2)^2\right)}{16}$

	$(EI_{yy})_d$	$n_{dh}E_h\frac{-\sqrt{n^2+1}}{144n}\Big((-n)(L_2-t_v)\frac{9L^2n^2(L_1-t_h)+(3L-6t_h)(L_2-t_v)^2}{\sqrt{n^2+1}}+2\Big((nL-nt_h-t_d\sqrt{n^2+1}+2t_v)^2+(2nL+nt_h+t_d\sqrt{n^2+1}-2t_v)^2\Big)\Big(t_d+t_v\frac{1}{\sqrt{n^2+1}}-\frac{nL_1}{\sqrt{n^2+1}}\Big)(-nL_1+t_d\sqrt{n^2+1}+t_v)+2\Big(t_d+t_v\frac{1}{\sqrt{n^2+1}}-\frac{nL_1}{\sqrt{n^2+1}}\Big)(-nL_1+t_d\sqrt{n^2+1}+t_v)^3\Big)$
If $EI_{xx}=EI_{yy}$ then $(I_{xx})_h+n_{vh}(I_{xx})_v+n_{dh}(I_{xx})_d-(I_{yy})_h-n_{vh}(I_{yy})_v-n_{dh}(I_{yy})_d=0$		

* $n_{vh}=E_v/E_h$, $n_{dh}=E_d/E_h$, $L_1=L-t_h$, $L_2=nL-t_v$

Using the cell's flexural rigidity (EI about the *x*- and *y*-axis, the flexural rigidity isotropy of the *Isoflex* cellular beam is assessed by calculating the anisotropicity ratio ($\alpha=EI_{yy}/EI_{xx}$), which is unity for materials with isotropic flexural rigidity. Three different moduli of elasticity and thickness for the horizontal, vertical and diagonal members are considered (**Figure 4-2**). It is worth mentioning that due to the inherent symmetry of the selected cell architecture, $I_{xy}=0$, and hence if $I_{xx}=I_{yy}$ the cell shows the same flexural rigidity equal to $\frac{EI_{xx}+EI_{yy}}{2}=EI_{xx}=EI_{yy}$ in all arbitrary directions θ based on the Mohr circle [23]:

$$I_\theta=\frac{I_{xx}+I_{yy}}{2}+\frac{I_{xx}-I_{yy}}{2}\cos 2\theta-I_{xy}sin2\theta \tag{4.3}$$

The slender cell members can also be made out of anisotropic materials, and since the mechanical behavior of these two-force members is mainly governed by the effective Young's moduli of their constituent solids along their length, without losing generality and accuracy, hypothetical isotropic mechanical behaviors (equivalent to the longitudinal mechanical properties of the members) are assumed instead of anisotropic properties. Furthermore, the effect of Poisson's ratio can be neglected in a two-force member when the member is slender and its cross-sectional dimensions are relatively small compared to its length [23].

The equations given in **Table 4-2** can be extended for cellular beams containing more than one cell in their cross-sections. The cross-section of the chosen multi-cell beam exhibits intrinsic

symmetry, leading to a moment of inertia value of zero in the *xy*-plane ($I_{xy} = 0$). The criterion for achieving isotropic rigidity in a beam featuring $k_x \times k_y$ *Isoflex* cells in its cross-section involves equating EI_{xx} and EI_{yy} as outlined below:

$$EI_{xx} = k_x\left[k_y(EI_{xx}^0) + L^2AS_x\right] \tag{4.4a}$$

$$EI_{yy} = k_y\left[k_x(EI_{yy}^0) + n^2L^2AS_y\right] \tag{4.4b}$$

$$k_x\left[k_y(EI_{xx}^0) + L^2AS_x\right] - k_y\left[k_x(EI_{yy}^0) + n^2L^2AS_y\right] = 0 \tag{4.4c}$$

where (EI^0) is the bending rigidity for a single cell (given in **Table 4-2**), and *A*, S_x and S_y are calculated in **Table 4-3**.

Table 4 - 3: Values of the parameters in Eq. (4.4).

Parameter		**Value**
S_x	k_y odd	$2\sum_0^{\frac{k_y-1}{2}} i^2$
	k_y even	$\frac{1}{2}\sum_1^{\frac{k_y}{2}}(2i-1)^2$
S_y	k_x odd	$2\sum_0^{\frac{k_x-1}{2}} i^2$
	k_x even	$\frac{1}{2}\sum_1^{\frac{k_x}{2}}(2i-1)^2$
A	Type A	$E_h[L_2t_h + n_{vh}Lt_v]$
	Type B	$E_h\left[n_{vh}Lt_v + L_2t_h + n_{dh}L_2L_1(1 - \left(\frac{t_d\sqrt{\left(\frac{L_2}{L_1}\right)^2 + 1}}{L_2} - 1\right)^2)\right]$
	Type C	$\frac{E_h}{n}\left[2n(n_{vh}t_vL_1 + t_hL_2) + n_{dh}(n(L_1 - t_h)(L_2 - t_v) - (-nL_1 + t_d\sqrt{n^2+1} + t_v)^2)\right]$

* $n_{vh} = E_v/E_h$, $n_{dh} = E_d/E_h$, $n_{dv} = E_d/E_v$, $L_1 = L - t_h$, $L_2 = nL - t_v$

To show the methodology's versatility, a 2D cellular architecture cell with only one reflection

symmetry (Type D) is chosen to show isotropic flexural rigidity properties by adjusting the members' thickness and the material (wood fiber content percentage). The presence of a single reflection symmetry in the selected cell architecture results in zero rigidity in the *xy* plane. To achieve isotropic bending rigidity, it is necessary to ensure equal rigidity around both the x and y axes, which can be determined by the following condition:

$$Lw\left(d+\frac{w}{2}-\frac{L}{2}\right)+n_{12}dh\left(\frac{d}{2}-x-\frac{h}{2}\right)=0 \tag{4.5}$$

where *L*, *w*, *d*, *x* and h are the dimensions shown in **Figure 4-2** and the module of elasticity ratio of material 1 to 2 is presented by n_{12}.

Section 4.3.3.1 verifies predictions of the analytical equations for multiple *Isoflex* composite cells with detailed numerical analysis and experimental tests.

4.2.4 3D printing and testing setup of architected cellular WF-PLA composite beam samples

To characterize the flexural rigidity of the developed architected cellular materials, cellular beams for three-point bending tests are 3D printed according to the process demonstrated in Section 4.2.2. Samples made of two materials (i.e., white PLA and WF-PLA 5 *wt%*) are 3D printed using a dual extruder Ultimaker FDM printer and bonded as shown in **Figure 4-3**, in which wall thicknesses of the WF-PLA horizontal members, white PLA diagonal members and white PLA vertical members are shown as t_h, t_d and t_v, respectively. The manufacturing limitations of the Ultimaker FDM printer for the minimum wall thickness of the cell members in the beam cross-section and the maximum beam length have implications for experimental testing accuracy. In this thesis, a beam thickness is chosen that is one-tenth of the beam length to minimize the error in the experimental results. The specific values selected for the beam thickness and length are 19.18 mm

and 191.8 mm, respectively.

Figure 4-3 also presents some possible combinations of geometrical features (i.e., t_h, t_v, t_d and *n*) for *Isoflex* cells of type A to C made of 5 *wt%* WF-PLA for horizontal members and white PLA for other members ($n_{vh} = n_{dh} = 0.4$) and the beam thickness of 19.18 mm. The manufacturing process for 3D printing places a constraint on the minimum value of t_h, which should be 1.6 mm due to the 0.8 mm nozzle used for printing 5 *wt%* WF-PLA. Additionally, the minimum values for t_v and t_d should be 0.5 mm and 0.25 mm, respectively, as the 0.25 mm nozzle is used for printing the vertical and diagonal members. To show the maximum isotropicity ratio improvement, the dimensions provided in **Table 4-4** are selected for the test samples while considering the manufacturing limitations.

At least three replicas are 3D printed for each of the single-material and multi-material *Isoflex* cellular beams out of the white PLA and 5 *wt%* WF-PLA filaments. The 3D-printed architected cellular beam specimens are all 191.8 mm long, which is the maximum possible printing height for Ultimaker FDM printer. To keep the printing and testing conditions consistent, 3D printing parameters are chosen based on **Table 4-1**, and test settings mentioned in Section 4.2.2 are used for the bending tests and measuring the rigidity of the cellular specimens using the extracted force-displacement curves and Eq. (4.2d). The experimental results are compared to the detailed numerical simulations in Section 4.3.3.2 to evaluate the consistency.

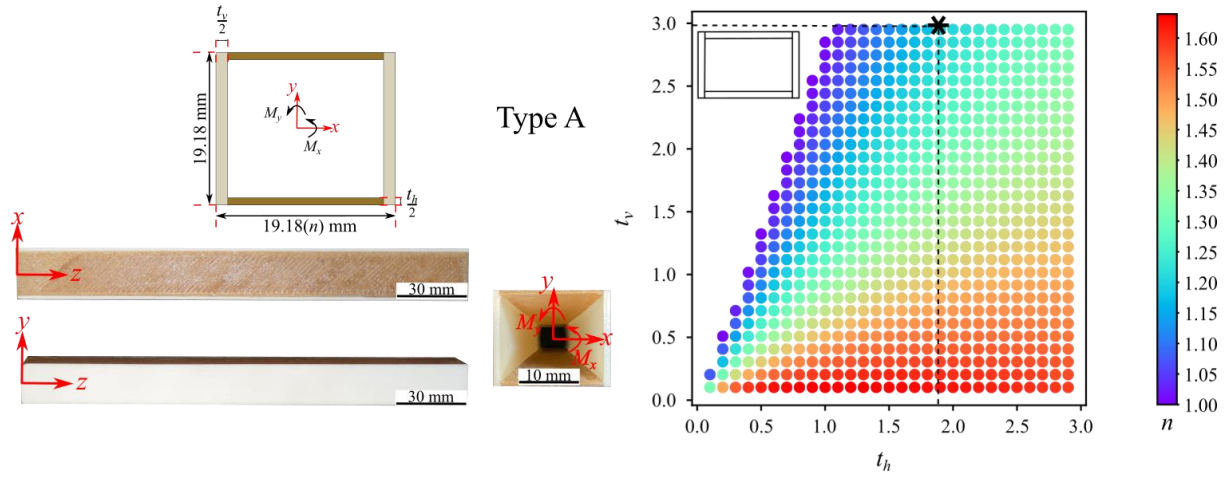
Type A
19.18 mm
19.18(n) mm
30 mm
10 mm
t_v
t_h
n

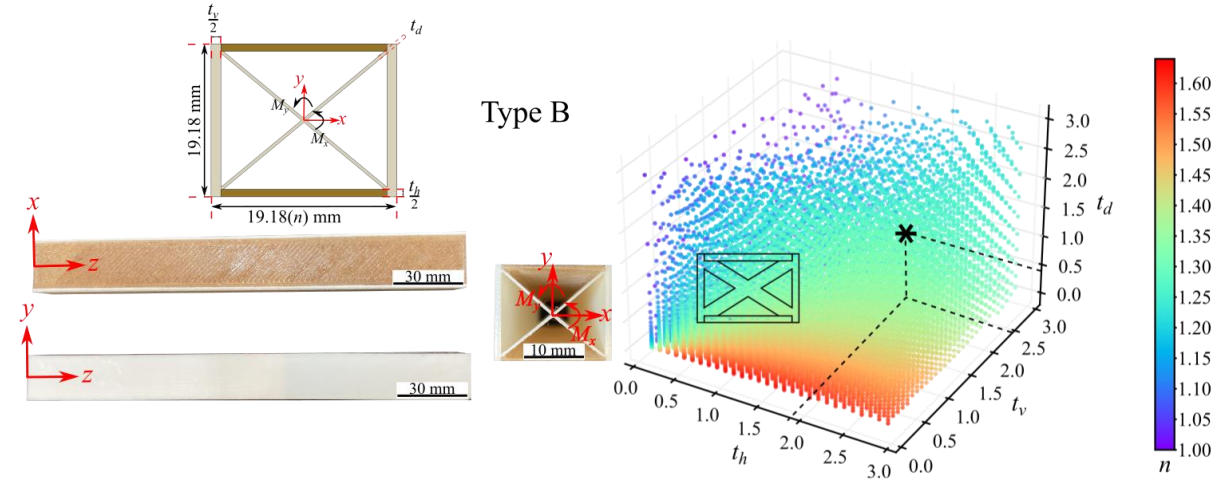
Type B
19.18 mm
19.18(n) mm
30 mm
10 mm
t_v
t_h
t_d
n

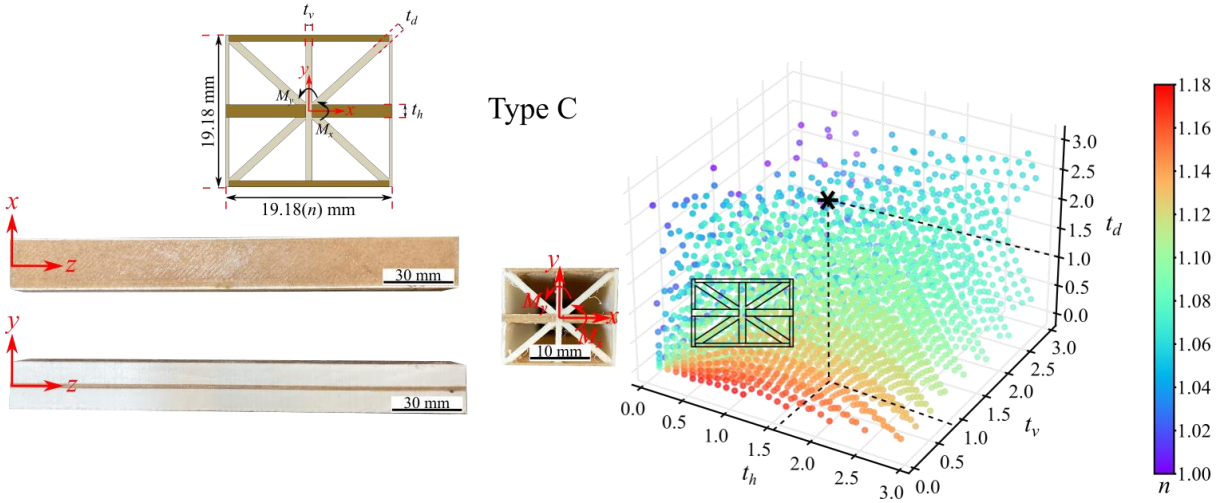
Type C
19.18 mm
19.18(n) mm
30 mm
10 mm
t_v
t_h
t_d
n

Figure 4 - 3: Correlation between the design parameters and 3D printed WF-PLA *Isoflex* cellular samples made out of white PLA and 5 *wt%* WF-PLA filaments. The symbol (*) in the figures represents the geometrical specifications of the design used for conducting experiments.

Table 4 - 4: Geometrical and material composition parameters for *Isoflex* experiment specimen.

Cell type	L(mm)	n	t_h (mm)	t_v (mm)	t_d (mm)	n_{vh}	n_{dh}
Type A	19.18	1.18	1.86	2.99	-	0.4	-
Type B	19.18	1.22	1.9	2.49	0.4	0.4	0.4
Type C	19.18	1.10	1.6	0.8	1.0	0.4	0.4

* $n_{vh} = E_v/E_h$, $n_{dh} = E_d/E_h$

4.2.5 Detailed finite element modeling of *Isoflex* cellular composite beams under a three-point bending test

In this research, a detailed numerical simulation (implemented in Abaqus ver.2019) on the as-designed cellular structure model is conducted to examine the discussed analytical findings and experimental results. Four types of the *Isoflex* cellular composite beams are modeled in SolidWorks, while the dimensions and materials of the modeling are chosen based on **Table 4-2**. To verify the numerical analysis by the experimental results, the mechanical properties of the base materials are imported in Abaqus from results obtained from the tensile tests on the 3D printed dogbone samples (**Figure 4-S1**, Section 4.5.3, Supporting Information).

To investigate the mechanical behavior of a solid structure under static loading conditions, an 8-node linear brick element (C3D8R) type is selected as the basis for the numerical model. The mesh size is chosen to ensure sufficient spatial resolution, with a minimum of two mesh elements spanning the structure's thickness. Three-point bending test simulations with loading along the Y-axis are completed using a stress analysis (Finite Element Analysis) tool. Loads and constraints are first assigned on the bottom and top of cellular samples resembling the real three-point bending test (i.e., the supports at the bottom of the sample are assumed to be fixed, and the displacement load at the rate of 5 mm.min^{-1} is applied to the middle of the sample top surface). The reaction

force of the beams along the Y direction is then obtained, and finally, the bending rigidity of the samples is calculated using the force-displacement curve and Eq. (4.2d). Considering the goal of obtaining only bending rigidity, no large deformation is considered in the simulation, and only the linear elastic response is studied.

4.3 Result and discussion

4.3.1 Flexural properties of WF-PLA composite

Figure 4-4 and **Table 4-5** present the density and three-point bending experimental data for flexural modulus, rigidity, strengths and failure strain for all of the 3D printed samples (6 types, each having at least 3 replicas). The force-displacement curves of the samples are presented in Section 4.5.4, Supporting Information.

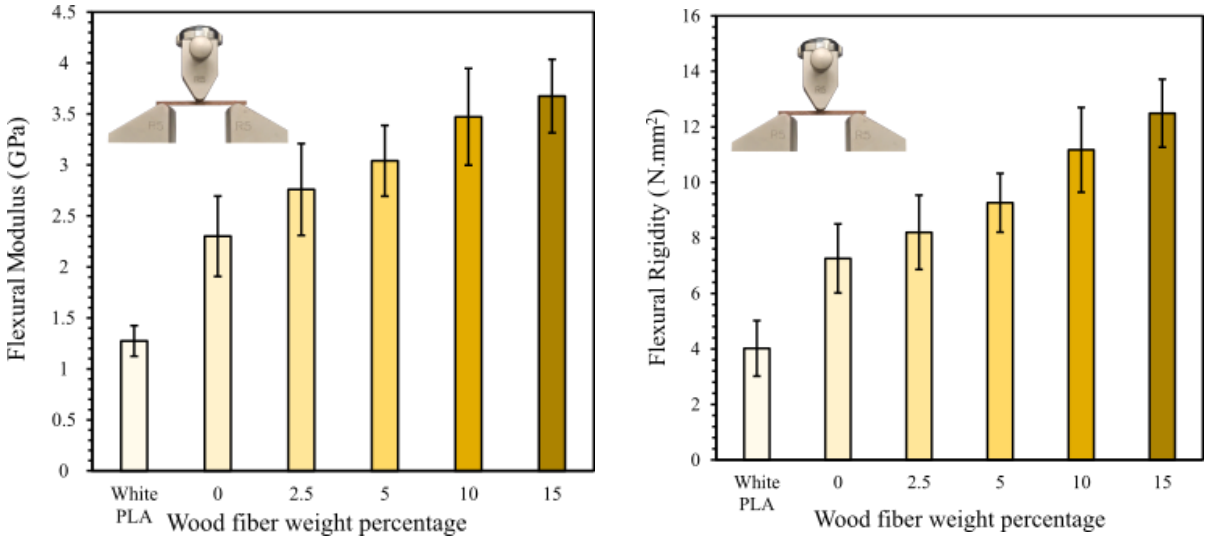

(a) (b)

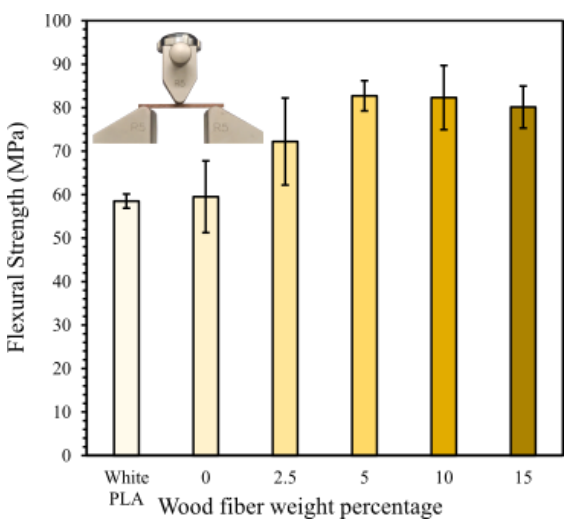

(c)

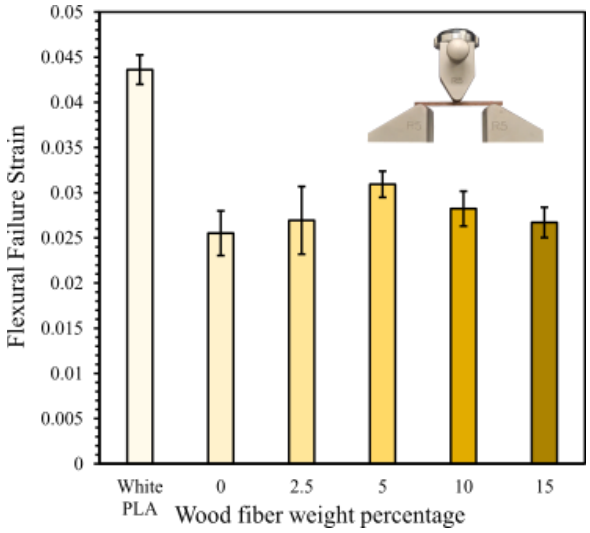

(d)

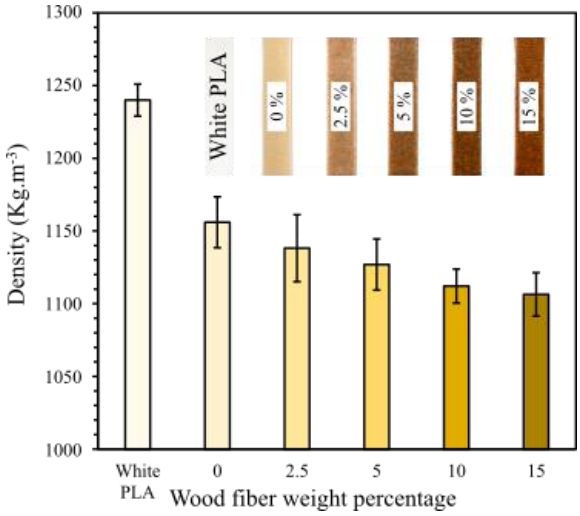

(e)

Figure 4 - 4: Comparing flexural mechanical properties of 3D-printed composites: (a) Flexural Modulus, (b) Flexural rigidity, (c) Flexural strength, (d) Flexural failure strain at outer surface and (e) Density.

Table 4 - 5: Material density and flexural properties of White PLA, pure PLA and WF-PLA composites.

	White PLA (Commercial)	**PLA 100% Wood 0%**	**PLA 97.5% Wood 2.5%**	**PLA 95% Wood 5%**	**PLA 90% Wood 10%**	**PLA 85% Wood 15%**
Density $[\times 10^{-2}\mathrm{Kg.\,m^{-3}}]$	12.40 ± 0.11	11.56 ± 0.17	11.38 ± 0.23	11.27 ± 0.17	11.12 ± 0.11	11.06 ± 0.15
Flexural modulus [MPa]	1273.7 ± 150	2301 ± 394	2760 ± 450	3041 ± 347	3472 ± 474	3676 ± 360
Flexural strength [MPa]	58.51 ± 1.62	59.52 ± 8.25	72.21 ± 10.0	82.72 ± 3.47	82.33 ± 7.37	80.14 ± 4.84
Flexural failure strain $[\times 10^{2}]$	4.36 ± 0.16	2.55 ± 0.24	2.69 ± 0.37	3.09 ± 0.14	2.82 ± 0.19	2.67 ± 0.16
Flexural rigidity $[\times 10^{2}\ \mathrm{N.\,mm^{2}}]$	401.76 ± 100	725.8 ± 124	819.9 ± 133	926.4 ± 105	1117.1 ± 152	1249.1 ± 122

As the experimental results show, increasing the wood fiber content enhances the flexural modulus and rigidity of WF-PLA. The flexural modulus and rigidity of 15 *wt%* WF-PLA is 60% and 72% greater than the pure PLA; however, the flexural modulus is only 5% higher than 10 *wt%* WF-PLA, suggesting that the flexural modulus of WF-PLA composite does not noticeably change beyond 10 *wt%* wood fiber content in the range considered in this thesis (**Figure 4-4a**, **b**). This is thought to be the result of inferior wood fiber dispersion in the samples for composites with higher wood fiber contents that causes agglomeration and plays an important role in the reduction of composite stiffness [32, 33]. The results of flexural strength presented in **Figure 4-4c** suggest that a percentage of wood fiber around 5 *wt%* maximizes the flexural strength of WF-PLA composite to surpass pure PLA. Beyond this optimum value, the flexural strength decreases by increasing the wood fiber content. The decreasing trend might be associated with the separation of wood fibers from the PLA matrix at stresses above the elastic limit due to the insufficient bonding of wood fibers and PLA, as no plasticizer has been used in this thesis for the low-cost manufacturing of composite filaments, creating gaps at the interface of matrix and wood fibers. Considering that wood fibers possess a higher strength than PLA [34, 35], until a percentage of wood fiber around 5 *wt%*, the increased flexural strength of PLA with added wood fibers is more than the weakening

effect of the imperfections; as the amount of wood fibers increases, introduced imperfect bonds and agglomeration surpass the strengthening effect of fibers. When the fiber content is about 5 *wt%* (**Figure 4-4d**), the flexural failure strain at the outer surface of the samples is also increased by 22% compared to the pure PLA. As opposed to commonly-found *performance trade-offs* [36, 37] in monolithic materials, where the enhancement of a specific material property commonly deteriorates another material's performance (e.g., trade-offs between material density and rigidity, strength and rigidity and rigidity and flexural failure strain), WF-PLA offers a new strategy to not only unravel the selected performance trade-offs to simultaneously enhance strength/modulus-to-density and rigidity/failure strain-to-density ratios (e.g., for 5 *wt%* of WF-PLA composite) (**Figure 4-4e**) but to also fabricate sustainable and recyclable advanced materials. If these WF-PLA composites are exploited to develop *architected materials*, a new class of advanced materials, i.e., *biocomposite metamaterials*, with unprecedented multifunctional properties (e.g., ultrahigh stiffness [38], programmable stiffness [39] and geometrical reconfiguration [40]) can be developed that inherit their exotic properties from both their architectural design and material composition of their constituents. **Table 4-5** reports the density and mechanical flexural properties of the 3D-printed WF-PLA composites. As presented, while reducing mass, the methodology reported in this thesis manages to enhance flexural modulus, strength, failure strain and rigidity. The corresponding empirical equations correlating the flexural mechanical properties to the wood fiber weight percentage (*wt%*) are presented in **Table 4-6** using the experimental data.

Table 4 - 6: Empirical equations for flexural mechanical properties of wood fiber-reinforced

Flexural modulus [MPa]	$E_f = \ 209310wt^3 - 101291wt^2 + 19614wt + 2307.9$
Flexural strength [MPa]	$\sigma_f = \ 21845wt^3 - 7415.7wt^2 + 760.9w_f + 59.04$
Flexural failure strain at the outer surface	$\varepsilon_f = \ 5.9096wt^3 - 1.9892wt^2 + 0.1756wt + 0.0251$
Flexural rigidity [$\times 10^2$ N.mm^2]	$EI_f = \ -75130wt^3 - 10099wt^2 + 3667.9wt + 725.19$

*$E_f, \sigma_f, \varepsilon_f, EI_f$: Flexural modulus, strength, failure strain at the outer surface and rigidity, respectively; *wt*: Wood fiber weight percentage.

4.3.2 Microstructure of WF-PLA samples

The morphology of the cross-sectional area of the broken WF-PLA bending samples with 10 and 15 *wt%* wood fiber contents is elicited by scanning electron microscopy (SEM) images shown respectively, in **Figure 4-5**. According to these figures, the reinforced samples feature more and larger internal voids with increasing wood fiber content, which is likely the result of extra vaporized moisture and trapped air remaining in the medium while mixing wood fibers with PLA to make the filament. Furthermore, the high porosity of wood fibers [35] can potentially introduce trapped air inside the system, forming void regions during the extruding process. The presence of longer wood fibers in the feedstock relative to the diameter of the nozzle can result in inconsistent material feeding during 3D printing, which can also be another reason for the existence of internal voids in the 3D printed samples. The ruptured fibers found in the cross-sectional images indicate effective load transfer between wood fibers and PLA matrix.

Furthermore, SEM images provide evidence of wood fibers that exhibit limited efficacy in reinforcement owing to their parallel orientation with respect to the section, as well as wood fibers that have been pulled out from the PLA matrix due to inadequate interfacial adhesion between the fiber and matrix, compounded by fiber agglomeration. To enhance the bonding between wood fiber and Polylactic acid (PLA), various approaches can be adopted. One of them is to increase the surface area of the wood fibers to provide more bonding opportunities, which can be achieved by

reducing the size of the fibers or using chemical or mechanical treatments to roughen the surface. Another method is to modify the surface of the wood fibers with chemical treatments such as acetylation or silanization to introduce functional groups that can react with the PLA and improve bonding. Additionally, coupling agents, compatibilizers and optimized processing conditions can be used to improve the adhesion between the two materials. Maleic anhydride-grafted polypropylene (MAPP) and polyethylene-graft-maleic anhydride (PE-g-MA) have been used as coupling agents and compatibilizers, respectively, to improve the bonding between wood fibers and PLA. These approaches should be tailored based on the specific application and desired properties of the final product [41, 42].

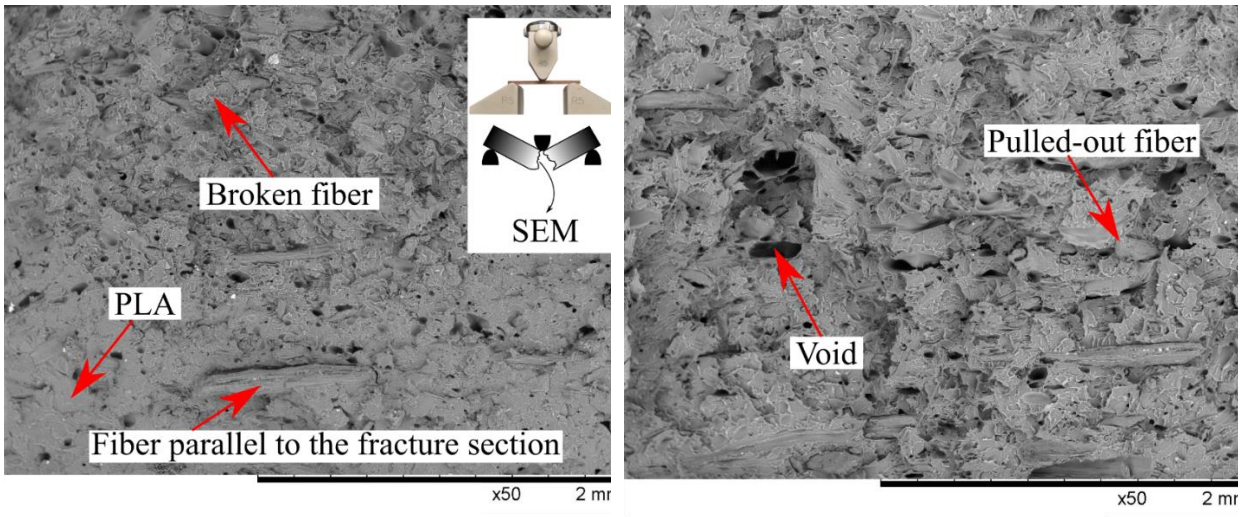

(a) (b)

Figure 4 - 5: SEM image of the fracture surface of 3D-printed WF-PLA test samples: (a) 10 *wt%* and (b) 15 *wt%*.

4.3.3 Flexural properties of architected cellular WF-PLA composite

4.3.3.1 Finite element simulation

To verify the discussed analytical findings, the anisotropy of flexural rigidity of cellular beams based on the *Isoflex* architectures is numerically analyzed. Three different *Isoflex* cell types are designed based on **Table 4-2** to evaluate and compare their isotropic bending rigidity. For all

samples, the length (l) is at least 20 times greater than the cross-section width. In **Figure 4-6a**, the analytical and simulation results for three different cell types with (i) the same height (10 cm) and width (11 cm) and (ii) the same height (10 cm) and a void fraction (0.9) (cell empty area to total cell area ratio), are compared.

Table 4 - 7: Geometrical and material composition parameters for *Isoflex* cells.

	Cell type	n	t_h (mm)	t_v (mm)	t_d (mm)	n_{vh}	n_{dh}	Void fraction
Figure 4-6a	Type A	1.1	0.01	0.55	-	0.0147	-	0.95
	Type B	1.1	0.01	0.69	0.01	0.01	1.79	0.93
	Type C	1.1	0.01	0.29	0.19	0.01	0.019	0.9
	Type A	1.9	0.031	1.9	-	0.00021		0.9
	Type B	1.7	0.12	1.54	0.006	0.01	0.0035	0.9
	Type C	1.1	0.01	0.29	0.019	0.01	0.02	0.9

*$n_{vh} = E_v/E_h$, $n_{dh} = E_d/E_h$.

Table 4-7 lists the cell width-to-height ratio (n), member's in-plane thicknesses, the ratio of modulus of elasticity (i.e., n_{vh}, n_{dh} and n_{dv}) and cell relative density, which are chosen based on equations given in **Table 4-2**. In order to ensure a fair comparison between this thesis's simulation results and analytical predictions, a minimum beam length-to-thickness ratio of 20 is maintained in the simulations. It should be noted that the classical Euler-Bernoulli Beam theory, which neglects the effect of transverse shear strain, tends to underestimate deflections. Nonetheless, for slender beams where the length-to-thickness ratio exceeds 20, the impact of these effects can be considered negligible [43]. The flexural rigidity anisotropicity ratio ($\frac{EI_{yy}}{EI_{xx}}$) of the cells based on detailed finite element analysis are compared with the samples made out of single material and provided in **Figure 4-6a**. The isotropic rigidity properties can be seen only in *Isoflex* composite samples, which confirms the accuracy of the equations given in **Table 4-2**.

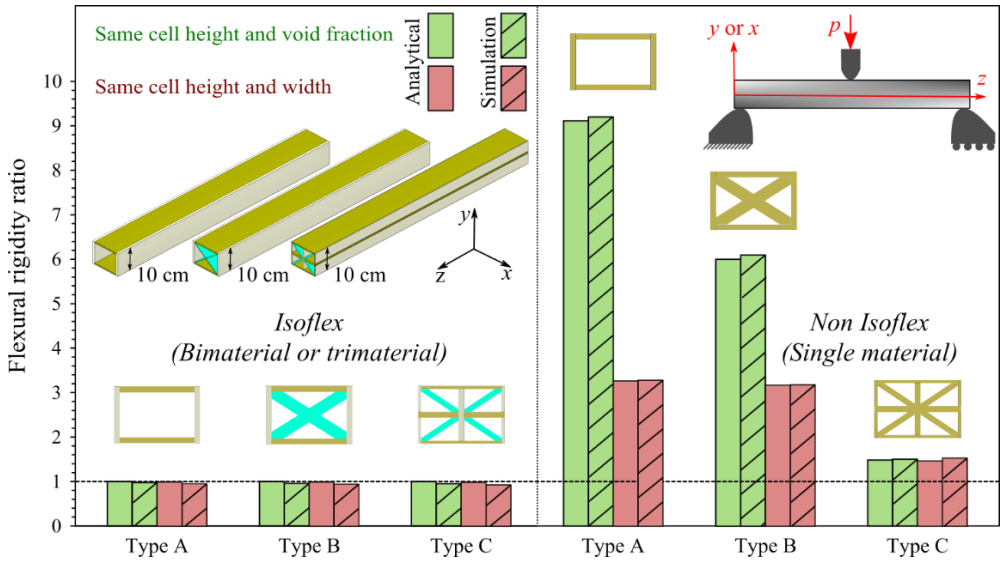
Same cell height and void fraction
Same cell height and width
Analytical
Simulation
Flexural rigidity ratio
10 cm
10 cm
10 cm
y or x
p
z
Isoflex
(Bimaterial or trimaterial)
Non Isoflex
(Single material)
Type A
Type B
Type C
Type A
Type B
Type C

(a)

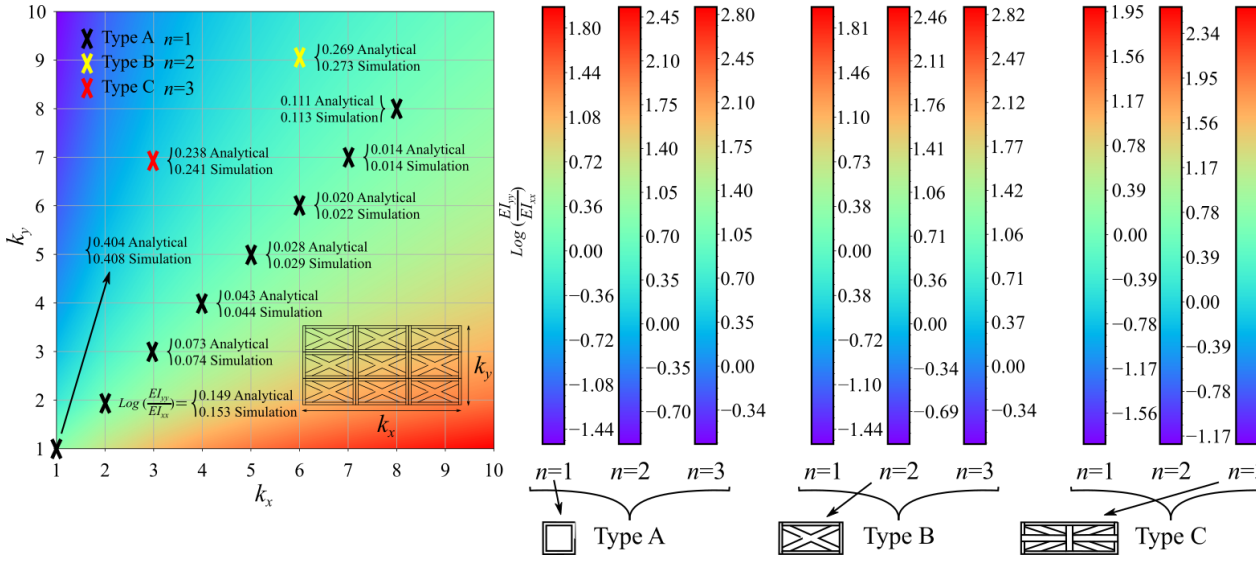
Type A n=1
Type B n=2
Type C n=3
0.269 Analytical
0.273 Simulation
0.111 Analytical
0.113 Simulation
0.238 Analytical
0.241 Simulation
0.014 Analytical
0.014 Simulation
0.020 Analytical
0.022 Simulation
0.404 Analytical
0.408 Simulation
0.028 Analytical
0.029 Simulation
0.043 Analytical
0.044 Simulation
0.073 Analytical
0.074 Simulation
0.149 Analytical
0.153 Simulation
n=1
n=2
n=3
Type A
Type B
Type C

(b)

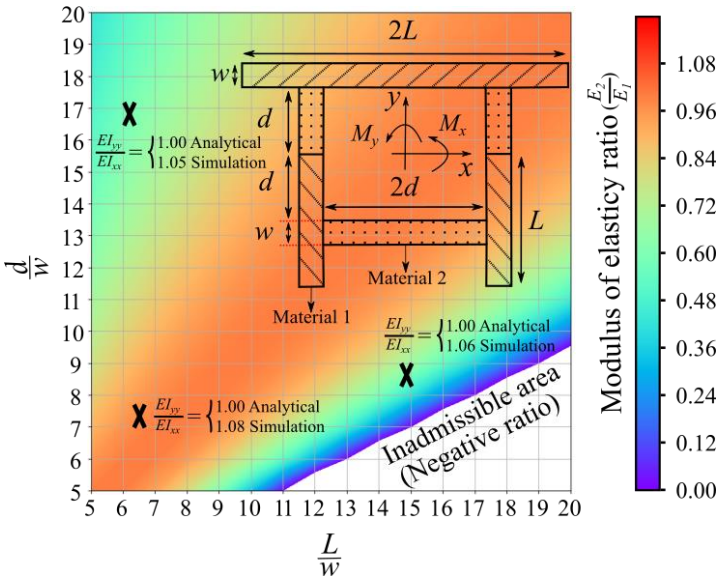

(c)

Figure 4 - 6: Comparison of the results obtained from analytical analysis and numerical simulation: (a) the rigidity anisotropicity for different types of *Isoflex* cells and the samples made out of single material: (i) cells with the same height and width, (ii) cells with the same height and void fraction, (b) Log of isotropicity ratio for a cross-section with kx × ky *Isoflex* cells for n = 1, 2, 3 and (c) Ratio of the module of elasticity to have isotropic flexural rigidity for unsymmetric cell type D.

In another investigation, the cross-section is extended to more than one cell. The logarithm of the flexural rigidity ratio ($log\frac{EI_{yy}}{EI_{xx}}$) is shown in **Figure 4-6b** for a cross-section with k_x by k_y Cells. As shown, regardless of cell type and constituent materials, for the number of cells approximately more than five, the most dominant parameter for the rigidity ratio is the number of cells in the *x* and *y*-directions and the cell width-to-height ratio (*n*). The approximate relationship is as follows:

$$\frac{EI_{yy}}{EI_{xx}} = \left(\mathrm{n}\frac{k_x}{k_y}\right)^2, \; k_x \; and \; k_y > 5 \tag{4.6}$$

In addition, to demonstrate the versatility of this thesis's method, an asymmetric cell is designed to exhibit isotropic bending properties by fabricating it from two materials. **Figure 4-6c** shows the condition of two materials (elastic modulus ratio of two materials) so that the cell shows

isotropic flexural rigidity. The white area in the diagram represents an area with no possible material design. As discussed in Section 4.3.1, choosing different fiber percentages along different cell members makes these designs possible.

4.3.3.2 Experimental tests

In this section, to better elucidate the effects of exploiting optimized material composition (traditional approach for enhancing material properties of base materials) and architected geometry (architected material approach for enhancing material properties by tuning spatial distribution of base materials) for controlling the mechanical performance of WF-PLA composites, experimental and FEM results of three-point bending tests for WF-PLA cellular composites type A, B and C *Isoflex* cells are presented. **Figure 4-7a** shows that cellular composites, 3D printed out of WF-PLA filament, possess greater flexural rigidity compared to the white PLA cellular specimens. For example, the specific flexural rigidity (rigidity over mass) of type A, B and C *Isoflex* cellular WF-PLA composites with 5 *wt%* wood fiber in (x, y) directions are, respectively, (118%, 37%), (120%, 30%) and (130%, 67%) higher than their counterparts made of pure PLA biopolymer. **Table 4-8** compares the specific flexural rigidity of cellular specimens made out of 5 *wt%* WF-PLA determined by conducting experimental testing (3 replicas), analytical method and numerical simulation through detailed FEM.

Table 4 - 8: Specific flexural rigidity of White PLA and WF-PLA cellular composites.

		Samples made out of only White PLA (Commercial) filament			***Isoflex* samples made out of WF-PLA filament**		
Specific flexural Rigidity $[N.m^2.Kg^{-1}]$		**Type A**	**Type B**	**Type C**	**Type A**	**Type B**	**Type C**
Analytical	X direction	272.97	261.93	189.58	565.61	525.02	364.45
	Y direction	432.56	399.98	211.86	565.60	525.02	364.45
Simulation	X direction	275.01	261.68	177.89	554.33	505.16	350.62
	Y direction	425.97	397.14	209.47	556.41	508.79	354.01
Experiment	X direction	263.96 ± 6.51	228.24 ± 5.70	145.43 ± 2.70	541.83 ± 6.94	503.59 ± 13.62	334.82 ± 9.37
	Y direction	393.08 ± 6.55	386.11 ± 8.7	202.50 ± 2.23	534.88 ± 18.37	501.629 ± 11.80	338.97 ± 12.31

Considering the reduction of material density of WF-PLA composite by adding the wood fiber content, the traditional approach presents a strategy for enhancing the rigidity-to-mass ratio of cellular solids by using an optimized material composition.

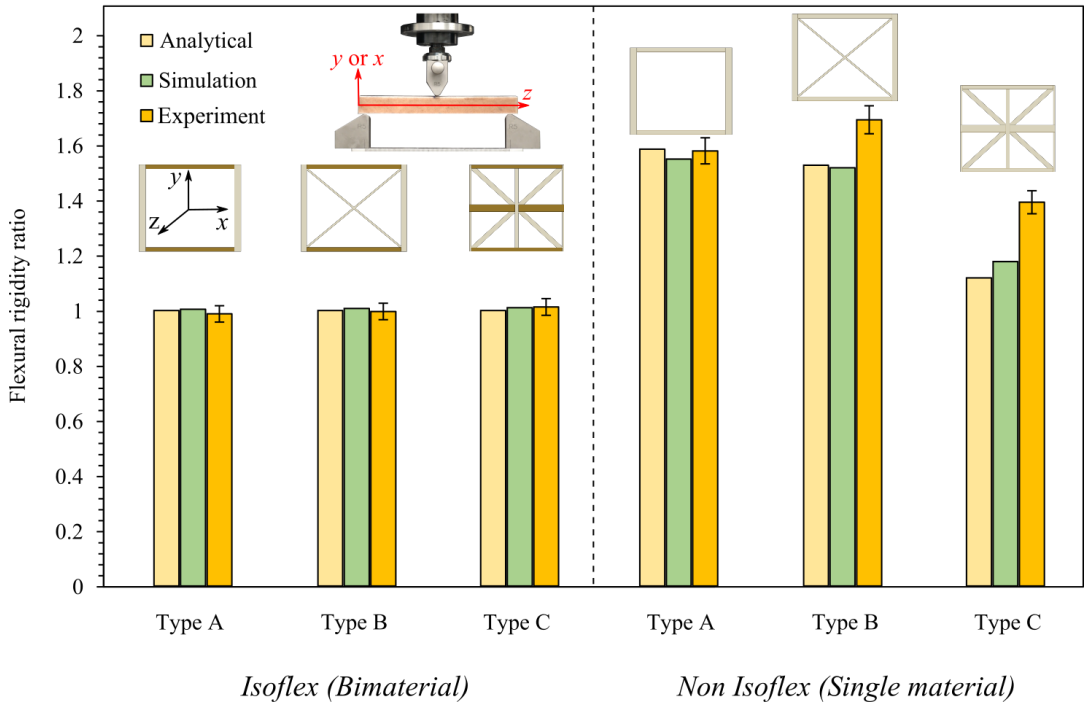

(a)

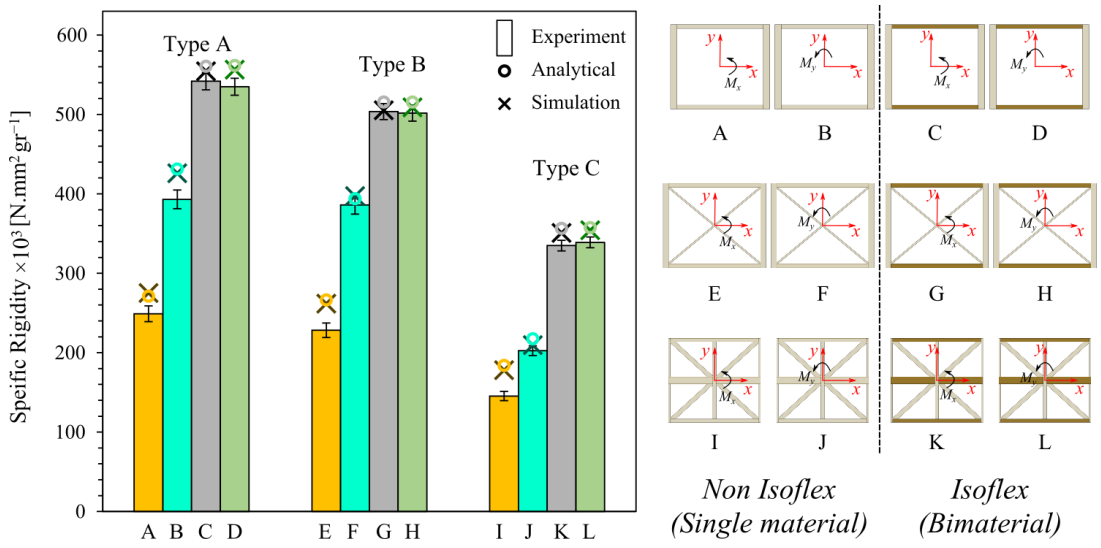

(b)

Figure 4 - 7: Comparison of (a) flexural rigidity ratio and (b) specific flexural rigidity obtained from the analytical analysis, experimental tests and numerical simulation for types A, B and C of Bimaterial *Isoflex* cell and the samples made out of single material.

In addition, engineering the architecture offers a unique strategy for programming the material properties of cellular solids by controlling their underlying geometry and, consequently, by tuning their effective properties. The experimental results in **Figure 4-7b** indicate that 3D printed *Isoflex* cellular specimens have not only higher rigidity but also isotropic rigidity compared to the pure PLA 3D printed samples. The discrepancy between FE analysis and experimental results is thought to be stemmed from the 3D printing defects.

4.4 Conclusions

This research introduces a low-cost additive manufacturing strategy for developing sustainable high-performance advanced materials. By integrating recycling and FDM 3D printing with a rational design of architected materials, architected wood fiber-reinforced polymeric (WF-PLA) cellular composites are designed and fabricated. While the sustainable cellular composite simultaneously benefits from the recyclability and biodegradability of wood and biopolymers and the high mechanical performance of wood fibers, it also offers controllable properties and

significant structural mass reduction. Mechanical tests on 3D printed WF-PLA composites show enhanced flexural modulus compared to pure PLA samples, e.g., 15 *wt%* addition of recycled wood fibers leads to a 60% increase in flexural modulus. The flexural strength can also be increased up to 39% when 5 *wt%* wood fiber is used for the fabrication of WF-PLA. To investigate the underlying failure mechanisms of the WF-PLA, the fractured surfaces of the 3D printed composite samples are studied using SEM micrographs, demonstrating the existence of ruptured fibers that confirm an effective load transfer between the wood fibers and the PLA matrix.

By exploiting the controllability of properties of lightweight cellular materials through tuning their underlying architecture and improving their constituent solid materials, a rational procedure is introduced, and engineered lightweight sheets of high-performance multi-material flexural-isotropic cellular architectures (*Isoflex*) are designed while they lack certain rotational symmetries of 2D square cells with 4-fold symmetries. To explore the efficacy of wood fiber addition to the pure PLA, WF-PLA filaments with 5 *wt%* wood fiber contents are used to 3D print three-point bending test samples of these *Isoflex* cellular architecture beams. In addition to the experimental tests, their effective flexural rigidity is investigated using detailed finite element modeling. The results demonstrate the possibility of simultaneous enhancement of the flexural isotropicity and flexural rigidity-to-mass ratio up to 130% and 99%, respectively, by optimizing cell architecture and material composition, showcasing a new dimension to engineering design and optimization, where lightweight and multifunctionality are achieved by multi-level engineering of the constitutive material and its underlying structure. The introduced design and manufacturing strategy results in the development of high-performance, sustainable advanced materials made of cost-effective, versatile, renewable and biodegradable constituents free of hazardous ingredients and can offer a paradigm shift in the fabrication of manmade green biocomposites for applications

in aerospace, automotive, construction and machinery sectors. The introduced approaches can potentially be tailored towards additive manufacturing of a wide range of biocomposite materials and structures out of other bio-compatible source materials, with controlled architecture and thermomechanical properties, delivering eco-friendly and application-specific multifunctional properties.

4.5 Supporting Information

4.5.1 Specifications of raw material

In this thesis, the wood fibers utilized are obtained by grinding sawdust from several hardwood species, including beech, northern red oak, black cherry, and white ash trees, provided by CANAWICK, located in Saint-Quentin, NB, Canada. The wood fibers are not treated with any additional chemicals. Previous studies have extensively reported on the mechanical properties of various types of hardwoods [44].

The specification of PLA pellet-4043D and commercial white PLA filaments are given in **Table 4-S1.**

Table 4-S1: Commercial **w**hite PLA filament and PLA pellets-4043D specification.

Parameter	Value	Parameter	Value
Filament diameter [mm]	2.85	Density [g.cm^{-3}]	1.24
Elongation at break	5.2%	Tensile strength [Mpa]	110-145
Elongation at yield	3.3%	Tensile modulus [MPa]	3300-3860
Filament density [g/cm3]	1.24	Melting temp. [^{o}C]	210 ± 8
Printing temperature [°C]	145 - 160	Feed temp. [^{o}C]	180
Tensile stress at yield MPa	49.5	Screw speed [rpm]	20-100
Tensile stress at break [MPa]	45.6		

4.5.2 Specifications of instruments

Filabot extruder and FDM Ultimaker S3 3D printer is used in this thesis to produce the

filaments and 3D print the test samples. **Table 4-S2** summarizes the specifications of this printer.

Table 4-S2: Specifications of Filabot extruder and Ultimaker S3 FDM printer.

Parameter	Value	Parameter	Value
Technology	Fused filament fabrication	Extruder length [cm]	22
Print head	Dual-extrusion	Extrusion temp. [ºC]	165
Build volume (XYZ) [mm^3]	230 × 190 × 200	Spooler pulling speed [mm.s-1]	28 ± 1
XYZ resolution [micron]	6.9, 6.9, 2.5	Feed screw driver speed [rpm]	17 ± 2
Nozzle diameters (mm)	0.25 – 0.8	Fan speed	70%
Operating sound (dB)	< 50	Nozzle diameter [mm]	3

4.5.3 Tensile moduli of elasticity of white PLA and WF-PLA 5 *wt%*:

In this thesis, the modulus of elasticity of commercial white PLA and WF-PLA (5 *wt%*) is measured using the dogbone tensile test as per the ASTM D638 standard. The stress-strain curves for the materials are shown in **Figure 4-S1** and present the modulus of elasticity.

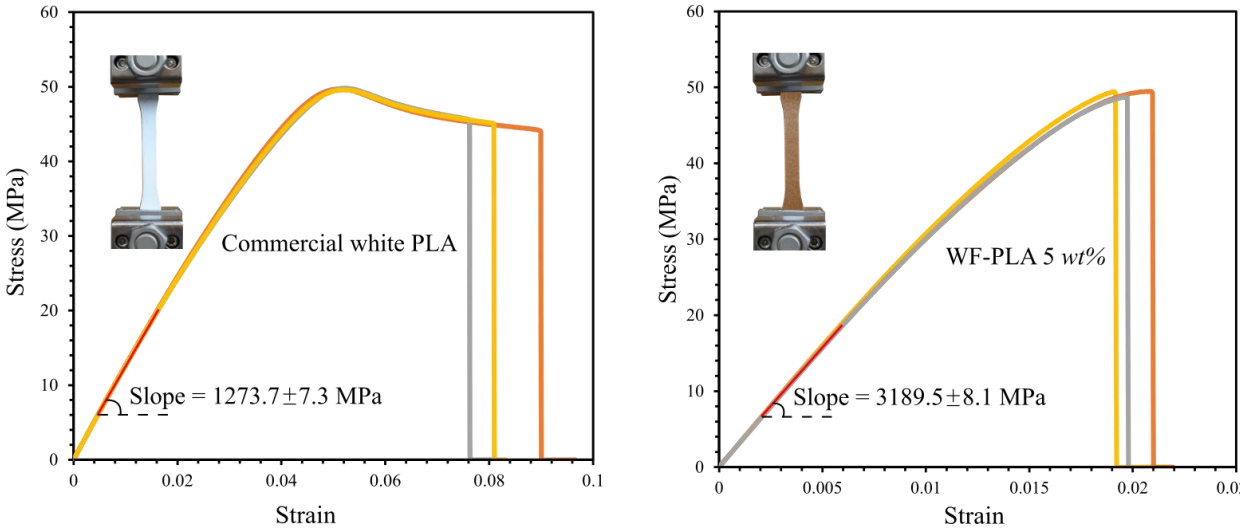

Figure 4-S1: Stress-strain curve for dogbone samples 3D printed by commercial white PLA and WF-PLA 5 *wt%* filaments.

4.5.4 Force-displacement curves for the three-point bending test samples

In this section, the Force-displacement curves extracted from the three-point bending tests are shown in **Figure 4-S2**.

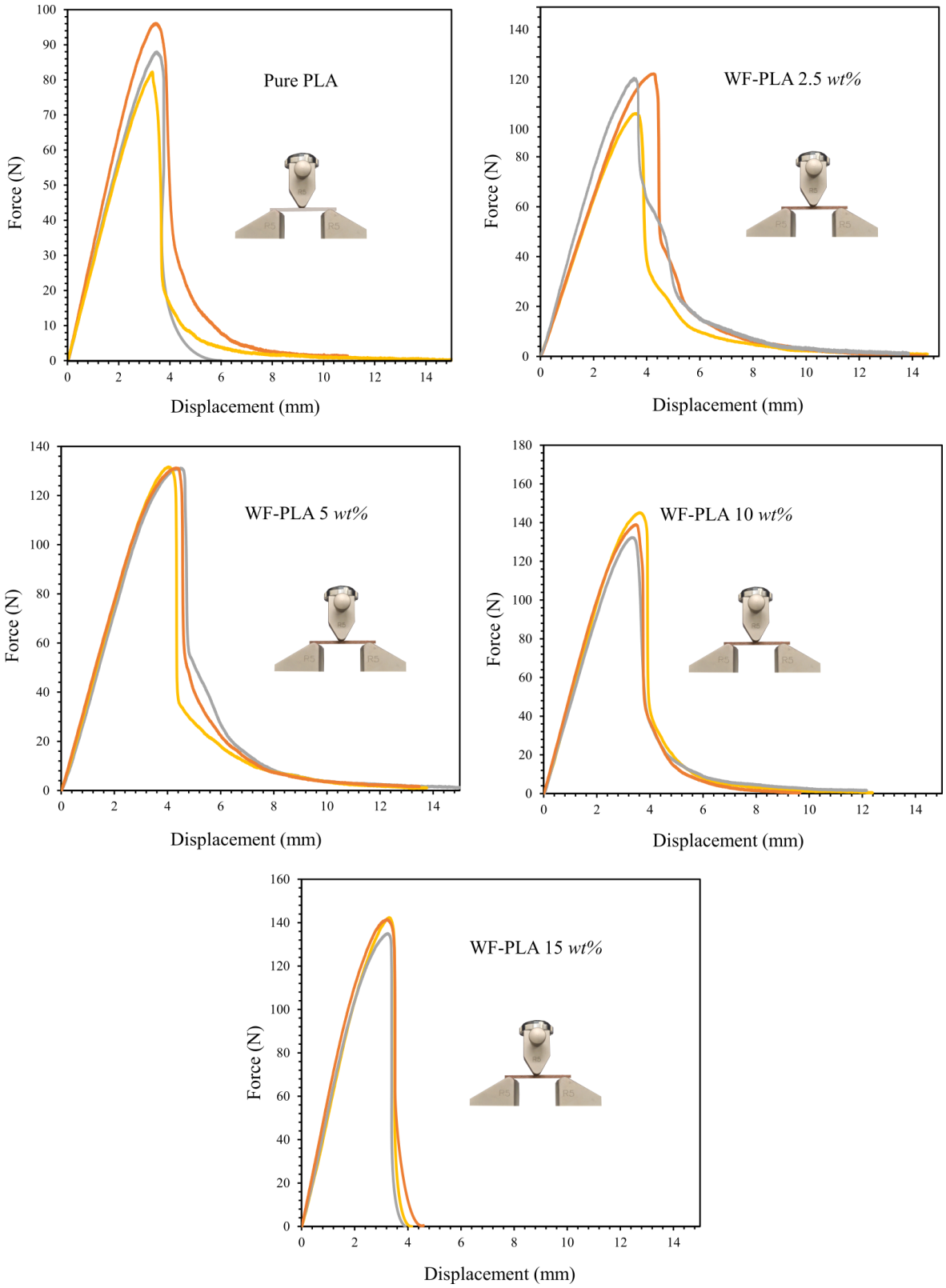

Figure 4-S2: Force-displacement curve for three-point bending test samples 3D printed by pure PLA, WF-PLA 2.5 *wt%*, 5 *wt%*, 10 *wt%* and 15 *wt%* filaments.

4.6 References

[1] Al-Ketan, O., R. Rowshan, and R.K. Abu Al-Rub, *Topology-mechanical property relationship of 3D printed strut, skeletal, and sheet based periodic metallic cellular materials.* Additive Manufacturing, 2018. 19: p. 167-183.

[2] Do, Q.T., C.H.P. Nguyen, and Y. Choi, *Homogenization-based optimum design of additively manufactured Voronoi cellular structures.* Additive Manufacturing, 2021. 45: p. 102057.

[3] Surjadi, J.U., L.B. Gao, H.F. Du, X. Li, X. Xiong, N.X. Fang, and Y. Lu, *Mechanical Metamaterials and Their Engineering Applications.* Advanced Engineering Materials, 2019. 21(3): p. 1800864.

[4] Mao, A., N. Zhao, Y. Liang, and H. Bai, *Mechanically Efficient Cellular Materials Inspired by Cuttlebone.* Adv Mater, 2021. 33(15): p. e2007348.

[5] Tao, Y., W.G. Li, K. Wei, S.Y. Duan, W.B. Wen, L.M. Chen, Y.M. Pei, and D.N. Fang, *Mechanical properties and energy absorption of 3D printed square hierarchical honeycombs under in-plane axial compression.* Composites Part B-Engineering, 2019. 176: p. 107219.

[6] Estakhrianhaghighi, E., A. Mirabolghasemi, Y.N. Zhang, L. Lessard, and A. Akbarzadeh, *3D-Printed Wood-Fiber Reinforced Architected Cellular Composites.* Advanced Engineering Materials, 2020. 22(11): p. 2000565.

[7] Hu, C., J.Q. Dong, J.J. Luo, Q.H. Qin, and G.Y. Sun, *3D printing of chiral carbon fiber reinforced polylactic acid composites with negative Poisson's ratios.* Composites Part B-Engineering, 2020. 201: p. 108400.

[8] Chen, X., G. Chen, G. Wang, P. Zhu, and C. Gao, *Recent progress on 3D-printed polylactic acid and its applications in bone repair.* Advanced Engineering Materials, 2020. 22(4): p. 1901065.

[9] Heidari-Rarani, M., M. Rafiee-Afarani, and A.M. Zahedi, *Mechanical characterization of FDM 3D printing of continuous carbon fiber reinforced PLA composites.* Composites Part B-Engineering, 2019. 175: p. 107147.

[10] Huang, W., M. Shishehbor, N. Guarin-Zapata, N.D. Kirchhofer, J. Li, L. Cruz, T. Wang, S. Bhowmick, D. Stauffer, P. Manimunda, K.N. Bozhilov, R. Caldwell, P. Zavattieri, and D. Kisailus, *A natural impact-resistant bicontinuous composite nanoparticle coating.* Nat Mater, 2020. 19(11): p. 1236-1243.

[11] Gouda, K., S. Bhowmik, and B. Das, *A review on allotropes of carbon and natural filler-reinforced thermomechanical properties of upgraded epoxy hybrid composite.* Reviews on Advanced Materials Science, 2021. 60(1): p. 237-275.

[12] Tran, T.Q., F.L. Ng, J.T.Y. Kai, S. Feih, and M.L.S. Nai, *Tensile Strength Enhancement of Fused Filament Fabrication Printed Parts: A Review of Process Improvement Approaches and Respective Impact.* Additive Manufacturing, 2022. 54: p. 102724.

[13] Sharafi, S., M.H. Santare, J. Gerdes, and S.G. Advani, *A review of factors that influence the fracture toughness of extrusion-based additively manufactured polymer and polymer composites.* Additive Manufacturing, 2021. 38: p. 101830.

[14] Le Duigou, A., G. Chabaud, R. Matsuzaki, and M. Castro, *Tailoring the mechanical properties of 3D-printed continuous flax/PLA biocomposites by controlling the slicing parameters.* Composites Part B: Engineering, 2020. 203: p. 108474.

[15] Solodov, A.N., J. Shayimova, D. Balkaev, A.S. Nizamutdinov, K. Zimin, A.G. Kiiamov, R.R. Amirov, and A.M. Dimiev, *High-throughput, low-cost and "green" production method for highly*

stable polypropylene/perovskite composites, applicable in 3D printing. Additive Manufacturing, 2022. 59: p. 103094.
[16] Vedrtnam, A., S. Kumar, and S. Chaturvedi, *Experimental study on mechanical behavior, biodegradability, and resistance to natural weathering and ultraviolet radiation of wood-plastic composites.* Composites Part B-Engineering, 2019. 176: p. 107282.
[17] Bi, X. and R. Huang, *3D printing of natural fiber and composites: A state-of-the-art review.* Materials & Design, 2022. 222: p. 111065.
[18] Guzzi, E.A. and M.W. Tibbitt, *Additive Manufacturing of Precision Biomaterials.* Adv Mater, 2020. 32(13): p. e1901994.
[19] Gao, X., S.X. Qi, X. Kuang, Y.L. Su, J. Li, and D.J. Wang, *Fused filament fabrication of polymer materials: A review of interlayer bond.* Additive Manufacturing, 2021. 37: p. 101658.
[20] Xiong, Y., Y.L. Tang, Q. Zhou, Y.S. Ma, and D.W. Rosen, *Intelligent additive manufacturing and design state of the art and future perspectives.* Additive Manufacturing, 2022. 59: p. 103139.
[21] Singh, G., J.M. Missiaen, D. Bouvard, and J.M. Chaix, *Copper extrusion 3D printing using metal injection moulding feedstock: Analysis of process parameters for green density and surface roughness optimization.* Additive Manufacturing, 2021. 38: p. 101778.
[22] Chang, S.M., S. Hur, J. Park, D.G. Lee, J. Shin, H.S. Kim, S. Eun, J.M. Baik, M. Kim, H.C. Song, and C.Y. Kang, *Optimization of piezoelectric polymer composites and 3D printing parameters for flexible tactile sensors.* Additive Manufacturing, 2023. 67: p. 103470.
[23] Beer, F.P., E.R. Johnston, J.T. DeWolf, and D.F. Mazurek, *Statics and mechanics of materials*. 2021: McGraw-Hill Education.
[24] Li, D., X. Bu, Z. Xu, Y. Luo, and H. Bai, *Bioinspired Multifunctional Cellular Plastics with a Negative Poisson's Ratio for High Energy Dissipation.* Adv Mater, 2020. 32(33): p. e2001222.
[25] Shi, J., H. Mofatteh, A. Mirabolghasemi, G. Desharnais, and A. Akbarzadeh, *Programmable Multistable Perforated Shellular.* Adv Mater, 2021. 33(42): p. e2102423.
[26] Tian, X. and K. Zhou, *3D printing of cellular materials for advanced electrochemical energy storage and conversion.* Nanoscale, 2020. 12(14): p. 7416-7432.
[27] Li, X., X. Yu, and W. Zhai, *Additively Manufactured Deformation-Recoverable and Broadband Sound-Absorbing Microlattice Inspired by the Concept of Traditional Perforated Panels.* Adv Mater, 2021. 33(44): p. e2104552.
[28] Al-Ketan, O. and R.K. Abu Al-Rub, *Multifunctional Mechanical Metamaterials Based on Triply Periodic Minimal Surface Lattices.* Advanced Engineering Materials, 2019. 21(10): p. 1900524.
[29] Jiang, Z. and J.H. Pikul, *Centimetre-scale crack-free self-assembly for ultra-high tensile strength metallic nanolattices.* Nat Mater, 2021. 20(11): p. 1512-1518.
[30] Zhou, Q.Y., J.Y. Lyu, G. Wang, M. Robertson, Z. Qiang, B. Sun, C.H. Ye, and M.F. Zhu, *Mechanically Strong and Multifunctional Hybrid Hydrogels with Ultrahigh Electrical Conductivity.* Advanced Functional Materials, 2021. 31(40): p. 2104536.
[31] Estakhrianhaghighi, E., A. Mirabolghasemi, J. Shi, L. Lessard, and A.H. Akbarzadeh, *Architected cellular fiber-reinforced composite.* Composites Part B-Engineering, 2022. 238: p. 109894.
[32] Ghasemi, A.R., M. Mohandes, R. Dimitri, and F. Tornabene, *Agglomeration effects on the vibrations of CNTs/fiber/polymer/metal hybrid laminates cylindrical shell.* Composites Part B-Engineering, 2019. 167: p. 700-716.
[33] Wu, Z., Y. Zhao, K. Yang, J. Guan, S. Wang, Y. Gu, M. Li, Y. Feng, W. Feng, and R.O. Ritchie, *Enhancing the Mechanical Performance of Fiber-Reinforced Polymer Composites Using*

Carbon Nanotubes as an Effective Nano-Phase Reinforcement. Advanced Materials Interfaces, 2023. 10(3): p. 2201935.
[34] Liu, W.D., T.T. Chen, M.E. Fei, R.H. Qiu, D.M. Yu, T.F. Fu, and J.H. Qiu, *Properties of natural fiber-reinforced biobased thermoset biocomposites: Effects of fiber type and resin composition.* Composites Part B-Engineering, 2019. 171: p. 87-95.
[35] Keplinger, T., F.K. Wittel, M. Ruggeberg, and I. Burgert, *Wood Derived Cellulose Scaffolds-Processing and Mechanics.* Adv Mater, 2021. 33(28): p. e2001375.
[36] Luo, X., D. Li, C. Yang, A. Gebert, H. Lu, T. Song, H. Ma, L. Kang, Y. Long, and Y. Li, *Circumventing the strength–ductility trade-off of β-type titanium alloys by defect engineering during laser powder bed fusion.* Additive Manufacturing, 2022. 51: p. 102640.
[37] Jeong, Y.B., T. Wada, S.H. Joo, J.M. Park, J. Moon, H.S. Kim, I.V. Okulov, S.H. Park, J.H. Lee, K.B. Kim, and H. Kato, *Beyond strength-ductility trade-off: 3D interconnected heterostructured composites by liquid metal dealloying.* Composites Part B-Engineering, 2021. 225: p. 109266.
[38] Peng, M., Z. Wen, L. Xie, J. Cheng, Z. Jia, D. Shi, H. Zeng, B. Zhao, Z. Liang, T. Li, and L. Jiang, *3D Printing of Ultralight Biomimetic Hierarchical Graphene Materials with Exceptional Stiffness and Resilience.* Adv Mater, 2019. 31(35): p. e1902930.
[39] Levine, D.J., K.T. Turner, and J.H. Pikul, *Materials with Electroprogrammable Stiffness.* Adv Mater, 2021. 33(35): p. e2007952.
[40] Kuang, X., S. Wu, Q. Ze, L. Yue, Y. Jin, S.M. Montgomery, F. Yang, H.J. Qi, and R. Zhao, *Magnetic Dynamic Polymers for Modular Assembling and Reconfigurable Morphing Architectures.* Adv Mater, 2021. 33(30): p. e2102113.
[41] Liu, R., S.P. Luo, J.Z. Cao, and Y. Peng, *Characterization of organo-montmorillonite (OMMT) modified wood flour and properties of its composites with poly(lactic acid).* Composites Part a-Applied Science and Manufacturing, 2013. 51: p. 33-42.
[42] Effah, B., A. Van Reenen, and M. Meincken, *Mechanical properties of wood-plastic composites made from various wood species with different compatibilisers.* European Journal of Wood and Wood Products, 2018. 76(1): p. 57-68.
[43] Witmer, E., *Elementary bernoulli-euler beam theory.* MIT Unified Engineering Course Notes, MIT, 1991. 1992: p. 114-164.
[44] Green, D., J. Winandy, and D. Kretschmann, *Mechanical properties of wood, Chapter 4.* Wood Handbook–Wood as an Engineered Material, FPL-GTR-113, USDA Forest Service, Forest Products Laboratory, Madison WI, USA, 1999.

5 Chapter five: General Conclusions

Cellular materials have been created for many years and used in a wide range of applications. As a result of the development of innovative manufacturing technologies, their underlying architectures and material composition have recently been engineered and developed. Most lattice materials, including those used in sandwich constructions and shock absorbers, have honeycomb made out of a single material. Nevertheless, cutting-edge manufacturing techniques have offered engineers fascinating opportunities to make creative designs and enhance the functionality of the structural components. The majority of these innovative designs are developed based on intricate patterns used as an RVE for periodic lattice materials. This dissertation not only aims to design the underlying architecture of lattice materials but also proposes the idea of engineering the material composition and rational material variation across the cellular structure to further enhance the functionalities of lightweight structures.

In this research, the performance of cellular materials has been studied using four main methods: analytical, homogenized modeling, detailed finite element modeling and experiments. The discrepancies in the results of these methods can be attributed to a variety of factors. First, one of the presumptions of the homogenization theory is that the lattice material is periodic; however, this assumption may not always be accurate in the random fiber-reinforced composite. Second, the boundary conditions represented in the homogenized and detailed finite element modeling are not exactly the same as those of tests. Finally, the manufactured examples might have imperfections and defects that affect the experiments' results, especially compared to the analytical method.

Although there are variations between the outcomes of these techniques in these four ways, overall, the results are in good agreement. This thesis's results indicate that architecting the cellular materials' underlying structure and material constitution is an effective tool for engineering and programming the mechanical properties of the cellular structures. A cellular solid's modulus, strength, toughness, strain, and flexural rigidity can be improved through rational design and by adding the optimum percentage of short fibers. The following statements can be used as a guideline for selecting the proper design and fiber percentages of cellular structures:

- The addition of an optimal amount of short fibers enhances the tensile and flexural modulus and strength of cellular materials compared to pure materials.
- The use of natural fibers, such as wood, can make cellular materials more sustainable and eco-friendly while simultaneously decreasing overall mass and enhancing thermomechanical properties.
- By engineering the material constitution and cell topology of cells, it is possible to control and program the mechanical properties of cellular materials.
- The variation of the fiber volume fraction across the member of cellular materials is more effective than using different materials in terms of achieving better adhesion of members to each other.

According to the application where cellular solids are used, the aforementioned results can assist designers in selecting the proper geometrical and material design as well as the short-fiber volume fraction in lattice structures. Some instances of industries that could profit from engineered cellular architectures are given below:

Automotive and Aircraft: Cellular materials are used in airplane and car bumpers to keep the structural integrity of the systems and to dampen exterior loads and forces coming from all directions. These cellular materials' mass and environmental hazards can be considerably reduced while maintaining or improving functionality if they are substituted with rationally designed cellular structures, such as *Isomixed* and *Isoflex*.

Construction: The essential components of construction-related structures, including buildings and bridges, are beams, particularly sandwich beams. By raising the stiffness and strength-to-mass ratio of the beams, this thesis's proposed approach can improve efficiency while keeping them environmentally benign and sustainable.

Energy: The suggested approach can be advantageous to the energy industry in a number of ways. First, lowering a vehicle's mass reduces fuel demand while improving its load-bearing capabilities. Additionally, the potential for recycling the rationally designed mechanical components used in industry can drop costs and energy consumption.

5.1 Limitations and challenges of wood fiber-reinforced composites

Wood fiber-reinforced composites have shown promising properties and potential in various applications, but they also come with certain limitations and challenges. Some of the limitations of wood fiber-reinforced composites include:

Moisture Sensitivity: Wood fibers have a tendency to absorb moisture from the environment, which can lead to dimensional changes, reduced mechanical properties, and degradation over time. This moisture absorption can impact the stability and durability of the composite material, particularly in humid or wet conditions.

Biodegradability: While the biodegradability of wood fibers is an environmentally friendly aspect, it can also be a limitation in certain applications where long-term durability is essential. Wood fibers may degrade over time, affecting the overall performance and lifespan of the composite material.

Susceptibility to Biological Attack: Wood fibers are susceptible to biological degradation by fungi, bacteria, and insects. In applications where the composite is exposed to outdoor or damp environments, these biological agents can compromise the structural integrity of the material.

Variability in Properties: The properties of wood fibers can vary depending on factors such as species, source, and processing methods. This natural variability can lead to inconsistencies in the mechanical and thermal properties of the composite material, making it challenging to predict and control performance.

Compatibility with Polymers: Achieving good bonding and compatibility between wood fibers and polymer matrices can be challenging. The hydrophilic nature of wood fibers and the hydrophobic nature of many polymers can lead to poor interfacial adhesion, affecting the overall strength and stiffness of the composite.

Limited High-Temperature Performance: Wood fibers are organic materials and can degrade or burn at high temperatures. This limits the use of wood fiber-reinforced composites in applications that involve exposure to elevated temperatures or fire.

Processing Challenges: Wood fibers can be abrasive and may cause wear on processing equipment, such as molds and extrusion dies. They can also lead to challenges in achieving uniform dispersion within the polymer matrix during manufacturing processes.

Cost and Availability: The cost and availability of wood fibers can vary based on factors like geographic location and demand. In some cases, wood fibers may be more expensive or less accessible compared to other reinforcement options.

Limited Design Flexibility: Wood fibers have certain inherent characteristics that may limit the design flexibility of the composite material. Complex shapes and intricate designs may be more challenging to achieve with wood fiber-reinforced composites.

Despite these limitations, ongoing research and development efforts are aimed at addressing these challenges and optimizing the performance of wood fiber-reinforced composites for various applications.

5.2 Possible applications of CFRCs

CFRCs can have real-life applications in a variety of industrial sectors, from aerospace (e.g., structural components), marine (e.g., boat hulls and decks) and automotive (e.g., door panels, bumper beams) in addition to energy (e.g., wind turbine blades, hydroelectric turbines and supports for solar panels). CFRCs are also increasingly finding applications in the field of medicine due to designs that have biocompatibility, mechanical strength and ability to be customized for specific applications. Some real-life applications of CFRCs in medicine include orthopedic implants (e.g., bone plates, screws and pins), dental restorations (e.g., crowns and bridges), prosthetic limbs (e.g., artificial legs and arms), wound dressings (e.g., bandages and dressings for burns and chronic wounds) and tissue engineering (e.g., scaffolds to support the growth of new tissue).

Isotropic mechanical properties of structures such as *Isomixed* and *Isoflex* are important for

the industry because they ensure consistent and predictable material behavior in all directions. This uniformity simplifies design and manufacturing processes, enhances structural integrity, and facilitates efficient and reliable performance in various applications. In aerospace, isotropic structures ensure uniform load distribution in aircraft frames and engine components. The automotive sector benefits from predictable performance in chassis and suspension systems. Shipbuilding relies on isotropic structures for consistent strength in marine structures. In civil engineering, bridges, buildings, and roadways utilize isotropic properties for stability. Consumer goods like sporting equipment and electronics leverage isotropy for consistent performance and protection. Medical devices and industrial equipment also employ isotropic structures to ensure even weight distribution, precision, and stability. The adoption of isotropic structures streamlines engineering processes and underpins the reliability of diverse structures across industries.

5.3 Future directions

Exploiting cellular solids' mechanical characteristics is the starting point for the majority of their early applications. The fabrication of cellular materials has significantly improved in recent decades from the perspective of solid mechanics, and more effective structures have been proposed and developed. This dissertation also focused on the material composition and future evolution of cellular solids; however, more research needs to be done on the suggested approach from different angles. This multidisciplinary dissertation holds significant implications for carbon sequestration and global warming mitigation through its innovative approach to recycling wood waste for the production of wood fiber-reinforced composites. By repurposing wood waste into durable composite materials, this research contributes to carbon sequestration by extending the lifespan of

stored carbon, reducing deforestation pressures, and lowering the embodied carbon in the final products. Through the substitution of high-carbon materials and the promotion of a circular economy, the project showcases sustainable practices that can inspire broader adoption in the field, making a tangible contribution towards addressing climate change challenges.

The following are some ideas for upcoming studies on fiber-reinforced architected cellular structures to enhance mechanical and multiphysical properties:

5.3.1 Mechanical aspect

The additional study can focus on the following topics in addition to the ones covered in this dissertation:

- In the realm of sustainable composite materials, a potential future endeavor involves investigating natural sizing agents to enhance bonding between waste wood fibers and matrix materials. Derived from renewable sources like plant extracts, biopolymers, and microbial polymers, these bio-based agents offer a viable alternative to conventional sizing agents. By incorporating these natural agents into the manufacturing process of fiber-reinforced composites, the mechanical properties and ecological footprint of the materials can be improved. Exploring the compatibility and efficacy of these agents with waste wood fibers, a readily available and environmentally friendly resource, holds promise for advancing both recycling efforts and the development of greener composite materials. This line of inquiry could lead to the formulation of optimized natural sizing agents tailored to the unique characteristics of waste wood fibers, ushering in a new era of sustainable composite manufacturing.
- Prospective future investigations may focus on manipulating fiber orientations within cellular

composites to intricately tailor their mechanical properties. By delving into techniques for precise microstructural control, a novel realm of material engineering emerges, offering the potential to redefine design paradigms.

- Prospective future studies could delve into the integration of Nano wood particles into the 3D printing process of composites, aiming to enhance mechanical properties and printability. This unexplored frontier holds the potential to advance additive manufacturing techniques, unravel synergistic interactions, and contribute to sustainable materials engineering for diverse applications.
- The future trajectory of material science could encompass the engineering of cellular materials featuring a gradient of fiber percentages along their length or thickness. This innovative approach holds the promise of finely tuning and customizing the mechanical attributes of these materials, ushering in a new era of controlled material properties. This pursuit not only invites exploration into fiber-material interactions but also hints at transformative applications across diverse industries.

5.3.2 Thermal aspect

The present thesis aims to investigate the isotropic mechanical properties of fiber-reinforced cellular composites through a novel methodology. While isotropic thermal properties are often crucial for CFRCs applications, this thesis's focus here is on the isotropicity of mechanical properties. It is demonstrated that the proposed methodology successfully achieves isotropic mechanical properties, providing a significant advancement toward developing CFRCs with improved mechanical performance. Further studies could be conducted to explore the correlation between the material properties and cell geometry to obtain the isotropic thermal properties of

CFRCs. This would provide valuable insights for designing and developing CFRCs in a wide range of applications. These findings could have important implications for the development of sustainable, high-performance materials with broad practical applications.

5.3.3 Multiphysical aspect

Aside from the mechanical aspect, cellular solids have promise in other fields, such as physics. They are used for their thermal, electrical and acoustic characteristics, as described in **Chapter 1**. Integrating these functions can also enrich cellular structures with vast potential and abilities. This thesis attempted to shed light on some of these capabilities by investigating the thermomechanical properties of fiber-reinforced cellular solids in tension and bending. Future research on this feature of cellular solids is, however, recommended to explore a few other fascinating topics:

- A compelling avenue for future research involves the meticulous engineering of fiber content and properties to attain comprehensive mechanical and thermal isotropy within cellular structures. This unexplored territory promises transformative outcomes across diverse industries, necessitating a strategic balance of fiber distribution, orientation, and composition. The resulting materials could redefine traditional boundaries, finding applications in aerospace, biomedicine, and beyond. This intriguing pursuit not only advances our knowledge of materials science and engineering but also holds the potential to reshape the very fabric of innovation.
- In prospective research, the exploration of short fibers endowed with electromagnetic and thermal properties presents a compelling avenue for fortifying cellular resistance along its

principal load-bearing orientation. These fibers, envisioned as actuating agents, possess the remarkable potential to respond to external fields, thereby enabling precise control and programmability over the shape, thermomechanical, and electromechanical characteristics of fiber-reinforced cellular structures. Additionally, delving into the intriguing realm of coupling electromagnetic and thermal stimuli could potentially usher in a new era of heightened cellular resilience, opening up uncharted vistas for advancing materials science and enriching the realm of structural integrity.